

Electronic Thesis and Dissertation Repository

---

12-4-2014 12:00 AM

## Scale-Up Methodology for Bench-Scale Slurry Photocatalytic Reactors Using Combined Irradiation and Kinetic Modelling


Patricio J. Valades Pelayo, *The University of Western Ontario*

Supervisor: Dr. Hugo I. de Lasa, *The University of Western Ontario*

A thesis submitted in partial fulfillment of the requirements for the Doctor of Philosophy degree in Chemical and Biochemical Engineering

© Patricio J. Valades Pelayo 2014

Follow this and additional works at: <https://ir.lib.uwo.ca/etd>

 Part of the [Catalysis and Reaction Engineering Commons](#), [Environmental Chemistry Commons](#), [Environmental Engineering Commons](#), [Physical Processes Commons](#), and the [Transport Phenomena Commons](#)

---

### Recommended Citation

Valades Pelayo, Patricio J., "Scale-Up Methodology for Bench-Scale Slurry Photocatalytic Reactors Using Combined Irradiation and Kinetic Modelling" (2014). *Electronic Thesis and Dissertation Repository*. 2528. <https://ir.lib.uwo.ca/etd/2528>

This Dissertation/Thesis is brought to you for free and open access by Scholarship@Western. It has been accepted for inclusion in Electronic Thesis and Dissertation Repository by an authorized administrator of Scholarship@Western. For more information, please contact [wlsadmin@uwo.ca](mailto:wlsadmin@uwo.ca).

SCALE-UP METHODOLOGY FOR BENCH-SCALE SLURRY PHOTOCATALYTIC  
REACTORS USING COMBINED IRRADIATION AND KINETIC MODELLING

(Thesis format: Integrated Article)

by

Patricio Javier Valades Pelayo

Graduate Program in Chemical and Biochemical Engineering

A thesis submitted in partial fulfillment  
of the requirements for the degree of  
Doctor of Philosophy

The School of Graduate and Postdoctoral Studies  
The University of Western Ontario  
London, Ontario, Canada

© Patricio Javier Valades Pelayo 2014

## Abstract

The present study focuses on developing a predictive methodology to scale-up a slurry annular photoreactor using a TiO<sub>2</sub> Degussa P25 from the bench-scale to a pilot-plant scale. The bench-scale photoreactor is a Photo-CREC-Water II (PCWII), a 2.65 L internally-irradiated slurry annular photocatalytic reactor (Total volume of slurry, 6.0 L). The pilot-plant scale photoreactor is a Photo-CREC Water Solar Simulator, a 9.8 L pilot-plant photoreactor, (Total volume, 18 liters of slurry) externally irradiated by eight lamps.

The proposed approach involves two Monte Carlo methods to model the Radiative Transfer Equation (RTE) inside each photoreactor. The adopted methodology allows the independent validation of radiative and kinetic models avoiding cross-correlation issues. With this end, a novel probe is developed to measure irradiance at different radial positions. This allows determining both adequate boundary conditions directly in the photo-CREC-Water II unit as well as establishing a geometry-independent phase function for Degussa P25 TiO<sub>2</sub> in the 25 to 400 mg l<sup>-1</sup> ranges. Uncertainty of LVREA was compared between different experimental methodologies currently found in the open literature for optical parameter estimation. In this regard, the proposed methodology was seen to outperform all other presented approaches.

On the other hand, a kinetic model and kinetic parameters are established by carrying out photocatalytic degradations of a model pollutant (Oxalic Acid). The determination of oxalic acid concentration is followed by TOC analysis in the PCWII reactor. Kinetic experiments are developed at different photocatalyst concentrations and various irradiance conditions. Additionally, convective and dispersive transport models are proposed and solved by Finite Element (FE) Method to determine the photocatalyst irradiation time in each photoreactor unit and ultimately to predict the overall photocatalytic efficiency. Finally the kinetic-irradiance based model is validated. This is done by successfully predicting irradiance profiles and degradation rates at different photocatalyst concentrations and irradiance conditions on the larger scale, externally irradiated eight-lamp Photophotoreactor.

## Keywords

Photocatalytic Reactors; Radiation Field; Monte Carlo, Phase Functions, Scale up, LVRPA.

## Co-Authorship Statement

This thesis was completed under the supervision of Professor Hugo de Lasa and Professor Benito Serrano Rosales. The four articles based on Chapter 3,4, 5, and 6 are all co-authored with them. Both, Dr. Hugo de Lasa and Dr. Benito Serrano, provided helpful recommendations throughout the whole research project and suggested key corrections to the draft versions of all four manuscripts. Additionally, for these four papers, the extent of the collaboration of every other co-author is stated below.

Chapter 3 is based on the first publication from this research project, entitled "*Boundary Conditions and Phase Functions in a Photo-CREC Water-II Reactor Radiation Field*". This article was published in Chemical Engineering Science Vol. 107 p. 123-136, in April, 2014. Dr. Jesus Moreira helped with the experimental set-up and the proposal of the experimental methodology, while assisting in the early versions of the article draft. The PhD Candidate developed an improved Monte Carlo simulation, performed the laboratory work, the model parameter fitting, the analysis of results, prepared the draft writing and implemented corrections.

Chapter 4 is based on the second publication, entitled "*Establishing Photon Absorption Fields in a Photo-CREC Water II Reactor Using a CREC-Spectroradiometric Probe*". The article was published in Chemical Engineering Science Vol. 116 p. 406-417, in September 2014. Dr. Jesus Moreira helped with the experimental work, the design of the spectroradiometric probe and the early draft corrections. Dr. Pastor Solano-Flores, assisted in the final details of the probe development. The PhD Candidate implemented modifications to the MC simulations to account for radial irradiance profiles. He developed the experimental methodology as well as the probe design. He prepared and completed the laboratory work. He calculated the model parameter fitting, performed the analysis of results, prepared the draft writing and implemented the corrections to the final manuscript.

Chapter 5 was written based on the third publication, entitled "*Photocatalytic Reactor Under Different External Irradiance Conditions: Validation of a Fully Predictive Radiation Absorption Model*". This manuscript was accepted for publication by Chemical Engineering Science on November 30th, 2014. M. Eng. Sc, Fabricio Guayaquil Sosa, helped with the laboratory work and experimental set-up modifications. The PhD Candidate developed the simulations, the experimental methodology and laboratory work. Furthermore, he calculated the parameter fitting, performed the data analysis, prepared the draft writing and implemented the corrections to the final article.

Finally, Chapter 6 is based on a fourth publication entitled "*Eight-Lamp Externally Irradiated Bench-Scale Photocatalytic Reactor: Scale-up and Performance Prediction*". This article was submitted to The Chemical Engineering Journal on November 16th, 2014. Msc. Fabricio Guayaquil Sosa, helped with the laboratory work. The PhD Candidate, developed the Finite-Element simulations as well as their integration with the Monte Carlo simulations. He developed the experimental methodology and the laboratory work. He calculated the parameter fitting, performed the data analysis, prepared the draft writing and implemented the corrections to the final manuscript version.

*To my mother,  
whose unconditional love  
is the reason for my existence.*

*"If I have seen further, it is by  
standing on the shoulders  
of giants"*

*Sir Isaac Newton*

## Acknowledgments

First and foremost I would like to thank The National Council of Science and Technology in Mexico (CONACyT-México), for the scholarship that allowed me to pursue my PhD at UWO. I would also like to thank my supervisors Dr. Hugo I. de Lasa and Dr. Benito Serrano Rosales. Without their support, advice and true sense of commitment, this opportunity of growth and enrichment would not have been possible. Dr. de Lasa and Dr. Serrano are deeply committed researchers, teachers, and advisors. Observing them for four years has helped me define my own research goals.

Special thanks to Jesus Moreira, for his truly invaluable support in the early years of my research. He helped guide my project in the right direction from the very beginning. I am grateful to Pastor Solano-Flores, for his technical support in the lab, for his curiosity, his insights and especially, for always making time to debate ideas. I am specially thankful to Fabricio Guayaquil, for his assistance and support at the very end of the project. I would also like to express my appreciation to Mrs. Florencia de Lasa who provided valuable support with the writing style of this PhD Dissertation.

Thanks to all the friends I met here in Canada: Luis Luque (Mencion Honorifica morro!) Sonia Gutierrez, Juan Manuel Restrepo, Natalia Lesmes, Diego Cufiño, Ana Maria Aguirre, Angel Lanza, Jose Muñoz, Yira Aponte, Gabriela Navarro, Noshin Hashim, Vanessa Rodgher, Mitesh Chaudhari, Valentina Lago, Estefania Ruiz, Francisco de Santiago, Monserrat Santiago. Thanks as well to all the members of the internationally recognized canadian/latin band "Last Patatas bravas!": Abelardo Escoto, Pablo Hennique and Jeff Pound. All of you have made this PhD truly an unforgettable experience, and for that I will always be grateful.

Lastly, and more importantly, I would like to thank my wife *Monica Gonzalez* for her unconditional love and unwavering support during the execution of my PhD project, even when that meant postponing her own to help pursue mine; and my son Gael Valades, for making it all come together.

# Table of Contents

Abstract .....	ii
Co-Authorship Statement.....	iii
Acknowledgments.....	v
Table of Contents .....	vi
List of Tables .....	xi
List of Figures .....	xii
Nomenclature .....	xxi
Chapter 1 .....	1
1 Introduction .....	1
1.1 Research Methodology .....	4
1.2 General Objectives.....	6
1.3 Specific Objectives .....	7
Chapter 2.....	8
2 Literature Review.....	8
2.1 Introduction.....	8
2.2 Reaction Mechanism.....	8
2.3 Kinetic Modeling .....	10
2.3.1 The Langmuir-Hinshelwood and rate equations.....	11
2.4 Radiation Modeling .....	13
2.4.1 Phase Functions .....	16
2.4.2 Lamp Emission modeling .....	16
2.4.3 Reflectors and interfaces.....	19
2.5 Monte Carlo Method.....	21
2.6 Photocatalytic Reactors.....	24

2.7 RTE Parameter Estimation .....	26
2.7.1 Phase Function Determination.....	27
2.7.2 Macroscopic Radiant Energy Balance .....	29
2.8 Photocatalytic Reactor Scale-up .....	30
2.9 Current research directions .....	32
2.10 Conclusions.....	33
2.11 References.....	34
Chapter 3.....	40
3 Boundary Conditions and Phase Functions in a Photo-CREC Water-II Reactor Radiation Field.....	40
3.1 Abstract.....	40
3.2 Introduction.....	41
3.3 Experimental and Mathematical Methods .....	41
3.3.1 Reactor Setup and Radiation Measurements .....	41
3.3.2 Mathematical Procedure Adopted for the MC Method .....	43
3.4 Results and Discussion .....	53
3.4.1 MC Simulation for an Isocratic Phase Function.....	53
3.4.2 Effect of catalyst concentration for isocratic phase function.....	54
3.4.3 Effect of the Scattering Mode at Constant Photocatalyst Concentration..	57
3.4.4 Inner and Outer Boundary Conditions.....	59
3.4.5 Experimental Study to Determine Scattering Phase Functions .....	61
3.4.6 Limitations of Macroscopic Radiation Balances (MRB) when Establishing Scattering Models in Annular Photoreactors. ....	63
3.4.7 Total Transmittance(TT) Measurements When Establishing Scattering Models in an Annular Reactor .....	65
3.5 Conclusions.....	67
3.6 References.....	68



Chapter 4.....	71
4 Establishing Photon Absorption Fields in a Photo-CREC Water II Reactor Using a CREC-Spectroradiometric Probe.....	71
4.1 Abstract.....	71
4.2 Introduction.....	72
4.3 Experimental Method.....	73
4.3.1 Reactor Setup.....	73
4.3.2 The CREC-SP Probe.....	74
4.3.3 Experimental procedure.....	76
4.4 Mathematical Models.....	77
4.4.1 RTE Simulation by Monte Carlo Method.....	77
4.4.2 Quantification of the LVRPA Span.....	82
4.5 Results and Discussion.....	83
4.5.1 Calculating Uncertainty in the LVRPA.....	93
4.6 Conclusions.....	95
4.7 References.....	95
Chapter 5.....	100
5 Photocatalytic Reactor Under Different External Irradiance Conditions: Validation of a Fully Predictive Radiation Absorption Model.....	100
5.1 Abstract.....	100
5.2 Introduction.....	101
5.3 Experimental Method.....	102
5.3.1 Reaction System Set-Up.....	102
5.3.2 Experimental procedure.....	105
5.4 Mathematical Model.....	107
5.4.1 Overview of the RTE MC method.....	107
5.4.2 MC method subroutines.....	113

5.5 Results and Discussion .....	119
5.6 Conclusions.....	129
5.7 References.....	129
Chapter 6.....	136
6 Eight-Lamp Externally Irradiated Bench-Scale Photocatalytic Reactor: Scale-up and Performance Prediction.....	136
6.1 Abstract.....	136
6.2 Introduction.....	137
6.3 Experimental.....	137
6.3.1 Bench-Scale and Scaled-up System Description .....	138
6.3.2 Additional equipment for photocatalytic degradations and tracer experiments .....	138
6.3.3 Determining RTD in both photoreactor systems .....	139
6.3.4 Degradations procedure in bench-scale system .....	140
6.3.5 Degradations procedure in scaled-up system.....	142
6.4 Mathematical Models and Scale-Up Methodology .....	143
6.4.1 Radiative models: pH Correction.....	143
6.4.2 Kinetic models: Charge separation and rate equation.....	144
6.4.3 Transport Models: Free radical distribution and photocatalyst activity .	147
6.4.4 Efficiency factor.....	150
6.5 Results and Discussion .....	152
6.6 Conclusions.....	157
6.7 References.....	158
Chapter 7.....	162
7 Conclusions and Recommendations .....	162
7.1 Conclusions.....	162
7.2 Future Work.....	165

Curriculum Vitae ..... 167

## List of Tables

<b>Table 2.1</b> Band gap of various photocatalysts (Bhatkhande et al., 2001) .....	9
Table 3.1 Characteristics and Dimensions of the Photoreactor and the UV-Lamp .....	43
Table 3.2. Total Transmission (TT) Squared Error for various ‘g’ Scattering Parameters and two sets of BCs. Case a: $P_{\text{absLamp}}=1$ , $P_{\text{absWall}}=1$ . Case b: $P_{\text{absLamp}}=0$ , $P_{\text{absWall}}=1$ .....	67
Table 4.1. $g$ , $P_{\text{absWALL}}$ and $P_{\text{absGLASS}}$ average values and spans for 95% C.I.....	89
Table 4.2. Span for the LVRPA when using TRPA, TT and Radial RPs.....	94
Table 5.1. Calculated average and maximum percentual errors for LVREA (%), for the reported lamp configurations and photocatalyst concentrations ( $\text{mg l}^{-1}$ ), at the reactor midsection ( $z=0$ ). .....	126
Table 6.1. Optimized parameters for the model considering Eq. 6-16 to Eq. 6-19. ....	154
Table 6.2. Optimized parameters for the model considering Eq. 6-20.....	155

## List of Figures

<b>Figure 1.1</b> Yearly mean of daily Irradiation in UV (280-400nm) on horizontal plane. Copyright Mines ParisTech / Armines 2008. ....	2
Figure 1.2 Problems regarding photocatalytic reaction engineering that this work seeks to address.....	3
Figure 2.1. Intermediate compounds formed during the photodegradation of phenol when Degussa P25 is used as a photocatalyst (Ortiz-Gomez, et al., 2008).....	10
<b>Figure 2.2.</b> Classification of radiation source models (PDI partially diff. incidence, DI diffused incidence model). Cassano et al, 1995.....	16
Figure 2.3. A rough surface can be treated by the tangent plane approximation, taken from (He et al., 1991). ....	20
Figure 2.4. Description of the different mechanisms through which radiation can be reflected from a solid surface, taken from (Wolff 1994).....	21
Figure 2.5 Optical Properties vs wavelength for Degussa P25 catalyst: solid line, $\beta^*_\lambda$ ; broken line $\sigma^*_\lambda$ ; dotted line $\kappa^*_\lambda$ ; broken dotted line, $g_\lambda$ . Taken from Satuf et al., 2005.....	28
Figure 3.1. Schematic Representation of the Photo-CREC Water-II Reactor (Adapted from Moreira et al, 2011).....	42
Figure 3.2 Schematic Representation of the Photo-CREC Water II Illustrating the Optical Fiber Sensor and the Wide Radiation View Angles (180 degrees semispherical solid view angle) of Measurements Performed. ....	42
Figure 3.3 Relative Spectral Distribution of the BL Lamp Used in the Experiments: (—) Experimental profile, ( $\Delta$ ) Polynomial Profile Fitting Function ( $\square$ ) Fourier Series Fitting Function. ....	44
Figure 3.4 3D View of the Coordinate System Adopted for MC Simulations (Adapted from Moreira et al 2010).....	46

Figure 3.5. $P(\theta)$ Distribution for (—) isocratic scattering function , a) H-G Phase Function for a (---) backward scattering , $g = -0.3$ and (.....) forward scattering ( $g = 0.3$ ) and b) Binomial Phase Function, (.....) backward scattering ( $I_{\text{asym}} = 1.5$ ) and (---) forward scattering ( $I_{\text{asym}} = -0.2$ ).....	48
Figure 3.6. General Structure of the MC Algorithm of the Present Study. The Reaction Space Subroutine is described with their inputs and their outputs.....	50
Figure 3.7. Algorithm of the Reaction Space Subroutine, employed in the MC simulation of the radiation field inside the annular section of the photoreactor.....	52
<b>Figure 3.8.</b> 3D Profile of the LVRPA Inside the Photo-CREC Water II Reactor for $0.05 \text{ g L}^{-1}$ , Isocratic Phase Function ( $g=0$ ). .....	53
Figure 3.9. 3D view of the LVRPA inside the annular reactor for $\text{TiO}_2$ concentrations of (a) $0.01$ , (b) $0.05$ , (c) $0.1$ , and (d) $0.2 \text{ g L}^{-1}$ . .....	55
Figure 3.10. Radial distribution of the LVRPA at $z = 0$ when isocratic phase function is used (x) $0.01$ , ( $\Delta$ ) $0.02$ , ( $\blacksquare$ ) $0.05$ , ( $\circ$ ) $0.1$ , ( $\bullet$ ) $0.15$ and ( $\diamond$ ) $0.2 \text{ g L}^{-1}$ . .....	56
Figure 3.11. Total Rate of Photon Absorption for Isocratic Phase Function vs. Catalyst Concentration.....	56
Figure 3.12. Radial LVRPA Profiles Using the H-G Phase Function (Figures a and c) and the Binomial Phase Function (Figures b and d) . Figures a and b are for $0.05 \text{ g L}^{-1}$ photocatalyst concentration, figures c and d are for $0.2 \text{ g L}^{-1}$ photocatalyst concentration. Outer boundary Condition: 100% of incident radiation. Codes for asymmetry factors: Broken double-dotted line (-••-) $-0.85$ , Broken line (- - -) $-0.2$ , Dotted line (••••) $0.2$ and Broken single-dotted line (-•-) $0.85$ . Full line (—) Isocratic phase function.....	58
Figure 3.13. Total Rate of Photon Absorption vs. Catalyst Concentration for (a) H-G and (b) binomial phase functions. Outer boundary condition: 100% of incident radiation. Codes for asymmetry factors: Broken double-dotted line (-••-) $-0.85$ , Broken line (- - -) $-0.2$ , Dotted line (••••) $0.2$ and Broken single-dotted line (-•-) $0.85$ . Full line (—) Isocratic phase function.....	59

**Figure 3.14.** Changes of LVRPA with Inner Boundary Conditions. Outer boundary condition: 100% of incident radiation. Photocatalyst concentration set at  $0.05 \text{ gL}^{-1}$ . Phase function used is H-G with (a) forward scattering  $g = 0.8$ , (b) isocratic scattering and (c) backward scattering  $g = -0.8$  phase functions. Symbols: ( $\circ$ ) total re-emission from the lamp and ( $\bullet$ ) total absorption in the lamp..... 60

Figure 3.15. LVRPA Changes with Outer Boundary Conditions. The H-G phase scattering function considers (a) backward scattering with  $g = -0.8$ , (b) isocratic scattering and (c) forward scattering with  $g = 0.8$ . Full circles ( $\bullet$ ) represent total absorption at the outer wall and open circles ( $\circ$ ) total diffuse reflection at the outer wall. Photocatalyst concentration set at  $0.05 \text{ gL}^{-1}$ ..... 61

Figure 3.16. a) Experimental TRPA or Total Rate of Photon Absorption reported as a percentual fraction of total photons absorbed by the slurry. b) Experimental TT or Total Transmittance reported in microwatts per square centimeter. Three measurements were performed for every experimental point. The error bars represent standard deviations. .... 62

Figure 3.17. Effect of Boundary Conditions on the TRPA, reported as a percent of the total emitted radiation as a function of catalyst concentration ( $\text{TiO}_2 \text{ mg/l}$ ) for (a)  $P_{\text{absLamp}} = 0.1$ ,  $P_{\text{absWall}} = 0.1$ , (b)  $P_{\text{absLamp}} = 0$ ,  $P_{\text{absWall}} = 0.2$ , (c)  $P_{\text{absLamp}} = 0$ ,  $P_{\text{absWall}} = 0$ , (d)  $P_{\text{absLamp}} = 0.2$ ,  $P_{\text{absWall}} = 0.2$ . With (—)  $g = -0.99$ , (—)  $g = -0.4$ , (—) isocratic, (—)  $g = 0.4$ , (---)  $g = 0.7$ , (---)  $g = 0.9$  and (---)  $g = 0.99$  and ( $\circ$ ) experimental data. .... 64

Figure 3.18. Effect of Boundary Conditions on the Transmitted Radiation (TT) as a Function of Catalyst for (a)  $P_{\text{absLamp}} = 1$ ,  $P_{\text{absWall}} = 1$ , (b)  $P_{\text{absLamp}} = 0$ ,  $P_{\text{absWall}} = 1$ , (c)  $P_{\text{absLamp}} = 1$ ,  $P_{\text{absWall}} = 0$ , (d)  $P_{\text{absLamp}} = 0$ ,  $P_{\text{absWall}} = 0$ . With (—)  $g = -0.99$ , (—)  $g = -0.4$ , (—) isocratic, (—)  $g = 0.4$ , (---)  $g = 0.7$ , (---)  $g = 0.9$  and (---)  $g = 0.99$  and ( $\circ$ ) experimental data. .... 66

Figure 3.19. Total Squared Error Variation with Respect to Scattering Mode at Different BCs. (—)  $P_{\text{absLamp}} = 1$ , ( $\bullet\bullet\bullet$ )  $P_{\text{absLamp}} = 0$ . Both for  $P_{\text{absWall}} = 1$ ..... 66

Figure 4.1. Reactor Schematics and Expanded View of the Probe Sensor Allowing Changes and Irradiation Measurements with a wide view angle at Various Radial Positions in the Photo-CREC Annular Channel. .... 74

Figure 4.2. Description of the CREC PS Probe while being placed in the Photo-CREC-Water II Reactor. ....	75
Figure 4.3. General Structure of the Monte Carlo Method Used to Model the Photo-CREC Water II. ....	79
Figure 4.4. Algorithm of the Main Subroutine within the MC Simulation Code, Used to Model the Reaction Media.....	80
Figure 4.5. Iterative Algorithm Used to Calculate the Radiation Flux Reaching the Sensor at Different Radial Positions. "Fluxsensor" is a vector containing the RP.....	81
Figure 4.6. Experimental RPs in micro watts cm-2 for Different Catalyst Concentrations at (○) water only, (■) 25, (◆) 50, (▲) 100, (★) 150, (×) 200, (□) 300, and (●) 400 mg l-1. Vertical bars report the typical standard deviation for the 4 repeats. ....	84
Figure 4.7 Outline of the Optimization Algorithm for Determining the Three Parameters Used in the Monte Carlo Method.....	85
Figure 4.8 Total Percentual Errors (%) between Experimental and Model Results for a High Catalyst Concentration Range of 200- 400 mg l-1, for different values of g. Total Percentual Error for 21 different data points. Minimum correspond to less than 1% average percentual error.....	86
Figure 4.9 Total Percentual (%) Error versus Probability of Absorption on Inner Glass (PabsGlass) and on Outer Reactor Wall (PabsWall).Each contour represents approx. 2% Total Percentual Error. 7 data points considered. Minimum corresponds to less than 2% average percentual error.....	87
Figure 4.10. Experimental and Model (g=0.68, P <sub>absWALL</sub> = 0.65 and P <sub>absGLASS</sub> =0.3) Radial Irradiance Profiles (RPs) for Different Catalyst Concentrations (—) MC simulation results, (○)water only, (■) 25, (◆) 50, (▲)100, (★)150, (×)200, (□)300, and (●)400 mg l <sup>-1</sup> .....	90
Figure 4.11. Total Transmitted Radiation for Different Photocatalyst Concentrations. (—) MC simulation for g=0.68, P <sub>absWALL</sub> = 0.65 and P <sub>absGLASS</sub> =0.3, (●) experimental.....	90



Figure 4.12. Calculated Radial LVRPA Values at $z = 0$ when $P_{\text{absWALL}} = 0.65$ , $P_{\text{absGLASS}} = 0.3$ and $g = 0.68$ for (····) 25, (— · —) 100, (— · —) 200, and (—) 400 $\text{mg l}^{-1}$ .....	91
Figure 4.13. Calculated Total Rate of Energy Absorption (TREA) as a function of Photocatalyst Concentration, for $P_{\text{absWALL}} = 0.65$ , $P_{\text{absGLASS}} = 0.3$ and $g = 0.68$ . Optimum photocatalyst concentration near $150 \text{ mg l}^{-1}$ .....	92
Figure 4.14. 3D Profile of the LVREA in $\mu\text{W cm}^{-3}$ inside the Photo-CREC Water II for a)50 $\text{mg l}^{-1}$ , b)100 $\text{mg l}^{-1}$ , c)150 $\text{mg l}^{-1}$ , d)200 $\text{mg l}^{-1}$ . $P_{\text{absWALL}}=0.65$ , $P_{\text{absGLASS}}=0.3$ , $g=0.68$ .....	92
Figure 4.15. LVRPA Percentual Span (%) Distribution for Volume Elements inside the Reaction Space for: a) $\Delta g = \pm 0.2$ , average Span of 50% or $\pm 25\%$ , b) $\Delta g = \pm 0.1$ , average Span of 24% or $\pm 12\%$ , c) $\Delta g = \pm 0.03$ , average Span of 10%. or $\pm 6\%$ .....	93
Figure 5.1 Schematic Representation of the Solar Simulator Photo-CREC Water Reactor.	102
Figure 5.2 Representation of the Photoreactor Inner (a)Front and (b) Side View with Dimensions in cm, Highlighting: 1) Annular Section, 2) Reflector Section and 3) Pulley Probe Mechanism.....	103
Figure 5.3 Sectioned a) Isometric and b) Top view. Inner and Outer Diameter of the Annular Section as well as its Relative Position to Two of the Four Reflectors, are shown. Dimensions shown in Centimeters.....	104
Figure 5.4 Reflector Schematics of Two Lamps and their relative location within the Reflector. The a) Side View and b) Front View. Dimensions reported in centimeters. ....	104
Figure 5.5 Schematic Representation of the Photo-CREC Solar Simulator Pulley Probe System. Dimensions reported in centimeters.....	105
Figure 5.6 Schematic Description of Simplified Reactor Used for MC Simulation: a) Top view and b) isometric view. Note: this schematic highlights symmetry planes and main regions, namely the scattering, emission and reflection regions. ....	107
Figure 5.7 MC representation of a photon trajectory being tracked in hypothetical 3D space. The photon trajectory is computed as a series of discrete interactions which account for both	

reactor geometry and photon-reactor interaction. Reactor walls are in solid blue lines. Equations are represented by dashed green lines..... 108

Figure 5.8 Hypothetical walls (dashed lines) are represented by a set of equations (black solid lines). (a) Concave geometry: locus where the “shortest positive non-zero photon flight-length” condition holds true. (b) Convex Geometry: locus where the “shortest non-negative, non-zero distance condition” does not apply. .... 109

Figure 5.9 Splitting of a geometrical space to achieve an ensemble of concave subspaces: (a) Space with coexisting non-concave and concave angles (blue solid lines), can be split into subspaces as shown in Figure 9b. (b) Subspaces that fulfill the concavity condition (red solid rectangles) are connected by "interphases" (thicker purple lines). .... 110

Figure 5.10 Areas within the Solar Simulator Photo-CREC Water geometry, split to avoid convex geometries from presenting themselves. Areas split into: 1) Lamp space, 2) Reflector space , 3) Gap between reflector and reactor, 4) Annular section and 5) Inner cylinder. .... 110

Figure 5.11 A rough surface can be modeled by the tangent plane approximation, taken from He et al., 1991. .... 111

Figure 5.12 Photon-particle interaction where direction is modified due to scattering. The scattering angle " $\theta$ " is chosen, according to the phase function and an azimuth angle " $\phi$ " from an uniform distribution. .... 113

Figure 5.13 Schematic Description of the Subroutine Structure within the MC method for the RTE in the "Solar Simulator Photo-CREC Water" photo reactor. Interphases are reported in red , planes in blue and green, symmetry planes in black and sensing surfaces in purple. .... 114

Figure 5.14 Surfaces considered for the reflector subroutine: 1) One totally specular virtual plane (symmetry plane), 2) Two partially reflective planes, 3) Two non-reflective planes and 4) One lamp surface. .... 116

Figure 5.15 Surfaces considered for the gap subroutine: 1) A totally transparent virtual surface delimiting the interface between the gap region and the reflector , 2)A totally

transparent virtual surface delimiting the reactor gap boundary with the annular reactor section, 3) Two virtual transparent symmetry planes and 4) Four non-reflective planes.... 116

Figure 5.16 Algorithm of the Annular Photo Reactor Section Subroutine, within the MC Simulation, Used to Model the Reaction Media. The schematic algorithm was adapted from Chapter 3 (Valades-Pelayo et al. 2014a). Note: "Cond1" establishes photon state after iteration. Cond1=0, means that photon trajectory is terminated by TiO<sub>2</sub> absorption. .... 118

Figure 5.17 Axial irradiance profiles in  $\mu\text{W}/\text{cm}^2$  at the reflector edges, (•) -2/2 cm and (o) -4/4 cm away from the reflector center plane (located between the two lamps) and simulation results for (—) -2, 2 cm and (••) -4, 4 cm..... 121

Figure 5.18 Changes of Total Transmittance in  $\mu\text{W}/\text{cm}^2$  with the photocatalyst concentration as measured within the central annulus, at the central axial position, from zero to 90  $\text{mg l}^{-1}$  photocatalyst concentration. Codes: (•) Experimental Data and (—) Simulated Results..... 121

Figure 5.19 Changes in Total Transmittance in  $\mu\text{W}/\text{cm}^2$  as measured within the central annulus, at different axial positions, in cm. Experimental data for (•) zero, (o) 20 and (▲)40  $\text{mg l}^{-1}$ , as well as simulations for (—) zero, (••) 20 and (---) 40  $\text{mg l}^{-1}$  are presented. .... 122

Figure 5.20 Total transmittance ( $\mu\text{W}/\text{cm}^2$ ), as measured within the central annulus, at different azimuthal values (degrees), with all four reflectors on. Experimental data for (•) zero, (o) 20 and (▲)40  $\text{mg l}^{-1}$ , as well as simulations for (—) zero, (••) 20 and (---) 40  $\text{mg l}^{-1}$  are presented. .... 123

Figure 5.21 TT ( $\mu\text{W}/\text{cm}^2$ ), as measured within the central annulus, at different azimuthal values (degrees), for the following reflectors on: a) three, b) two opposite, c) two adjacent, and d) one. Experimental: (•) zero, (o) 20 and (▲)40  $\text{mg l}^{-1}$ . Simulations: (—) zero, (••) 20 and (---) 40  $\text{mg l}^{-1}$  ..... 125

Figure 5.22. The Total Rate of Photon Absorption (TRPA) is calculated for photocatalyst concentrations ranging from zero to 200  $\text{mg l}^{-1}$ , for (—) four, (••) three, (- -) two adjacent, (- •-) two opposite and (— —) one reflector "on". The optimum photocatalyst concentration is found, for all cases, to be close to 91  $\text{mg l}^{-1}$ . .... 126

Figure 5.23. LVREA profiles, for a 91 mg<sup>l</sup><sup>-1</sup> photocatalyst concentration and 4 reflectors "on", in μW/cm<sup>3</sup>, at a) constant axial positions for Z = 15, 0 and -15 cm, and at b) constant azimuth for zero, 90, 180 and 270 degrees. Energy absorption ranges from 4000 μW/cm<sup>3</sup> to zero. Each contour represents a 10% drop..... 127

Figure 5.24. LVREA profiles at constant axial position, for a) 40, b) 90 and c) 200 mg<sup>l</sup><sup>-1</sup> photocatalyst concentrations and all reflector combinations, in μW/cm<sup>3</sup>. Each contour represents a 10% drop with respect to the scale presented to the right of each contour plot. .... 128

Figure 6.1. Empirical equation, correlating the input voltage for the UV-Lamp and the percentual emission, determined while the reactor was filled with water only. .... 142

Figure 6.2 Radial Irradiance Profiles (μW/cm<sup>2</sup>) obtained as proposed by Valades-Pelayo et al. 2014b at five different radial positions for three photocatalyst loadings: a) water only, b) 50 mg<sup>l</sup><sup>-1</sup> and c) 100 mg<sup>l</sup><sup>-1</sup>. At a pH=7 (○) and a pH=3.25(▲), MC simulations with g=0.41 (—) and g=0.68 (---) are shown..... 144

Figure 6.3 Figure 8 RTD tracer experiments (•) and simulations (-) for (a)the Photo-CREC Water II and (b)the scaled-up Photo-CREC Solar Simulator. Simulations used axial dispersion coefficients (**Dz**) of (a) 12.0 cm<sup>2</sup>s<sup>-1</sup> and (b) 65.0 cm<sup>2</sup>s<sup>-1</sup>. Both systems had a volumetric flow of 13.5 cm<sup>3</sup>s<sup>-1</sup>..... 153

Figure 6.4 Experimental degradation rates for oxalic acid in the Photo-CREC Water II Photoreactor, under a) different lamp irradiances at (●) 25 mg<sup>l</sup><sup>-1</sup>, (□) 50, (■) 75 and (○) 100 mg<sup>l</sup><sup>-1</sup> photocatalyst loadings. (b) Degradation rates at (○) different photocatalyst loadings (100% lamp emission) in the Photo-CREC Water II photoreactor. Simulations (-) presented for both cases. .... 154

Figure 6.5 (○) Experimental and (-) simulated degradation rates for oxalic acid in the Photo-CREC Water Solar Simulator (Photo-CREC-Water II) under different photocatalyst loadings at nominal lamp emission (100% lamp emission), with all 8 lamps turned on. .... 156

Figure 6.6 a) Photocatalytic Thermodynamic Efficiency Factors (PTEF) and b) Quantum Yields (QY) are presented for (—) the photo-CREC Water II and (···) the Photo-CREC Solar Simulator, for photocatalyst concentrations of 25 mg<sup>l</sup><sup>-1</sup> to 150 mg<sup>l</sup><sup>-1</sup> ..... 156

# Nomenclature

## General

$a$	gap between lamp and reactor (m)
$A$	parameter for free radical source term ( $\text{m}^3 \text{g}^{-1} \text{s}^{-1}$ )
$B$	parameter for charge generation/recombination ( $\text{mg} \mu\text{W}^{-1}$ )
$C_{cat}$	photocatalyst Concentration ( $\text{mg l}^{-1}$ )
$C_{ox}$	oxalic Acid Concentration (ppm of C)
$C_f$	adsorbed free radical concentration per unit volume ( $\text{mol m}^{-3}$ )
$C_{f_o}$	reference $C_f$ , considered as the maximum average ( $\text{mol m}^{-3}$ )
$D_z$	axial dispersion coefficient ( $\text{m}^2/\text{s}$ )
$E$	Einsteins (moles of photons $\text{s}^{-1}$ )
$E_{bg}$	energy band gap (eV)
$e_x, e_y, e_z$	direction cosines (-)
$[e^-]$	electron surface concentration ( $\text{mol e m}^{-2}$ )
$g$	Henye-Greenstein phase function dimensionless parameter (-)
$G$	total incident radiation (einstein $\text{m}^{-2} \text{s}^{-1}$ )
$[h^+]$	electron-holes surface concentration ( $\text{mol h}^+ \text{m}^{-2}$ )
$[H_2O_{ads}]$	adsorbed water surface concentration ( $\text{mol H}_2\text{O m}^{-2}$ )
$I_{asym}$	asymmetry factor of the Binomial Phase Function (-)
$I$	irradiance, ( $\mu\text{W cm}^{-2}$ )
$K_A$	oxalic acid adsorption constant ( $\text{ppm}^{-1}$ )
$k_{all}$	kinetic constant for total free radical depletion, sink term ( $\text{mol OH m}^{-3} \text{s}^{-1}$ )

$k_{rec}$	zeroth order constant of recombination of free radicals ( $\text{mol OH m}^{-3} \text{s}^{-1}$ )
$k_{ox}$	zeroth order constant for oxalic acid degradation ( $\text{ppm s}^{-1}$ )
$k^*$	reaction rate constant for dimensionless free radicals conc ( $\text{mol OH s}^{-1} \text{m}^{-3}$ )
$k^{**}$	lumped zero-th order kinetic constant ( $\text{ppm s}^{-1}$ )
$k_1$	reaction rate constant between reaction of $[h^+]$ and $[H_2O_{ads}]$ ( $\text{m}^2 \text{mol}^{-1} \text{s}^{-1}$ )
$k_2$	reaction rate constant between reaction of $[h^+]$ and $[H_2O_{ads}]$ ( $\text{m}^2 \text{mol}^{-1} \text{s}^{-1}$ )
$k_3$	reaction rate constant between reaction of $[e^-]$ and $[O_{2ads}]$ ( $\text{m}^2 \text{mol}^{-1} \text{s}^{-1}$ )
$k_r$	reaction rate constant for charge recombination ( $[h^+]$ and $[e^-]$ ) ( $\text{m}^2 \text{mol}^{-1} \text{s}^{-1}$ )
$k_\lambda$	reaction rate constant $[h^+]$ and $[e^-]$ generation (charges) ( $\text{mol } \mu\text{W}^{-1} \text{s}^{-1}$ )
$L$	length of the photoreactor units (m)
$l$	length of the photon flight (m)
$N_{phot}$	total number of tracked photons per Monte Carlo simulation (events)
$\dot{N}_{te}$	number of emitted photons per unit time ( $\text{mol photons s}^{-1}$ )
$[OH_{ads}]$	adsorbed OH surface concentration ( $\text{mol OH m}^{-2}$ )
$[O_{2ads}]$	adsorbed $O_2$ surface concentration ( $\text{mol } O_2 \text{ m}^{-2}$ )
$p(\Omega' \rightarrow \Omega)$	phase Function for scattering in RTE ( $\text{rad}^{-1}$ )
$P_{absGlass}$	absorption probability at the glass interface or inner BC (-)
$P_{absWall}$	absorption probability at the outer wall or outer BC (-)
$P(a)$	photocatalyst absorption probability (1- albedo) (-)
$P(\theta)$	probability Density Function for scattering angle ( $\text{rad}^{-1}$ )
$P_{ze}$	Probability of emission at a axial position on the lamp surface (-)
$r$	radial spatial coordinate (m)
$r_{ext}$	annular section external radius (m)

$r_{int}$	annular section internal radius (m)
$r_{lamp}$	lamp radius (m)
$r_{free\ rad}$	free radicals generated per unit time unit surface ( $\text{mol OH s}^{-1} \text{ m}^{-2}$ )
$r_{all}$	overall rate of free radical consumption per unit volume ( $\text{mol OH s}^{-1} \text{ m}^{-3}$ )
$r_{ox}$	oxalic acid reaction rate per unit volume ( $\text{ppm s}^{-1} \text{ m}^{-3}$ )
$R_n$	uniformly distributed random number (-)
$R_{1...6}$	random numbers (-)
$s$	linear coordinate along the direction $\Omega$ , (m)
$S_p$	external surface area per unit mass ( $\text{m}^2 \text{ g}^{-1}$ )
$\text{Span}_{\text{LVRPA}}$	percentual range of the 95% C.I. for LVREA absorption field (%)
$t$	time (s)
$x,y$	cartesian coordinates (m)
$z$	axial coordinate (m)
$z^*$	dimensionless photoreactor unit length (-)

## Acronyms

BC	Boundary Condition
BL lamp	Black Light Lamp
CI	Confidence Interval
DO	Discrete Ordinate
FV	Finite Volume
H-G	Heney-Greenstein
LVREA	Local Volumetric Rate of Energy Absorption ( $\mu\text{W m}^{-3}$ )
LVRPA	Local Volumetric Rate of Photon Absorption ( $\text{E m}^{-3}$ )



MC	Monte Carlo
PTEF	Photochemical Thermodynamic Efficiency Factor (-)
ppm	parts per million ( $\text{mg l}^{-1}$ )
RP	Radial Irradiance Profile ( $\mu\text{W cm}^{-2}$ )
RTE	Radiative Transfer Equation
RTD	Residence Time Distribution (-)
TREA	Total Rate of Energy Absorption ( $\mu\text{W}$ )
TRPA	Total Rate of Photon Absorption (E)
TT	Total Transmittance ( $\mu\text{W cm}^{-2}$ )
QY	Quantum Yield (mol OH consumed/ mol photons absorbed)

### **Greek**

$\alpha$	constant for free radicals source term per unit surface area ( $\text{mol OH s}^{-1} \text{m}^{-2}$ )
$\beta$	extinction coefficient ( $\text{m}^{-1}$ )
$\beta_i$	free radicals stoichiometric coefficient (-)
$\gamma$	charge recombination kinetic parameter ( $\text{m}^2 \mu\text{W}^{-1}$ )
$\Delta g$	range for the 95% C.I. for g. (-)
$\eta$	performance factor for the photocatalytic system (-)
$\theta$	particle reflection or scattering angle ( $^\circ$ )
$\theta^*$	azimuth position (rad)
$\theta_f$	free radicals coverage of photocatalyst surface area (-)
$\theta_{lamp}$	lamp azimuth position (rad)
$\kappa$	absorption coefficient ( $\text{m}^{-1}$ )
$\lambda$	wavelength of radiation (nm)

$v_z$	axial Velocity ( $\text{m s}^{-1}$ )
$\dot{v}$	volumetric flow ( $\text{m s}^{-1}$ )
$\vartheta$	dimensionless adsorbed free radicals per unit volume. (-)
$\sigma$	scattering coefficient ( $\text{m}^{-1}$ )
$\tau_{tank}$	mixing tank average residence time (s)
$\phi$	azimuth angle for the new scattering direction ( $^\circ$ )
$\varphi^*$	dimensionless LVREA (-)
$\Phi_{reactor}$	ratio between reactor volume and total system volume (-)
$\Omega$	solid angle (steradian)

### **Subscripts and Superscripts**

$\lambda$	indicates dependence on wavelength
$f$	corresponds to free radicals
$opt$	refers to an optimized value
$old$	Indicates outdated/previous location
$new$	Indicates updated/ new location
$lamp$	Indicates spatial coordinates on the lamp surface

### **Superscripts**

$tank$	indicates it is located in the mixing tank
--------	--

## Chapter 1

### 1 Introduction

Heterogeneous photocatalysis is an emerging technology with potential use in many oxidation and reduction chemical transformations (Cassano et al. 2000). Interest in photocatalysis started in the 1970s when attractive proposals were considered for water splitting for hydrogen production (Fujishima et al. 1975). It was not until the 1980s that new potential applications were proposed for environmental remediation (Bahnemann, 2004). From this point on, the interest in this promising technology has done nothing but increase (Ahmed et al., 2010). Among these new applications, outstanding examples are water purification (Herrmann, 1999), air purification (Garcia Hernandez et al., 2010), self-cleaning surfaces and the production of high energy molecules, such as hydrogen among others (Escobedo-Salas et al. 2013).

As other AOPs (Advanced Oxidation Processes), heterogeneous photocatalysis is characterized by the production of hydroxyl radicals ( $\text{OH}\cdot$ ). These radicals are extremely powerful and non-selective oxidants, which are capable of oxidizing the majority of organic compounds very rapidly (Moreira 2011). Heterogeneous photocatalysis was found to be very efficient and advantageously versatile, specifically in the removal of a wide variety of organic contaminants present in water (Li Puma et al., 2007; Moreira et al., 2010; Chong, et al., 2010; Ahmed et al., 2011).

From a technical perspective, water treatment is based on various mechanical, physical, biological and chemical processes. These treatments can be organized in three categories: (1) Primary treatments, which rely on physical separation and are used to eliminate suspended particles; (2) Secondary treatments, which are based on biological treatments and remove bacteria and microorganisms; (3) Tertiary treatments, which consist of more effective and non-reactive systems used to remove pollutants hard to degrade or separate by other means.

Drinking water sources may contain some organic contaminants since industrial manufacturers and households wastewaters, in many instances, discharge in ground wells

and surface water. Some of these organic contaminants, characterized by high chemical stability, are not removed via primary and secondary treatments. Thus, for these water resources to achieve drinking standards it is necessary to make use of tertiary treatments, which are of paramount importance, in a world where about 80% of the population lives in areas where fresh water supply is not secure or accessible (BBC News Science and Environment 2009).

Moreover, Andrew Hudson, the UN's principal director of the United Nations Development Programme (UNDP) in 2009, stated that access to water and sanitation is by far the strongest driver of the Human Development Index (HDI), a UN measure to determine how societies are doing socially and economically. According to UNDP, water scarcity has very little to do with the physical availability of water and much more with the availability of energy, to purify water. (BBC News Science and Environment 2009).

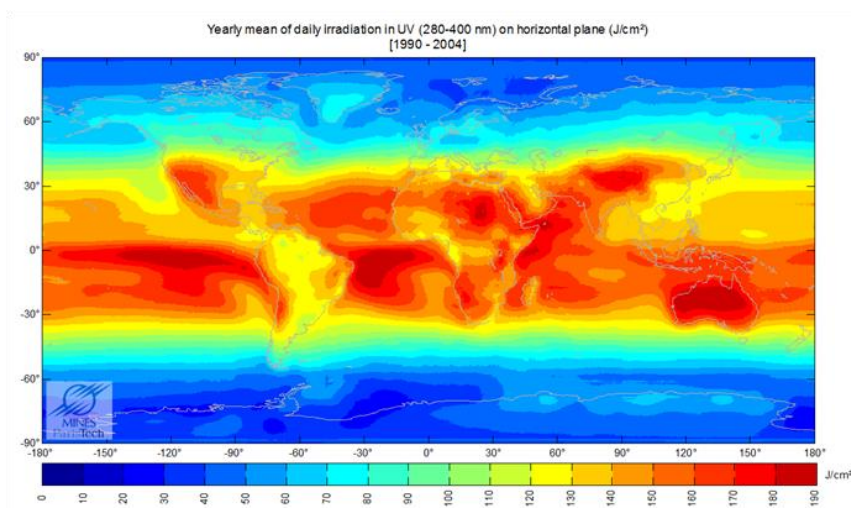


**Figure 1.1** Yearly mean of daily Irradiation in UV (280-400nm) on horizontal plane.

Copyright Mines ParisTech / Armines 2008.

On the other hand, if the regions where drinking water scarcity are of major social concern are located in a world map distribution of UV radiation, such as the one presented in **Figure 1.1**, it can be easily concluded that most of these regions present moderate to relatively high solar irradiance. As photocatalytic reactions are the result of the interaction of photons having the appropriate wavelength, with a solid semiconductor

(Malato et al., 2004, Franch et al., 2005; Fujishima et al., 2008), sunlight can become the main energy source driving the photocatalytic decontamination process. Thus, heterogeneous photocatalysis, using solar radiation and an inexpensive semiconductor photocatalysts can t help to mitigate some of the social development issues in third world countries.

However, for photocatalytic technologies to achieve their full potential, several issues still need to be addressed (Ismail and Bahnemann, 2014). One of these challenges is the required increase of the efficiency of photocatalytic systems at larger scales (Marugan et al., 2010). In this regard, significant progress is needed from the engineering design and modelling point of view, for the successful application of laboratory data and models to large-scale operations (Gaya and Abdullah, 2008). A main issue limiting photoreactor scale-up is the lack of suitable radiation models (Changrani & Raupp, 1999) as well as the lack of appropriate kinetics and design procedures (Li Puma et al., 2007; Moreira et al., 2012). Particularly, the behavior of UVA radiation and light inside the heterogeneous media and its impact on the pollutant local degradation rate is still not well understood (Minero, 1999).

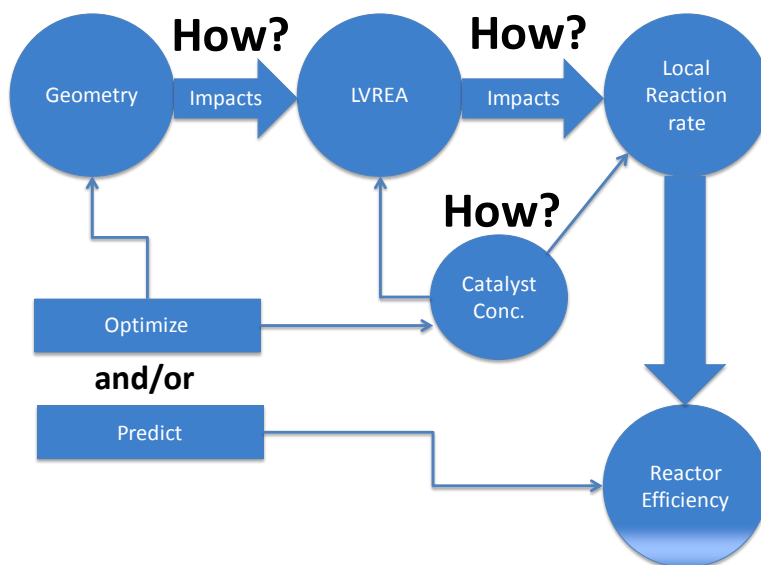


**Figure 1.2** Problems regarding photocatalytic reaction engineering that this work seeks to address.

In all these respects, it is required to consider design variables such as the reactor geometry and configuration, photocatalyst concentration, and radiation sources in the context of physically sound models. Being able to account for all of these factors, would very significantly help the development of a comprehensive model capable of predicting photocatalytic performance. This would allow one to make a smooth transition from artificially and internally irradiated bench-scale photocatalytic reactors to solar and externally irradiated pilot-plant scale photocatalytic reactors. Figure 1.2, explains the kind of interrelation that can be found when trying to use a predictive approach to either design or to optimize these design variables, while changing scales.

It is for this reason that the present study centers on the development of a practical and accurate approach, to account for relevant design parameters. The proposed model is validated by successfully predicting the behaviour of a bench-scale )externally irradiated photocatalytic reactor.

## 1.1 Research Methodology

In order to address the aforementioned issues, this study was divided into four main stages: i) The development of a radiative transfer model with scale-up capabilities for slurry photocatalytic reactors, ii) The establishment of a methodology to determine the radiative model parameters in the bench scale system, iii) The validation of the radiative model for different scales and irradiance set-ups and iv) The establishment of a kinetic model suitable for the scale-up of bench-scale to pilot-plant scale, of solar irradiated, suspended photocatalytic reactors.

In the *first phase* of this PhD study, a Monte Carlo (MC) method was implemented to solve the Radiative Transfer Equation (RTE) and to calculate the Local Volumetric Rate of Energy Absorption (LVREA) inside of an annular 2.65 L Photo-CREC Water II Photoreactor. This model includes relevant radiative boundary conditions (BCs) and suspended photocatalyst anisotropic radiation absorption and scattering effects. Simulation results were compared against experimentally determined Total Transmittance (TT) and Total Rate of Photon Absorption (TRPA). The model irradiance

and LVREA sensitivities on the phase functions and boundary conditions were also assessed.

In the *second phase* of this PhD dissertation, the simulation data from the first phase were analyzed using a novel probe and an experimental methodology developed to measure internal irradiance profiles (RP). This experimental method was applied along the radial coordinate and inside the annular section of the bench-scale Photo-CREC Water II Photoreactor. The MC method was modified to account for probe intrusion effects, obtaining model radial irradiance profiles (RP). As a result, boundary conditions and more importantly, the " $g$ " scattering parameter for the  $\text{TiO}_2$  phase function, were determined with increased accuracy, establishing LVREA at different photocatalyst concentrations and emission conditions with acceptable levels of accuracy.

In the *third phase* of this PhD study, the proposed radiative model was validated as a fully predictive tool for the determination of the LVREA. This methodology was implemented in a 10 L externally and asymmetrically irradiated reactor designated as a Photo-CREC III Reactor. This is a slurry photocatalytic reactor four times larger than the 2.5 L concentric Photo-CREC Water II unit. It was in this set-up where the influence of different photocatalyst concentrations and five different irradiance set-ups were considered. It was shown that the proposed model over-predicts the LVREA, on average, by 6% error.

In the *fourth phase* of this PhD dissertation, a scale-up model was developed and validated. To accomplish this, a kinetic model for the degradation of a model pollutant was proposed, based on a Langmuir-Hinshelwood kinetic equation and a simplified charge separation/ recombination scheme accounting for the LVREA. In this case, experiments using oxalic acids were developed in the Photo-CREC Water II with a variable emission. Kinetic parameters were determined for different photocatalyst concentrations and lamp irradiances. Additionally, the developed kinetic model was employed to compare oxalic acid degradation rates, between the Photo-CREC Water II and the Photo-CREC III (Solar Simulator). This comparison accounted for their respective Residence Time Distributions (RTDs) and Radiation Absorption Fields

(LVREA). It was proven that the model developed displayed good predictability of the photocatalytic performance.

## 1.2 General Objectives

The present study aims to advance photocatalytic reaction engineering by developing a comprehensive model for scale-up of bench-scale slurry photoreactors. This will help us to better understand the interrelations between chemical kinetics, transport processes and radiation field distribution as functions of radiation sources, photocatalyst loading and geometry. In this regard, the objectives of this PhD dissertation can be divided into 3 main sub-objectives:

- a) To develop a radiation field model in an externally irradiated photocatalytic reactor by using a predictive Monte Carlo method. This model shall be as detailed as possible, incorporating irradiation absorption, forward and backward scattering with parameters validated at different scales, photocatalyst concentrations and irradiance conditions.
- b) To establish kinetic models for the photoconversion of model pollutants in externally irradiated photocatalytic reactors. Kinetic models shall account for important photoreactor parameters such as: a) reactor geometry, b) local irradiance conditions, and c) photocatalyst concentration employed.
- c) To develop a comprehensive model able to predict photocatalytic reactor performance in scaled-up internally-irradiated lab-scale photoreactors as well in externally irradiated pilot-plant photoreactors. The comprehensive model shall incorporate radiative transfer, reaction kinetics and mass and momentum balances. It is anticipated that the resulting set of equations will be solved using Finite Element (FE) methods combined with Monte Carlo (MC) methods, with this leading to adequate evaluations of reactor performance and reactor energy efficiency.



### 1.3 Specific Objectives

On the basis of the above, the specific objectives or milestones for this research include the following:

- The development of a Matlab program for Monte Carlo simulations for the Photo-CREC Water II Photoreactor.
- The development of a novel probe and methodology for optical parameter estimation with increased accuracy in the Photo-CREC water II Photoreactor.
- The development of a Matlab program for Monte Carlo (MC) simulations in the Photo-CREC Solar Simulator Photoreactor.
- The validation of the MC methodology for the Photo-CREC Solar Simulator using various irradiance conditions.
- The development of a kinetic reaction model for oxalic acid photodegradation, based on a Langmuir-Hinshelwood mechanism and a scheme considering charge separation and recombination.
- The estimation of kinetic parameters for oxalic acid and model experimental validation, at different photocatalyst concentrations and lamp emissions inside the Photo-CREC Water II Photoreactor.
- The development of Finite Element (FE) simulations coupling chemical reactions, mass transfer, and radiative transfer, inside both Photo-CREC Photoreactors.
- The determination of energy efficiency using thermodynamic efficiency factors (PTEF), quantum yields (QY) and rates of reaction for both reactors using the MC and FE simulations.
- The validation of a scale-up approach which allows moving from centrally irradiated bench scale units to non-symmetric irradiated (solar irradiated) pilot-plant units. This will be accomplished by comparing the model and experimental reaction rates and overall photocatalytic performance.

## Chapter 2

### 2 Literature Review

An extensive literature review of photocatalytic reaction engineering is provided in this chapter. The following topics are considered: i) Reaction Mechanisms, ii) Kinetic Modelling, iii) Radiation Modelling, iv) Monte Carlo Method, v) Reactors Configurations, vi) RTE Parameter Estimation, vii) Reactor Scale-up, viii) Current Research Directions and ix) Conclusions.

#### 2.1 Introduction

The present chapter, reports a review of the technical literature, covering important topics regarding various scale-up approaches for photocatalytic reactors. First, the information focuses on the reaction mechanisms for photocatalytic processes, followed by the most commonly applied kinetics for photocatalytic reactions. Then, existing radiation models for photocatalytic reactor modelling are reported. This is expanded in a subsection on the Monte Carlo (MC) method as a mean for accurate radiation absorption field determination. Afterwards, a review is reported on the most commonly used configurations and photocatalytic reactor designs as described in the technical literature. Lastly, issues on parameter determination for the radiative transfer equation (RTE) are covered, followed by the current research directions on the scale-up of suspended photocatalytic reactors.

#### 2.2 Reaction Mechanism

Photocatalytic degradation of model pollutants is a multi-staged mechanism in which model pollutants produce intermediate compounds before complete mineralization is achieved. In this respect, one could argue that all the degradation mechanisms share a common initiation step: a charge separation induced by the interaction between a photon and a solid semiconductor. However, not every photon that reaches the catalyst particle will be able to produce the “ $e^-/h^+$ ” pair. In fact, only those photons with energy equal or greater than the semiconductor’s band gap will be able to produce the  $e^-/h^+$  charge

separation. This band gap represents the energy required by an electron to jump from the valence band to the conduction band (Cassano et al., 2000; Fujishima et al., 2008).

The energy required for the electron excitation, depends on the particular characteristics of every semiconductor. This minimum photocatalyst band gap necessary for the photo-excitation is a function of the wavelength. **Table 2.1** reports values of the band gap energies for different semiconductors. In this regard, TiO<sub>2</sub> Degussa P25 has proven to be the most active catalyst in the near-UV-region (Ray et al., 2000; Zhou et al., 2006; Moreira et al., 2012), characterized by its high stability, good performance and relatively low cost (Fujishima and Zhang 2006).

After charge separation, both free electrons and electron holes can either undergo different reaction pathways or be recombined. In this respect, the “h<sup>+</sup>” site can interact with a molecule of adsorbed water to form an adsorbed OH<sup>•</sup> free radical. On the other hand, the electron can react with an oxygen molecule, and then be neutralized by a proton in the solution, to form hydrogen peroxide, which dissociates the free radicals (Navio et al 1996; Lenigrini et al 1993; Hoffman et al 1995; Litter et al 1999, de Lasa et al, 2006).

**Table 2.1** Band gap of various photocatalysts (Bhatkhande et al., 2001)

Photocatalyst	Band-gap (eV)	$\lambda_{bg}$	Photocatalyst	Band-gap (eV)	$\lambda_{bg}$
Si	1.1	1127	$\alpha$ -Fe <sub>2</sub> O <sub>3</sub>	3.1	400
WSe <sub>2</sub>	1.2	1033	ZnO	3.2	388
Fe <sub>2</sub> O <sub>3</sub>	2.2	564	TiO <sub>2</sub> (Anatase)	3.2	388
CdS	2.4	517	SrTiO <sub>3</sub>	3.4	365
WO <sub>3</sub>	2.7	459	SnO <sub>2</sub>	3.5	354
TiO <sub>2</sub> (Rutile)	3.0	413	ZnS	3.7	335

Organic pollutants may react with OH<sup>•</sup> radicals until they reach simpler, more stable intermediate states. This process can be repeated several times, until the organic compounds are completely oxidized forming CO<sub>2</sub> and water. Thus, one can notice that every time the model pollutant molecules form an intermediate species, they can, in the

presence of  $\text{OH}^\bullet$  radicals, be further oxidized until the pollutant is fully mineralized. It has been reported by our research group (Ortiz-Gomez 2007 and 2008; Moreira et al., 2012) that the photodegradation of phenols yields intermediate aromatic and intermediate carboxylic species. Figure 2.1, summarizes these findings. These authors reported that phenols yield catechol, benzoquinone, hydroquinone, formic and oxalic acids.

It is also interesting to point out that free radicals are adsorbed on the catalyst surface. Therefore, when interacting with the  $\text{OH}^\bullet$ , the pollutants and intermediates are in the adsorbed state on the catalyst surface.

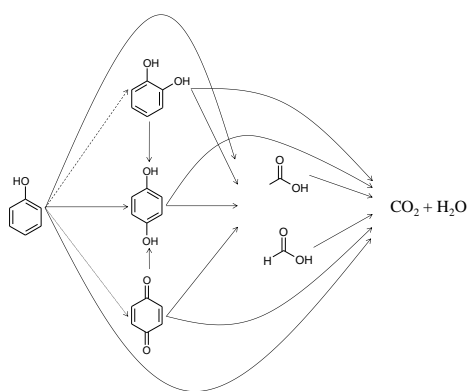


**Figure 2.1.** Intermediate compounds formed during the photodegradation of phenol when Degussa P25 is used as a photocatalyst (Ortiz-Gomez, et al., 2008).

## 2.3 Kinetic Modeling

Based on the previous general degradation mechanism, several approaches have been developed for the kinetic modeling of the photodegradation of organic compounds in water. However, most kinetic models proposed in the literature still deal with a single model chemical species. This assumption may render models that fit experimental data very well, with narrow confidence intervals for the kinetic constants. Nonetheless, these methods have a lot of shortcomings and none or very little applicability in real-life scenario. There are a few examples, like the studies presented by Moreira et al. 2012, Li Puma et al 2007 and Gora et al. 2006 where multicomponent kinetic models are

discussed. These kinetic models were found to be applicable over a wide range of initial concentrations.

A kinetic model based on the Langmuir-Hinshelwood (L-H) mechanism provides a good tool for describing the behaviour of the model compounds and intermediate species in a photocatalytic process (Moreira et al. 2012). This approach has demonstrated the applicability to model multiple components photodegradation as shown in several published papers (Salaices et al., 2004; Ortiz-Gomez et al., 2007 and 2008).

For the case of phenol, Moreira et al. 2012 obtained a unified kinetic model studying four different photocatalysts, while measuring the total organic carbon, degradation of phenol, as well as the formation of intermediate compounds (hydroquinone, catechol, benzoquinone and acetic and formic acids) considering L-H adsorption isotherms. Adsorption constants were determined independently, which minimized the cross-correlation among optimized kinetic constants. In this work, a general unified reaction mechanism was presented. This general reaction mechanism was found to be applicable when used with the different TiO<sub>2</sub> photocatalysts studied. Although this approach was found to predict experimental results very well, it still lacks considering the effect of different reactor geometries and radiation intensities in the model as well as different catalyst loadings. This turns out to be of greater importance, since the kinetic constants are related to the radiation distribution inside the reactor, which will change if the reactor is to be scaled up.

### 2.3.1 The Langmuir-Hinshelwood and rate equations

The general form for the L-H equation for photocatalytic reactions is given by (Moreira et al., 2012, Moreira 2011):

$$r_i = \frac{k_i^k K_i^A C_i}{1 + \sum_{j=1}^n K_j^A C_j} \quad \text{Eq. 2-1}$$

where a) subscript i refers to component “i”, b)  $r_i$  is the reaction rate (mol gcat<sup>-1</sup> min<sup>-1</sup>), c)  $k_i^k$  is the reaction kinetic constant (mol gcat<sup>-1</sup> min<sup>-1</sup>), d)  $K_i^A$  is the absorption constant

(mol<sup>-1</sup> l), e)  $C_i$  is the concentration of the participating species (mol. l<sup>-1</sup>) and f) “j” is the subscript denoting each component of the n chemical species.

When a reactor is operated in a batch mode as in the case of the photoreactors considered in this study, a balance equation for each component “i” can be expressed as follows:

$$r_i = \frac{1}{W} \frac{dN_i}{dt} = \frac{V}{W} \frac{dN_i/V}{dt} = \frac{V}{W} \frac{dC_i}{dt} \quad \text{Eq. 2-2}$$

where  $W$  is the mass of the solid catalyst (g<sub>cat</sub>),  $V$  is the reactor volume (l),  $N_i$  is the number of moles i (mol) and  $t$  represents the time (min).

By substituting Eq. 2-1 into Eq. 2-2, the reaction rate for each chemical species in the context of the slurry reaction unit can be obtained:

$$\frac{dC_i}{dt} = \frac{\frac{W}{V} k_i^k K_i^A C_i}{1 + \sum_{j=1}^n K_j^A C_j} \quad \text{Eq. 2-3}$$

This last equation can also be expressed as:

$$\frac{dC_i}{dt} = \frac{k_i C_i}{1 + \sum_{j=1}^n K_j^A C_j} \quad \text{Eq. 2-4}$$

with  $k_i$  being:

$$k_i = \frac{W}{V} k_i^k K_i^A \quad \text{Eq. 2-5}$$

The rate constants in Eq. 2-5 represent apparent constants in min<sup>-1</sup>. The intrinsic kinetic constant can be calculated using the following relationship:

$$k_i^I = \frac{V_{CSTR} + V_{PFR}}{V_{PFR}} k_i \quad \text{Eq. 2-6}$$

where  $V_{\text{CSTR}}$  stands for the volume of the tank and  $V_{\text{PFR}}$  represents the volume of the photoreactor in  $l$ .

Eq. 2-6 is a practical way of expressing that the photocatalyst is active as long as it is being irradiated. This equation however, neglects any dynamic effects that may arise from the changes in irradiance within the irradiated volume. It assumes there is no reaction at all in the non-irradiated volume of the system.

From the discussion presented above, it can be concluded that for every component participating in the reaction scheme, an equation with the form of Eq. 2-4 can be obtained to represent the photocatalytic oxidation of the model compounds and its intermediates.

Several kinetic and adsorption parameters need to be numerically estimated. One limitation of the L-H model is that for a large number of chemical species, a large number of kinetic and adsorption parameters need to be determined. This may lead to models with high cross-correlation. This issue can be solved by the independent determination of the adsorption constants of the participating components as previously presented by [Moreira et al. 2012](#).

## 2.4 Radiation Modeling

In a strict sense, all the mass balances (one for each reacting species) and the energy balance should be written for monochromatic radiation ([Cassano et al., 2000](#)). Thus, one would have a set of differential equations (mass and energy balances) for each wavelength within the interval in which radiation is being absorbed.

To avoid this problem, it is assumed that the kinetic effects of the absorbed photons at different wavelengths are additive, as long as the photon energy is equal or higher than the energy band gap. All monochromatic contributions are put together into one energy balance and one mass balance for each reacting species. The sum of all monochromatic contributions is referred as to the Local Volumetric Rate of Energy Absorption (LVREA) and this involves solving the Radiative Transfer Equation (RTE) ([Moreira et al., 2010](#)).

Mass and energy balances, are coupled through the reaction rate terms as usual. This coupling is extended to the radiation balance through the reaction rate. This is due to the effect that the reactant has, on the radiation absorption properties of the media (Cassano et al., 2000). However, the radiation balance must be treated separately from the thermal energy balance. This is the case, given that the radiation that affects the photochemical reactions is usually in the range of 200 nm to 600 nm, a range that is ineffective for heating (Cassano et al., 2000). Infrared radiation, if eventually produced by the lamp, is usually eliminated by the lamp cooling devices. Emissions within the slurry, on the other hand, can usually be ignored, since most photochemical reactions occur at moderate temperatures.

The initiation step of  $e^-/h^+$  formation is very fast (time constant approx.  $10^{15} \text{ s}^{-1}$ ), and when the reactor is well illuminated, radiation intensity stops being a determinant step. On the other hand, the uniform illumination of a reactor is very difficult to maintain within the reactor space (Cassano et al., 1995).

This radiation distribution inside a photoreactor is determined by the nature of the reactor walls, the lamp type, the lamp-reactor geometry (de Lasa et al., 2005) and the optical properties of the medium (Braun et al., 1991). All of these can be seen as factors that cannot be neglected while developing an accurate photoreactor model. Distribution and absorption of irradiation can be achieved by solving the RTE (a photon balance) and by using the appropriate boundary conditions. In this respect, one should combine the momentum balance, the energy balance and the mass conservation equations with RTE, in order to accurately model and design photocatalytic reactors.

From the radiative point of view, the application of the Radiative Transfer Equation (RTE) must be carried out (Eq. 2-7), and the resulting equation can be expressed as:

$$\frac{dI_{\lambda}(s, \Omega)}{ds} = -(\kappa_{\lambda} + \sigma_{\lambda})I_{\lambda}(s, \Omega) + j_{\lambda}^e(s) + \frac{1}{4\pi}\sigma_{\lambda} \int_0^{4\pi} p(\Omega' \rightarrow \Omega)I_{\lambda}(s, \Omega')d\Omega' \quad \text{Eq. 2-7}$$

where  $I_{\lambda}$  is the spectral intensity of radiation, with units being  $\text{einstein m}^{-2} \text{ s}^{-1} \text{ sr}^{-1}$ ,  $\kappa_{\lambda}$  and  $\sigma_{\lambda}$  are the wavelength specific absorption and scattering coefficients, respectively, with



units of  $m^{-1}$ .  $p(\Omega' \rightarrow \Omega)$  is the phase function, a property that accounts for the probability of a photon being scattered from an incident direction  $\Omega'$  to a  $\Omega$  scattered direction. Since photocatalysis is carried out at low temperatures, the emission term can be neglected (Eq. 2-8) and thus:

$$\frac{dI_\lambda(s, \Omega)}{ds} = -\beta_\lambda I_\lambda(s, \Omega) + \frac{1}{4\pi} \sigma_\lambda \int_0^{4\pi} p(\Omega' \rightarrow \Omega) I_\lambda(s, \Omega') d\Omega' \quad \text{Eq. 2-8}$$

where the extinction coefficient  $\beta_\lambda = \kappa_\lambda + \sigma_\lambda$ . If the local incident radiation is integrated for all directions (Eq. 2-9), then  $G_\lambda$  can be defined as:

$$G_\lambda(x, y, z) = \int_{\Omega=0}^{\Omega=4\pi} I_\lambda(s, \Omega) d\Omega \quad \text{Eq. 2-9}$$

Where  $G_\lambda$ , multiplied by the spectral absorption coefficient, can be regarded as the wavelength specific local volumetric rate of energy absorption as (Eq. 2-10):

$$LVREA_{l,\lambda}(x, y, z) = \kappa_\lambda G_\lambda(x, y, z) \quad \text{Eq. 2-10}$$

Finally, by adding the different wavelength contributions (Eq. 2-11), the local volumetric rate of energy absorption (LVREA), can be expressed as:

$$LVREA = \sum_{\lambda \leq \lambda_{bg}} E_{l,\lambda}(x, y, z) = \sum_{\lambda \leq \lambda_{bg}} \kappa_\lambda G_\lambda(x, y, z) \quad \text{Eq. 2-11}$$

Additionally, a Total Rate of Photon Absorption can be obtained via integration of LVRPA within the reactor volume, according to the following equation:

$$TRPA = \iiint_V (LVRPA) dV \quad \text{Eq. 2-12}$$

Besides the calculations in slurry region, consideration has to be given to the selection of proper boundary conditions. These boundary conditions can encompass several physical phenomena, happening outside of the photoreactor. These are caused by lamps, reflectors and other devices, as will be pointed out in the upcoming subsection.

### 2.4.1 Phase Functions

Another important criterion in radiation modeling of photoreactors is the parameter describing the scattering mode, which is the phase function. The phase function is related to the probability of photon scattering from the direction of incidence in the catalyst particle, to a new direction. Thus, an adequate phase function is important given the following: i) the need to provide an accurate representation of the scattering, ii) the requirement of accomplishing this, under manageable computation times (Satuf et al., 2005).

### 2.4.2 Lamp Emission modeling

In order to solve the RTE for a photocatalytic reactor, boundary conditions need to be established. These boundary conditions are based on the mathematical model assumed for the radiation source, and therefore it is very important to choose an appropriate lamp model. There is a number of radiation source models proposed by different researchers (Alfano et al., 1986). The next figure shows a general classification of them.

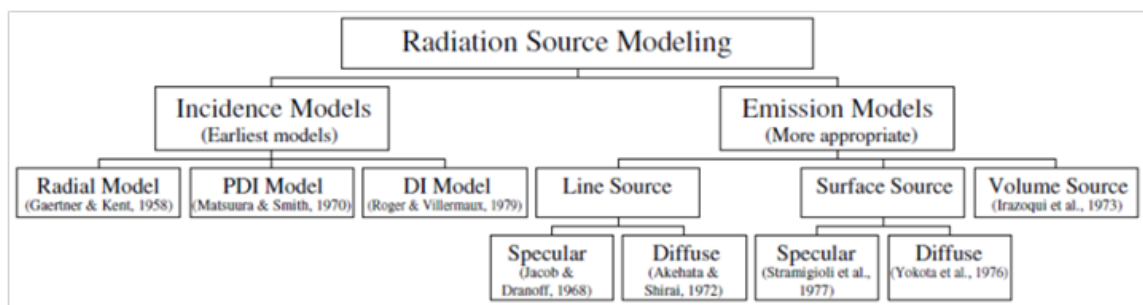


**Figure 2.2.** Classification of radiation source models (PDI partially diff. incidence, DI diffused incidence model). Cassano et al, 1995.

#### 2.4.2.1 Incidence models

The incidence model assumes a specific energy distribution in the reactor space (Alfano et al., 1986). These methods do not use operating variables (output power, lamp dimensions, etc), they only contain 1 or 2 adjustable parameters obtained by curve fitting to experimental data.

The following model is designated as the radial incidence model (Gärtner et al., 1958), where axial and angular dependencies of radiation emission are neglected (Cassano et al., 2008; Schechter et al., 1958):

$$G_v = G_{v,w} \frac{R_1}{r} (e^{-\kappa_v l}) \quad \text{Eq. 2-13}$$

This partially diffuse incidence model, includes partially diffused radiation. The various incidence radiation models include parameters that need to be experimentally determined (Pareek et al., 2008). These parameters vary significantly with the reactor configuration, its size and its operation conditions. This makes incidence radiation unsuitable as a predictive tool (or to scale-up)

#### 2.4.2.2 Emission Models

The emission models require multiple integration. They are becoming the preferred choice to model the effects of lamps in photoreactors (Alfano et al., 1986). There are different (mathematical) ways in which a lamp may be represented in the emission model.

Lamps may be represented as an emitting line, as an emitting surface (with specular or diffuse emission) or as an emitting volume. Mercury arc and neon lamps, can be represented by specular emission. On the other hand, diffuse emission is exhibited by most fluorescent lamps (Takashi & Takashi., 1972).

When the line source model is used, the lamp is assumed to be an emitting line. This can usually be assumed when the lamp diameter is small, in comparison with the reactor diameter (Pareek et al., 2008). that is:

$$dN_v = K_v dh \quad \text{Eq. 2-14}$$

Where:

$$K_{v1} = \frac{N_v}{2L} \quad \text{Eq. 2-15}$$

From this assumption, there are two possibilities, specular and diffuse emission. For specular emission the following Eq. 2-16 can be considered:

$$G_v = \frac{K_{v1}}{4\pi} \int_{-L}^L \frac{dh}{(r^2 + (z-h)^2)} = \frac{K_{v1}}{4\pi} \left( \tan^{-1} \left( \frac{z+L}{r} \right) - \tan^{-1} \left( \frac{z-L}{r} \right) \right) \quad \text{Eq. 2-16}$$

For diffuse emission the following Eq. 2-17 can be adopted :

$$G_v = \frac{K_{v1}}{4\pi} \int_{-L}^L \frac{\cos \varphi dh}{(r^2 + (z-h)^2)} = \frac{K_{v1}}{4\pi} \int_{-L}^L \frac{rdh}{(r^2 + (z-h)^2)^{3/2}} \quad \text{Eq. 2-17}$$

On the other hand, Surface source model assumes that all radiation is being produced on the lamp's surface and no radiation is emitted from the interior points. For specular emission (Pareek et al., 2008):

$$G_v = \int_{h=-L}^{h=+L} \int_{\varphi=-\pi/2}^{\varphi=+\pi/2} \frac{\frac{K_{v1}}{4\pi} r_1 d\varphi dh}{((r \cos \theta - r_1 \cos \varphi)^2 + (r \sin \theta - r_1 \sin \varphi)^2 + (z-h)^2)} \quad \text{Eq. 2-18}$$

and for diffuse emission:

$$G_v = \int_{h=-L}^{h=+L} \int_{\varphi=-\pi/2}^{\varphi=+\pi/2} \frac{\frac{K_{v1}}{4\pi} (r \cos \theta - r_1 \cos \varphi) r_1 d\varphi dh}{((r \cos \theta - r_1 \cos \varphi)^2 + (r \sin \theta - r_1 \sin \varphi)^2 + (z-h)^2)} \quad \text{Eq. 2-19}$$

In the volume source model, photons are considered to be emitted by the surface and the interior of the lamp. Therefore, the number of photons emitted by a volume element is given by (Pareek et al., 2008):

$$dN_v = K_{v3} \eta d\eta dh d\varphi \quad \text{Eq. 2-20}$$

where:

$$K_{v3} = \frac{N_v}{(2\pi r_1^2 L)} \quad \text{Eq. 2-21}$$

The incident radiation at each point of the reactor geometry, is given by integrating the following equation 2-22 over the entire lamp volume:

$$G_v = \int_{h=-L}^{h=+L} \int_{\eta=0}^{\eta=r1} \int_{\varphi=-\pi/2}^{\varphi=+\pi/2} \frac{\frac{K_{v3}}{4\pi} \eta d\eta d\varphi dh}{((r \cos \theta - \eta \cos \varphi)^2 + (r \sin \theta - \eta \sin \varphi)^2 + (z - h)^2)} \quad \text{Eq. 2-22}$$

The Volume Source Model was considered to be the only emission model to give good results for reactors involving curved reflectors (Alfano et al., 1986 ; Irazoqui et al., 2000). However, it was recently proven that the superficial diffuse emission performs as well under near and far field measurements (Duran et al., 2010). Besides the emission model in the lamp, absorption, refraction and reflection on the lamp's surface cannot be neglected since they considerably improve the accuracy in predicting both near and far field measurements (Imoberdorf et al., 2008). Technically, the only aim of a source method, is to provide boundary conditions at the beginning of the absorbing reactive medium. All other geometric factors are taken into account by the numerical method used to solve the RTE.

Regarding the radiation sources emission spectra, spectral purity is not a very critical factor in photocatalytic processes. However, for reactors using titanium dioxide as a photocatalyst, the lamp should be able to emit radiation with wavelengths equal or less than 387.5 nm (Braun et al., 1991). The types of lamps available are arc lamps, incandescent lamps, fluorescent lamps and lasers.

Incandescent lamps tend to emit (mostly) radiation in the visible region, which does not have enough energy to promote the electron-electron hole formation. Lasers tend to be too expensive to be suitable for this kind of application. The most used lamps are fluorescent lamps and medium-pressure mercury lamps with an emission between 190 and 600nm (Phillips et al., 1983).

### 2.4.3 Reflectors and interfaces

Reflectors are important factors to be considered when properly defining boundary conditions. They are most commonly used in solar pilot-plant scale reactors. The phenomena taking place at these interfaces, when occurring in complex geometries, can be described by using the tangent plane approximation, when the wavelength of the

electromagnetic wave is small compared to the local curvature of the surface (He et al., 1991).

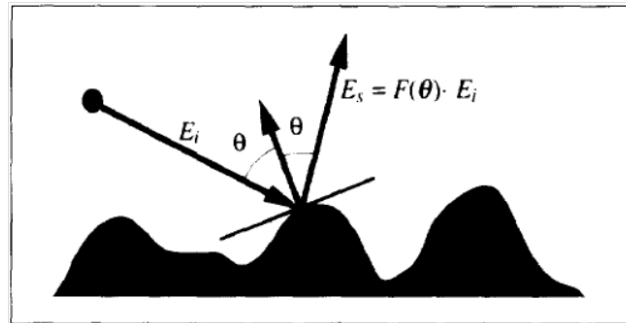


**Figure 2.3.** A rough surface can be treated by the tangent plane approximation, taken from (He et al., 1991).

In general, reflection and diffraction have already been extensively studied. Snell's Law is used for refraction. Reflection can be separated into three cases: a) specular, b) ideal diffuse and c) directional diffuse. All of these reflection mechanisms are taken into account by the BRDF model (Bidirectional Reflectance Distribution Function Model), where the three mechanisms are added, as a total reflectance (He et al., 1991). BRDF Models are currently actively being researched (Berger et al. 2012; Colbert et al., 2006). However, in some cases, idealized behaviour can be applied to simplify the mathematical treatment of reflection phenomena (Hyde et al., 2009), such as is the case for: ideal specular, ideally diffuse, directional diffuse and total absorptive surfaces, among others.

Specular reflection refers to mirror-like reflection, where radiation bounces off the interface (also called first surface reflection), as shown in Figure 2.3. This leaves the angle between the vector parallel to the radiation direction and the angle between the vector normal to the tangent plane, unchanged (before and after radiation interacted with the material).

Diffuse Reflection is caused by multiple subsurface reflections (in dielectric materials). It is sometimes caused by surface roughness which causes multiple surface reflections (Wolff 1994). In the case of ideal diffuse reflection, also called Lambertian reflectance, reflection is independent of the angle of incidence and is described by Lambert's Cosine

Law with respect to the surface normal vector. Directional diffuse emission, on the other hand, is not independent of the angle of incidence. When combining all reflection mechanisms (i.e. specular, ideally diffuse and directional diffuse ), Figure 2.4 depicts how a probability distribution for reflection would look.

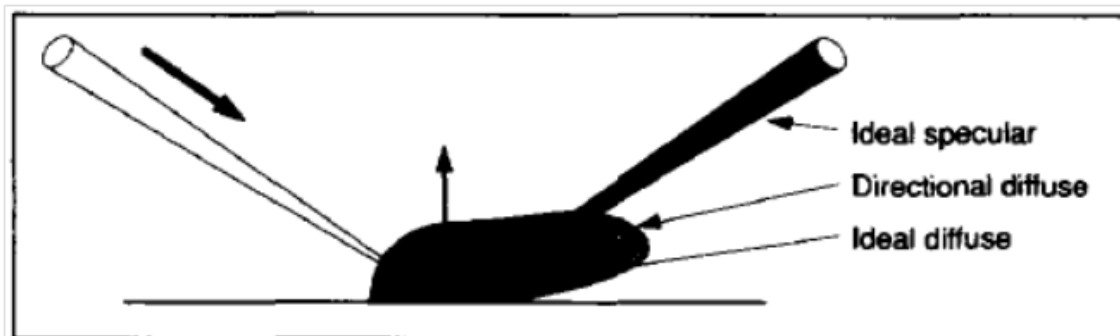


**Figure 2.4.** Description of the different mechanisms through which radiation can be reflected from a solid surface, taken from (Wolff 1994)

## 2.5 Monte Carlo Method

The analytical solution of the RTE for heterogeneous media is a rather complex task and is so far only achievable in a restricted number of idealized reactor models (Grčić and Li Puma 2013).  $\text{TiO}_2$  particles inside the photoreactor annular section cause near-UV radiation scattering. Thus, establishing the scattering mechanism poses extra challenges, given that it is a function of many variables such as: a) lamp emission spectra, b) reactor geometry, c) type of photocatalyst (band-gap), d) optical properties (scattering and absorption coefficients), e) chemical properties (agglomeration, charge trapping), and f) nature of reactor walls, among other factors (Salaices et al., 2002; Pareek et al., 2003).

To address these issues, the RTE in photocatalytic reaction engineering has been, most commonly, solved numerically. Among the most used methods, are: i) the Monte Carlo Method (MC) (Pareek et al., 2008; Changrani & Raupp, 1999; Yokota et al., 1999; Valades-Pelayo et al. 2014), ii) the P1 Method (Cuevas et al., 2007; Arancibia-Bulnes and Cuevas, 2004) and iii) Discrete Ordinate Method (Duran et al. 2010), and more specifically, iv) the Two-Flux and v) the Six-Flux Absorption Scattering Methods (Li

Puma & Brucato, 2007; Li Puma, 2003). It has been demonstrated that the MC Method is preferable over deterministic methods to calculate the LVRPA with complicated geometries (Changrani & Raupp, 1999). This is due to the physical correctness adopted in the method (Pareek et al., 2003). Furthermore, it is frequently used to validate other Radiation Transport Methods (Iwabuchi, 2006).

The MC Method consists of tracing individual photons or photon bundles from their generation by the UV-radiation source until they are absorbed or scattered inside the slurred system. In addition, it has also been shown that a statistical method provides a very effective approach in predicting the absorption and scattering phenomena in slurry systems (Yokota et al., 1999).

When solving the RTE in photocatalytic reactors, the following is required:

- (1) TiO<sub>2</sub> optical parameters such as absorption and scattering coefficients are to be provided. Romero et al., (1997) reported values for the absorption and scattering coefficients of Degussa P25 for a concentration range of 5-500 mg l<sup>-1</sup>. Absorption and scattering coefficients for Degussa P25 as a function of wavelength were also given by Romero et al., (2003) for a range from 275 to 405 nm.
- (2) Photoreactor boundary conditions have to be carefully selected. The radiation emitted by the radiation source has to be accurately defined and the optical properties of the reactor walls must also be properly identified.
- (3) A scattering phase function has to be established (Piskozub and McKee 2011). Phase functions calculate the angle at which photons are scattered from one direction to another. As a result, selecting a phase function in heterogeneous photocatalysis allows calculating multiple scattering events (Binzoni et al., 2006). It is important to mention that in the MC Simulations, the most computer intensive step is frequently the one of establishing the new direction of the scattered photon (Moreira et al., 2011). As a result, the use of phase functions requiring intensive computations should be limited as much as possible.



Regarding the numerical method "*per se*", the RTE is solved by running random events where "photons" are emitted. The trajectory of each "emitted" photon is followed and the final location and wavelength of the absorbed photon are stored in a matrix. The trajectory of each photon is defined based on a stochastic process, in which the events, outcomes and probabilities for each possible photon are chosen in a way that they represent the natural phenomena occurring inside the reactor.

From a general perspective, the Monte Carlo Simulation starts with given conditions for the reflectors and the reactor walls. These conditions will depend on the used materials and the geometry. The total energy input and the radiation spectrum will be a function of the lamp used. However, when the photons are inside the reactive heterogeneous medium, the probability of either being absorbed or scattered will be determined by the reaction medium itself (Moreira et al., 2010).

More specifically, photons are traced for each wavelength. Random numbers are generated to set the location in the lamp, from which the photon will be "emitted". Once the position is set, the direction of emission is also identified by random zenith and azimuth angles. The photon trajectory is traced until it penetrates the reaction medium. Additionally, the probability of a photon being absorbed by one of the reactor walls is based on the transmittance of the material.

Emission is considered to be a stochastic process, and is defined by lamp specifications, such as: a) the wavelength distribution (radiation spectra), b) the number of photons per unit time, and/or c) the type of emission pattern that the lamp presents (coherent or diffuse emission).

In the case of reflecting surfaces, diffuse reflection, specular reflection or absorption of each photon should be taken into account. If needed, this can be set as a function of the wavelength and incidence angle (Wolff 1994). Shadowing during reflection can be hard to take into account (He et al., 1991). In order to include this phenomenon in a Monte Carlo Method, only one additional stochastic event needs to be added. The outcome for each specific event is determined by the relation between the probability distributions and the random numbers defined for the specific events: a Markov chain.

In the reaction media, the photon can be absorbed or scattered. If the photon is absorbed, its trajectory is terminated. If the photon is scattered, the scattering angle will, then need to be redefined. The outcome will be chosen according to the phase function and its relation with another randomly generated number. The trajectory of the photon will be modified and the process will repeat itself (Moreira et al. 2010). This will occur until the photon is absorbed or reaches a reactor wall, where it can exit the reaction medium or be absorbed into the reactor wall.

The probability of each event and each possible outcome depends on the physical properties of the heterogeneous medium. Once the photon is absorbed by the reaction media, its location is stored in a matrix. This action will allow calculating the LVRPA by adding all the photons that where absorbed in every single location.

MC simulations are simple to implement, provided that one is able to capture the physical phenomena involved, as a conglomerate of probability density functions. Despite all of its advantages, the MC Method still presents certain issues: (1) the large number of events that need to be accounted for in the random path simulation, (2) the computationally extensive ray tracing at each photon collision and (3) the phase function required to calculate scattering angles at each collision point. Thus, large computer power is needed for the MC simulation (Li Puma, 2005).

In spite of this, nowadays, the MC Method is becoming prevalent. Thi is due to computational power availability and the possibility of establishing accurate radiation models in the context of asymmetric radiation fields. This is the case, given that when the geometries are complicated and the medium is heterogeneous, overall, Monte Carlo is the most effective tool (Yokota et al., 1999).

## 2.6 Photocatalytic Reactors

Photocatalytic reactors for water treatment can be classified according to their design characteristics, the majority of them fall under the next categories (de Lasa et al. 2005; Malato et al., 2004):

- a) State of the TiO<sub>2</sub> catalyst (suspended or attached to a support).
  - Slurry reactors.
  - Immobilized photocatalyst.
- b) Type of reactor irradiation source.
  - Artificial UV radiation, UV polychromatic lamps.
  - Solar light.
- c) Position of the radiation source.
  - Reactors with an immersed radiation source.
  - Reactors with an external radiation source.
  - Reactors with distributed radiation sources such as reflectors and light conductors or optical fibers.

The majority of the photocatalytic reactors currently in use for water treatment are slurry reactors. While supported catalyst are still on use, avoiding the need of any separation step once the pollutants are degraded, studies have shown that reaction rates from 2 to 5 times greater are observed in the suspended case (de Lasa et al., 2005).

There are three standard, most widely used, geometrical configurations of photoreactors: annular, parabolic and elliptic. Additionally, a lot of novel designs of photoreactors have been used, such as: a) fountain, b) optical fiber, c) monolith, d) falling film, e) U-tube reactors, f) double skin sheet, g) rotating disk, h) packed bed, i) Taylor vortex, j) fluidized bed and k) corrugated plate reactors among others (Pareek et al., 2008; Braham et al., 2009; McCullagh et al. 2011). Annular photoreactors allows high throughputs and continuous operation. These types of reactors, when using suspended photocatalyst, have shown the largest photocatalytic activity when compared to reactors with TiO<sub>2</sub>

immobilized on a support (de Lasa et al., 2005). Usually an additional cooling assembly can be used if isothermal operation is required.

Elliptical reactors are used when high throughputs are not required or if the reactions are highly exothermic with high pollutant concentrations. In these reactors, two parallel cooling mechanisms are needed (one for the lamp and another one for the reactor). Parabolic reactors are suitable for opaque liquid irradiation. Reflectivity of the container wall is very crucial in both parabolic and elliptical geometries

Falling film reactors are basically a combination of the annular and parabolic reactors (a thin film in a parabolic container). Optical fibre reactors, as the name suggests use optical fibres to ensure adequate illumination of all photocatalyst-coated surfaces. When correctly designed, they can overcome photon and mass transfer limitations even with a supported catalyst (Denny et al., 2010).

## 2.7 RTE Parameter Estimation

The LVREA can be determined by solving the RTE, which is a property of major interest for photocatalytic reaction engineering (Li Puma, 2005). Nonetheless, the optical properties of the reaction medium must be known. This is the case, given that reaction rates are dependent on photon absorption and not on the photon irradiation “per se”. As a result, knowing the radiation absorbed by the photocatalyst in a given reactor system, allows one to establish the chemical species rate of change as a function of the energy absorption rate (Minero & Davide, 2006). This also permits one to calculate energy efficiencies, such as the quantum yield (QY) and the photochemical thermodynamics efficiency factor (PTEF) (de Lasa et al., 2005).

It is important to mention that the LVREA, has never been measured directly. It has, instead, been indirectly estimated, i.e. via calculations, by fitting to irradiance and/or to actinometrical measurements (Alfano et al., 2000). This inability to measure the property of interest, poses an additional challenge in photocatalytic reaction engineering. Using actinometry for the estimation of the radiation absorbed by the photocatalyst particles, tends to present issues due to non-selective absorption by the actinometer (Turchi &

Ollis, 1989). The data obtained by these means is often called “apparent radiation absorption” (Brandi et al., 2003). Specifically for irradiance-based RTE parameter fittings, the Total Transmittance (TT), the Volumetric Rate of Photon Absorption (VRPA) and the Total Rate of Photon Absorption (TRPA) are the most widely used variables to determine the LVREA (Valades-Pelayo et al., 2014; Li Puma et al., 2010). It should be noted that the TRPA divided by the reactor volume equals the VRPA and as a result, one is proportional to the other.

### 2.7.1 Phase Function Determination

The specific selection of the adequate phase functions still remains until today an area of uncertainty (Moreira et al. 2010; Moreira et al. 2011; Satuf et al. 2005; Marugan et al. 2006). However, both isocratic and Henyey-Greenstein phase functions are the most widely used, when finding the solution of the RTE for  $\text{TiO}_2$  in photocatalytic reaction engineering. Furthermore, the effect of the scattering mode in the calculated LVREAs is not reported nor discussed. In this respect, it has been suggested by different authors that a precise evaluation of the scattering mode (or phase function) appears not to be critical for a good TRPA representation of experimental values (Moreira et al., 2010; Pasquali et al., 1996).

Moreira et al. (2010) concluded that for  $\text{TiO}_2$ , the Henyey-Greenstein phase functions with  $g$  values in the range  $-0.7 < g < 0.7$  are satisfactory. Pasquali et al (1996) also studied Isocratic and Diffuse Phase Functions, concluding that both scattering modes render close results in the modelling of the radiation field in a photoreactor. It is worth mentioning that, with titanium dioxide, the main problem is that the coefficients for powders depend strongly on the radiation wavelength. Hence, the RTE must be solved for each wavelength. Romero et al. (1997), however, used a wavelength averaged absorption and scattering coefficients for experiments carried out in the 220 nm to 1370 nm range. They proved that this process could be performed without major loss of accuracy.

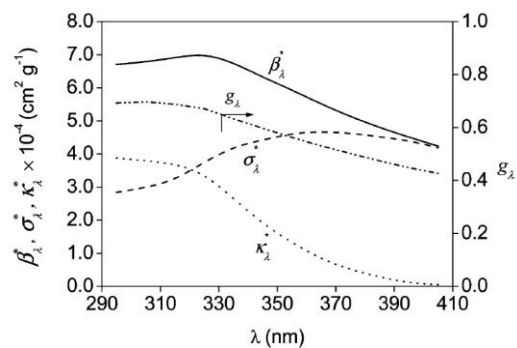


**Figure 2.5** Optical Properties vs wavelength for Degussa P25 catalyst: solid line,  $\beta^*_\lambda$ ; broken line  $\sigma^*_\lambda$ ; dotted line  $\kappa^*_\lambda$ ; broken dotted line,  $g_\lambda$ . Taken from [Satuf et al., 2005](#).

[Satuf et al. \(2005\)](#), reported specific spectral values for the  $g$  scattering parameter when using Degussa P25, as shown in Figure 2.5. These results were determined by measuring the total transmittance of  $\text{TiO}_2$  suspensions in quartz cells, with a 1 to 2 cm internal depth. To achieve optimal optical thickness, photocatalyst concentrations considered by this study were varied from 200 to 2000  $\text{mg l}^{-1}$ .

It should be noted that the phase function determined by [Satuf et al. \(2005\)](#), for Degussa P25, is of limited applicability for bench-scale and pilot-plant photoreactors. This is the case, given that optimal photocatalyst concentrations in these reactors are about ten times smaller than the ones considered by [Satuf et al. \(2005\)](#). In this respect, effects such as severe deposition of Degussa P25 at the reactor walls and photocatalyst agglomeration are expected to affect the slurry optical properties ([Ballari et al., 2010](#)). For instance, for a small bench-scale photoreactor, such as the Photo-CREC Water II (2.65 L annular photoreactor), the optimum photocatalyst concentration for Degussa P25 was reported to lay at 150  $\text{mg l}^{-1}$  ([Salaices et al., 2002](#)).

In previous works, our research group developed a MC Method for solving of the Radiation Transfer Equation (RTE) in an annular photoreactor ([Moreira et al., 2010](#); [Moreira et al., 2011](#); [Valades-Pelayo et al., 2014](#)). Isocratic and Henyey-Greenstein Phase Functions were adopted. The predicted results for the Total Rate of Photon Absorption (TRPA) and Total Transmittance (TT) were validated with experimentally established macroscopic radiation balances as presented in [Salaices et al. \(2002\)](#).

[Cabrera et al. \(1995\)](#) studied the effect of different scattering phase functions on the solution of the RTE. These authors considered three cases for the phase function: (1) specular with partial reflection, (2) isotropic scattering and (3) scattering centers with a diffuse type of reflection. Phase functions from backward to forward types of scattering were considered. The experimental validation of this model was performed through monitoring degradation rates using actinometry.

[Changrani & Raupp, 1999](#) used Monte Carlo Simulations to replicate a polychromatic UV radiation field with direction angles included. Different authors reported the solution of the RTE in annular photoreactors. [Yokota et al., \(1999\)](#) also developed a MC Simulation Model. These authors consider an attenuation coefficient, a probability of photon absorption and isotropic and anisotropic scattering modes. These authors also found that the simulation results agreed with the experimental data for most cases of the phase functions.

Other semi-empirical approaches like the two-flux and the six-flux absorption-scattering models ([Li Puma and Brucato, 2007](#)) have proven to predict radiation reasonably well for bench-scale photoreactors, as well as degradation rates for specific reactor geometries ([Grčić & Li Puma 2013](#)), but none with applicability for scale-up purposes.

## 2.7.2 Macroscopic Radiant Energy Balance

The macroscopic radiation balance was performed in an annular slurry photocatalytic reactor ([Salaices et al., 2002](#)), to estimate the rate of photon absorption, in the following way:

$$P_a = P_i - P_{bs} - P_t \quad \text{Eq. 2-23}$$

Where the rate of absorbed photons ( $P_a$ ), equals the rate of photons entering the slurry ( $P_i$ ), minus the rate of photons being backscattered ( $P_{bs}$ ) and transmitted ( $P_t$ ). When performing this balance,  $P_i$  is estimated from the difference between the total emitted photons from the lamp ( $P_o$ ) and the photons that are absorbed or reflected by the reactor wall (or any other interphase that the photons must cross to enter the slurry). To calculate

the back-scattered photons ( $P_{bs}$ ), a measurement must be performed to obtain it from the following equation (Eq. 2-24):

$$P_{bs} = P_i - P_{c \rightarrow 0+} - P_t \quad \text{Eq. 2-24}$$

Where,  $P_{c \rightarrow 0+}$  is the rate of photons transmitted when the catalyst concentration approaches zero, according to [Salaices et al., 2002](#).

## 2.8 Photocatalytic Reactor Scale-up

The comprehensive design of a photocatalytic reactor requires the description of physicochemical phenomena using constitutive equations ([de Lasa et al., 2005](#)). In this respect, many of the general guidelines for dealing with catalytic reactions can be adapted for photocatalytic reactions ([Cassano et al., 2000](#)). However, when it comes to specific scale-up strategies, most of the traditional procedures used in thermally-activated chemical processes, have been of very limited applicability ([Marugan et al., 2013](#)). The reason being is that, for photocatalytic reactions, radiation absorption occurs at the very beginning of the whole photocatalytic process. They are, therefore, strongly dependent on both radiation intensity and distribution ([Changrani & Raupp, 1999](#); [Cassano et al., 2000](#)). This is true to the point that, the LVREA can be regarded as the master variable in photocatalytic reaction engineering ([Moreira et al., 2010](#); [Camera-Roda et al., 2005](#)).

The differences, for photocatalytic reactor modelling, are due to the unconventional role that the photocatalyst fulfills, when compared to most catalytic processes: it absorbs radiation to induce charge separation, while at the same time; it is responsible for the scattering effects that determine radiation distribution itself ([Cassano and Alfano, 2000](#)). In this regard, given that radiation distribution tends to drop abruptly in heterogeneous slurry media ([Changrani & Raupp, 1999](#)), it is hard to investigate kinetic models independently from radiation models. This is true, to the point that, for bench-scale photoreactors operating at near optimum photocatalyst concentrations, this effect is unavoidable ([Marugan et al., 2013](#); [Marugan et al. 2010](#); [Valades-Pelayo et al. 2014a](#)).



For this reason, an accurate estimation of the LVREA is critical in the design, scale-up and performance evaluation of photoreactors (Pareek et al., 2008 ; Pasquali et al., 1996). In addition, the correct estimation of the radiation field inside the photoreactor allows for the accurate determination of energy efficiencies, such as the QY and the PTEF. The main parameters affecting the LVREA are: i) the reactor geometry, ii) the radiation sources emission intensity and iii) the photocatalyst concentration and optical properties, among others.

Regarding these parameters, it has been reported that the reaction rate presents a square-root dependence with respect to lamp irradiance, being linear at very low irradiances (Motengh et al. 2012 ; Camera-Roda et al., 2005). The dependence of the reaction rate on the photocatalyst concentration, has been reported to be linear at low photocatalyst concentrations. It then transitions to a square-root dependence as concentration increases. Finally, it converts to a zeroth-order/asymptotic dependence that, ultimately, tends to decrease for extremely high photocatalyst concentrations (Kawaguchi, 1994; Kapinus et al. 2009; Curco, 2002)

Moreover, when conceived for scale-up purposes, photocatalytic kinetic models require the accounting of several additional phenomena at the photocatalyst particle level, besides radiation absorption. One of these phenomena is charge separation and recombination at the photocatalyst particle surface (Bahnemann, 2004). Several physically meaningful models have been proposed in this regard (Turchi and Ollis, 1989 ; Minero, 1999). They will be explained in section 6.4.2. Furthermore, after charge separation is induced in the photocatalyst particles, adsorbed free radicals and desorbed aqueous free radicals within the particle vicinity, are generated (Liao and Reitberger, 2013). It is through them (Lawless et al., 1991) that a great number of photocatalytic reactions are made thermodynamically possible (Mohameda and Bahnemann , 2012).

Moreover, while spatial gradients can be neglected for the concentrations of the degraded organic species (de Lasa, 2005), this is not necessarily the case for the free radicals adsorbed on the photocatalyst particles (Davydov, et al. 2001). This is due to two

main reasons: i) the spatial distribution of the LVREA and ii) the reaction system hydrodynamics. Hydrodynamics can be an important factor to properly predict photocatalytic reactor performance when changing reactor scale and/or geometry (Koci et al., 2011). This is the case, as hydrodynamics affects the photocatalyst Residence Time Distribution (RTD) in the photoreactor unit, and therefore, the time of irradiation (Davydov, et al. 2001).

## 2.9 Current research directions

In the last decade, the development and implementation of predictive/scale-up procedures for photocatalytic reactor modelling has been a subject of active research for laboratory to bench-scale units, where they have shown to be accurate. On this specific subject, Imoberdorf et al. (2007) scaled-up a laboratory scale flat plate reactor to a reactor having 5,209 cm<sup>2</sup> of irradiated area. Imoberdorf et al. (2008), developed a radiation distribution predictive model for a fluidized bed photocatalytic reactor (approx. 2.15 L) where he used the experimental effective transmittance (Total Transmittance) to validate the simulated radiation. Li Puma et al. (2007), scaled-up a laboratory scale annular photoreactor to compare the two-flux and six-flux methods. Pareek et al. (2008) simulated the radiation intensity distribution of a photocatalytic reactor. The validation of the model was carried out using experimental data from the photodegradation of a Bayer liquor. Marugan et al. (2009) reported a methodology to scale-up a slurry annular lab-scale photoreactor (0.12 L) to a litre bench-scale (1.25 L) reactor. Finally, Marugan et al. (2013) recently simulated a bench-scale annular photoreactor (1.25 L) operating at optimum photocatalyst concentration by using a predictive procedure and kinetic data from a laboratory scale photoreactor (0.188 L).

Thus, it is noticed that predictive models have been shown to be adequate for the scale-up of laboratory to bench-scale symmetrically-irradiated photoreactors, not surpassing the 2 to 3 liters scale. In spite of this significant progress, in recent years, special interest has been shown to extend the applicability of the kinetic models by using semi-empirical radiation methods, for bench to pilot-plant scale photocatalytic reactors (Duran et al., 2010; Oyama, et al., 2011; Baniyadi et al., 2012). To our knowledge, no kinetic model

validation has been done based on predictive RTE models, to scale-up bench to pilot plant scale photoreactors, with different irradiance conditions.

Our research group studied a bench-scale annular photoreactor of 2.65 L irradiated volume, named the Photo-CREC Water II Reactor (Salaices et al., 2005; Moreira et al., 2011). Using this unit, diverse kinetic models have been obtained (Ortiz-Gomez, et al., 2008; Moreira et al., 2012 ; Escobedo-Salas, et al., 2013). However, no validation at different irradiance conditions, photocatalyst concentrations, or different scales has been acquired. The reactor used in all these studies was irradiated from the center by a 15 W Black-Light (BL) UVA lamp.

Finally, it is worth mentioning that the majority of the laboratory and bench-scale reactors studied up to now were irradiated using both artificial radiation sources and symmetric irradiation. This type of symmetry of irradiation is not expected to be achieved in large scale units, which will most likely be powered by solar energy (Malato et al., 2002). On this basis, it is expected that scale-up methodologies will need to account for drastic changes in the irradiance boundary conditions and reactor geometry, in general (Valades-Pelayo et al. 2014c).

## 2.10 Conclusions

There is a need for the established predictive scale-up methodologies to be extended from bench to pilot-plant photoreactors. These scale-up methodologies should be based on physically sound models, with independently validated radiative and kinetic models.

Moreover, these models should be capable of accounting for variables such as: i) different photocatalyst concentrations, ii) diverse irradiance configurations and intensities, and ultimately for iii) different reactor scales and configurations.

Additionally, establishing radiative models at different scales requires several geometry independent parameters to be determined. On this subject, there is a discrepancy in the literature, regarding the selection of phase functions and their applicability at different scales and operating conditions.

Given these facts and to account for any effects arising from the photocatalyst agglomeration or wall deposition, a methodology should be developed to determine optical parameters directly from the bench-scale units.

## 2.11 References

Ahmed, S., Rasul, M., Martens, W., Brown, R., & Hashib, M. (2011). Advances in Heterogeneous Photocatalytic Degradation of Phenols and Dyes in Wastewaters: A Review. *Water Air and Soil Pollution* , 215, 3-29.

Ahmed, S., Rasul, M., Martens, W., Brown, R., & Hashib, M. (2010). Heterogeneous photocatalytic degradation of phenols in wastewater: A review on current status and developments. *Desalination* , 261, 3-18.

Alfano, O. M., Bahnemann, D., Cassano, A. E., Dilliert, R., & Goslich, R. (2000). Photocatalysis in Water Environments Using Artificial and Solar Light. *Catalysis Today* , 58, 199-230.

Alfano, O. M., Cabrera, M. I., & Cassano, A. E. (1997). Photocatalytic Reactions Involving Hydroxyl Radical Attack. *Journal of Catalysis* , 172, 370–379.

Bahnemann, D. (2004). Photocatalytic Water Treatment: Solar Energy Applications. *Solar Energy* , 77, 445-459.

Ballari, M. d., Alfano, O. M., & Cassano, A. E. (2010). Mass transfer limitations in slurry photocatalytic reactors: Experimental Validation. *Chemical Engineering Science* , 65, 4931-4942.

Baniasadi, E., Dincer, I., & Naterer, G. F. (2012). Radiative heat transfer and catalyst performance in a large-scale continuous flow photoreactor for hydrogen production. *Chemical Engineering Science* , 84, 638-645.

Berger, K., Weidlich, A., Wilkie, A., & Magnor, M. (2012). Modeling and Verifying the Polarizing Reflectance of Real-World Metallic Surfaces. *IEEE Computer Graphics and Applications* , 32(2).

Bhatkhande, D., Pangarkar, V., & A.A., B. (2001). Photocatalytic degradation for environmental applications: a review. *Journal of Chemical Technology and Biotechnology* , 77, 102-116.

Black, R. (2009, february 2nd). *Water-another global 'crisis'?* Retrieved from BBC News Science and Environment: <http://news.bbc.co.uk/2/hi/science/nature/7865603.stm>

Braham, R. J., & Harris, A. T. (2009). Review of major design and scale-up considerations for solar photocatalytic reactors. *Industrial and Engineering Chemistry Research* , 48, 8890-8905.

Braun, M., Maurete, M., & Oliveros, E. (1991). *Photochemical Technology* (Eds. D.F. Ollis, N. Serpone). Chichester: Wiley.

Camera-Roda, G., Santarelli, F., & Martin, C. A. (2005). Design of photocatalytic reactors made easy by considering the photons as immaterial reactants. *Solar Energy* , 79, 343-352.

Cassano, A., & Alfano, O. (2008). Photoreactor Modelling: Applications to advanced Oxidation Processes. *International Journal of Chemical Reactor Engineering* , Vol. 6.

Cassano, A., & Alfano, O. (2000). Reaction engineering of suspended solid heterogeneous photocatalytic reactors. *Catalysis Today* , 58, 167-197.

Cassano, A., Martin, C., Brandi, R., & Alfano, O. (1995). Photoreactor Analysis and Design: Fundamentals and Applications. *Industrial Engineering Chemistry Research* , 34, 2155-2201.

Changrani, R., & Raupp, G. (1999). Monte Carlo Simulation of the Radiation Field in a Reticulated Foam Photocatalytic Reactor. . *AIChE* , 45(5), 1085.

Colbert, M., Patanaik, S., & Krivanek, J. (2006). BRDF-Shop: creating physically correct bidirectional reflectance distribution functions. *IEEE Computer Graphics and Applications* , 26(1) , p. 30-36.

Curcó, D., Giménez, J., Addardak, A., Cervera-March, S., & Esplugas, S. (2002). Effects of radiation absorption and catalyst concentration on the photocatalytic degradation of pollutants. *Catalysis Today* , 76, 177-188.

Davydov, L., Tsekov, R., & Smirniotis, P. G. (2001). Optimal radiation field in one-dimensional continuous flow heterogeneous photocatalytic reactors. *Chemical Engineering Science* , 56, 4837-4847.

de Lasa, H., Serrano, B., & Salaices, M. (2005). *Photocatalytic Reaction Engineering*. New York: Springer.

Denny, F., Scott, J., Pareek, V., Peng, G., & Amal, R. (2010). Computational fluid dynamics modelling and optimal configuring of a channelled optical fibre photoreactor. *Chemical Engineering Science* , 65, 5029-5040.

- Duran, A., Monteagudo, J. M., San Martin, I., & Aguirre, M. (2010). Decontamination of industrial cyanide-containing water in a solar CPC pilot plant. *Solar Energy* , 84 1193-1200.
- Fujishima, A., Kohayakawa, K., & Honda, K. (1975). Hydrogen Production under Sunlight with an Electrochemical Photocell. *Journal of Electrochemical Society* , Vol. 22, Issue 11 , pag. 1487-1489.
- Gaya, U. I., & Abdullah, A. H. (2008). Heterogeneous photocatalytic degradation of organic contaminants over titanium dioxide: A review of fundamentals, progress and problems. *Journal of Photochemistry and Photobiology C:Photochemistry Reviews* , 9, 1-12.
- Gora, A., Toepfer, B., Puddu, V., & Li Puma, G. (2006). Photocatalytic oxidation of herbicides in single-component and multicomponent systems: Reaction kinetics analysis. *Applied Catalysis B: Environmental* , 65, 1-10.
- He, X. D., Torrance, K. E., Sillion, F. X., & Greenberg, D. P. (1991). A Comprehensive Physical Model for Light Reflection. *Computer Graphics* , Vol. 25, Num4. Pag. 177-182.
- Hoffmann, M., Scot, T., Wonyong, C., & Bahnemann, D. (1995). Environmental Applications of Semiconductor Photocatalysis. *Chemical Reviews* , 95, 69-96.
- Hyde, M. W., Schmidt, J. D., & Havrilla, M. J. (2009). A geometrical optics polarimetric bidirectional reflectance distribution function for dielectric and metallic surfaces. *Optics Express* , Vol. 17 , Issue 24, pag. 22138-22153.
- Imoberdorf, G. E., Irazoqui, H. A., Alfano, O. M., & Cassano, A. E. (2007). Scaling-Up from first principles of a photocatalytic reactor for air pollution remediation. *Chemical Engineering Science* , 62, 793-804.
- Imoberdorf, G. E., Taghipour, F., Keshmiri, M., & Mohseni, M. (2008). Predictive radiation field modeling for fluidized bed photocatalytic reactors. *Chemical Engineering Science* , 63, 4228-4238.
- Irazoqui, H. I., & A., C. (2000). Simplified Extense Source Model for Photoreactor Analysis and design. *Industrial and Engineering Chemistry Research* , 39, 4260-4271. .
- Ismail, A. A., & Bahnemann, D. W. (2014). Photochemical splitting of water for hydrogen production by photocatalysis: A review. *Solar Energy Materials & Solar Cells* , 128, 85-101.

Kapinus, E., Viktorova, T., & Khalyavka, T. (2009). Dependence of the rate of photocatalytic decomposition of safranin on the catalyst concentration. *Theoretical and Experimental Chemistry* , Vol. 45, No.2 .

Kawaguchi, H. (1994). Dependence of Photocatalytic Reaction Rate On Titanium Dioxide Concentration In Aqueous Suspensions. *Environmental Technology* , 15:2, 183-188.

Koċı, K., Reli, M., Kozák, O., Lacny', Z., Plachá, D., Praus, P., et al. (2011). Influence of reactor geometry on the yield of CO<sub>2</sub> photocatalytic reduction. *Catalysis Today* , 176, 212-214.

Lawless, D., Serpone, N., & Meisel, D. (1991). Role of the OH radicals and trapped Holes in Photocatalysis. A Pulse Radiolysis Study. *Journal of Physical Chemistry* , 95, 5166-5170.

Li Puma, G. (2005). Dimensionless Analysis of Photocatalytic Reactors Using suspended Solid Photocatalyst. *Chemical Engineering Research and Design* , 83(A7), 820-826.

Li Puma, G. (2003). Modelling of Thin-Film Slurry Photocatalytic Reactors Affected by Radiation Scattering. *Environmental Science & Technology* , 37, 5783-5791.

Li Puma, G., & Brucato, A. (2007). Dimensionless analysis of slurry photocatalytic reactors using two-flux and six-flux radiation absorption–scattering models. *Catalysis Today* , 122, 78-90.

Li Puma, G., Puddu, V., Tsang, H. K., Gora, A., & Toepfer, B. (2010). Photocatalytic oxidation of multicomponent mixtures of estrogens under UVA and UVC radiation: Photon absorption, quantum yields and rate constants independent of photon absorpt. *Applied Catalysis B: Environmental* , 99, Issue3-4, 388-397.

Li Puma, G., Toepfer, B., & Gora, A. (2007). Photocatalytic Oxidation of Multicomponent Systems of Herbicides: Scale-up of Laboratory Kinetics Rate Data to Plant Scale. *Catalysis Today* , 124, 124-132.

Liao, H., & Reitberger, T. (2013). Generation of Free OH Radicals by Black Light Illumination of Degussa (Evonik) P25 TiO<sub>2</sub> Aqueous Suspensions. *Catalysts* , 3, 418-443.

Malato, S., & Blanco, J. (2004). Engineering of Solar Photocatalytic Reactors. *Solar Energy* , Vol. 77, Pag. 513-524.

- Malato, S., Blanco, J., Vidal, A., & Richter, C. (2002). Photocatalysis with solar energy at a pilot-plant scale: an overview. *Applied Catalysis B: Environmental* , 37, 1-15.
- Marugan, J., Van Grieken, R., Alfano, O., & Cassano, A. (2006). Optical and Physicochemical Properties of Silica-Supported TiO<sub>2</sub> Photocatalysts. *AIChE* , 52(8), 832.
- Marugan, J., van Grieken, R., Cassano, A. E., & Alfano, O. M. (2009). Scaling-up of slurry reactors for the photocatalytic oxidation of cyanide with Ti<sub>2</sub>O and silica-supported Ti<sub>2</sub>O suspensions. *Catalysis Today* , 144, 87-93.
- Marugan, J., van Grieken, R., PAblos, C., & Sordo, C. (2010). Analogies and differences between photocatalytic oxidation of chemicals and photocatalytic inactivation of microorganisms. *Water Research* , vol.44 , 789-796.
- Marugan, J., van Grieken, R., Pablos, C., Satuf, L. M., & Cassano, A. E. (2013). Modeling of a bench-scale photocatalytic reactor for water disinfection from laboratory-scale kinetic data. *Chemical Engineering Science* , 224, 39-45.
- McCullough, C., Skillen, N., Adams, M., & Robertson, P. (2011). Photocatalytic reactors for environmental remediation: a review. *Journal of Chemical Technology and Biotechnology* , 86, 1002-1017.
- Minero, C., & Davide, V. (2006). A quantitative evaluation of the photocatalytic performance of Ti<sub>2</sub>O slurries. *Applied Catalysis B: Environmental* , 67, 257-269.
- Mohameda, H. H., & Bahnemann, D. W. (2012). The role of electron transfer in photocatalysis: Fact and fictions. *Applied Catalysis B: Environmental* , 128, 91-104.
- Moreira, J., Serrano, B., Ortiz, A., & de Lasa, H. (2011). TiO<sub>2</sub> absorption and scattering coefficients using Monte Carlo method and macroscopic balances in a photo-CREC unit. *Chemical Engineering Science* , 66, 5813-5821.
- Motegh, M., Cen, J., Appel, P. W., van Ommen, R., & Kreutzer, M. T. (2012). Photocatalytic-reactor efficiencies and simplified expressions to assess their relevance in kinetic experiments. *Chemical Engineering Journal* , 207-208, 607-615.
- Ortiz-Gomez, A., Serrano-Rosales, B., Salaices, M., & De Lasa, H. (2007). Photocatalytic Oxidation of Phenol: Reaction Network, Kinetic Modeling, and Parameter Estimation . *Industrial & Engineering Chemistry Research* , 46(23), 7394-7409.
- Oyama, T., Otsu, T., Hidano, Y., Takayoshi, K., Serpone, N., & Hidaka, H. (2011). Enhanced remediation of simulated wastewaters contaminated with 2-chlorophenol and



other aquatic pollutants by TiO<sub>2</sub>-photoassisted ozonation in a sunlight-driven pilot-plant scale photoreactor. *Solar Energy* , 85, 938-944.

Pasquali, M., Santarelli, F., Porter, J., & Yue, P. (1996). Radiative Transfer in Photocatalytic Systems. *AIChE* , 42(2), 532.

Salaices, M., Serrano, B., & de Lasa, H. (2002). Experimental Evaluation of photon absorption in an aqueous TiO<sub>2</sub> Slurry reactor. *Chem. Eng. J.* , 90, 219.

Takashi, A., & Takashi, S. (1972). Effect of Light-Source Characteristics On the Performance Of Circular Annular Photochemical Reactor. *Journal of Chemical Engineering of Japan* , 5, 385-391.

Turchi, C., & Ollis, D. (1989). Photocatalytic Degradation of Organic Water Contaminants: Mechanisms Involving Hydroxyl Radical Attack. *Journal of Catalysis* , 122, 178-192.

Valades-Pelayo, P. J., Moreira, J., Serrano, B., & de Lasa, H. I. (2014a). Boundary conditions and phase functions in a Photo-CREC Water-II Reactor Radiation Field. *Chemical Engineering Science* , 107, 123-136.

Valades-Pelayo, P. J., Moreira, J., Solano-Flores, P., Serrano, B., & De Lasa, H. (2014b). Establishing photon absorption fields in a Photo-CREC Water II Reactor using a CREC-spectroradiometric probe. *Chemical Engineering Science* , 116, 406-417.

Valades-Pelayo, P.J., Guayaquil-Sosa, F., Serrano, B., de Lasa, H. (2014c). Scaled-up Photocatalytic Reactor Under Different Irradiance Conditions: Validation of a Fully Predictive Radiation Absorption Model. *Chemical Engineering Science*. Accepted in November 2014.

Yokota, T., Cesur, S., Suzuki, H., Baba, H., & Takahata, Y. (1999). Anisotropic Scattering Model for the Estimation of Light Absorption Rates in Photoreactor with Heterogeneous Medium. *J. Chem. Eng. Jpn.* , 32, 314.

## Chapter 3

### 3 Boundary Conditions and Phase Functions in a Photo-CREC Water-II Reactor Radiation Field

The information presented in this chapter is based on the article entitled "Boundary Conditions and Phase Functions in a Photo-CREC Water-II Reactor Radiation Field", published in Chemical Engineering Science Vol. 107 p. 123-136, in April, 2014. The sections presented in this chapter consist of stage i) in section 1.1 and present results towards the partial completion of general objective a) in section 1.2.

#### 3.1 Abstract

This chapter analyses issues and limitations regarding the definition of the Local Volumetric Rate of Photon Absorption (LVRPA) in an annular Photo-CREC Water II reactor. This analysis is carried out in order to establish the influence of the scattering phase functions and Boundary Conditions (BC) on the LVRPA. To accomplish this, macroscopic radiation quantities such as the Total Rate of Photon Absorption (TRPA) and the Total Transmitted Radiation (TT) as functions of photocatalyst concentration are experimentally determined. On the other hand, the Radiative Transfer Equation (RTE) is solved using a Monte Carlo Method (MC). Boundary conditions accounting for lamp absorption/re-emission effects and diffuse reflection/absorption at the inner and outer reactor walls are employed. The Henyey-Greenstein and the binomial phase functions are used to simulate both forward and backward scattering phase functions. The significant influence of the phase functions on the radiation field is assessed for various BCs. Simulation results show that in annular photo-reactors, the sensitivity of the LVRPA towards the "g" scattering parameter increases when "g" is set in the forward scattering range. Moreover, the comparison with experimental macroscopic quantities proves that Degussa P25 displays mostly forward scattering. The investigation of various possible BCs also proves that TT and TRPA fitting yields scattering parameters in restricted ranges. Consideration of the more physically sound BCs applicable in the Photo-CREC Water II, with complete absorption in the outer wall leads to a "g" value in the 0.6-0.8 range. It is proven that the MC simulation and the use of TT measurements in

the Photo-CREC-Water II reactor with selected BCs are of critical importance for establishing phase functions and scattering parameters in photo-catalytic reactors.

## 3.2 Introduction

As mentioned in Chapter 2, to advance in photocatalytic reactor simulation this chapter addresses several closely linked issues vis-à-vis of phase functions and BCs selection. This chapter focuses on performing a parametric sensitivity analysis showing the influence of phase functions and BCs selection on LVRPA. Furthermore, this also allows the determination of the statistical limits for both phase functions and LVRPA distributions. With this end in view Isocratic, Binomial and Henyey-Greenstein phase functions describing forward, isotropic and backward scattering are used to simulate the radiation profile inside a photoreactor with TiO<sub>2</sub> Degussa P25. It is also proven that a MC method using a one parameter Henyey-Greenstein phase function (within a narrow “*g*” range) and properly selected BCs are able to describe TT in a wide range of conditions. We are not aware of a similar contribution for photocatalytic reactor numerical simulation in this critical area of phase function definition.

## 3.3 Experimental and Mathematical Methods

### 3.3.1 Reactor Setup and Radiation Measurements

The RTE was solved inside an annular photoreactor previously described by [Moreira et al.\(2011 and 2010\)](#). The Photo-CREC Water-II photoreactor measurement section is reported in Figure 3.2. This unit is comprised of the following components: (1) a 15-W black light lamp, (2) a Pyrex glass inner tube, (3) silica windows (4) a black outer tube, (5) an outlet and (6) an inlet. The lamp used in the photoreactor is a 15-W 1.33-cm radius, 41.3-cm length, black-light UV lamp. It is positioned at the center inside the inner tube of the reactor. For this reason, based on its high transmittance, the inner Pyrex reactor tube was selected.

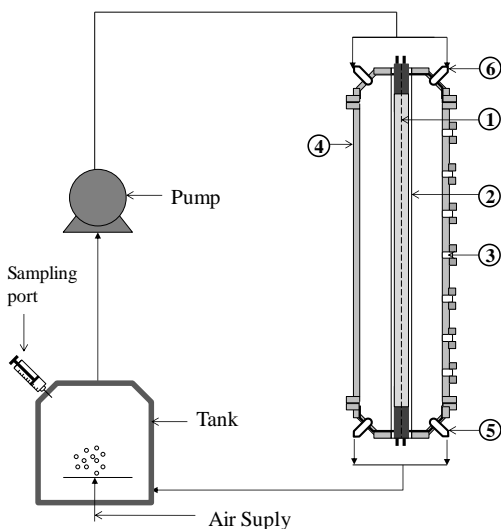


**Figure 3.1.** Schematic Representation of the Photo-CREC Water-II Reactor (Adapted from [Moreita et al, 2011](#))

The complete reactor setup allows having the suspended  $\text{TiO}_2$  in recirculation in a closed system. This system is composed of a photocatalytic reactor, a stirred tank, and a centrifugal pump. The pump allows a recirculation flow rate of  $16 \text{ L min}^{-1}$ . Characteristics and dimensions of the concentric photoreactor and the UV lamp are reported in Table 3.1.

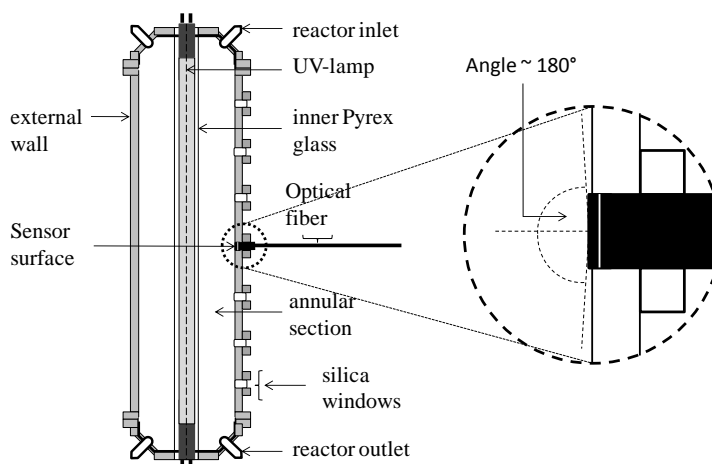


**Figure 3.2** Schematic Representation of the Photo-CREC Water II Illustrating the Optical Fiber Sensor and the Wide Radiation View Angles (180 degrees semispherical solid view angle) of Measurements Performed.

Figure 3.2 describes both the positioning of the UV sensor and the geometry of the annular reactor. It can be observed that the silica windows allow the positioning of the detector flushed to the silica window. This provides a wide solid angle of irradiation detection (very close to a semi sphere with a 180 degrees solid angle). These kinds of measurements at the annular reactor outer wall were developed as follows: a) in an empty unit, b) in a reactor filled with water (TEW), c) in a reactor filled with different photocatalysts at various concentrations (TT). Furthermore, available experimental data allow performing a macroscopic energy balance to evaluate the TRPA as the difference between the TEW and the TT. Additional details about the Photo-CREC Water-II photoreactor accessories and radiation measurements are also reported in [Moreira et al \(2011\)](#).

### 3.3.2 Mathematical Procedure Adopted for the MC Method

The spectral distribution of the UV-lamp was measured and is reported in Figure 3.3. For MC, the spectral emission distribution is calculated by fitting an eight term Fourier series in the 360-380nm range, and a third order polynomial fitting to the 345-360 and 380-388 nm ranges. It was found experimentally that the BL lamp emits  $3.58 \times 10^{18}$  photons  $s^{-1}$ . MC simulations trace the photon's fate from emission until it is either absorbed or scattered outside the reacting system. The number of events played in MC computations will directly impact the accuracy of the final solution. All MC simulations reported here are performed by using spectral distribution of the absorption and scattering coefficients as obtained from [Romero et al., 1997](#).

**Table 3.1** Characteristics and Dimensions of the Photoreactor and the UV-Lamp

Component	Parameter	Value
Photo-CREC Water-II annular reactor	Internal radius	1.76 cm
	External radius	4.44 cm
	Height	44.5 cm
	Pyrex glass thickness	0.23 cm
Black Light Lamp (F15T8/BLB)	input power	15 W
	output power	~2 W
	length	41.3 cm
	radius	1.33 cm
	emission range	300 - 420 nm
	emission rate	$5.95 \times 10^6$ einsteins $s^{-1}$

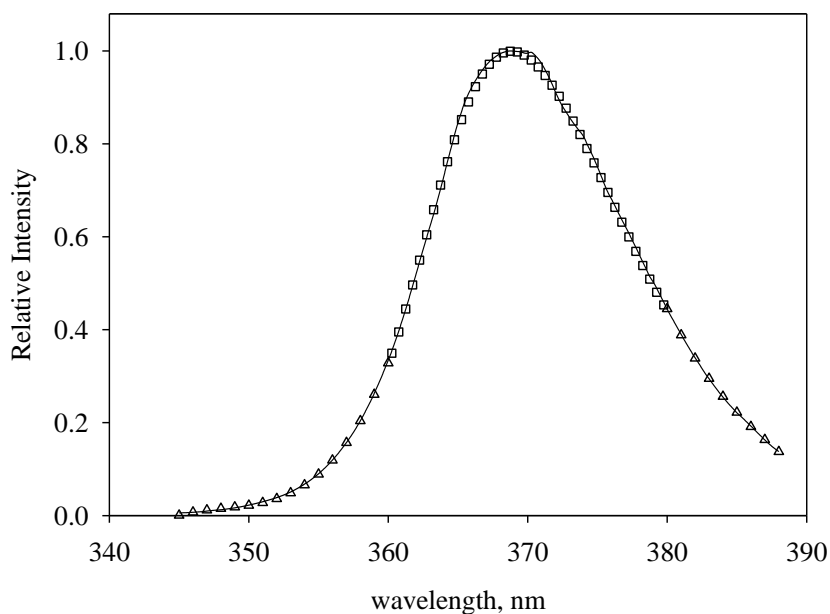


**Figure 3.3** Relative Spectral Distribution of the BL Lamp Used in the Experiments: (—) Experimental profile, ( $\Delta$ ) Polynomial Profile Fitting Function ( $\square$ ) Fourier Series Fitting Function.

In order to develop MC calculations minimizing statistical fluctuations in LVRPA computations, the annular section of the photoreactor space was divided into 27 and 47 cells in the radial and axial direction respectively. Photon tracking involves tracing through emission, reflection and absorption. When photon absorption takes place, the location of the absorption site (reactor coordinates) and wavelength are identified and stored. According to the number of photons stored in each cell and the specific energy of every absorbed one, the total energy absorbed per unit time at each cell is calculated. Dividing the photon number in each cell, by the specific cell volume, the LVRPA distribution for the entire reactor volume is established.

Regarding trajectories and absorption positions, they are calculated by using the following steps:

(1) Photon Emission from the lamp surface is determined with two random numbers uniformly distributed between [0, 1]. A first random number ( $R_1$ ) sets the angular position on the lamp surface according to Eq.3-1:

$$\begin{aligned}\theta_{lamp} &= 2\pi R_1 \\ x_{lamp} &= r_{lamp} \cos(\theta_{lamp}) \\ y_{lamp} &= r_{lamp} \sin(\theta_{lamp})\end{aligned}\quad \text{Eq.3-1}$$

Position in the axial direction is obtained by generating a second random number ( $R_2$ ) and a probability distribution function presented in Eq.3-2, as reported by Tsekov and Smirniotis, 1997:

$$P_{ze} = \frac{z-a}{\sqrt{r_{lamp}^2 + (z-a)^2}} - \frac{z-a-L}{\sqrt{r_{lamp}^2 + (z-a-L)^2}} \quad \text{Eq.3-2}$$

where  $r_{lamp}$  is the lamp radius,  $L$  is the reactor length,  $a$  is the gap between the lamp and the reactor,  $z$  represents the axial coordinate and  $P_{ze}$  is the probability that a photon will be emitted at that specific height  $z$  (Tsekov and Smirniotis, 1997).

The direction of emission is determined by two random numbers ( $R_3$  and  $R_4$ ) representing a Lambertian source emission distribution as shown in Eq.3-3:

$$\begin{aligned}Dir(1) &= \sqrt{1-R_3} \cos(2\pi R_4) - \sqrt{R_3} \sin(2\pi R_4) \sin(2\pi R_4) \\ Dir(2) &= \sqrt{1-R_3} \sin(2\pi R_4) - \sqrt{R_3} \sin(2\pi R_4) \cos(2\pi R_4) \\ Dir(3) &= \sqrt{R_3} \cos(2\pi R_4)\end{aligned}\quad \text{Eq.3-3}$$

The wavelength of the emitted photon is calculated from a PDF proportional to the experimental lamp emission spectra, shown in Figure 3.3. The irradiation distribution is modeled fitting polynomials in the 345-360 and 380-390 nm ranges and a Fourier Series in the 360-380 nm central emission spectral section.

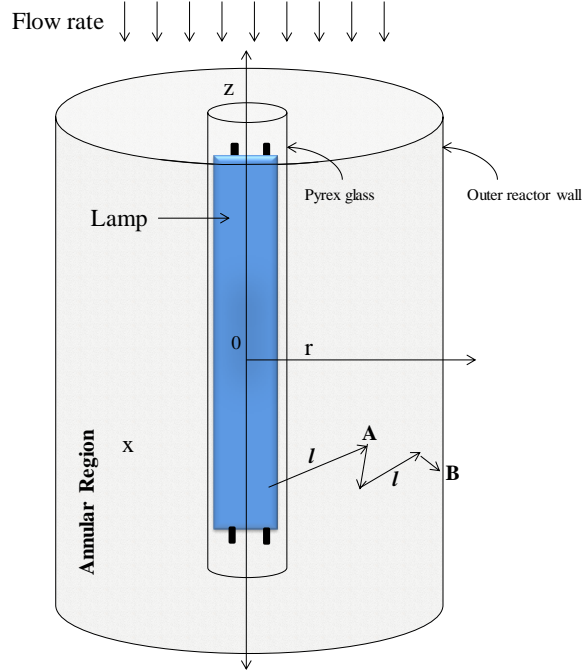


**Figure 3.4** 3D View of the Coordinate System Adopted for MC Simulations (Adapted from [Moreira et al 2010](#)).

(2) Once the position and direction of a photon emitted on the lamp surface is determined, the next step is to calculate the photon flight  $l$  inside the annular reactor section. The photon under consideration travels a distance  $l$  before it interacts with a  $\text{TiO}_2$  particle. The probability of such an event is calculated using a power decay law involving an extinction coefficient as suggested by [Pareek et al.\(2008\)](#):

$$P(l) = e^{-\beta_\lambda l} \quad \text{Eq.3-4}$$

where  $\beta_\lambda$  is the extinction coefficient of the medium at the  $\lambda$  emission wavelength. The  $\beta_\lambda$  parameter represents the sum of the water extinction coefficient and the  $\text{TiO}_2$  Degussa P25 absorption and scattering coefficients. Thus, as a result of Eq.3-4, a flight length  $l$  can be generated using a random number  $R_5$  ( $R_5 < 1$ ) as follows:

$$l = -\frac{1}{\beta_\lambda} \ln(R_5) \quad \text{Eq.3-5}$$



(3) Following the photon flight analysis, photon positioning inside the annular photoreactor section is determined by calculating the directional cosines designated as  $e_x$ ,  $e_y$  and  $e_z$ . Furthermore, a Cartesian coordinate system is selected given its computational advantage for determining a photon position uniquely specified by directional cosines (Changrani et al., 1999). Thus, after traveling a distance  $l$ , a photon has an associated location such is the case in point ‘‘A’’ (refer to Figure 3.4) with coordinates determined by:

$$\begin{aligned}x_{new} &= x_{old} + e_x l \\y_{new} &= y_{old} + e_y l \\z_{new} &= z_{old} + e_z l\end{aligned}\tag{Eq.3-6}$$

One should note that in Eq.3-6, ‘‘old’’ refers to the previous location of the photon under consideration in the photoreactor and ‘‘new’’ establishes the updated location once the photon has traveled a distance  $l$ . Details about the directional cosines involved in Eq.3-6 are given in Prahl et al. (1989).

(4) Moreover, once a photon is located in a position A as described in Figure 3.4, its fate is next determined by the probability of photon absorption. In this step, probability of photon absorption is calculated as recommended by Changrani et al. (1999):

$$P(a) = \frac{\kappa_\lambda}{\beta_\lambda} = \frac{\kappa_\lambda}{\kappa_\lambda + \sigma_\lambda}\tag{Eq.3-7}$$

Thus, at this point, the photon’s fate is determined by another random number ( $R_6 < 1$ ). If  $P(a) > R_6$  then the photon is absorbed and its corresponding position is stored. As a result, the photon’s evolution is considered complete and another photon is emitted by the lamp which means going back to step (1). On the other hand, if the photon is not absorbed by the medium, then the photon is scattered in a new direction.

(5) Finally, the photon scattering direction at point A is calculated by the following phase functions: isotropic (Eq.3-10), binomial (Eq.3-8) or H-G (Eq.3-9).

$$P_{Binomial}(\theta) = \frac{I}{2} (I_{asym} + I) \left[ \frac{1 + \cos(\theta)}{2} \right]^{I_{asym}} \quad \text{Eq.3-8}$$

$$P_{HG}(\theta) = \frac{I}{2} \frac{1 - g^2}{(1 + g^2 - 2g \cos(\theta))^{3/2}} \quad \text{Eq.3-9}$$

where  $\theta$  is the scattering angle and  $I_{asym}$  and  $g$  represent the asymmetry factors of the scattered radiation distribution.

Values for the asymmetry factors can vary from -1 to 1. This gives phase functions ranging from completely backward to completely forward scattering. One should note that when  $I_{asym}$  and  $g$  equal zero, Eq.3-8 and Eq.3-9 yield an isotropic phase function given by:

$$P_{isocratic}(\theta) = \frac{I}{2} \quad \text{Eq.3-10}$$

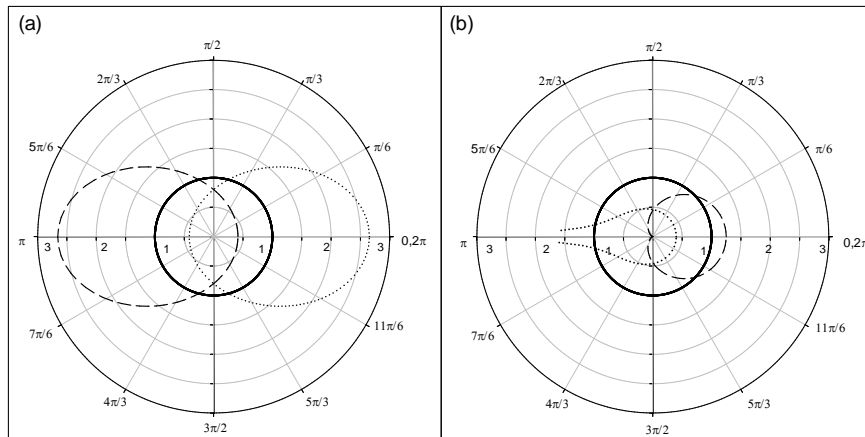


**Figure 3.5.**  $P(\theta)$  Distribution for (—) isotropic scattering function , a) H-G Phase Function for a (---) backward scattering ,  $g = -0.3$  and (.....) forward scattering ( $g = 0.3$ ) and b) Binomial Phase Function, (.....) backward scattering ( $I_{asym} = 1.5$ ) and (---) forward scattering ( $I_{asym} = -0.2$ ).

Figure 3.5 reports both the H-G and the binomial phase functions showing the possible PDF changes from almost completely backward to essentially completely forward scattering. In the case of H-G, negative values for “g” (g =-0.3) give mainly backward scattering, whereas positive “g”(g=0.3) yields dominantly forward scattering. Meanwhile, with a negative  $I_{\text{asym}}$  ( $I_{\text{asym}} =-0.2$ ) the binomial phase function gives forward scattering with the opposite being true for  $I_{\text{asym}} =1.5$ . Regarding these various phase function alternatives available, four “g” values were considered in this study as will be described later: -0.85, -0.2, 0.2 and 0.85.

Regarding the direction angle assigned to a scattered photon as in point A moving towards point B (Figure 3.4), the magnitude of this angle can be calculated using Eq.3-8, Eq.3-9 or Eq.3-10. In this respect, a zenith angle is determined with a random number from 0 to 1 in the  $[0,1]$  interval such as proposed by [Binzoni et al \(2006\)](#):

$$\int_0^{\theta'} p(\theta)d\theta = R_7 \quad \text{Eq.3-11}$$

Thus, the calculation of the zenith angle yields a relationship between  $\cos \theta$ , as a function of  $R_7$  and the “g” parameter . Therefore, the scattering angle  $\theta$  can be expressed for all the different phase functions by:

$$\cos(\theta) = \begin{cases} 1 - 2(1 - R_7)^{\frac{1}{I_{\text{asym}}+1}}, & \text{Binomial phase function} \\ \frac{1}{2g} \left[ 1 + g^2 - \left( \frac{1 - g^2}{1 - g + 2gR_7} \right)^2 \right], & \text{H - G phase function} \\ 2R_7 - 1, & \text{Isocratic phase function} \end{cases} \quad \text{Eq.3-12}$$

Furthermore, to fully describe the direction of the scattered photon, the  $\phi$  azimuth angle is required. In order to be able to calculate  $\phi$  azimuth angle, a second  $R_8$  random number is needed. Thus, both scattering angles are determined as follows:

$$\begin{aligned} \theta &= \arccos(\cos(\theta)) \\ \phi &= 2\pi R_8 \end{aligned} \quad \text{Eq.3-13}$$

Once the scattered angles are determined, the photon trajectory is fully established. Thus, as a result, one can go back to step (2) of the Monte Carlo method and reconsider a

photon as being either interacting with the slurry medium or interacting with reactor boundaries as follows: a) the inner reactor's walls, b) the outer reactor's wall, c) the top/bottom reactor's walls, d) the BL-Lamp or e) the sensor's surface. If as a result of these events, a photon is absorbed, calculations are ended and the algorithm restarts at step (1). This process is continued until a statistically adequate number of photons are considered.

Figure 3.6 reports a simplified structure of the MC code and its subroutines including the following: a) random photon emission (direction, position, wavelength as explained in Step (1) above), b) interaction between the photon and the air-glass-water interface, c) photon events in slurry media (Reaction Space Subroutine which includes Steps 2 to 5), d) Calculation of average irradiation distributions (LVRPA and TRPA).

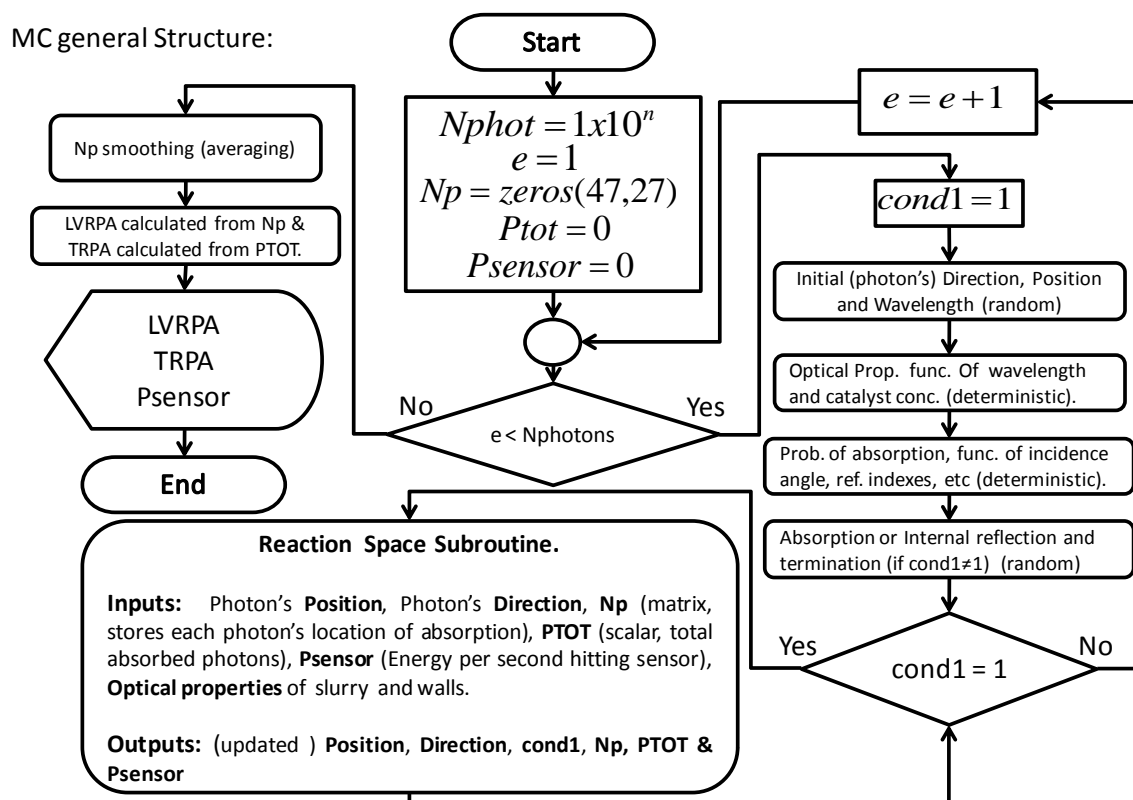


**Figure 3.6.** General Structure of the MC Algorithm of the Present Study. The Reaction Space Subroutine is described with their inputs and their outputs.

Figure 3.6 describes the Matlab program algorithm developed to solve the RTE inside an annular photoreactor. It can be noticed that a counter limit is set as " $N_{\text{phot}}$ " and is used to account for every photon that is emitted.  $N_{\text{phot}}$  are to be kept in excess to  $10^6$  to keep the statistical fluctuations of the MC method below 5%. It can also be observed that the algorithm is divided in: a) a stochastic emission section where the photon wavelength, initial position and direction are defined, b) a deterministic section where the photons optical properties and their interaction with the inner Pyrex glass are determined according to Snell's law, c) a slurry region entrance conditions, as described in Figure 3.7, d) a photon termination coordinate assignment section at the absorption cell location, e) a LVRPA, TRPA and irradiance profiles calculation module.

With this end as well, the RAND function is used to generate random numbers. RAND has a period of  $(2^{19937}-1)/2$ , exceeding any computational possible number of simulation events needed in this MC method. Simulations were performed by changing both asymmetry factors in the binomial and H-G phase functions; values of -0.85, -0.2, 0.2 and 0.85 were considered. Simulations for an isotropic phase function were also performed. All runs were completed for the following TiO<sub>2</sub> concentrations: 0.01, 0.02, 0.05, 0.1, 0.2, 0.3 and 0.4 g L<sup>-1</sup>.

Figure 3.7 shows additional details of the "Reaction Space Subroutine" which are not included in the algorithm of Figure 3.6. This subroutine is employed for describing the radiation field and involves various steps described at the beginning of the mathematical MC section. Once the fate of the photon is terminated, the subroutine exits and another photon is reemitted in the lamp with new direction, position and wavelength.

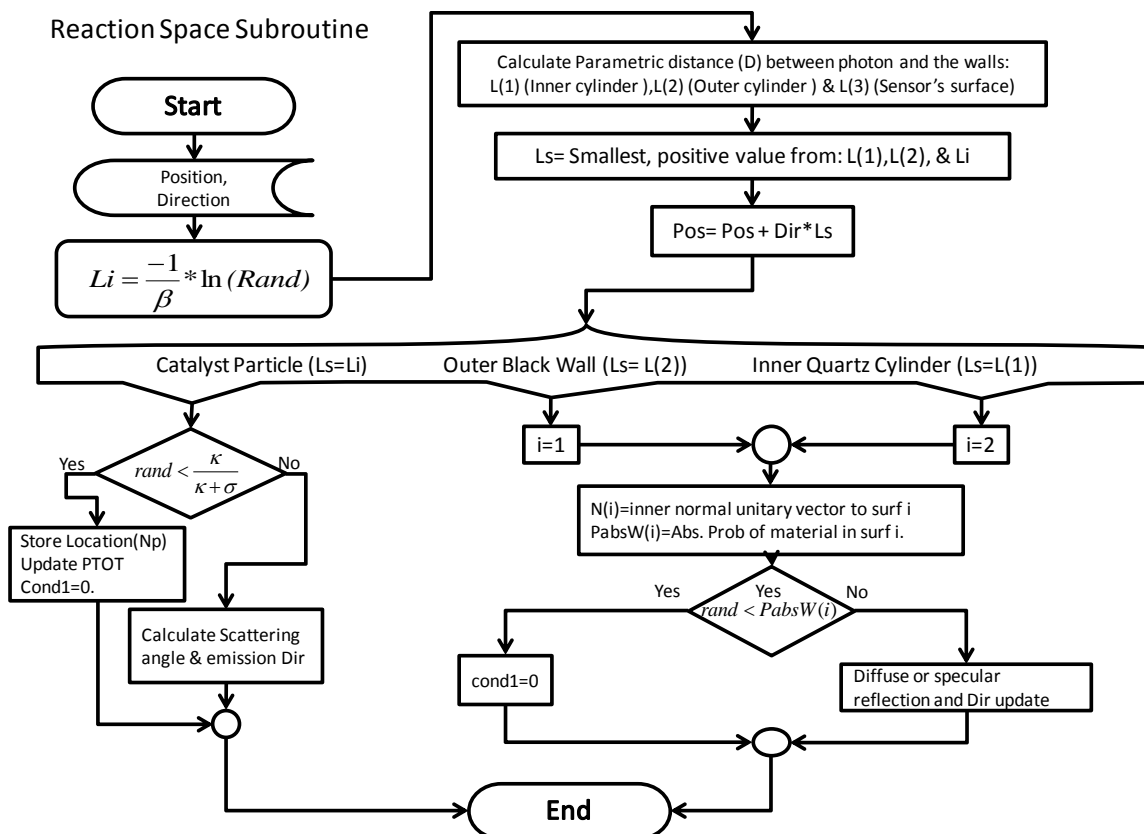


**Figure 3.7.** Algorithm of the Reaction Space Subroutine, employed in the MC simulation of the radiation field inside the annular section of the photoreactor.

The described Monte Carlo method, should be run for a large number of photons until the recorded reflection, transmission, and absorption profiles approach steady values. However, the number of events should be small enough so that simulations can still be handled in a PC computer. For the simulations in this chapter, the fate of  $6 \times 10^7$  photons were tracked in a computer with a 2nd generation Intel i7 quad core at 2.0 GHz. This number of computed events resulted in manageable computer time with an accurate response (e.g. 2% deviations on consecutive LVRPA calculated profiles). For instance, when an isocratic phase function was used, a total of 32 hours were needed for all catalyst concentrations. Runs were performed at least three times to ensure reproducibility and small statistical fluctuations. This approach ensures that the number of events computed using the MC method is sufficient to assume adequate accuracy of simulations.

## 3.4 Results and Discussion

### 3.4.1 MC Simulation for an Isocratic Phase Function

The MC method of this sub-section was considered for a photocatalyst concentration of  $0.05 \text{ g L}^{-1}$ . In this simulation, the isocratic phase function was used in order to assess the different results that one can obtain with the MC approach. As described in section 3.3.2, the MC code was intended to be used to calculate 3D profiles of the LVRPA inside the annular photoreactor. Furthermore, the MC method was set to deliver the total rate of energy absorption (TRPA), i.e. the light absorbed by the  $\text{TiO}_2$  catalyst in the entire reactor volume, as well as the radiation reaching the external walls (TT, Total Transmitted Radiation). **Figure 3.8** reports the 3D profile of the LVRPA inside the annular reactor when both a concentration of  $0.05 \text{ g L}^{-1}$  of catalyst and an isotropic phase function are employed.

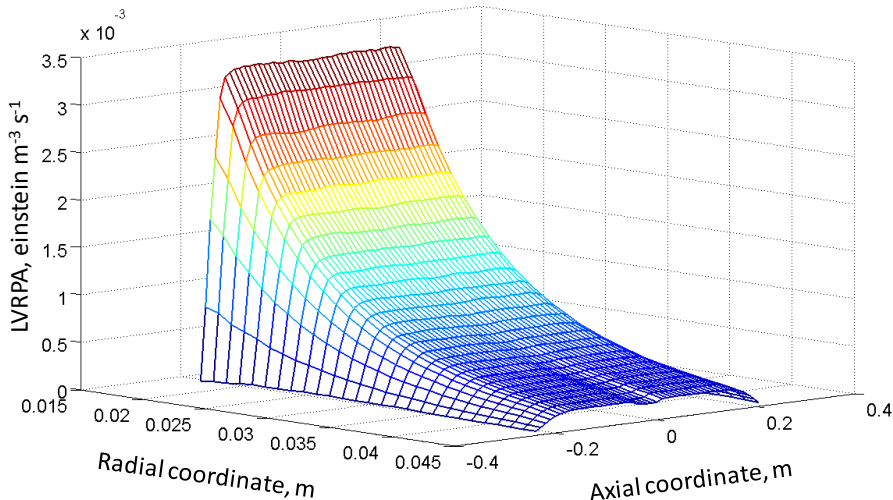


**Figure 3.8.** 3D Profile of the LVRPA Inside the Photo-CREC Water II Reactor for  $0.05 \text{ g L}^{-1}$ , Isocratic Phase Function ( $g=0$ ).

Results reported in Figure 3.8 show that  $\text{TiO}_2$  particles close to the center of the reactor (radial coordinate =  $0.0177 \text{ m}$ ) display a higher rate of energy absorption. As the radial coordinate approaches the outer wall of the reactor (radial coordinate =  $0.044 \text{ m}$ ), the

LVRPA profile decreases due to shadowing effects from the photocatalyst closer to the lamp. This creates the radial profile of the LVRPA inside the reactor. Regarding the axial profile of the LVREA, one can notice that this is due to the fact that the lamp emits higher radiation intensities at the center and lower towards the lamp edges. Thus, more radiation is absorbed by the TiO<sub>2</sub> photocatalyst in this central (z=0) reactor region. Furthermore, considering the TRPA as defined by Eq.2-12, it was found to be  $1.84 \times 10^{-6}$  einsteins m<sup>-3</sup>s<sup>-1</sup>. Total transmitted radiation at the external wall of the reactor (radial position = 0.044 m) was 257.41 μW cm<sup>-2</sup>.

Concerning the simulations to be reported in the upcoming sections, the same MC method as described for the isocratic function (Figure 3.8) and 0.05 gL<sup>-1</sup> concentration, was used with some minor adaptations. This allowed us to establish the effect of different parameters in the radiation field as follows: a) photocatalyst concentration, b) scattering phase functions and c) boundary conditions. LVRPA data was also valuable to evaluate boundary conditions and scattering parameters.

### 3.4.2 Effect of catalyst concentration for isocratic phase function

Simulations with the isocratic phase function (g=0) were performed at different photocatalyst concentrations. Figure 3.9 reports a 3D comparison of the LVRPA for four different photocatalyst loadings.

One can notice that at higher photocatalyst loadings the LVRPA displays a steeper decay in the radial direction. It can also be observed that for higher photocatalyst concentrations, larger values of LVRPA are found in the "high irradiation" region, located close to the radiation source (r<0.03m). For instance, when simulating a 0.2 g L<sup>-1</sup> of TiO<sub>2</sub> slurry, values of  $1.75 \times 10^{-2}$  einstein m<sup>3</sup>s<sup>-1</sup> are observed for the LVRPA in the near glass wall regions. In contrast for the 0.01 g L<sup>-1</sup> photocatalyst concentration, values of  $6.21 \times 10^{-4}$  Einsteins m<sup>-3</sup> s<sup>-1</sup> are obtained in the same region.



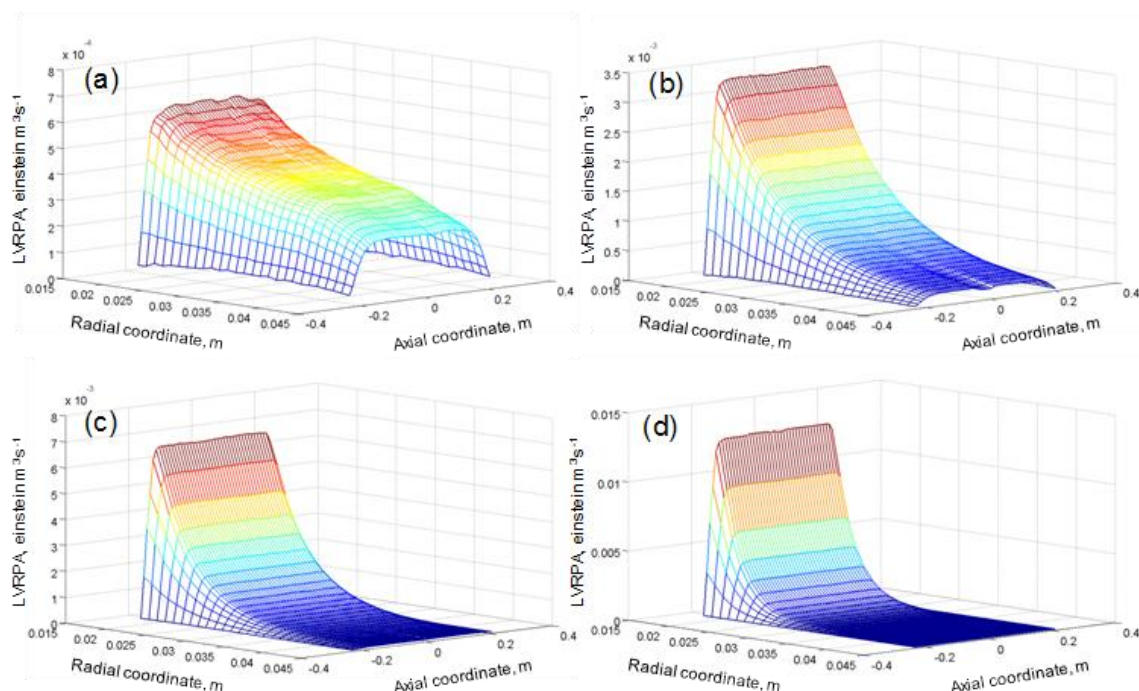


**Figure 3.9.** 3D view of the LVRPA inside the annular reactor for  $\text{TiO}_2$  concentrations of (a) 0.01, (b) 0.05, (c) 0.1, and (d)  $0.2 \text{ g L}^{-1}$ .

To more effectively describe how the radial profile for the LVRPA is influenced by photocatalyst loading, a 2D plot is reported in Figure 3.10. This figure shows the radial profile at  $z = 0$ , describing the significant changes of LVRPA with radial position and photocatalyst loadings. Figure 3.10 also reports the tendency of the Photo-CREC Water II reactor to form poorly irradiated zones (dark zones) in the outer concentric tube regions, under these conditions.

Regarding LVRPA, Figure 3.10 shows a quick and uniform drop with respect to the radial direction. Again, for the higher photocatalyst loadings,  $\text{TiO}_2$  particles closer to the inner wall (or radiation source) absorb most of the radiation entering the reactor. In this sense, when a sufficiently high concentration of  $\text{TiO}_2$  is used, the photocatalyst near the external reactor wall would be poorly irradiated. This leads to a radial LVRPA profile with highly irradiated zones near the inner wall and poorly irradiated regions for particles near the outer wall. In order to determine proper photocatalyst loading, (i.e. the one that ensures optimally irradiated conditions inside the photoreactor while avoiding poorly

irradiated zones), one has to quantify two competing effects: i) the photocatalyst capacity to absorb radiation which is determined by the absorption coefficient, ii) the shadowing effect which is influenced mainly by the photocatalyst scattering coefficient and in general the scattering mode (Cabrera et al., 1996).

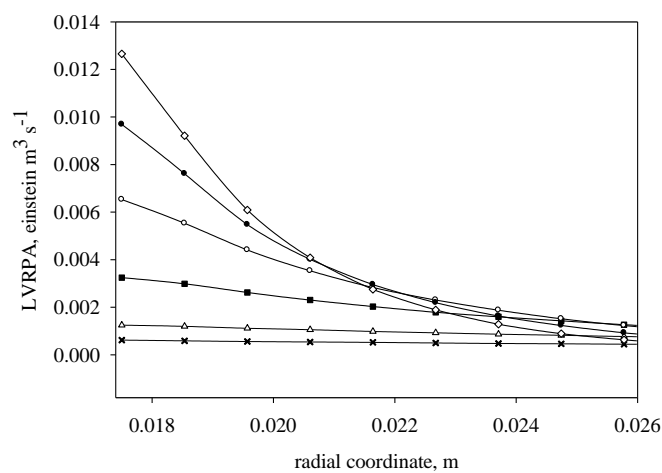


**Figure 3.10.** Radial distribution of the LVRPA at  $z = 0$  when isocratic phase function is used (x) 0.01, ( $\Delta$ ) 0.02, ( $\blacksquare$ ) 0.05, ( $\circ$ ) 0.1, ( $\bullet$ ) 0.15 and ( $\diamond$ ) 0.2  $\text{g l}^{-1}$ .

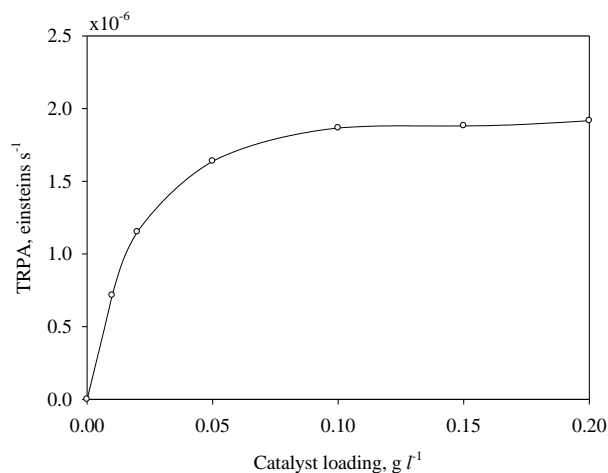


**Figure 3.11.** Total Rate of Photon Absorption for Isocratic Phase Function vs. Catalyst Concentration.

Figure 3.11 shows the TRPA, for the entire annular section of the 2.65 liter Photo-CREC Water II reactor and their changes with photocatalyst loading. Radiation absorbed by the  $\text{TiO}_2$  reaches a close to asymptotic value at  $0.10 \text{ g L}^{-1}$  or at 95% of the maximum TRPA. This point can be regarded as a condition of “minimum” photocatalyst loading ensuring maximum radiation utilization with the smallest amount of photocatalyst. The TRPA value related to this “minimum” photocatalyst concentration depends as it is shown in the upcoming section of this manuscript, on the specific photocatalyst scattering mode (phase function used) and the selected boundary conditions.

### 3.4.3 Effect of the Scattering Mode at Constant Photocatalyst Concentration

Scattering phase functions can have a major influence on the radial LVRPA profile and on the TRPA. To demonstrate this, MC simulations using the H-G and the binomial phase functions are compared with respect to MC results employing the isocratic phase function. The isocratic function is used as a reference given its frequent use by other authors ([Moreira et al. 2010](#), [Moreira et al. 2011](#), [Satuf et al. 2005](#), [Marugan et al. 2006](#))

Figure 3.12a reports radial LVRPA profiles for different scattering modes at  $0.05 \text{ g L}^{-1}$  of  $\text{TiO}_2$  employing the H-G phase function. Similarly, Figure 3.12b shows the radial LVRPA profiles for the binomial phase function. In an analogous fashion, Figure 3.12c shows the same results for a higher concentration of  $0.2 \text{ g L}^{-1}$  in the case of H-G and Figure 3.12d for the binomial phase function.

Figure 3.12 shows that there are important LVRPA deviations from MC isocratic simulations in all cases considered with the “ $g$ ” parameter changing in the  $-0.85$  to  $0.85$  range. All simulations within this subsection consider the external wall absorption probability of 100%. These significant LVRPA deviations were observed for both  $0.05$  and  $0.2 \text{ g L}^{-1}$  photocatalyst concentrations. The major deviations, however, occur for highly forward scattering parameters ( $g = 0.85$  for H-G and  $I_{\text{asym}} = -0.85$ ) and using the H-G phase function. Furthermore, very significant percentual deviations are noticed at low concentrations for  $g = 0.85$  and  $I_{\text{asym}} = -0.85$ . While comparing the LVRPA resulting from the binomial phase function, one can observe closer values as predicted by the MC

isocratic simulations and on the other hand, important differences with respect to the H-G phase function model predictions.

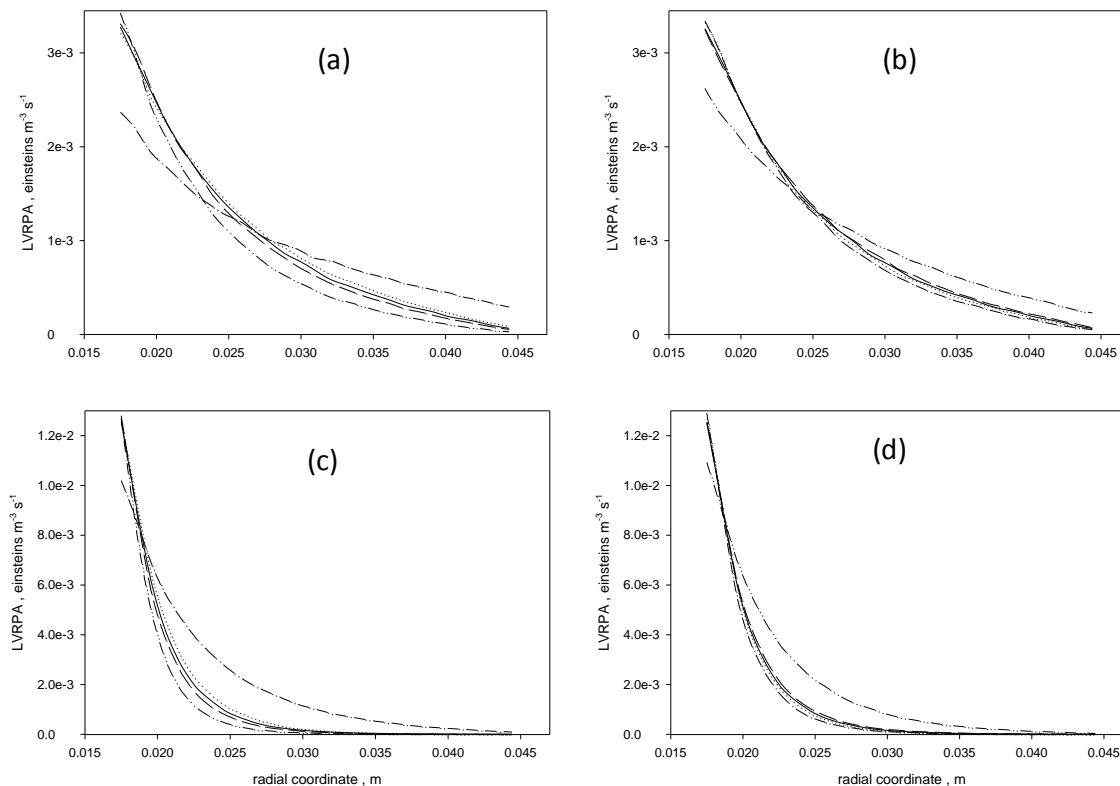


**Figure 3.12.** Radial LVRPA Profiles Using the H-G Phase Function (Figures a and c) and the Binomial Phase Function (Figures b and d). Figures a and b are for  $0.05 \text{ g L}^{-1}$  photocatalyst concentration, figures c and d are for  $0.2 \text{ g L}^{-1}$  photocatalyst concentration.

Outer boundary Condition: 100% of incident radiation. Codes for asymmetry factors: Broken double-dotted line (-••-) -0.85, Broken line (- - -) -0.2, Dotted line (••••) 0.2 and Broken single-dotted line (-•-) 0.85. Full line (—) Isocratic phase function.

Additionally, Figure 3.13 reports the TRPA for H-G, binomial and isocratic phase functions. It is observed in this figure that the selection of the scattering phase function plays a very significant role in the calculated TRPA values.

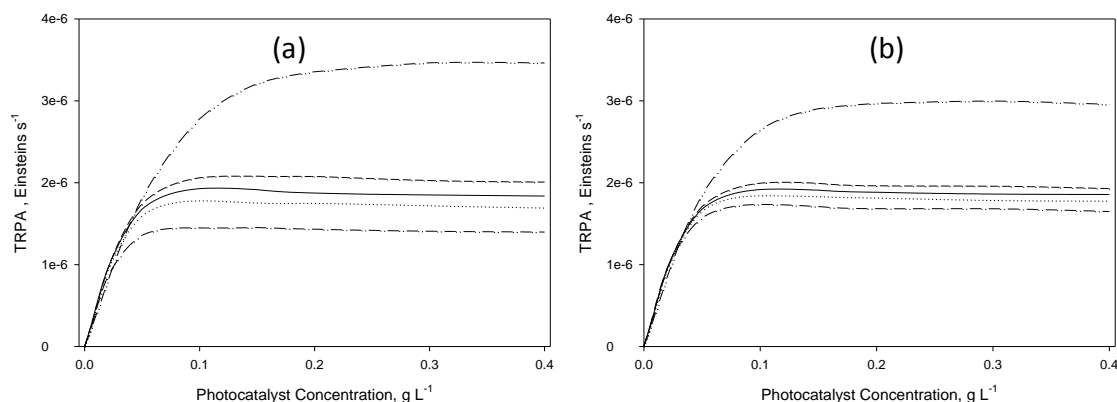


**Figure 3.13.** Total Rate of Photon Absorption vs. Catalyst Concentration for (a) H-G and (b) binomial phase functions. Outer boundary condition: 100% of incident radiation. Codes for asymmetry factors: Broken double-dotted line (-••-) -0.85, Broken line (- - -) - 0.2, Dotted line (•••) 0.2 and Broken single-dotted line (-•-) 0.85. Full line (—) Isocratic phase function.

Thus, the above analysis allows us to conclude that the selection of the correct phase function and unit boundary conditions are critical and can, in some cases, lead to quite different LVRPAs. These results are in contrast with the findings of [Moreira et al., 2010](#) and [Pasquali et al., 1996](#) who concluded that the form of the phase function does not have significant effect on MC simulation results. Reasons on this disagreement can be assigned to restricted variations of BCs by the above mentioned authors.

It is postulated in the present study that the selection of a phase function involves: i) both LVRPA radial profiles and TRPA, ii) a large variation of photocatalyst concentrations, iii) carefully selected boundary conditions for both the inner and outer reactor walls.

#### 3.4.4 Inner and Outer Boundary Conditions

Figure 3.14 shows simulations for the H-G phase function including forward, isocratic and backward probability distributions. In these Monte Carlo simulations, the extreme conditions at the inner boundary of the concentric reactor are varied from total absence of photon reemission ( $P_{\text{absLamp}}=1$ ) to complete photon reemission ( $P_{\text{absLamp}}=0$ ).

Figure 3.14 reports that the photon interaction with the lamp (inner BC) plays a critical role in the radial LVRPA profile. From the reported results, one can notice the significant LVRPA variations assuming either total photon absorption or total photon re-emission. This observation holds true for various scattering cases considered in this study. For instance, one can notice in Figure 3.14a at  $g=0.8$  that varying the inner BC yields 25-30% LVRPA variations. A similar effect is observed in Figure 3.14b (for the isocratic case) with 50-55% LVRPA variations. Lastly, Figure 3.14c displays as much as 65-70% LVRPA variations for  $g=-0.8$ .

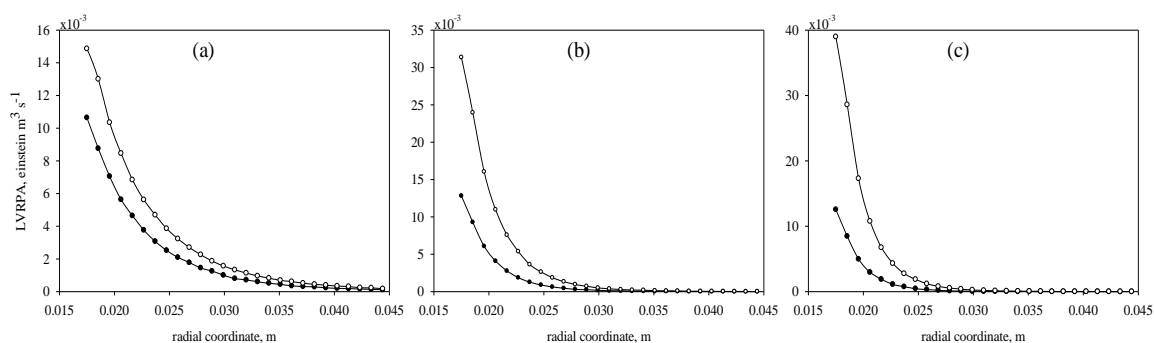


**Figure 3.14.** Changes of LVRPA with Inner Boundary Conditions. Outer boundary condition: 100% of incident radiation. Photocatalyst concentration set at  $0.05 \text{ gL}^{-1}$ . Phase function used is H-G with (a) forward scattering  $g = 0.8$ , (b) isocratic scattering and (c) backward scattering  $g = -0.8$  phase functions. Symbols: ( $\circ$ ) total re-emission from the lamp and ( $\bullet$ ) total absorption in the lamp

Figure 3.15 reports simulations describing the effect of the outer BC. These simulations consider the two extreme cases of total absorption ( $P_{\text{abswall}}=1$ ) and total diffuse reflection ( $P_{\text{abswall}}=0$ ) in the outer reactor wall. Simulations for the H-G phase function include forward ( $g=0.8$ ), isocratic ( $g=0$ ) and backward ( $g=-0.8$ ) probability distributions. Figure 3.15a, Figure 3.15b and Figure 3.15c show that the outer BC is critical for LVRPA radial profile simulations. In this respect, they all show an increasing deviation of LVRPA as  $g$  decreases, namely 30-50% for Figure 3.15a ( $g=-0.8$ ) to 70-90% for Figure 3.15c ( $g=0.8$ ). Thus, it can be seen from these results that the outer BC is always

significant for a photocatalyst concentration of  $0.05 \text{ gL}^{-1}$ . Furthermore, for positive “g” scattering parameters ( $g > 0$ ) outer BCs become of increased importance.

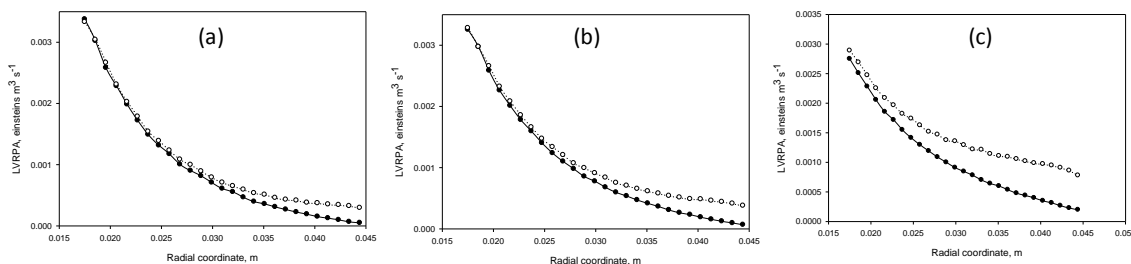


**Figure 3.15.** LVRPA Changes with Outer Boundary Conditions. The H-G phase scattering function considers (a) backward scattering with  $g = -0.8$ , (b) isocratic scattering and (c) forward scattering with  $g = 0.8$ . Full circles (•) represent total absorption at the outer wall and open circles (○) total diffuse reflection at the outer wall. Photocatalyst concentration set at  $0.05 \text{ gL}^{-1}$ .

### 3.4.5 Experimental Study to Determine Scattering Phase Functions

Moreira et al., (2010 and 2011) were one of the first authors to investigate the Monte Carlo method to simulate the radiation field in the Photo-CREC Water II reactor. This approach was able to predict the TRPA as a function of photocatalyst concentration using Degussa P25 and Anatase  $\text{TiO}_2$ . It was concluded that the form of the phase function is not “in principle” critical for obtaining a good representation of the radiation field inside the annular section. Boundary conditions considered in Moreira et al., were restricted to: a) the inner BC: back scattered photons reaching the BL lamp return all of them to the slurry media ( $P_{\text{absLamp}} = 0\%$ ), b) the outer BC: transmitted photons reaching the external reactor wall are totally absorbed by this wall ( $P_{\text{abswall}} = 100\%$ ). Furthermore, simulation results as per Moreira et al. (2010 and 2011) require experimental TRPA profiles obtained using Macroscopic Radiation Balances (MRB).

Given the data of this study as reported in section 3.4 and more specifically in subsection 3.4.3, it is clear that Moreira et al's (2010) approach requires further refinements with the consideration of adequate BCs to truly discriminate between scattering models. For instance, it is well acknowledged that certain  $\text{TiO}_2$  photocatalysts could eventually adhere

to the external reactor walls forming a thin  $\text{TiO}_2$  layer. This  $\text{TiO}_2$  layer would most likely reflect a fraction of the photons coming from the annular section. On the other hand, and according to Duran et al., 2010, accurate lamp irradiance predictions require the consideration of both lamp absorbance and lamp photon re-emission contributions.

To address these issues, a photocatalytic reactor model is considered in this study where two probabilistic functions are considered:  $P_{\text{absLamp}}$  and  $P_{\text{out-wall}}$  representing lamp absorption and external wall absorption respectively. In addition, the model reported here is further enhanced by incorporating a Lambertian lamp emission model in the MC approach used. This Lambertian emission model is needed to properly capture the various photon trajectories from the lamp into the annular photoreactor.

To validate the calculated LVRPA, measurements were effected as follows: a) TRPA from radiometric measurements using a MRB and b) TT radiation measurements using a StellarNet EPP2000C-25 LT16 spectrometer. Figure 3.16 a) and Figure 3.16b) report TRPA and TT data respectively, as observed in the Photo-CREC-Water II reactor. Lamp emission parameters were determined by independent measurements. Lamp emissions values were found to be  $5.96 \cdot 10^{-6}$  E/s, that is 1.92 W/sec (12.8% efficiency from the nominal 15 watts).

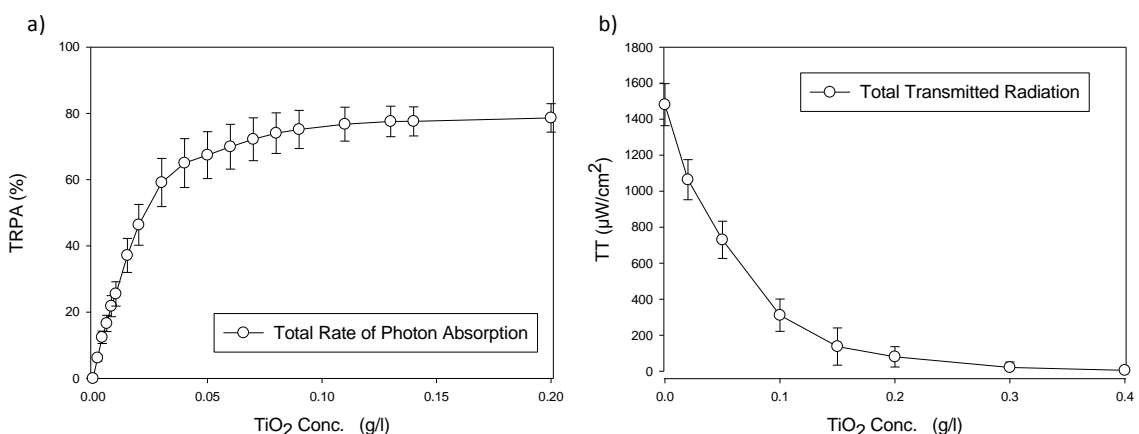


**Figure 3.16.** a) Experimental TRPA or Total Rate of Photon Absorption reported as a percentual fraction of total photons absorbed by the slurry. b) Experimental TT or Total



Transmittance reported in microwatts per square centimeter. Three measurements were performed for every experimental point. The error bars represent standard deviations.

As shown in Figure 3.16a) TRPA rises steadily with catalyst concentration until it reaches an asymptotic value, close to 78%. Figure 3.16b) reports a similar decreasing behavior for TT, with TT dropping from 1500  $\mu\text{w}/\text{cm}^2$  to close to zero at 0.4  $\text{gl}^{-1}$ . TRPA and TT standard deviations were 2-7.4% and 4-116  $\mu\text{w}/\text{cm}^2$  respectively. It is hypothesized that these radiation variations are the consequence of the following: a) photocatalyst tendency to form a thin layer of variable thickness close to the reactor wall. Thickness of this thin layer may depend on: i) local turbulence, ii) particular catalyst local loading and b) natural lamp emission power variations due to small voltage changes.

#### 3.4.6 Limitations of Macroscopic Radiation Balances (MRB) when Establishing Scattering Models in Annular Photoreactors.

The Macroscopic Radiation Balance (MRB) is a valuable tool for assessing absorbed radiation as reported by [Salaices et al. \(2002\)](#). This allows one to obtain the Total Rate of Photon Absorption (TRPA) as the difference between the total emitted radiation and Total Transmitted Radiation (TT). Although the MRB provides an approximation to obtain TRPA, it does not provide enough information on the radial distribution of radiation absorbed inside a photoreactor annular section.

Some of the MRB assumptions are not in agreement with the MC simulation assumptions presented in this study. For instance, the MRB neglects forward scattering effects away from the outer reactor wall. This becomes more significant as the photocatalyst concentration decreases and/or when forward scattering behavior is prevalent. Furthermore, the MRB fails to account for photons absorbed both in the inner and outer walls reactor top and bottom and the lamp itself. Such assumptions might hold true in homogeneous systems or heterogeneous systems at very low photocatalyst concentrations.

Figure 3.17(a-d) reports the TRPA changes as a function of catalyst concentration with different sets of BCs for various H-G phase function cases, ranging from full forward to

full backward scattering modes. It is shown in Figure 3.17(c) and Figure 3.17 (d) that when both BCs are outside the 0 to 0.2 absorption probability range, no phase function is able to fit the calculated TRPA profiles, confining the BCs to an unrealistic low absorption range. Figure 3.17a and Figure 3.17b also show that in the 0 to 0.2 absorption probability range, there is low parametric sensitivity towards the “g” scattering parameter. Given the above mentioned reasons, the TRPA obtained by MRB is not reliable for phase function model discrimination.

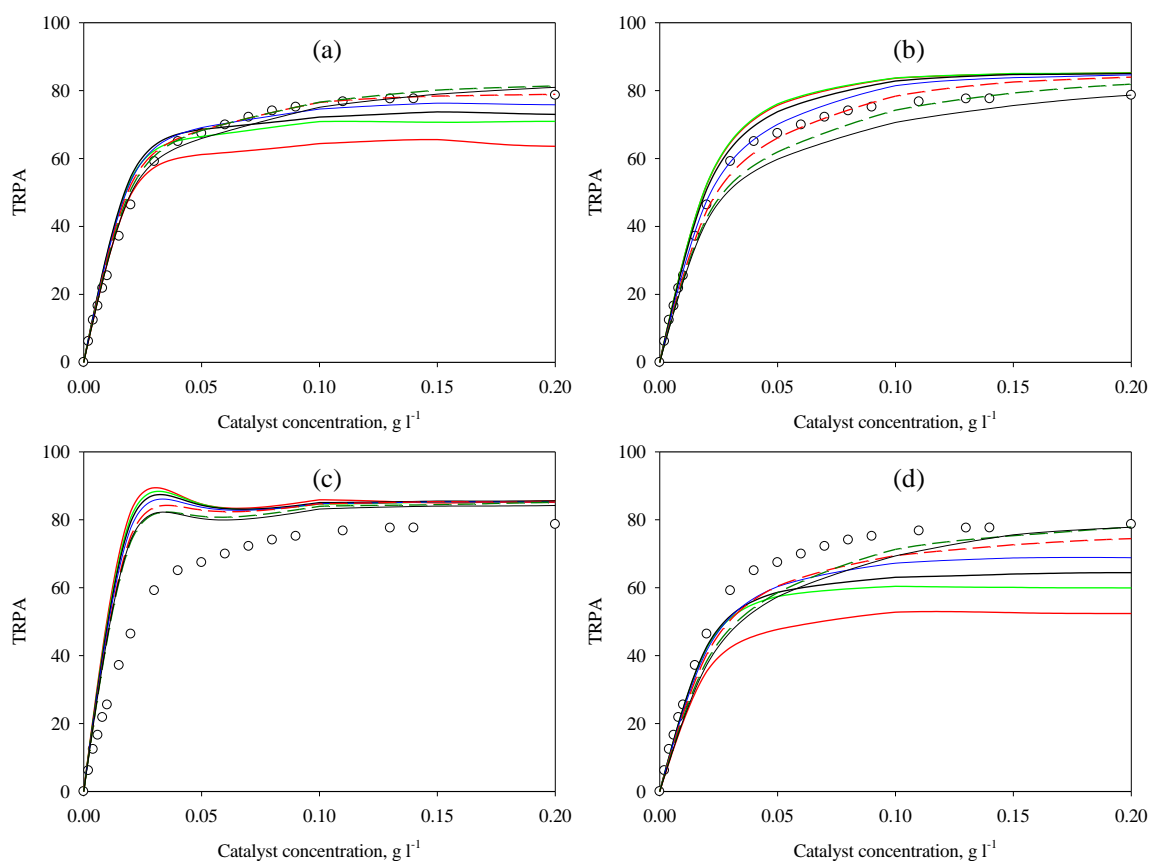


**Figure 3.17.** Effect of Boundary Conditions on the TRPA, reported as a percent of the total emitted radiation as a function of catalyst concentration (TiO<sub>2</sub> mg/l) for (a)  $P_{\text{absLamp}} = 0.1, P_{\text{absWall}} = 0.1$ , (b)  $P_{\text{absLamp}} = 0, P_{\text{absWall}} = 0.2$ , (c)  $P_{\text{absLamp}} = 0, P_{\text{absWall}} = 0$ , (d)  $P_{\text{absLamp}} = 0.2, P_{\text{absWall}} = 0.2$ . With (—)  $g = -0.99$ , (—)  $g = -0.4$ , (—) isocratic, (—)  $g = 0.4$ , (---)  $g = 0.7$ , (---)  $g = 0.9$  and (---)  $g = 0.99$  and (○) experimental data.

### 3.4.7 Total Transmittance(TT) Measurements When Establishing Scattering Models in an Annular Reactor

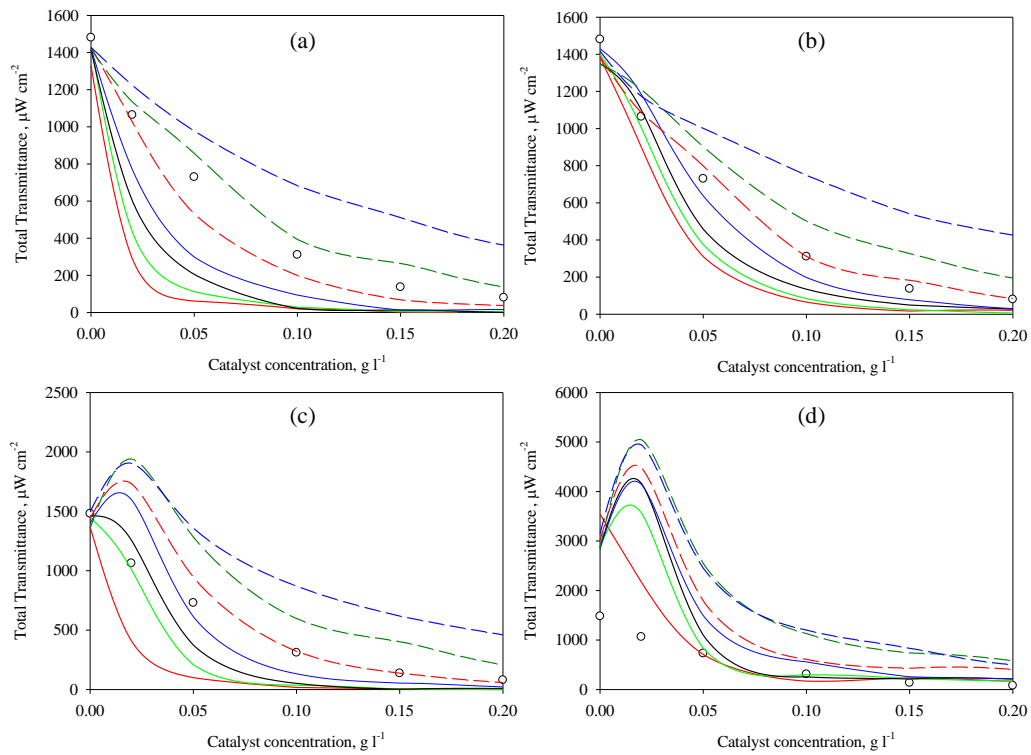
Total Transmittance (TT) measurements as described in the introduction section of this manuscript, are a key parameter for the determination of LVRPA in photocatalytic reactors. In fact, the evaluation of TT and its changes with catalyst concentration does not require special assumptions to be made (as is the case for TRPA) so that BC's and scattering models can be established with increased confidence. On this basis, it is expected that this methodology could yield better model discrimination.

Figure 3.18(a-d) report the TT and its changes with catalyst concentration while using the H-G phase function model for the limiting combinations of BCs: i) Figure 3.18a with  $P_{\text{absLamp}} = 1$ , and  $P_{\text{absWall}} = 1$ , ii) Figure 3.18b with  $P_{\text{absLamp}} = 0$  and  $P_{\text{absWall}} = 1$ , iii) Figure 3.18c with  $P_{\text{absLamp}} = 1$  and  $P_{\text{absWall}} = 0$ , and iv) Figure 3.18d with  $P_{\text{absLamp}} = 0$  and  $P_{\text{absWall}} = 0$ .

In this respect, Figure 3.18c and Figure 3.18d are valuable to discard two extreme model cases where  $P_{\text{absLamp}} = 1$  and  $P_{\text{absLamp}} = 0$  with  $P_{\text{absWall}}$  being consistently zero. For these two extreme cases, no single “g” value of the H-G phase function capable of representing the experimental data with low residuals.

On the other hand, Figure 3.18a and Figure 3.18b with  $P_{\text{absLamp}} = 1$  and  $P_{\text{absLamp}} = 0$  respectively and with  $P_{\text{absWall}}$  set at 1, yield TT values adequately representing the experimental transmittance data within a narrow range of “g” parameter values. For instance, one can observe that adjustments of experimental TT in Figure 3.18a and Figure 3.18b, leads to a “g” scattering parameter in the 0.6 to 0.8 range.

Table 3.2 and Figure 3.19 describe the residuals for the models of Figure 3.18a and Figure 3.18b. It can be seen that in both cases there is consistently an optimum “g” value: a) 0.6 for  $P_{\text{absLamp}} = 0$  and b) 0.8 for  $P_{\text{absLamp}} = 1$ . Given the above analysis, one can notice that the TT experimental data are most valuable to discriminate in between boundary conditions and to calculate between possible g parameter values.



**Figure 3.18.** Effect of Boundary Conditions on the Transmitted Radiation (TT) as a Function of Catalyst for (a)  $P_{\text{absLamp}} = 1$ ,  $P_{\text{absWall}} = 1$ , (b)  $P_{\text{absLamp}} = 0$ ,  $P_{\text{absWall}} = 1$ , (c)  $P_{\text{absLamp}} = 1$ ,  $P_{\text{absWall}} = 0$ , (d)  $P_{\text{absLamp}} = 0$ ,  $P_{\text{absWall}} = 0$ . With (—)  $g = -0.99$ , (—)  $g = -0.4$ , (—) isocratic, (—)  $g = 0.4$ , (---)  $g = 0.7$ , (---)  $g = 0.9$  and (---)  $g = 0.99$  and (○) experimental data.

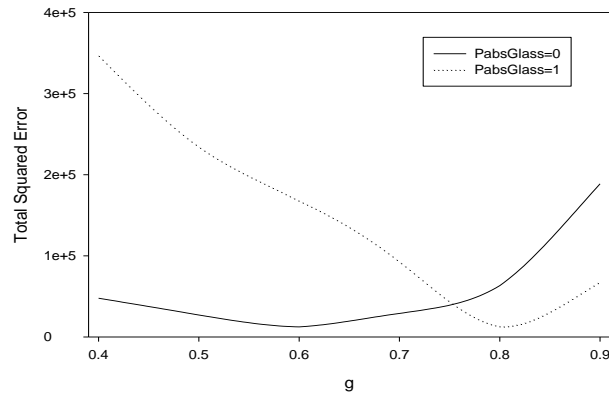


**Figure 3.19.** Total Squared Error Variation with Respect to Scattering Mode at Different BCs. (—)  $P_{\text{absLamp}} = 1$ , (••••)  $P_{\text{absLamp}} = 0$ . Both for  $P_{\text{absWall}} = 1$ .

**Table 3.2.** Total Transmission (TT) Squared Error for various “g” Scattering Parameters and two sets of BCs. Case a:  $P_{\text{absLamp}}=1$ ,  $P_{\text{absWall}}=1$ . Case b:  $P_{\text{absLamp}}=0$ ,  $P_{\text{absWall}}=1$ .

<b>g</b>	<b>Case a</b>	<b>Case b</b>
0.4	47,729	346,551
0.5	27,010	234,026
0.6	12,406	167,457
0.7	28,956	92,358
0.8	63,214	12,992
0.9	188,709	68,179

Given that a small fraction of the radiation reaching the outer reactor wall is expected to be reflected ( $P_{\text{absWall}}=1$  or close to one) and that one would anticipate reemission to be limited ( $P_{\text{absLamp}}$  equal or close to one) as postulated by Duran et al. 2010, Figure 3.18a is considered to be close to the actual applicable model for irradiance calculations using the H-G phase function.

### 3.5 Conclusions

- a) It is shown that a MC method is able to simulate the three dimensional field for the LVRPA inside an annular photoreactor. The proposed stochastically based MC model accounts for radiation absorption through the inner Pyrex glass, reflection of photons reaching the inner and outer walls of the concentric unit and photons absorption and scattering inside the photocatalyst slurry .
- b) It is proven that MC calculations using isocratic, H-G and binomial scattering models play a significant role in the identifying critical simulation factors such as BCs and scattering parameters.
- c) It is shown that TRPA measurements, given the uncertainty of underlying assumptions, allow limited discrimination between scattering models and BCs, when compared to TT irradiance measurements.

e) It is proven that the H-G phase function with a positive 0.6-0.8 “ $g$ ” scattering parameter and  $P_{\text{absWall}}=1$  and  $P_{\text{absLamp}}=1$  boundary conditions yields adequate prediction of TT experimental values.

### 3.6 References

Binzoni, T., Leung, T., Gandjibakhche, A., & Rufenacht, D. (2006). The Use of the Henyey-Greenstein Phase function in Monte Carlo simulation in biomedical optics. *Phys.Med. Biol.* , 51,N313.

Brandi, R., Citroni, M., Alfano, O., & Cassano, A. (2003). Absolute quantum yields in photocatalytic slurry reactors. *Chem. Eng. Sci.* , 58,979.

Cabrera, M. O. (1995). Scattering Effects Produced by Inert Particles in Photochemical Reactors 2. A Parametric Study. *Ind. Eng. Chem.* , 34, 500-509.

Cabrera, M., Alfano, O., & Cassano, A. (1996). Absorption and Scattering Coefficients of Titanium Dioxide Particles Suspensions in Water. *Journal of Physical Chemistry* , 100, 20043-20050.

Changrani, R., & Raupp, G. (1999). Monte Carlo Simulation of the Radiation Field in a Reticulated Foam Photocatalytic Reactor. . *AIChE* , 45(5), 1085.

Chong, M., Jin, B., Chow, C., & Saint, C. (2010). Recent developments in photocatalytic water treatment technology: A review. *Water Research* , 44, 2997-3027.

de Lasa, H., Serrano, B., & Salaices, M. (2005). *Photocatalytic Reaction Engineering*. New York: Springer.

Duran, J. E., Taghipour, F., & Mohseni, M. (2010). Irradiance modeling in annular photoreactors using finite-volume method. *Photoch. Photobio. A*, 215, Issue 1, p.81-89.

Fujishima, A., & Zhang, X. (2006). Titanium dioxide photocatalysis: present situation and future approaches. *Comptes Rendus Chimie* , 9, 750-760.

Fujishima, A., Zhang, X., & Tryk, D. (2008). TiO<sub>2</sub> photocatalysis and related surface phenomena. *Surface Science Reports* , 63, 515-582.

Grčić, I., & Li Puma, G. (2013). Photocatalytic Degradation of Water Contaminants in Multiple Photoreactors and Evaluation of Reaction Kinetic Constants Independent of Photon Absorption, Irradiance, Reactor Geometry, and Hydrodynamics. *Environmental Science & Technology*. 47, (23), pp 13702-13711.

- Li Puma, G., & Brucato, A. (2007). Dimensionless analysis of slurry photocatalytic reactors using two-flux and six-flux radiation absorption-scattering models. *Catalysis Today* , 122 78-90.
- Martin, C., Baltanas, M., & Cassano, A. (1996). Photocatalytic reactors II. Quantum efficiencies allowing for scattering effects. An experimental approximation. *Photoch. Photobio. A.* , 94, 173.
- Marugan, J., Van Grieken, R., Alfano, O., & Cassano, A. (2006). Optical and Physicochemical Properties of Silica-Supported TiO<sub>2</sub> Photocatalysts. *AIChE* , 52(8), 832.
- Moreira, J., Serrano, B., Ortiz, A., & de Lasa, H. (2010). Evaluation of Photon Absorption in an Aqueous TiO<sub>2</sub> Slurry Reactor Using Monte Carlo Simulations and Macroscopic Balance. *Industrial and Engineering Chemistry Research* , 49, 10524-10534.
- Moreira, J., Serrano, B., Ortiz, A., & de Lasa, H. (2011). TiO<sub>2</sub> absorption and scattering coefficients using Monte Carlo method and macroscopic balances in a photo-CREC unit. *Chemical Engineering Science* , 66, 5813-5821.
- Pareek, V., Ching, S., Tade, M., & Adesina, A. (2008). Light intensity distribution in heterogeneous photocatalytic reactors. *Asia-Pac. J. Chem. Eng.* , 3, 171.
- Pareek, V., Cox, S., & Adesina, A. (2003). Light intensity Distribution in Photocatalytic Reactors Using Finite Volume Method. *Third International Conference on CFD in the Minerals and Process Industries*. CSIRO, (p. 229). Melbourne, Australia.
- Pasquali, M., Santarelli, F., Porter, J., & Yue, P. (1996). Radiative Transfer in Photocatalytic Systems. *AIChE* , 42(2), 532.
- Piskozub, J., & McKee, D. (2011). Effective scattering phase functions for the multiple scattering regime. *Optic Express* , 19(5), 4786.
- Prahl, S. K. (1989). *A Monte Carlo Model of Light Propagation in Tissue, Dosimetry of Laser Radiation in Medicine and Biology: SPIE Institute Series*. IS 5, 102-111.
- Romero, R., Alfano, O., & Cassano, A. (1997). Cylindrical Photocatalytic Reactors. Radiation Absorption and Scattering Effects Produced by Suspended Fine Particles in an Annular Space. *Ind. Eng. Chem. Res.* , 36, 3094.
- Romero, R., Alfano, O., & Cassano, A. (2003). Radiation Field in an Annular, Slurry Photocatalytic Reactor. 2. Model and Experiments. *Ind. Eng. Chem. Res.* , 42, 2479.

Salaices, M., Serrano, B., & de Lasa, H. (2002). Experimental Evaluation of photon absorption in an aqueous TiO<sub>2</sub> Slurry reactor. *Chem. Eng. J.* , 90, 219.

Satuf, M., Brandi, R., Cassano, A., & Alfano, O. (2005). Experimental Method to evaluate the Optical Properties of Aqueous Titanium Dioxide Suspensions. *Ind. Eng. Chem. Res.* , 44, 6643.

Toepfer, B. G. (2006). Photocatalytic oxidation of multicomponents solutions of herbicides: reaction kinetics analysis with explicit photon absorption effects. *Applied Catalysis B* , 68, 171.

Tsekov, R. S. (1997). Radiation Field in Continuous Annular Photocatalytic Reactors: Role of the Lamp Finite Size. *Chemical Engineering Science* , 52(10), 1667-1671.

Yokota, T., Cesur, S., Suzuki, H., Baba, H., & Takahata, Y. (1999). Anisotropic Scattering Model for the Estimation of Light Absorption Rates in Photoreactor with Heterogeneous Medium. *J. Chem. Eng. Jpn.* , 32, 314.

Zhou, J., Zhang, Y., Zhao, X., & Ray, A. (2006). Photodegradation of Benzoic Acid over Metal-Doped TiO<sub>2</sub>. *Industrial and Engineering Chemistry Research* , 45, 3503-3511.



## Chapter 4

### 4 Establishing Photon Absorption Fields in a Photo-CREC Water II Reactor Using a CREC-Spectroradiometric Probe

The information presented in this chapter is based on the article entitled "Establishing Photon Absorption Fields in a Photo-CREC Water II Reactor Using a CREC-Spectroradiometric Probe", published in Chemical Engineering Science Vol. 116 p. 406-417, in September, 2014. The results reported in this chapter address stage ii) of section 1.1, and significantly contribute towards the partial completion of general objective a) in section 1.2.

#### 4.1 Abstract

The scattering mode and the appropriate boundary conditions in a Photo-CREC Water II annular reactor are assessed from experimental data. These data are obtained using a novel spectroradiometric probe (CREC-SP). This probe is designed to measure irradiance at different radial positions within the concentric channel. Radiation data obtained are analyzed using a calculated Monte Carlo radiation field inside the slurry photoreactor. The effect of the phase function and the boundary conditions, as relevant to the photoreactor walls are fully determined. The MC method proposed in section 3.3.2 is modified in the present chapter to account for refraction, absorption and reflection at the probe surface. Lamp emission, refraction and reemission as well as wavelength-dependent absorption and scattering are accounted for. Regarding Degussa P25, a Henyey-Greenstein phase function with a  $g=0.68\pm 0.03$  is needed. On this basis, a 3D LVRPA field, is established. This approach also allows one to independently set boundary conditions, avoiding cross-correlation with scattering parameters, an issue present when using past experimental methodologies, as presented in Chapter 3. As a result, the approach presented in this chapter establishes scattering phase functions and radiation absorption fields with improved accuracy. Clarification of these matters is of crucial importance for the design and scale-up of photocatalytic reactors.

## 4.2 Introduction

The experimental approach presented in section 3.4.6 and 3.4.7 (Valades-Pelayo et al., 2014) recently described significant limitations of the most common experimental irradiance data: a) they do not provide sufficient information regarding reactor internal radiation gradients, b) they do not allow accurate validation of boundary conditions (BCs) when scattering parameters are to be determined. These issues are mainly attributed to the intrinsic nature of two compensating effects: reflection at the reactor boundaries and backscattering from the near-wall slurry region. Furthermore, the LVRPA calculated values are strongly affected by uncertainty in the angular dependent phase functions (Yang et al., 2005). As a result, a potentially high cross-correlation between phase functions, scattering parameters and Boundary Conditions (BC) may be observed, which is the case for annular reactors (Valades-Pelayo et al., 2014). Moreover, the accurate determination of the LVRPA spatial distribution within the photocatalytic reactor is an important factor (Alfano et al., 1994), mainly due to both the inability to render precise kinetic information from averaged photon absorption rates (Brandi, et al., 2003) and the strong non-uniformities inherent to radiation propagation in scattering-absorption media.

It is the researcher's view, that for further development of photocatalytic reaction engineering, the precision of the irradiance field determination is required to improve, and thus, the accuracy of the calculated LVRPA. Specifically, in annular photoreactors, the radial dependence of the irradiance field is expected to gather vast information regarding the slurry optical properties. To accomplish this, in the present chapter, “radial irradiance profiles”(RP) at different photocatalyst loadings are determined. RP are obtained by measuring irradiance, with the sensor surface pointing towards the reactor centerline (where the lamp is located) while changing the radial position of the sensor. This approach allows accounting for the internal radiation gradients in the slurry, unlike the total transmittance (TT) and the Total Rate of Photon Absorption (TRPA). Moreover, the adequacy of the proposed method is proven to be satisfactory by analyzing the uncertainties on the obtained LVRPAs. As a result of this analysis, it is also shown that one can considerably reduce the uncertainty on the applicable phase function.

## 4.3 Experimental Method

### 4.3.1 Reactor Setup

A schematic representation of the Photo-CREC Water II photoreactor was reported in previous studies by our research group (Moreira et al., 2010; Moreira et al., 2011 and Valades-Pelayo et al., 2014). A schematic representation of the Photo-CREC Water II Photoreactor is already presented in Figure 3.2 and Figure 4.1. Additionally, details regarding its configuration can be found in section 3.3.1.

The Photo-CREC-Water II Reactor is operated in a down-flow mode with a lean TiO<sub>2</sub> suspension flowing through the concentric unit channel. The Photo-CREC-Water II Reactor is configured with a special geometry with a conical bottom section. These characteristics are essential to avoid any potential photocatalyst sedimentation in the corners of the bottom section.

The Photo-CREC-Water II unit is operated with slurry velocities many times the agglomerate settling velocity, thereby avoiding any particle settling effect. In fact if one calculates the particle terminal velocity for Degussa P25 particles, using the Stokes law, for a particle agglomerate diameter, as suggested by Salaices et al. (2002), of 1340 nm, a TiO<sub>2</sub> density of 4,260 kg m<sup>-3</sup>, and a fluid density and viscosity equal to water at 20° C, the terminal velocity is several orders of magnitude smaller than the downwards fluid velocity in the annular section.

Furthermore, Figure 4.1 shows an expanded view of the CREC-PS probe with its in-depth positioning device. The CREC-PS operates in conjunction with a fiber optic-spectroradiometer system, allowing irradiance measurements at various radial positions in the Photo-CREC Reactor annular channel with a wide view angle as the sensor points towards the reactor central axis.

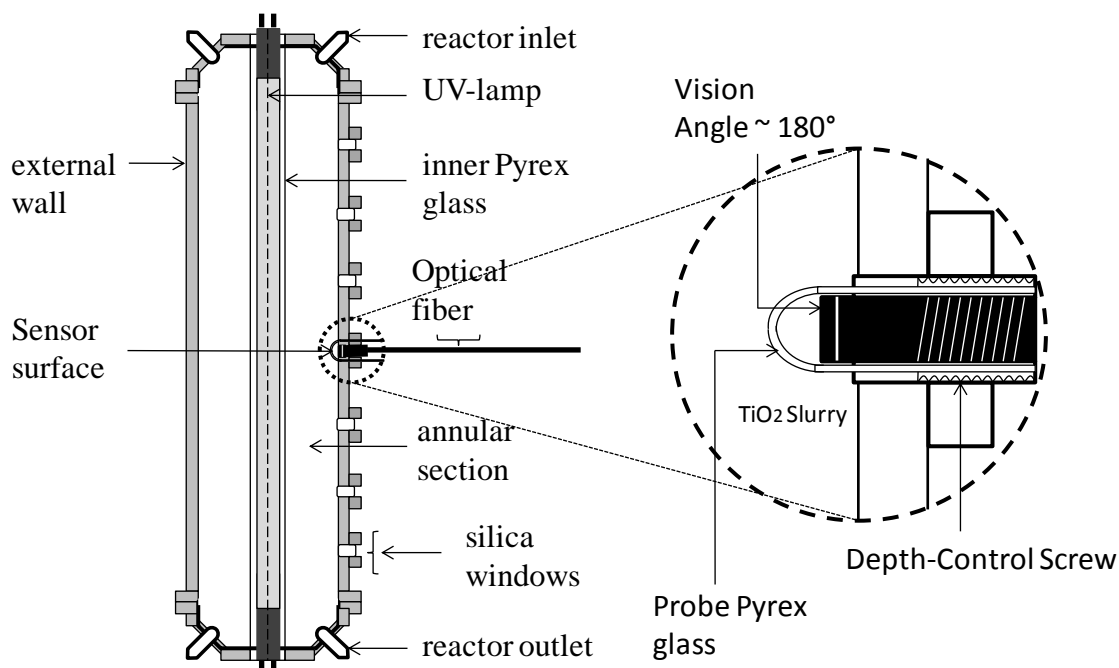


**Figure 4.1.** Reactor Schematics and Expanded View of the Probe Sensor Allowing Changes and Irradiation Measurements with a wide view angle at Various Radial Positions in the Photo-CREC Annular Channel.

The spectrometric system, consists of a StellarNet EPP2000C-25LT16 (Black-Comet) Spectrometer able to detect radiation in the 190 nm to 850 nm range. This spectrometer has a 0.75 nm resolution, with stray light ranging from 0.02% to 0.2% at 435nm and 220nm respectively. Exposure times can vary from 4 ms to 60 s to avoid sensor saturation. For irradiance measurements in the 4,000 to 200  $\mu\text{W}/\text{cm}^2$  range and using the BLB Lamps (F15T8-BLB), standard deviations were observed to stay below 1%. In the 200 to  $\sim 10 \mu\text{W}/\text{cm}^2$ , percent-wise, standard deviations increased to up to 10%, but were never above 20  $\mu\text{W}/\text{cm}^2$ . For the present study exposure time was set between 40 and 100 ms in order to avoid sensor over-saturation. 30 to 40 irradiance spectra were averaged to minimize measurement variations due to the use of short exposure times.

#### 4.3.2 The CREC-SP Probe

As described in Figure 4.1 and Figure 4.2, the CREC-PS probe was designed to introduce the radiometer's sensor into the slurry at different radial positions within the reactor channel. The CREC-PS is made of stainless steel, HDPE and a thin Pyrex cylinder ( $\sim 0.7$

mm thick). The Pyrex cylinder allows a high fraction of radiation in the 340-388 nm range, to reach the sensor inside the probe. The probe is designed to go as deep as 25.5 mm within the annular section (refer to Figure 4.2b).

Figure 4.2a shows the CREC-PS screw-like mechanism that allows changing the radial positions with high precision. A double o-ring design prevents reactor leaks while the CREC-PS probe depth is being adjusted.

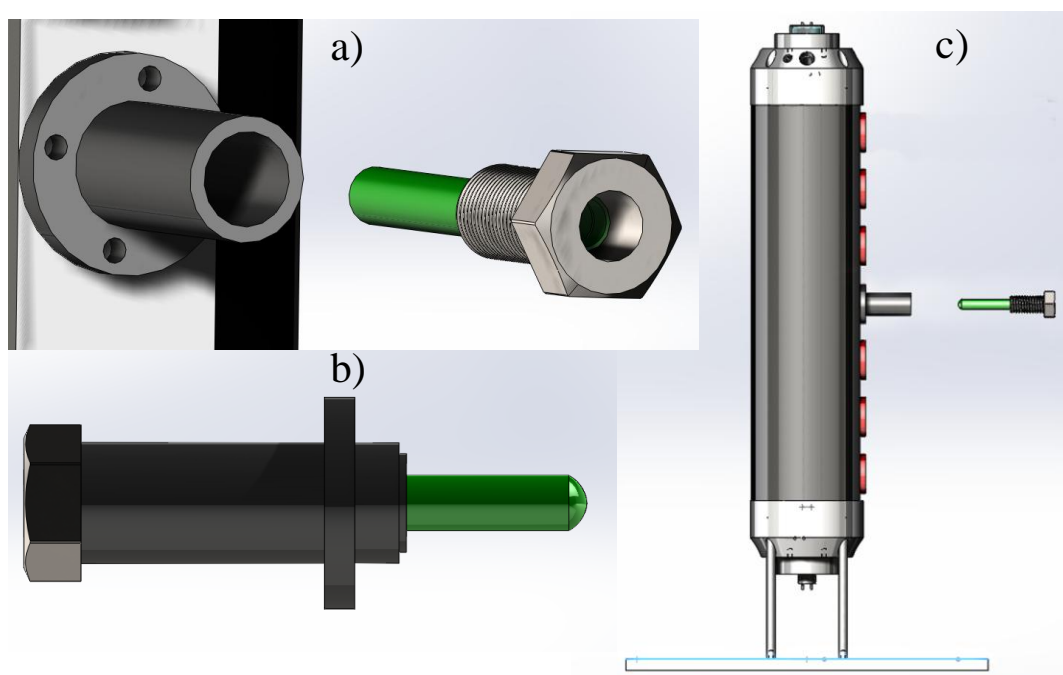


**Figure 4.2.** Description of the CREC PS Probe while being placed in the Photo-CREC-Water II Reactor.

The Photo-CREC-Water II Reactor has 7 window slots that are located at several axial reactor positions, allowing the CREC-PC to be placed in each of them. Figure 4.2c shows the CREC-PC probe mounted into the middle window. During the experimental runs, the probe was moved as needed. Thus, radial measurements at various radial positions were obtained by twisting the screw-like end of the probe between the inner ( $r=0.0175$  m) and outer bounds ( $r=0.0445$  m) of the slurry region.

### 4.3.3 Experimental procedure

The head of the spectrophotometric sensor was placed inside the CREC-PS probe. Once its position was carefully adjusted, its back-end was connected to a StellarNetEPP2000C-25LT16 spectrometer port via an optical fiber cable (refer to Figure 4.1). One should mention that the CREC-PS Probe was mounted onto one of the windows of the Photo CREC-Water II Reactor (refer to Figure 4.2c).

Prior to The Photo-CREC-Water II Unit operation, the slurry suspension was allowed to enter the reactor from the top. A valve located in the reactor bottom section was closed, so that the water slurry could accumulate inside the reactor unit. While the reactor was being filled, air was being pushed out through a top vent. Once all the air had been removed from the unit, the vent was closed and hermetically sealed. This methodology ensures that no empty zones or air pockets remain, during operation, within the annular reactor section.

Once the reactor system was filled with 6L of water, the pump and the 15 watts BL lamp were turned on. As the lamp emission was stabilized, the irradiation measurements were effected. The sensor was placed during each run at seven different radial positions from the reactor centerline: 4.12cm., 3.72 cm., 3.32cm., 2.92cm., 2.52cm., 2.12 cm. and 2 cm (Figure 4.1). The probe depth was varied by using an adjustable Vernier scale. Three measurements were performed at every location and the average local values were then calculated. By using these local averages, each radial irradiation profile (RP) was established.

Moreover, by progressively adding Degussa P25, eight RP were generated at 0, 25, 50, 100, 150, 200, 300 and 400  $\text{mg l}^{-1}$  photocatalyst concentrations. pH was kept at 7 for all runs. It should be noted that every time the photocatalyst concentration was adjusted, the photocatalytic reactor was left in operation for at least 5 minutes until the photocatalyst concentration was homogenous and, as a result, radiation measurements were stabilized.

All of the above mentioned steps were repeated at least four times until mean values, low standard deviations and reduced 95% confidence intervals, as reported in Figure 4.6, were obtained.

## 4.4 Mathematical Models

### 4.4.1 RTE Simulation by Monte Carlo Method

The Monte Carlo method consists of tracing trajectories of photons until they are absorbed or scattered by the slurry medium (Prah, 1989). This statistical method has been extensively used to model near UV propagation in photocatalytic reactors (Moreira et al., 2010; Moreira et al., 2011). Chapter 3 already clarifies the methods of, and the issues with, Monte Carlo applications used in a Photo-CREC Water II Reactor (Valades-Pelayo et al., 2014).

The MC method simulates photon bundle evolution in the photoreactor. Therefore, it is based on the physical nature of thermal radiation. This is one of the most used methods to solve radiation problems since it is very easy to adapt to complex problems and it also provides close to exact solutions within statistical limits (Demirkaya et al., 2005). Section 3.4 (Valades-Pelayo et al., 2014) described the Monte Carlo Method for modeling radiation transport in an annular Photo-CREC water II reactor with a suspended photocatalyst. The main focus of this section is to determine the effect that the phase function parameters have on the numerical simulation of the LVRPA for different catalyst concentrations. Different boundary conditions for the inner glass and outer walls were assumed and their validity was also studied for different catalyst loadings.

Given the above considerations, a Monte Carlo approach is considered in the present chapter. This approach includes assumptions applicable to both the photocatalytic reactor and the CREC-PS probe:

(a) Emission of photons by the lamp is assumed to be non uniform in the axial direction, according to Tsekov & Smirniotis (1997). In conjunction with this a Lambertian source emission model is considered to establish the direction of the emitted

photons. This process is considered to be stochastic. Absorption and reemission of photons by the lamp were also considered.

(b) The inner reactor Pyrex tube absorption is set at 6% of all photons emitted by the lamp (Moreira et al., 2010; Moreira et al., 2011).

(c) Different scattering modes are simulated with the H-G phase function for different values of the “ $g$ ” scattering parameter.

(d) Photons that hit the reactor walls have a certain probability of being absorbed and terminated. Alternatively, these photons can be reflected by a specularly-diffuse reflection mechanism.

(e) Absorption and scattering coefficients are uniform throughout the annular section. The wavelength-specific coefficients were used in accordance to Cabrera et al. (1996).

(f) Transmission, refraction and absorption in the CREC-PS tip are assumed to follow the Fresnel equations for unpolarized light and are treated according to Monte Carlo numerical principles, as applicable to the semi-spherical glass-water and glass-air interfaces.

(g) Simulated radial irradiation profiles (RPs), as viewed by the CREC-PS sensor-probe, are described using multiple independent MC simulations at different sensor radial positions.

Figure 4.3 reports the algorithm used. It describes emissions in the MC simulation with photons being absorbed/reemitted by the lamp as well as photons being refracted and absorbed at the reactor’s boundaries. One can also see in Figure 4.3, that photons may display values for "cond1", where: a) “cond1”=0 represents the bouncing inside the reactor, b) “cond”=1 describes photon absorption and trajectory termination. Furthermore, Figure 4.4 portrays the so-called “Reaction Space Subroutine”. This subroutine provides the logic structure by which the scattering and absorption phenomena are accounted within the annular section of the Photo-CREC Water II Reactor. This subroutine also considers surface interactions with the walls and the CREC-SP probe.



The Monte Carlo method shown in Figure 4.3, begins by launching a photon with a specific wavelength from the UV lamp surface into the annular section of the photoreactor. The photon's initial direction is chosen according to a Lambertian light source distribution. The position of the emission in the axial direction is chosen according to the model presented by Tsekov & Smimiotis (1997). On this basis, a uniformly distributed random number and a wavelength are chosen according to a probability distribution function (PDF). The photon distribution function (Lamp emission spectra) is obtained by using a Finite Fourier series and a polynomial fitting to the lamp's emission spectra.

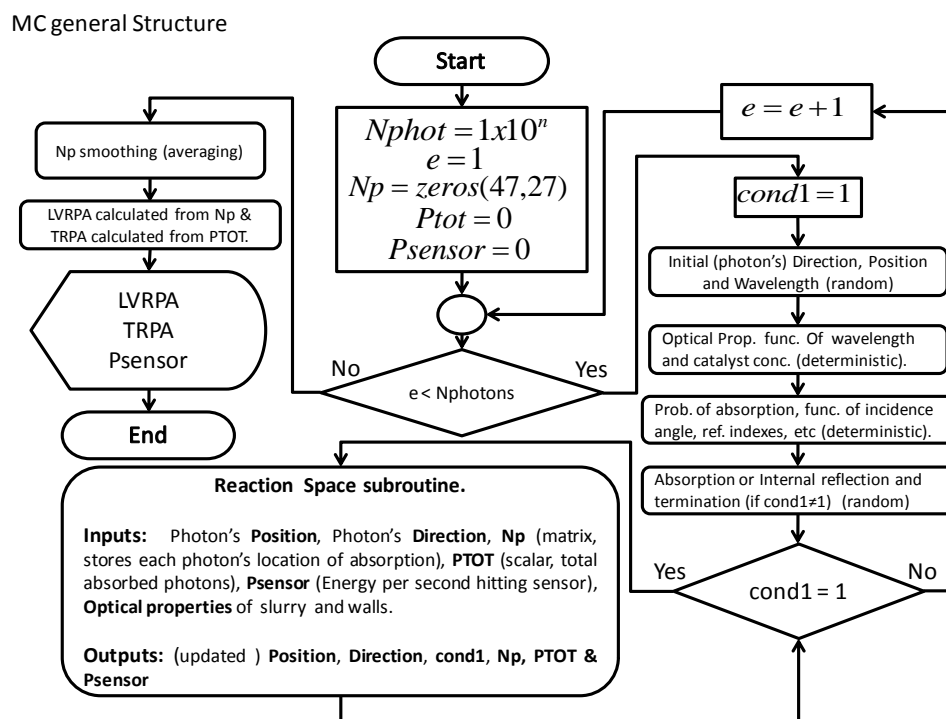


**Figure 4.3.** General Structure of the Monte Carlo Method Used to Model the Photo-CREC Water II.

After the photon is emitted by the lamp, it finds the quartz-air interface where it can be either reflected or refracted (as displayed in Figure 4.3). The refraction probability at each interface is determined according to the Fresnel's equations for unpolarized radiation. In other words, it is a function of the angle of incidence and the material refraction indexes. The same procedure is applied to both, the air-quartz and water-quartz

interfaces. As a result, photons have a 6% probability of being absorbed in the quartz inner cylinder. This absorption probability was also determined experimentally by [Moreira et al. \(2010\)](#).

As shown in Figure 4.4, once a photon evolves inside the annular section, its location can be uniquely established by its position and direction. This can be accomplished using three spatial coordinates and two directional angles, respectively. As can be seen in Figure 4.4, a given photon flight length "Li" is set at every stage of photon evolution. Afterwards, three different types of surfaces can interact with the photon: a) a catalyst particle, b) the CREC-SP probe and c) both boundaries of the annular section. The required formulas for photon direction and angular position at every stage of photon evolution were reported by [Valades-Pelayo et al. \(2014\)](#).

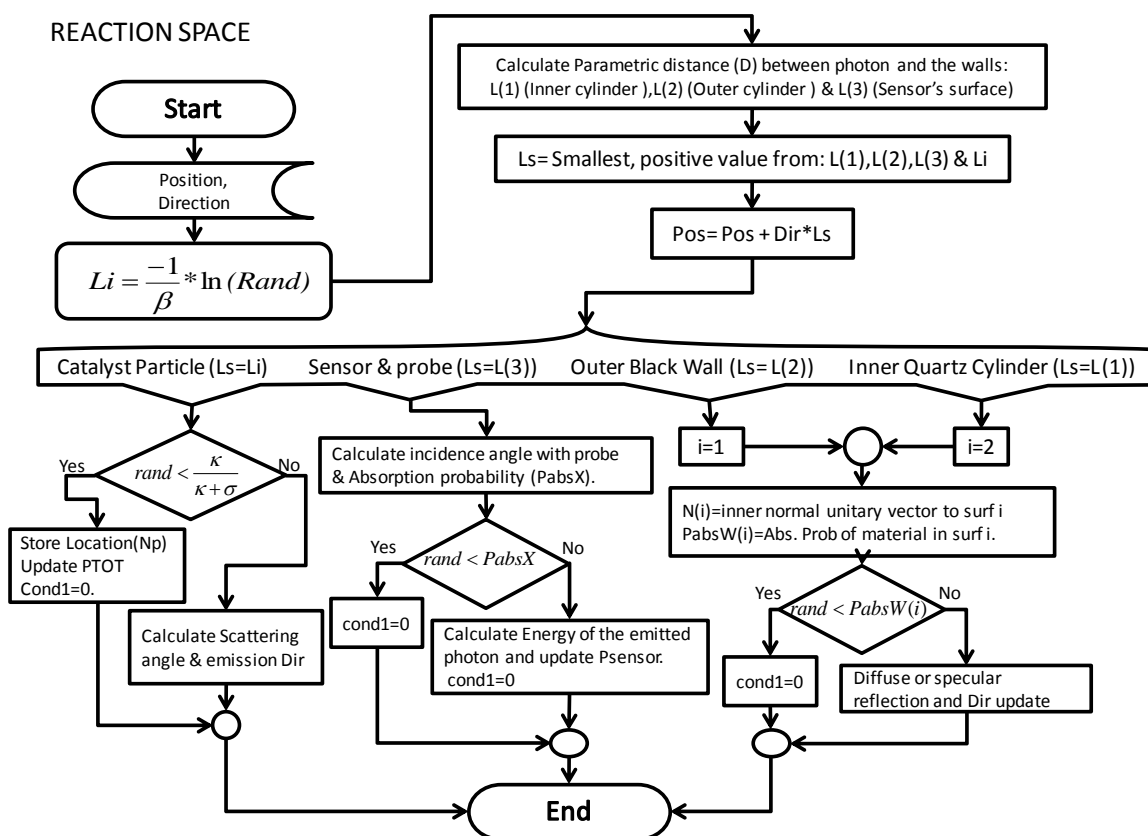


**Figure 4.4.** Algorithm of the Main Subroutine within the MC Simulation Code, Used to Model the Reaction Media.

For sensor probe interactions, the photon's angle of incidence with the probe surface is calculated, where the probe Pyrex glass is considered to be a semi sphere (refer to Figure 4.2b). By use of the incidence angle and the Fresnel equations for unpolarized light, a probability of absorption is, then, obtained. Lastly, a stochastic absorption process takes place and if the photon transmits through the probe, it is considered to collide with the sensor's surface.

On the other hand, when a photon reaches the outer reactor wall, several possibilities are considered at this boundary. Photon interaction at the outer wall may ideally involve diffuse walls (He et al., 1991) with a  $P_{\text{absWall}}$  absorption probability. Furthermore, when a photon reaches the lamp again, its trajectory can be terminated with the photon hitting the lamp either being absorbed or reflected. The probability of absorption, in this case, is determined by the  $P_{\text{absGlass}}$  parameter. As a result, having the incident radiation reaching the spectroradiometric sensor (refer to Figure 4.4), one can undertake radiation flux evaluations at different radial positions as shown in Figure 4.5.

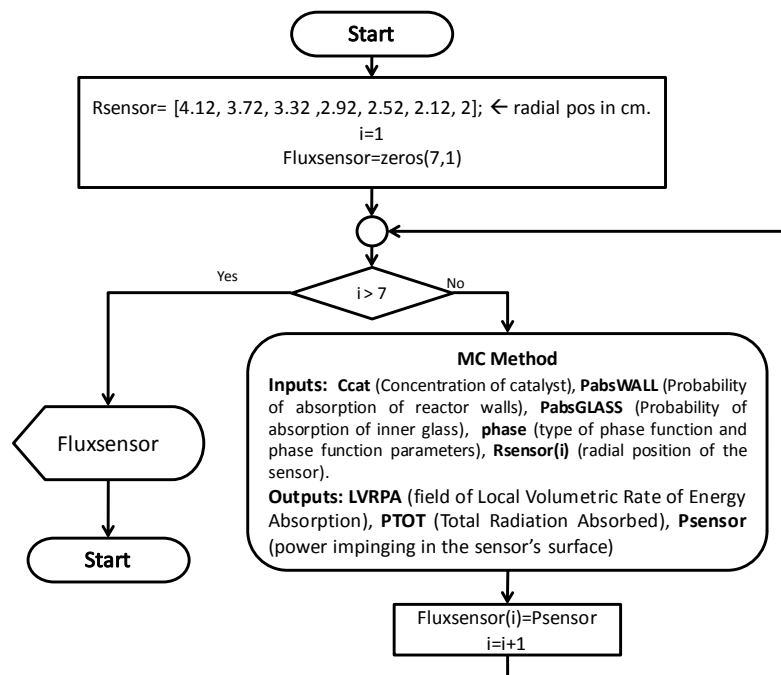


**Figure 4.5.** Iterative Algorithm Used to Calculate the Radiation Flux Reaching the Sensor at Different Radial Positions. "Fluxsensor" is a vector containing the RP.

Furthermore, the algorithm implemented in Figure 4.5 involves a stepwise, discrete process that mimics the experimental irradiance measurements in the concentric photocatalytic reactor. The radial positions chosen for the sensor in the MC method are mentioned in Figure 4.5.

One should mention that in addition to the steps mentioned in Figure 4.3 to Figure 4.5, the LVRPA field definition requires an averaging (smoothing) procedure. This smoothing treatment reduces the introduced statistical fluctuations inherent in the MC method. One should mention that the LVRPA data presented in later sections of this manuscript includes such a smoothing algorithm.

#### 4.4.2 Quantification of the LVRPA Span.

The LVRPA is a critical local property in photocatalytic reactors. In the present study, the LVRPA is considered a function of the axial and the radial positions, the " $g$ " scattering parameter and the photocatalyst concentration:

$$LVRPA = f(r, z, g, C_{cat}) \quad \text{Eq. 4-1}$$

where  $C_{cat}$  is the photocatalyst concentration,  $g$  is the scattering parameter in the H-G phase function, and " $r$ " and " $z$ " are the spatial coordinates in the radial and axial directions, respectively. The " $g$ " scattering parameter can be defined in a narrow band as:

$$g = \bar{g} \pm \Delta g \quad \text{Eq. 4-2}$$

Where  $g$  represents the sum of a  $\bar{g}$  average value, and  $\Delta g$  corresponds to the  $g$  span for the 95% Confidence Interval (C.I.).

On this basis and considering the potential local variations of " $g$ ", one can establish local LVRPA deviations using the higher and lower " $g$ " values. These upper and lower " $g$ "s provide upper and lower bounds for LVRPA as follows:

$$Span_{LVRPA}(r, z, \bar{g}, \Delta g, C_{cat}) = \frac{|LVRPA(r, z, \bar{g} + \Delta g, C_{cat}) - LVRPA(r, z, \bar{g} - \Delta g, C_{cat})|}{LVRPA(r, z, \bar{g}, C_{cat})}. \quad (100) \quad \text{Eq. 4-3}$$

One should note that in the context of the present study, the " $\text{Span}_{\text{LVRPA}}$ " function, as shown in Eq. 4-3, refers to the percentual 95% C.I. deviation for the LVRPA within the annular reactor space. Thus, as considered, the " $\text{Span}_{\text{LVRPA}}$ " is a function of the photocatalyst concentration, the "r" and "z" spatial coordinates and "g"s with 95% C.I. span.

One should note that Eq. 4-3 provides a comprehensive basis for comparing various experimental methodologies when determining RTE parameters such as boundary conditions or phase functions. The proposed " $\text{Span}_{\text{LVRPA}}$ " function will be later and specifically used in this chapter, highlighting the significance of measuring radial RPs when determining the LVRPA.

## 4.5 Results and Discussion

Figure 4.6 reports the measured changes of irradiance at various radial positions and photocatalyst concentrations, as described in section 4.3.3. Bars in Figure 4.6 report the standard deviations for the 4 repeats of each measurement. Furthermore, to have a comprehensive description of the irradiance profiles, eight different photocatalyst concentrations were used: 0, 25, 50, 100, 150, 200, 300 & 400  $\text{mg l}^{-1}$ .

Figure 4.6, shows that the measured irradiance decreased progressively when increasing both radial position and photocatalyst concentration. There is, however, a range near the inner reactor wall ( $r < 0.025$  m) at low photocatalyst loadings (between zero and 50  $\text{mg l}^{-1}$ ) where an increase in the sensor irradiance is observed with increasing photocatalyst loading. This is expected to happen in annular reactors with partially reflective/transmissive inner boundaries, as suggested by the parametric sensitivity analysis from section 3.4.4. (Valades-Pelayo et al. 2014). This apparently counter intuitive increase in the sensor irradiance is mainly due to the redirectioning of light towards the sensor by multiple BC-particle reflections. As photocatalyst increases, the distance from the inner BC and magnitude at which this phenomena contributes is reduced.

In addition, one can notice that the photocatalyst loading affects, to a very significant extent, the RP at high photocatalyst concentrations in the near inner wall region. Under these conditions, the combined effects of back scattering at the inner glass wall and radiation absorption due to the formation of a photocatalyst layer (Ballari et al., 2010) are considered to be main factors affecting RPs.

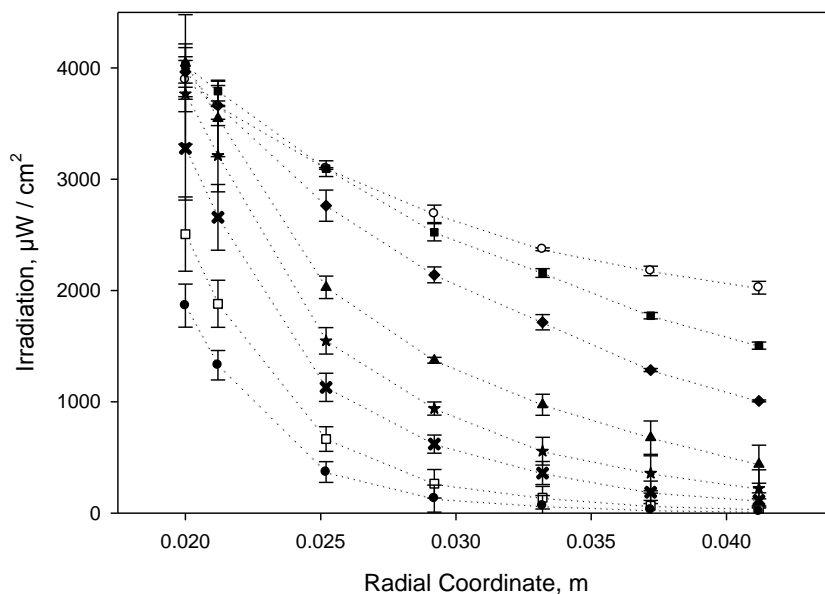


**Figure 4.6.** Experimental RPs in micro watts cm<sup>-2</sup> for Different Catalyst Concentrations at (○) water only, (■) 25, (◆) 50, (▲) 100, (★) 150, (×) 200, (□) 300, and (●) 400 mg l<sup>-1</sup>. Vertical bars report the typical standard deviation for the 4 repeats.

Once the experimental data of Figure 4.6 were obtained using the CREC-SP probe, they were compared with the predictions of the Monte Carlo based irradiance model. One should note that the MC method includes three parameters to be adjusted. These phenomenological-based parameters are: (1) the  $P_{\text{absGLASS}}$  probability or probability of photon absorption by the inner glass and by the lamp. This represents the fraction of photons that do not bounce back in the reaction space once they collide with the inner reactor boundary, (2) the  $P_{\text{absWALL}}$  or probability of photon absorption by the outer reactor wall. This represents the fraction of photons that are absorbed once they collide with the outer boundary and (3) the " $g$ " parameter or scattering for the H-G phase function. This

parameter determines the scattering mode or the shape of the probability density function for the scattering angle.

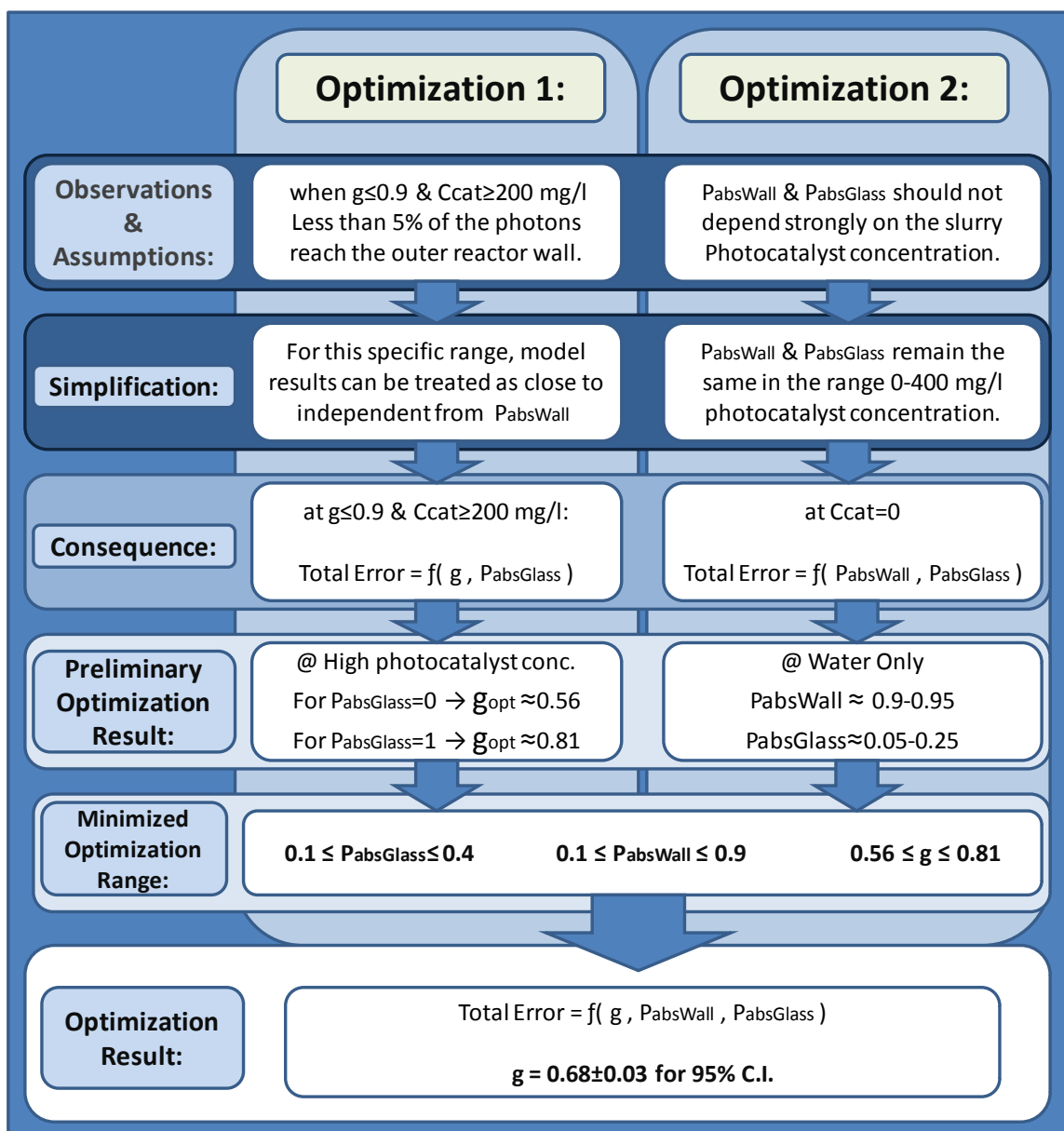
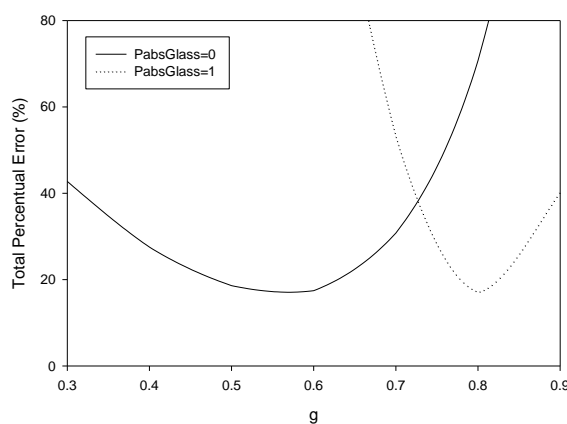


**Figure 4.7** Outline of the Optimization Algorithm for Determining the Three Parameters Used in the Monte Carlo Method.

The adjustment of these three parameters in the context of the MC method is computer intensive and as a result, a special calculation strategy was implemented in the present study. This special strategy allows narrowing down the optimization range of the

parameters and thus, minimizing the computational resources needed. Besides the optimization of the computational resources, another strong justification for using this approach is the need of breaking the cross-correlations between boundary conditions (BCs) and scattering parameters. This allows treating the experimental data as subsets where different factors dominate, as will be further explained.

Figure 4.7 describes the general optimization algorithm. Two main simplifications are considered in this calculation: (1) For photocatalyst concentrations equal or higher than  $200 \text{ mg l}^{-1}$ , the RP is considered independent of  $P_{\text{absWALL}}$ . This is adequate given that under these conditions (refer to Figure 4.7) very few photons reach in fact, the outer reactor boundary (Valades-Pelayo et al., 2014). (2) For catalyst concentration zero, irradiance profiles are scattering mode independent, and therefore a non-dependency on the “ $g$ ” parameter is noticed, more specifically, it is assumed that the BCs will, roughly, remain the same as photocatalyst is added.



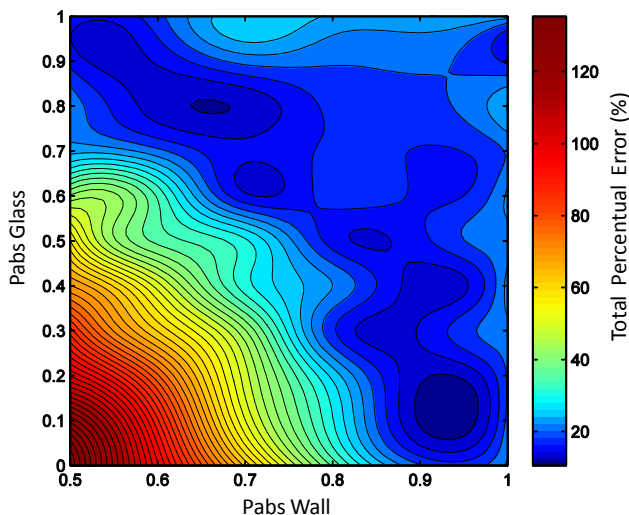
**Figure 4.8** Total Percentual Errors (%) between Experimental and Model Results for a High Catalyst Concentration Range of 200- 400  $\text{mg l}^{-1}$ , for different values of  $g$ . Total Percentual Error for 21 different data points. Minimum correspond to less than 1% average percentual error.

Figure 4.8 reports the total percentual error (%) of 21 measurements (seven different radial positions at three different photocatalyst concentrations) and two limiting inner BC values. Photocatalyst concentrations considered are in the 200 to 400  $\text{mg l}^{-1}$  range,



presented in Figure 4.6. One can notice that minimum total percentual errors are achieved for both a “ $g$ ” of 0.81, and a  $P_{\text{absGLASS}} = 1$  and for a “ $g$ ” of 0.56 and  $P_{\text{absGLASS}} = 0$ . Thus, one can conclude that the scattering in the irradiance model always lies in a forward scattering mode with the “ $g$ ” having a weak dependence on the inner reactor boundary conditions. These results, while in a slightly narrower range, are in agreement with the ones reported in section 3.4.7 (Valades-Pelayo et al., 2014).

Figure 4.9 describes the total percentual error (%) surface for various probabilities of absorption of the inner and outer boundaries. This error surface is generated for a zero photocatalyst concentration, as described in the 2nd optimization scheme shown in Figure 4.7. Under these conditions, irradiance in the photocatalytic reactor is independent of the scattering mode. Different colors in this figure represent the total errors between the MC irradiation model and the experimental radial irradiation data. It can be observed, on this basis, that lower total errors were obtained with a  $P_{\text{absWALL}}=0.9-0.95$  and a  $P_{\text{absGLASS}} =0.05-0.25$ .



**Figure 4.9** Total Percentual (%) Error versus Probability of Absorption on Inner Glass (PabsGlass) and on Outer Reactor Wall (PabsWall). Each contour represents approx. 2% Total Percentual Error. 7 data points considered. Minimum corresponds to less than 2% average percentual error.

Thus, given the above results, one can conclude the following: i) For 200 to 400 mg l<sup>-1</sup> photocatalyst concentrations and values of 0 and 1 for the inner BCs ( $P_{\text{absGLASS}}$ ), a 0.56 and 0.81 “g” respectively, minimizes the error between model and experimental irradiation data and ii) for photocatalyst concentrations equal to zero, the “g” does not affect calculations and BCs parameters ( $P_{\text{absWALL}}$  and  $P_{\text{absGLASS}}$ ), rendering average percentual errors of about 2% for  $P_{\text{absWALL}}$  and  $P_{\text{absGLASS}}$ , in the 0.9-0.95 and 0.05-0.25 range, respectively.

Based on these assumptions, the parameter ranges could be limited. However, it is worth mentioning, that BCs ranges should not be reduced solely based on the evidence provided by Figure 4.9, as the photocatalyst sticking to the reactor walls is expected to have an effect at higher photocatalyst concentrations. More specifically, the BCs actual value is expected to fall somewhere between the absorption probability of the BC's when using water only and that of a photocatalyst layer fully adhered to the walls. The probability of absorption of the photocatalyst layer is expected to be close to 0.13, namely one minus the wavelength-averaged albedo of Degussa P25.

On the basis of these considerations, the g, and the  $P_{\text{absWALL}}$  and  $P_{\text{absGLASS}}$  parameters were optimized by simultaneously using a limited domain of variation. This domain was set to be in the 0.1 to 0.9 range for  $P_{\text{absWALL}}$ , 0.1 to 0.4 for  $P_{\text{absGLASS}}$ , and in the 0.56 to 0.81 range for g. This optimization was again carried out by minimizing the deviation between the MC simulation irradiance and the experimental irradiance data. The obtained fitting yielded, as reported in Table 1, a value for the g scattering parameter of  $0.68 \pm 0.03$ , with 0.03 representing the span for the 95% confidence interval. This value is within the range suggested in section 3.5 (Valades-Pelayo et al., 2014).

Furthermore, the  $P_{\text{absWALL}}$  (outer boundary parameter) calculated is consistent with both the results shown in sections 3.4.6 and 3.4.7 (Valades-Pelayo et al., 2014) and the expected physical properties of the black PVC surface. For the inner boundary, even though no previous determination was made, the obtained  $P_{\text{absWALL}}$  value fell within the expected range, as suggested by Duran et al. (2010).

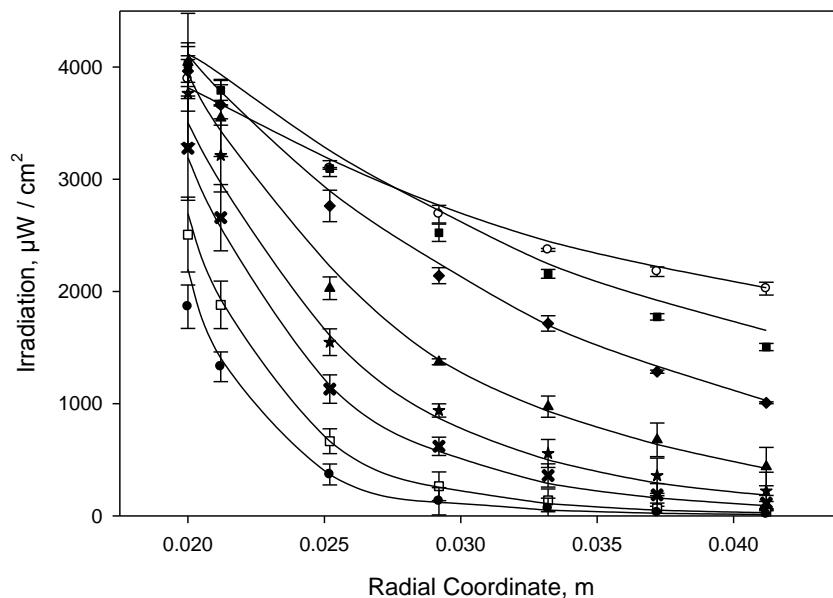
Regarding the " $g$ " scattering parameter a value of 0.68 was obtained. It was found to represent slightly higher forward scattering than the 0.51 value, obtained from the data reported by [Satuf et al. \(2005\)](#) by integrating according to the BL-lamp emission spectra. The difference between both values is due the former being determined under photocatalyst concentrations ten times smaller than the later. According to the literature, severe deposition of Degussa P25 at the reactor walls is known to happen ([Ballari et al., 2010](#)). Therefore, it is expected, that the value obtained in this study represents reduced additional backscattering effects. This is the case given the experimental set-up used in the present study displays reduced photocatalyst wall-sticking effects and allows adequate consideration of irradiance gradients within the annular section.

**Table 4.1.**  $g$ ,  $P_{\text{absWALL}}$  and  $P_{\text{absGLASS}}$  average values and spans for 95% C.I.

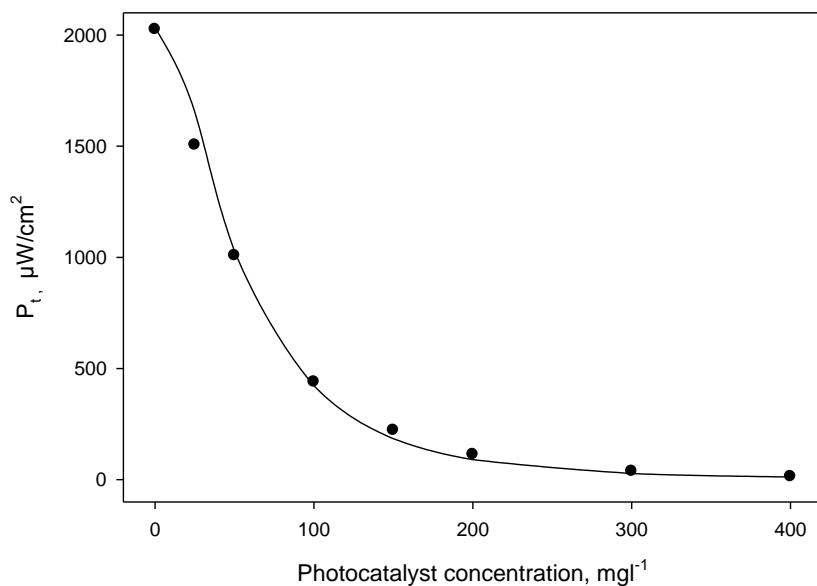
Parameter:	Mean	95% C.I.
$g$	0.68	$\pm 0.03$
$P_{\text{absGlass}}$	0.30	$\pm 0.05$
$P_{\text{absWall}}$	0.65	$\pm 0.05$

The MC irradiance distribution inside the annular photoreactor for the optimized parameters ( $g=0.68$ ,  $P_{\text{absWALL}}= 0.65$  and  $P_{\text{absGLASS}}=0.30$ ), are presented in Figure 4.10 with the experimental measurements. One should notice from Figure 4.10 that deviations between model and experimental results were in all cases smaller than 5% for a 0 to 200  $\text{mg l}^{-1}$  catalyst concentration range. For higher concentrations (200 to 400  $\text{mg l}^{-1}$ ) and radial position higher than 3 cm, deviations of up to 20% were observed. This change in the percentual errors can be explained given that at high optical thicknesses, irradiation measurements significantly drop by a factor of  $3 \times 10^2$ , the equivalent of  $\sim 10 \mu\text{W cm}^{-2}$ .

Furthermore, Figure 4.11 shows the total transmittance (TT) from the model and its comparison with experimental TT data. As can be seen, TT measurements are equally well described by this approach with deviations in a  $\pm 5\%$  band. The deviations at low photocatalyst concentrations for the total transmittance in Figure 4.11 are likely to be a consequence of assuming that the BC's are not strongly dependent on the photocatalyst concentration. Thus, deviations are induced at the last optimization stage (Figure 8), tentatively as an attempt to correct the BC's within the zero to 400  $\text{mg l}^{-1}$  range.



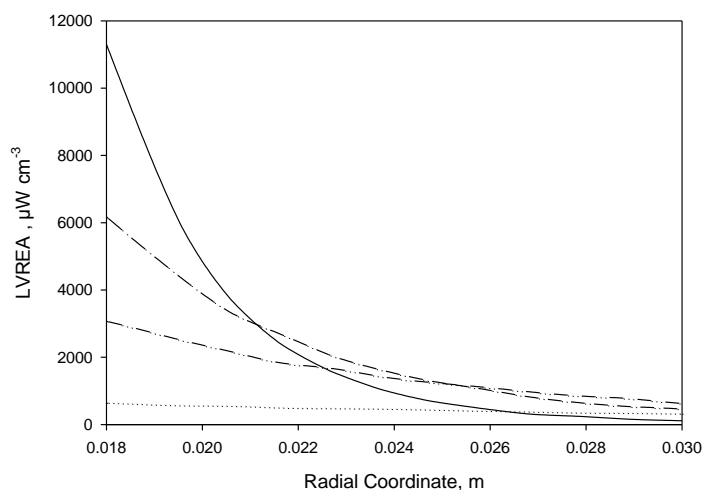
**Figure 4.10.** Experimental and Model ( $g=0.68$ ,  $P_{\text{absWALL}}=0.65$  and  $P_{\text{absGLASS}}=0.3$ ) Radial Irradiance Profiles (RPs) for Different Catalyst Concentrations (—) MC simulation results, (○)water only, (■) 25, (◆) 50, (▲)100, (★)150, (×)200, (□)300, and (●)400  $\text{mg l}^{-1}$ .



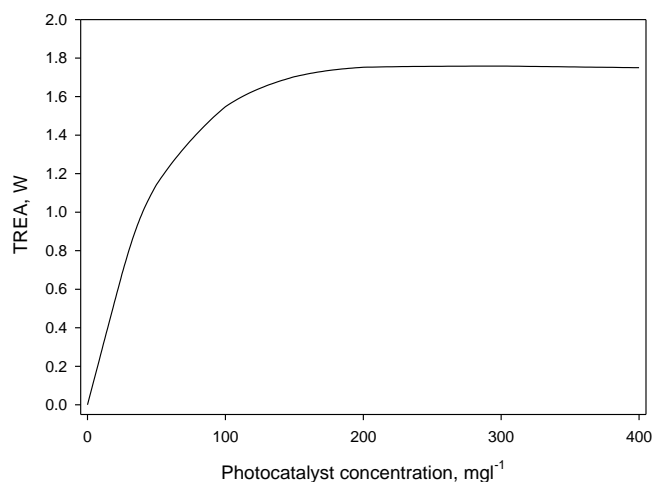
**Figure 4.11.** Total Transmitted Radiation for Different Photocatalyst Concentrations. (—) MC simulation for  $g=0.68$ ,  $P_{\text{absWALL}}=0.65$  and  $P_{\text{absGLASS}}=0.3$ , (●) experimental.

Figure 4.12 reports the calculated radial profiles for LVREA at  $z = 0$  (central axial position) for different photocatalyst concentrations. Moreover, Figure 4.13 displays the Total Rate of Energy Absorption (TREA), equivalent to the TRPA, from zero to  $400 \text{ mg l}^{-1}$  photocatalyst concentration. As experimentally determined, the lamp emits  $2.56 \text{ W}$ , the asymptotic value of the rate of energy absorption corresponds to 68% of total emitted radiation. As can be seen, the TREA reaches 95% of the maximum TREA near the  $150 \text{ mg l}^{-1}$  photocatalyst concentration. This photocatalyst concentration is considered as an optimum for Photo-CREC Water II operation, as experimentally determined by [Salaices et al. \(2002\)](#).

In addition, the apparent optical thickness for this optimum operation point was calculated as proposed by [Li Puma & Brucato \(2007\)](#) for the optimized H-G phase function ( $g = 0.68$ ) by using an average extinction coefficient of  $5.32 \text{ m}^2/\text{g}$  and an albedo of  $0.87$ . These optical parameters correspond to the wavelength-averaged MC parameters in accordance to the lamp emission spectra. Under the above mentioned assumptions, the apparent optical thickness was found to fall in the  $1.80\text{-}3.40$  range, as recommended by [Li Puma \(2003\)](#) for Degussa P25, with a  $3.11$  value being obtained.



**Figure 4.12.** Calculated Radial LVRPA Values at  $z = 0$  when  $P_{\text{absWALL}} = 0.65$ ,  $P_{\text{absGLASS}} = 0.3$  and  $g = 0.68$  for (····) 25, (— · · —) 100, (— · —) 200, and (—) 400  $\text{mg l}^{-1}$ .



**Figure 4.13.** Calculated Total Rate of Energy Absorption (TREA) as a function of Photocatalyst Concentration, for  $P_{\text{absWALL}} = 0.65$ ,  $P_{\text{absGLASS}} = 0.3$  and  $g = 0.68$ . Optimum photocatalyst concentration near  $150 \text{ mg l}^{-1}$ .

Figure 15 reports the 3D LVREA at four different photocatalyst concentrations as calculated by the MC radiation model.

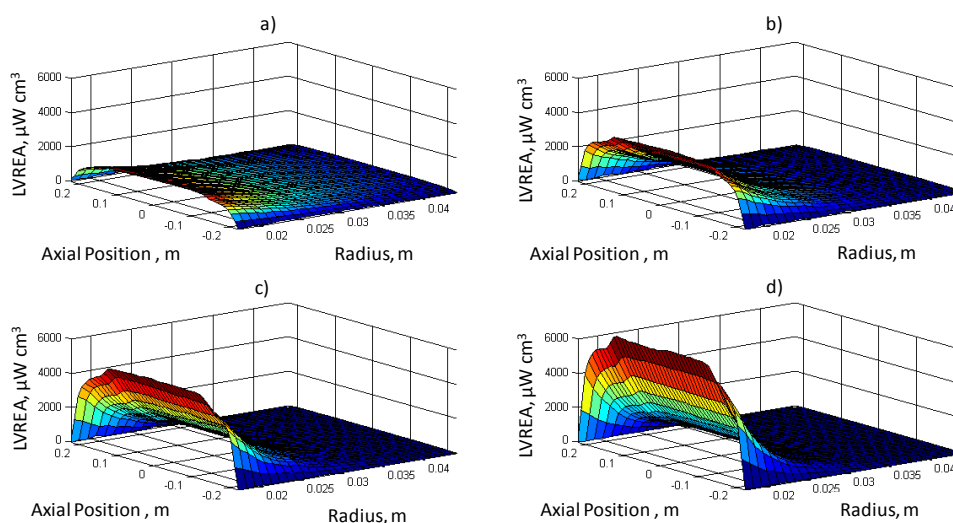


**Figure 4.14.** 3D Profile of the LVREA in  $\mu\text{W cm}^{-3}$  inside the Photo-CREC Water II for a)  $50 \text{ mg l}^{-1}$ , b)  $100 \text{ mg l}^{-1}$ , c)  $150 \text{ mg l}^{-1}$ , d)  $200 \text{ mg l}^{-1}$ .  $P_{\text{absWALL}}=0.65$ ,  $P_{\text{absGLASS}}=0.3$ ,  $g=0.68$ .

### 4.5.1 Calculating Uncertainty in the LVRPA

In this section, the method to quantify the percentual span in the LVRPA ( $Span_{LVRPA}$ ) is applied to the Photo-CREC Water II with photocatalyst concentrations ranging from 0 to 400 mg l<sup>-1</sup>. It is expected that the span of the LVRPA (Refer for Eq. 4-3) at every given point will vary depending on i) location (within the annular section), ii)  $Span_{LVRPA}$  for  $g$  and, iii) sensitivity of the LVRPA for that specific range of  $g$ .

To accomplish this, three types of data sets are compared when fitting the " $g$ " scattering parameter: a) the TRPA, b) the TT and c) the RP. In addition, the accuracy of every experimental method is quantified as follows: i) Local  $Span_{LVRPA}$  as per Eq. 4-3, ii) Probability density function (PDF) generated from the local  $Span_{LVRPA}$  values.

In addition, for the MC method used in this study, when generating the LVRPA, the reaction volume is discretized in 27 radial positions and 47 axial positions. As a result, PDF calculations consider discretized spatial variables. One should mention that for every PDF, its mean, mode and standard deviation are calculated.

Figure 4.15 report the  $Span_{LVRPA}$  functions as defined in section 4.4.2. One should notice, for instance, that when the highest bars are closer to zero (e.g. Figure 4.15c), there is a greater fraction of the reactor volume displaying small spans for the LVRPA 95% C.I. .On the other hand, when high bars shift considerably from zero, one can forecast a significant fraction of the reaction volume displaying large spans for LVRPA.

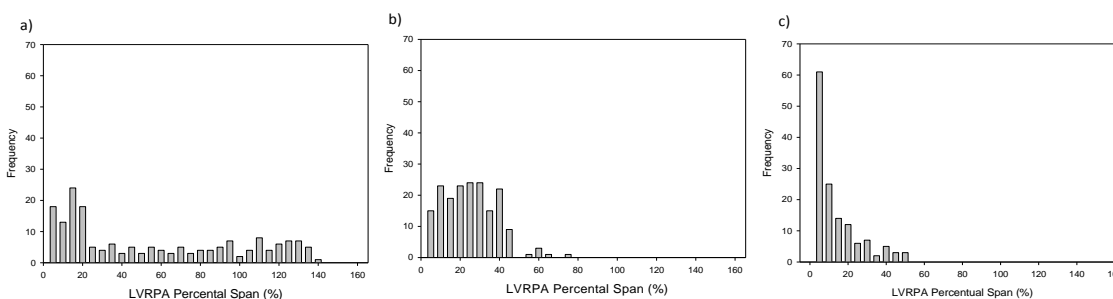


**Figure 4.15.** LVRPA Percentual Span (%) Distribution for Volume Elements inside the Reaction Space for: a)  $\Delta g = \pm 0.2$  , average Span of 50% or  $\pm 25\%$  , b)  $\Delta g = \pm 0.1$  , average Span of 24% or  $\pm 12\%$ , c)  $\Delta g = \pm 0.03$  , average Span of 10%. or  $\pm 6\%$ .

Regarding LVRPA spans, if one uses the data from sections 3.4.6 and 3.4.7 (Valades-Pelayo et al., 2014), it can be noted that Macroscopic Radiation Balances and calculated TRPA, lead to a “ $g$ ” ranging from 0.5 to 0.9 ( $\Delta g = \pm 0.2$ ). Furthermore, for the TT, the admissible “ $g$ ” value is in the range of 0.6 to 0.8 ( $\Delta g = \pm 0.1$ ).

Based on the above, when inputting these parameters into the MC simulation and in the Eq. 4-3 for the TRPA ( $\Delta g = \pm 0.2$ ), as reported in Figure 4.15a, the mean of the span field variable changes as much as  $\pm 25\%$ . Nonetheless, when using TT ( $\Delta g = \pm 0.1$ ), the average span drops to  $\pm 12\%$  (Figure 4.15b). As reported in section 3.5 (Valades-Pelayo et al., 2014), the TT is, under these conditions, better suited to discriminate between scattering modes.

On the other hand, when using RPs (local irradiance measurements at 7 radial positions), as in the present study, a  $\Delta g = \pm 0.03$  and a mean of  $\pm 6\%$  is obtained for the LVRPA span (Figure 4.15c). All the above mentioned results, are presented in Table 2. Thus, it is shown that radial irradiance measurements (RP) and the ensuing proposed MC analysis greatly increase the accuracy when determining the absorption field.

**Table 4.2.** Span for the LVRPA when using TRPA, TT and Radial RPs.

Data Type	LVRPA Percentual Span
Total Rate of Photon Absorption (TRPA)	$\pm 25\%$
Total Transmittance (TT)	$\pm 12\%$
Radial Irradiance Profiles (RP)	$\pm 6\%$

It can therefore, be postulated that the most desirable parameter discrimination (refer to Figure 4.15c) is obtained with radial irradiance data (RP) as given by the CREC-SP. The present study also successfully establishes a narrow range for “ $g$ ” with a resulting narrow span and reduced uncertainty for LVRPA. This is accomplished by breaking cross-correlations between the BCs and the scattering parameters while properly considering irradiance gradients within the reactor space.



## 4.6 Conclusions

- (a) A new approach involving a novel spectrophotometric probe (CREC-PS) was employed to obtain radial irradiance distributions in the annular channel of the Photo-CREC Water II Reactor.
- (b) These radial measurements allow one to break correlations between boundary conditions and phase functions. Thus, the accuracy of the radiation model is greatly increased while compared to other methods based on Total Transmittance or Total Rate of Photon Absorption measurement.
- (c) On this basis, the MC model from section 3.3.2 (Valades-Pelayo et al. 2014) was modified to account for the probe intrusion inside the annular section of Photo-CREC Water II. This modified MC model and the experimental irradiance data were employed to predict via numerical regression, a “ $g$ ” H-G scattering coefficient with a much narrower span.
- (d) The combined MC model results and the experimental radial irradiance profiles obtained allowed us to clarify both boundary conditions for the Radiative Transfer Equation and radiation gradients within the annular section to accurately predict suitable phase functions.

## 4.7 References

- Ahmed, S., Rasul, M., Martens, W., Brown, R., & Hashib, M. (2011). Advances in Heterogeneous Photocatalytic Degradation of Phenols and Dyes in Wastewaters: A Review. *Water Air and Soil Pollution*, 215, 3-29.
- Alfano, O. M., Bahnemann, D., Cassano, A. E., Dilliert, R., & Goslich, R. (2000). Photocatalysis in Water Environments Using Artificial and Solar Light. *Catalysis Today*, 58, 199-230.
- Alfano, O. M., Cabrera, M. I., & Cassano, A. E. (1994). Modeling of Light Scattering in Photochemical Reactors. *Chemical Engineering Science*, 49, 5327-5246.

- Ballari, M. d., Alfano, O. M., & Cassano, A. E. (2010). Mass transfer limitations in slurry photocatalytic reactors: Experimental Validation. *Chemical Engineering Science*, 65, 4931-4942.
- Brandi, R. J., Citroni, M. A., Alfano, O. M., & Cassano, A. E. (2003). Absolute quantum yields in photocatalytic slurry reactors. *Chemical Engineering Science*, 58, 979-985.
- Cabrera, M. I., Alfano, O. M., & Cassano, A. E. (1995). Scattering Effects Produced by Inert Particles in Photochemical Reactors 2. A Parametric Study. *Ind. Eng. Chem.*, 34, 500-509.
- Cabrera, M., Alfano, O., & Cassano, A. (1996). Absorption and Scattering Coefficients of Titanium Dioxide Particles Suspensions in Water. *Journal of Physical Chemistry*, 100, 20043-20050.
- Cassano, A., & Alfano, O. (2000). Reaction engineering of suspended solid heterogeneous photocatalytic reactors. *Catalysis Today*, 58, 167-197.
- Changrani, R., & Raupp, G. (1999). Monte Carlo Simulation of the Radiation Field in a Reticulated Foam Photocatalytic Reactor. *AIChE*, 45(5), 1085.
- Chong, M., Jin, B., Chow, C., & Saint, C. (2010). Recent developments in photocatalytic water treatment technology: A review. *Water Research*, 44, 2997-3027.
- Cuevas, S., Serrano Rosales, B., & Arancibia, C. (2007). Radiation Field in an Annular Photocatalytic Reactor by the P1 Approximation. *International Journal of Chemical Reaction Engineering*, 5, 1-14.
- de Lasa, H., Serrano, B., & Salaices, M. (2005). *Photocatalytic Reaction Engineering*. New York: Springer.
- Demirkaya, G., Arinç, F., Selçuk, N., & Ayranci, I. (2005). Comparison between performances of Monte Carlo method and method of lines solution of discrete ordinates method. *Journal of Quantitative Spectroscopy & Radiative Transfer*, 93, 115-124.
- Duran, J. E., Taghipour, F., & Mohseni, M. (2010). Irradiance modeling in annular photoreactors using finite-volume method. *Photoch. Photobio. A*, 215, Issue 1, p.81-89.
- Escobedo Salas, S., Serrano Rosales, B., & De Lasa, H. (2013). Quantum yield with platinum modified TiO<sub>2</sub> photocatalyst for hydrogen production. *Applied Catalysis B: Environmental*, 140, 523-536.

Fujishima, A., & Zhang, X. (2006). Titanium dioxide photocatalysis: Present situation and future approaches. *Comptes Rendus Chimie*, 9, 750-760.

Fujishima, A., Zhang, X., & Tryk, D. (2008). TiO<sub>2</sub> photocatalysis and related surface phenomena. *Surface Science Reports*, 63, 515-582.

Garcia Hernandez, J. M., Serrano Rosales, B., & de Lasa, H. (2010). The photochemical thermodynamic efficiency factor (PTEF) in photocatalytic reactors for air treatment. *Chemical Engineering Science*, 166, 891-901.

He, X. D., Torrance, K. E., Sillion, F. X., & Greenberg, D. P. (1991). A Comprehensive Physical Model for Light Reflection. *Computer Graphics*, Vol. 25, Num4. Pag. 177-182.

Herrmann, J. (1999). Heterogeneous photocatalysis: fundamentals and applications to the removal of various types of aqueous pollutants. *Catalysis Today*, 53, 115-129.

Imoberdorf, G., Taghipour, F., Keshmiri, M., & Mohseni, M. (2008). Predictive radiation field modeling for fluidized bed photocatalytic reactors. *Chemical Engineering Science*, 63, 4228-4238.

Iwabuchi, H. (2006). Efficient monte carlo methods for radiative transfer modeling. *Atmos. Sci.*, 63, 2324–2339.

Li Puma, G. (2003). Modelling of Thin-Film Slurry Photocatalytic Reactors Affected by Radiation Scattering. *Environmental Science & Technology*, 37, 5783-5791.

Li Puma, G. (2005). Dimensionless Analysis of Photocatalytic Reactors Using suspended Solid Photocatalyst. *Chemical Engineering Research and Design*, 83(A7), 820-826.

Li Puma, G., & Brucato, A. (2007). Dimensionless analysis of slurry photocatalytic reactors using two-flux and six-flux radiation absorption–scattering models. *Catalysis Today*, 122, 78-90.

Li Puma, G., Puddu, V., Tsang, H. K., Gora, A., & Toepfer, B. (2010). Photocatalytic oxidation of multicomponent mixtures of estrogens under UVA and UVC radiation: Photon absorption, quantum yields and rate constants independent of photon absorpt. *Applied Catalysis B: Environmental*, 99, Issue3-4, 388-397.

Li Puma, G., Toepfer, B., & Gora, A. (2007). Photocatalytic Oxidation of Multicomponent Systems of Herbicides: Scale-up of Laboratory Kinetics Rate Data to Plant Scale. *Catalysis Today*, 124, 124-132.

Minero, C. (1999). Kinetic analysis of photoinduced reactions at the water semiconductor interface. *Catalysis Today*, 54, 205-216.

Minero, C., & Davide, V. (2006). A quantitative evaluation of the photocatalytic performance of TiO<sub>2</sub> slurries. *Applied Catalysis B: Environmental*, 67, 257–269.

Moreira, J., Serrano, B., Ortiz, A., & De Lasa, H. (2010). Evaluation of Photon Absorption in an Aqueous TiO<sub>2</sub> Slurry Reactor Using Monte Carlo Simulations and Macroscopic Balance. *Industrial and Engineering Chemistry Research*, 49, 10524-10534.

Moreira, J., Serrano, B., Ortiz, A., & de Lasa, H. (2011). TiO<sub>2</sub> absorption and scattering coefficients using Monte Carlo method and macroscopic balances in a photo-CREC unit. *Chemical Engineering Science*, 66, 5813-5821.

Moreira, J., Serrano, B., Ortiz, A., & de Lasa, H. (2012). A unified kinetic model for phenol photocatalytic degradation over TiO<sub>2</sub> Photocatalysts . *Chemical Engineering Science*, 78, 186-203.

Pareek, V., Ching, S., Tade, M., & Adesina, A. (2008). Light intensity distribution in heterogeneous photocatalytic reactors. *Asia-Pac. J. Chem. Eng.*, 3, 171.

Pareek, V., Cox, S., & Adesina, A. (2003). Light intensity distribution in photocatalytic reactors using a finite volume method. *Third International Conference on CFD in the Minerals and Process Industries* (pp. 229-234). Melbourne Australia: CSIRO.

Prahl, S. K. (1989). *A Monte Carlo Model of Light Propagation in Tissue, Dosimetry of Laser Radiation in Medicine and Biology: SPIE Institute Series. IS 5*, 102-111.

Ray, A., Chen, D., & Li, M. (2000). Effect of Mass Transfer and Catalyst Layer Thickness on Photocatalytic Reaction. *A.I.Ch.E. Journal*, 46, 1034-1045.

Salaices, M., Serrano, B., & de Lasa, H. (2002). Experimental Evaluation of photon absorption in an aqueous TiO<sub>2</sub> Slurry reactor. *Chem. Eng. J.*, 90, 219.

Satuf, M., Brandi, R., Cassano, A., & Alfano, O. (2005). Experimental Method to evaluate the Optical Properties of Aqueous Titanium Dioxide Suspensions. *Ind. Eng. Chem. Res.*, 44, 6643.

Tsekov, R., & Smirniotis, P. G. (1997). Radiation Field in Continuous Annular Photocatalytic Reactors: Role of the Lamp Finite Size. *Chemical Engineering Science*, 52(10), 1667-1671.

Turchi, C. S., & Ollis, D. F. (1989). Mixed reactant photocatalysis: Intermediates and Mutual rate inhibition. *Journal of Catalysis*, 119, 483-496.

Valades-Pelayo, P. J., Moreira, J., Serrano, B., & de Lasa, H. I. (2014). Boundary conditions and phase functions in a Photo-CREC Water-II Reactor Radiation Field. *Chemical Engineering Science*, 107, 123-136.

Yang, Q., Ang, P. L., Ray, M. B., & Pehkonen, S. O. (2005). Light distribution field in catalyst suspensions within an annular photoreactor. *Chemical Engineering Science*, 60, 5255-5268.

Zhou, J., Zhang, Y., Zhao, X., & Ray, A. (2006). Photodegradation of Benzoic Acid over Metal-Doped TiO<sub>2</sub>. *Industrial and Engineering Chemistry Research*, 45, 3503-3511.

## Chapter 5

### 5 Photocatalytic Reactor Under Different External Irradiance Conditions: Validation of a Fully Predictive Radiation Absorption Model.

The information presented in this chapter is based on the article entitled " Scaled-up Photocatalytic Reactor Under Different Irradiance Conditions: Validation of a Fully Predictive Radiation Absorption Model.". This article was accepted for publication by Chemical Engineering Science journal. The results reported in this chapter address stage iii) of section 1.1 and significantly contribute towards achieving the general objective a) of section 1.2.

#### 5.1 Abstract

The present chapter considers the absorption field in a scaled-up and externally-irradiated Photo-CREC Water Solar Simulator Photoreactor with 9.8 L of irradiated volume. This photo reactor consists of an annular slurry region surrounded by four curved and equally spaced reflector units. Each reflector unit consists of a polished metal reflector surface containing of two 15W UVA lamps. Each pair of lamps can be independently turned "on" or "off", generating different absorption fields within the annular region. Irradiance measurements were obtained at different axial and angular locations and for different external irradiance conditions and photocatalyst loadings. Experimental irradiance data was compared to Monte Carlo (MC) simulations accounting for: a) Lambertian emission at the lamp surface, b) specular and ideally diffuse reflection, refraction and absorption at all interfaces and c) wavelength specific absorption and scattering coefficients. This MC model includes a Henyey-Greenstein(H-G) phase function with a "g" scattering parameter of 0.68. This H-G phase function obtained in section 4.5 (Valades et al., 2014b), using symmetric irradiance and a smaller scale annular reactor unit. This fully predictive model shows good agreement with experimental irradiance data in an ample range of conditions studied for a non-symmetrically irradiated unit. It is thus concluded, that the proposed MC approach as implemented in 3.3.2 (Valades et al., 2014b), is a

reliable predictive tool to scale-up externally and unevenly irradiated photoreactors, as is the case in solar irradiated units.

## 5.2 Introduction

Given the developments shown in Chapter 3 and Chapter 4, it can be stated that MC is a reliable tool for photocatalytic reactor modeling. However, endorsing MC method as a modeling tool does not necessarily validate it for scale-up purposes, which, as stated in Chapter 2, is of great importance for photocatalytic reaction engineering. Thus, stage iii), in section 1.1 is still to be accomplished, as there are still important questions that need to be addressed, such as: a) Could an irradiance model such as the one established in section 3.3.2 (Valades-Pelayo et al. 2014a) be extended to photoreactors of larger scale and external-asymmetric irradiance?, b) Could model parameters presented in section 4.5 (Valades-Pelayo et al. 2014b) be used in scaled-up reactors utilizing a fully predictive modeling approach?.

In order to address these important issues, the present chapter, considers a Monte Carlo (MC) model with no adjustable parameters. The MC method accounts for: 1) a Lambertian-surface emission model at the lamp, 2) Specular and ideally diffuse reflection, refraction and absorption at all interfaces, 3) Wavelength specific absorption and scattering coefficients and 4) a Henyey-Greenstein (H-G) phase function describing the scattering phenomena. Results of this model are compared with irradiance measurements developed for different outer irradiance conditions. Results show good agreement between predicted and experimental data for photocatalyst concentrations from 20 mg l<sup>-1</sup> to 400 mg l<sup>-1</sup>.

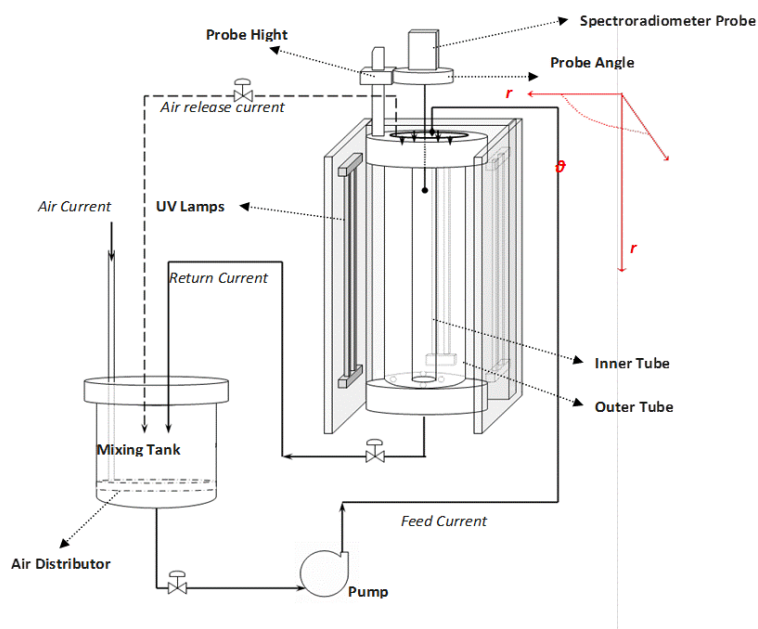
Thus, the proposed MC model is able to accurately predict local photon absorption rates in scaled-up reactors with asymmetric irradiation. This is the first study, as far we are aware of, where a MC method is established as a reliable scale-up tool, with no adjustable parameters for this type of photoreactor system. This approach is successfully used for the scale-up of slurry annular photocatalytic reactors, from the bench scale.

## 5.3 Experimental Method

### 5.3.1 Reaction System Set-Up

In the present study, an externally-irradiated Solar Simulator Photo-CREC Water Photoreactor with 9.8 L of irradiated volume and a 24 L total capacity, is used. This photo reactor consists of an annular slurry region bounded by two pieces of cylindrical quartz glass. The annular section is encircled by four equally spaced reflector units. Each reflector unit consists of a polished metal reflector containing two 15 W UVA lamps. The reflectors can be independently turned off, which allows generating different absorption fields within the annular region. Additional information regarding this unit is provided in the upcoming section of this manuscript.

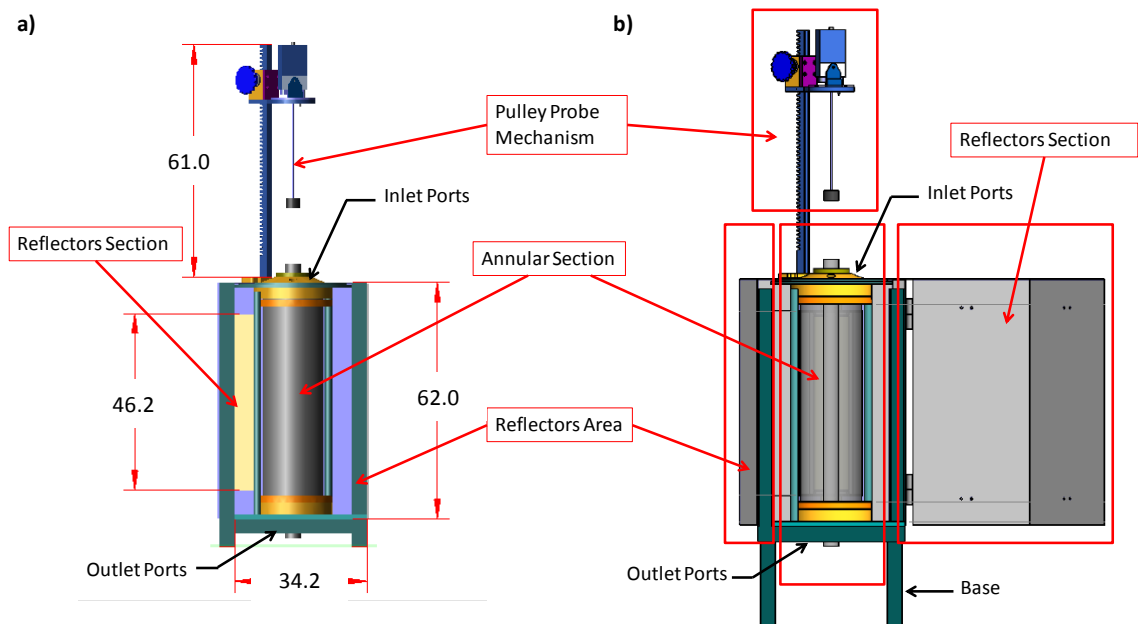
The photocatalytic reactor system with accessories are reported in Figure 5.1. The entire set-up consists of the following: (a) a Solar Simulator Photo-CREC Water Unit, (b) a 20 L mixing tank, (c) a port where the photocatalyst is added, and (d) a pump able to recirculate the slurry at up to  $16 \text{ l min}^{-1}$ . The photo reactor unit has four inlets and two outlets at the top and bottom, respectively. A ventilation system to maintain the UV lamp temperature controlled is attached to the reactor doors, as shown in Figure 5.1.



**Figure 5.1** Schematic Representation of the Solar Simulator Photo-CREC Water Reactor

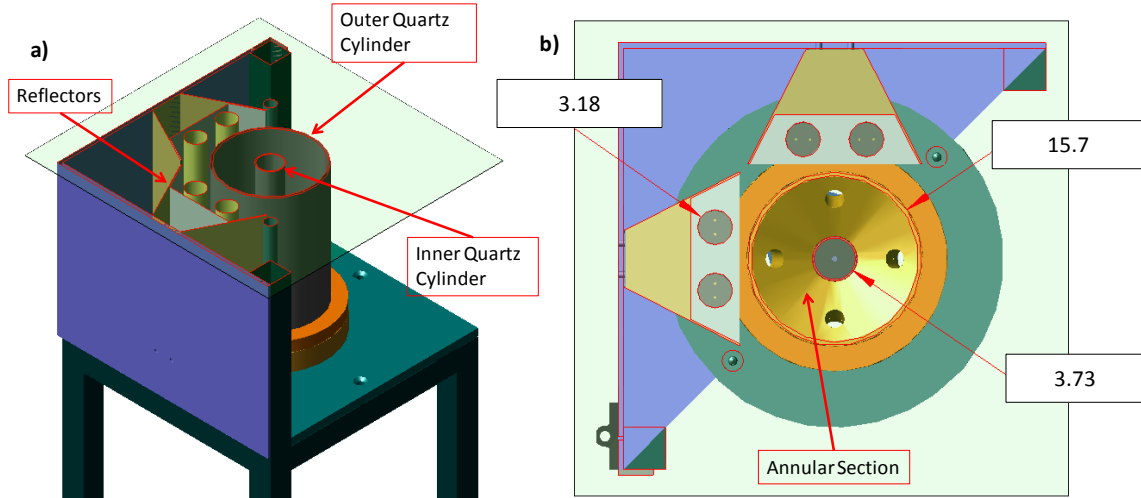


As reported in Figure 5.2, the Solar Simulator Photo-CREC Water Photoreactor unit consists of 1) an annular section where the slurry flows downwards, 2) a reflector section containing reflectors housing 8 lamps and 3) a pulley mechanism designed to introduce a probe along the central axis of the annular section at carefully controlled heights and angles. Figure 5.2, describes a side view of the reactor showing details of the reflectors mounted on reactor doors, surrounding the slurry annular section. Figure 5.2 also shows the pulley mechanism located at the reactor top section.



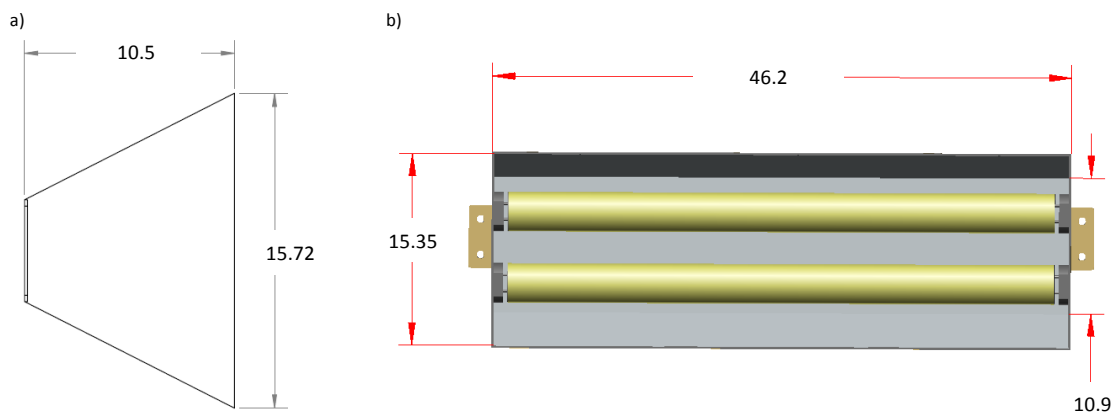
**Figure 5.2** Representation of the Photoreactor Inner (a)Front and (b) Side View with Dimensions in cm, Highlighting: 1) Annular Section, 2) Reflector Section and 3) Pulley Probe Mechanism.

Figure 5.3a shows the reactor annular section, formed by two ~3 mm thick concentric quartz glass cylinders. The outer and inner quartz cylinders are 16 cm and 3 cm in diameter, respectively. The annular section is 48 cm long. The reflector section consists of four reflectors placed around the annular section. They are arranged at 90 degrees from each other. Figure 5.3a and Figure 5.3b also show a top and isometric sectioned view describing the relative position between the reflectors and the annular section.



**Figure 5.3** Sectioned a) Isometric and b) Top view. Inner and Outer Diameter of the Annular Section as well as its Relative Position to Two of the Four Reflectors, are shown. Dimensions shown in Centimeters.

Each reflector has a 46.2 cm length and 15.7 cm width. Each reflector houses two near UV lamps. Other reflector dimensions are also shown in Figure 5.4 for both (a) side and (b) front views. The eight lamps used in the Solar Simulator Photo-CREC Water unit are 15 W, have a 1.33-cm radius, a 41.3-cm length, and are black-light UV lamps.



**Figure 5.4** Reflector Schematics of Two Lamps and their relative location within the Reflector. The a) Side View and b) Front View. Dimensions reported in centimeters.

Regarding experimental irradiance measurements, they were obtained by using a StellarNet EPP2000C-25 LT16 Spectrometer. The spectrometer is attached to an optical fiber cable, connected to a polished quartz sensor. The sensor is introduced into a probe system designed to help the sensor descend through the central axis of the annular section, mounted on a disk that can rotate 360 degrees. The probe, shown in Figure 5.5, allows one to measure the radiation transmitted by the annular section at different azimuthal and axial coordinates at the reactor centerline.

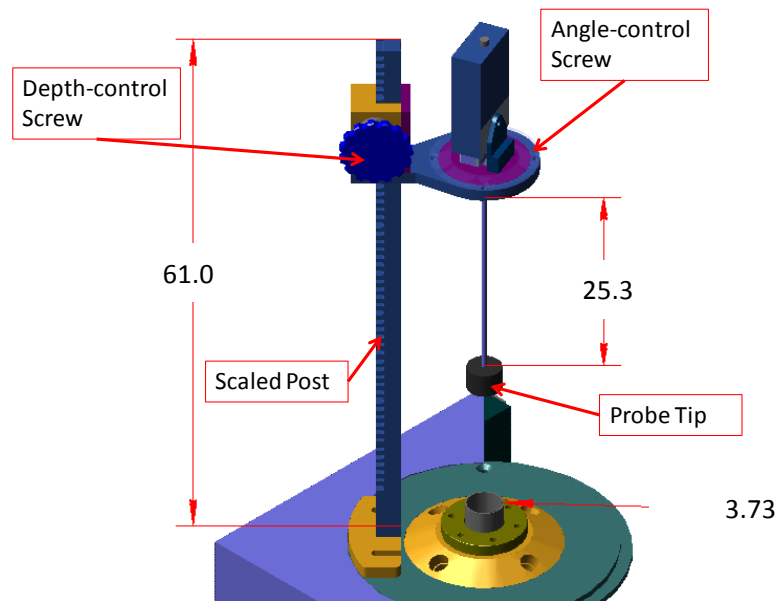


**Figure 5.5** Schematic Representation of the Photo-CREC Solar Simulator Pulley Probe System. Dimensions reported in centimeters.

### 5.3.2 Experimental procedure

To accomplish radiation measurements, the head of a spectrometric sensor is placed inside the Photo-CREC Water probe (refer to Figure 5.5). Once it is adjusted, its back-end is connected to a StellarNetEPP2000C-25LT16 Spectrometer Port. The slurry suspension is then allowed to enter the reactor from the top. During this first period, the valve located in the reactor bottom section is closed, so that the water slurry accumulates inside the annular section. While the reactor is being filled, air is being dislodged through a top vent. Once all the air is removed from the unit, the vent is hermetically sealed, thereby ensuring that no empty zones or air pockets remain.

With the reactor system filled with 20L of water, the pump and the BL lamps are then turned on. Once the lamp emission is stabilized (in about 2 minutes), the Total Transmittance is measured at different locations. To accomplish this, the probe depth and angle are varied by using a pre-calibrated screw mechanism (refer to Figure 5.5). At least four measurements are performed at every location and the average local values are then, calculated. Irradiance is measured at eight angles and five different heights. In this way, Total Transmittance (TT) profiles of the annular section are established for the azimuthal and axial directions.

The above mentioned procedure was repeated at different photocatalyst loadings. With this aim, various Degussa P25 amounts were progressively added to achieve photocatalyst concentrations of 0, 10, 20, 30, 40, 50, 70 and 90 mg $l^{-1}$ , respectively. One should notice that every time the photocatalyst concentration was changed; the photocatalytic reactor was left in operation for at least five minutes until the photocatalyst concentration was homogenized and as a result, radiation measurements were stable. All of the above mentioned steps were repeated at least four times until mean values with standard deviations below 5% were obtained.

To further validate the applicability of the proposed model, the aforementioned procedures were repeated for five different configurations of reflectors with their respective pairs of lamps turned either “on” or “off”. More specifically, this was the case when: i) four reflectors (or all the eight lamps) were “on”, ii) three reflectors were “on”, iii) two opposite reflectors were “on”, iv) two adjacent reflectors were “on” and v) one reflector was “on”.

Lastly, axial and azimuthal irradiance profiles at the reflector edges were measured using a separate reflector set-up. This set-up, which was equipped with a pair of lamps, as well, had the advantage of excluding the influence of the other neighbouring reflector units as could happen with the Photo-CREC set-up. The irradiance profiles were measured at the reflector edges having the sensor guided with a double-arm retort stand with two modified clamps. Measurements at the reflector edges were repeated at least five times at four different azimuthal and eleven different axial positions.

## 5.4 Mathematical Model

Given both the desired predictive nature of the mathematical method and the complex photo reactor/radiation source configuration involved in the present chapter, the MC method was chosen as the preferred modeling approach. In the following section, the specific simplifications and assumptions to apply the Monte Carlo (MC) method for solving the Radiative Transfer Equation (RTE), as relevant for the Photo-CRE Water Solar Simulator Photoreactor, will be explained. If a general approach is needed regarding principles, justifications and rationale behind the MC method applied to RTE solving, they can be found elsewhere in the literature.

### 5.4.1 Overview of the RTE MC method

The MC method proposed for this study is based on the fact that the reactor geometry presents periodicity with respect to the azimuthal direction. From Figure 5.6a, periodicity can be observed to be 45 degrees. By choosing boundary conditions that appropriately capture this important aspect, the complete reactor can be represented just by considering an octant of it. Placing "perfect mirrors" that reflect all photons on each side of the octant, as shown in Figure 5.6a, allows one to achieve this, both in a rigorous and less computationally intensive scheme. Once this consideration is applied, the octant under study, as reported in Figure 5.6b, is split into different regions: 1) the emission region, 2) the reflection region and 3) the scattering region.

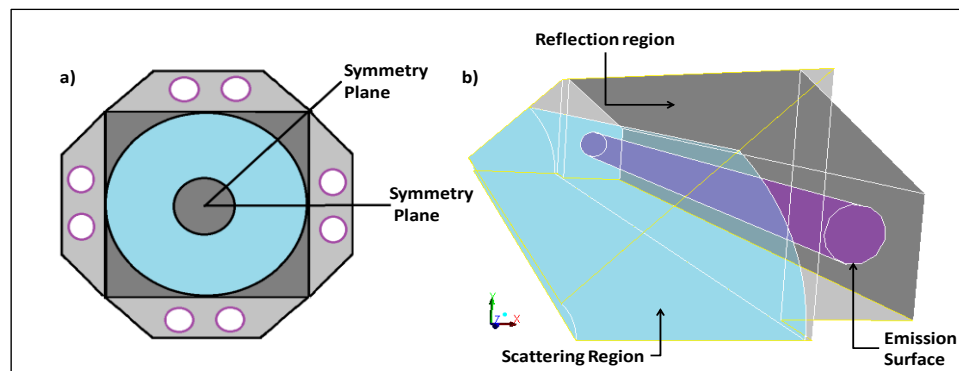


**Figure 5.6** Schematic Description of Simplified Reactor Used for MC Simulation: a) Top view and b) isometric view. Note: this schematic highlights symmetry planes and main regions, namely the scattering, emission and reflection regions.

The trajectory of the photons is followed from their initial location and direction as they evolve within the reactor and through their interactions with the reactor walls, lamps and photocatalyst particles. With this end, the following scheme is considered: 1) the reactor geometry is represented by surfaces and the photon trajectory by a parametric straight line, 2) the resulting non-linear system of equations for both geometry and photon trajectory are solved, 3) the parametric distance between the photon and each surface are, as a result, calculated, 4) the interaction between photons and surfaces is established based on the "shortest positive non-zero distance", 5) the fate of all photon-surface interactions are determined stochastically and 6) the resulting photon trajectories are then established, as a cumulative sequence of the above described steps.

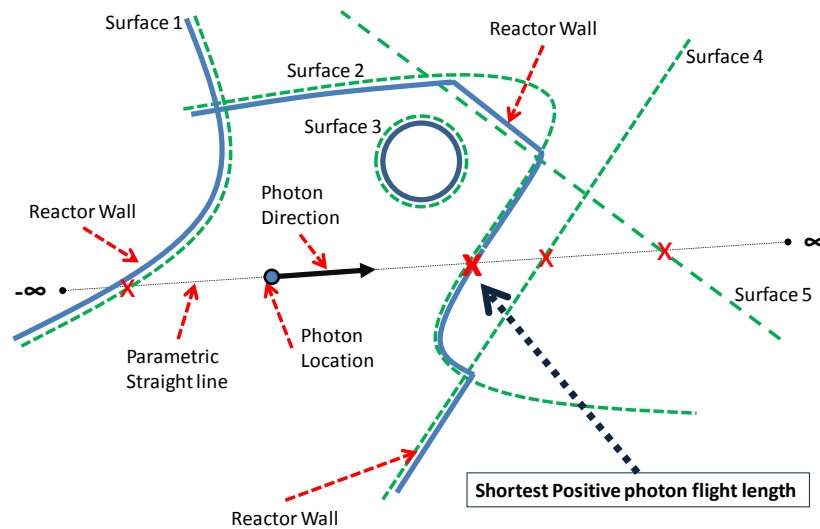


**Figure 5.7** MC representation of a photon trajectory being tracked in hypothetical 3D space. The photon trajectory is computed as a series of discrete interactions which account for both reactor geometry and photon-reactor interaction. Reactor walls are in solid blue lines. Equations are represented by dashed green lines.

Regarding photon trajectory, a parametric straight line is used to represent it, as reported in Figure 5.7. At every interaction, the parametric line equation, is determined by both the photon current location and the direction in the 3D space. Figure 5.7 illustrates a hypothetical geometry describing the approach used to calculate the photon flight-length. The blue solid-lines in Figure 5.7 represent the actual walls and the green dotted-lines

describe the model equations (or MC surfaces). To determine the location of the next photon-surface interaction, the “shortest positive non-zero photon flight-length” distance is selected. This condition, as described in Figure 5.8, is only applicable for determining the location of the photon-surface interactions in concave geometries (a geometry whose interior is concave).

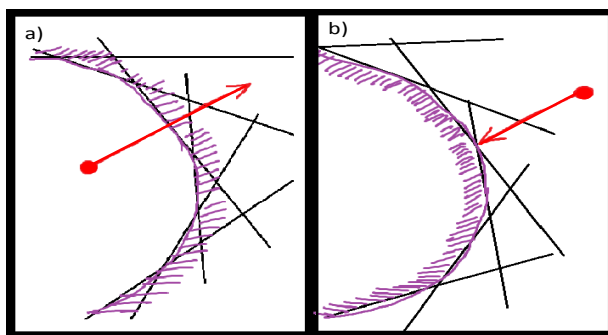


**Figure 5.8** Hypothetical walls (dashed lines) are represented by a set of equations (black solid lines). (a) Concave geometry: locus where the “shortest positive non-zero photon flight-length” condition holds true. (b) Convex Geometry: locus where the “shortest non-negative, non-zero distance condition” does not apply.

As described in Figure 5.8a, only concave geometries are considered in photon fate calculations. Let us assume that both non-concave and concave geometries coexist in a geometrical space, as is the case in the geometric space presented in Figure 5.9a (blue solid lines). Thus, the MC photon tracing can encounter both concave and non-concave angles while evolving in the photoreactor media. This would render the “shortest positive non-zero photon flight-length” non-applicable (refer to the red dotted circles in Figure 5.9a). However, the non-concave geometry can be split into concave subspaces connected by interphases, as reported in Figure 5.9b (represented by red rectangles). On this basis, the “shortest positive non-zero flight length” condition holds true only when considering surfaces within the subspaces where the photons are located.

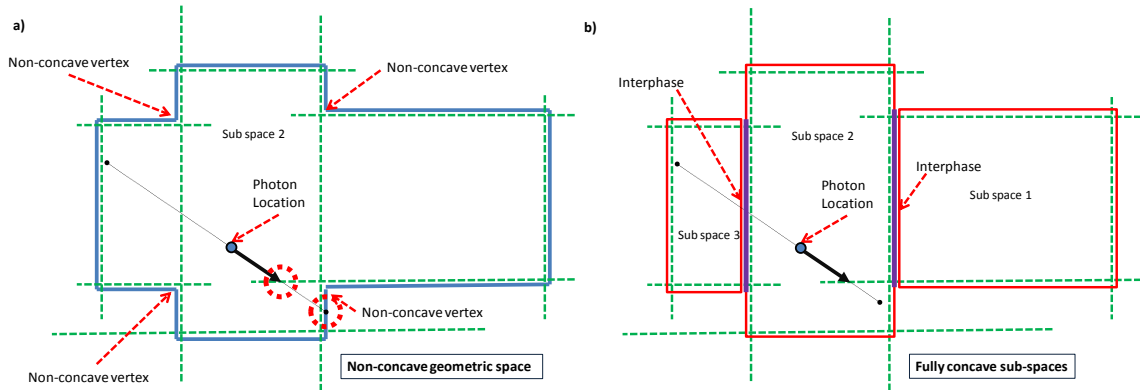


**Figure 5.9** Splitting of a geometrical space to achieve an ensemble of concave subspaces: (a) Space with coexisting non-concave and concave angles (blue solid lines), can be split into subspaces as shown in Figure 9b. (b) Subspaces that fulfill the concavity condition (red solid rectangles) are connected by "interphases" (thicker purple lines).

For instance, when applying the MC method to a geometry, such as the one found in the Solar Simulator Photo-CREC-Water Reactor (refer to Figure 5.6b), the reactor must be split into concave subspaces. More specifically, to maintain concavity, one can consider the subsections as highlighted in Figure 5.10. As shown in Figure 5.10a and Figure 5.10b, every reactor subsection is limited by an "interphase" with reactor subsections identified with numbers. One should also note that only the surfaces adjacent to or within the subsection where the photon is located, are considered for the iterative scheme proposed.

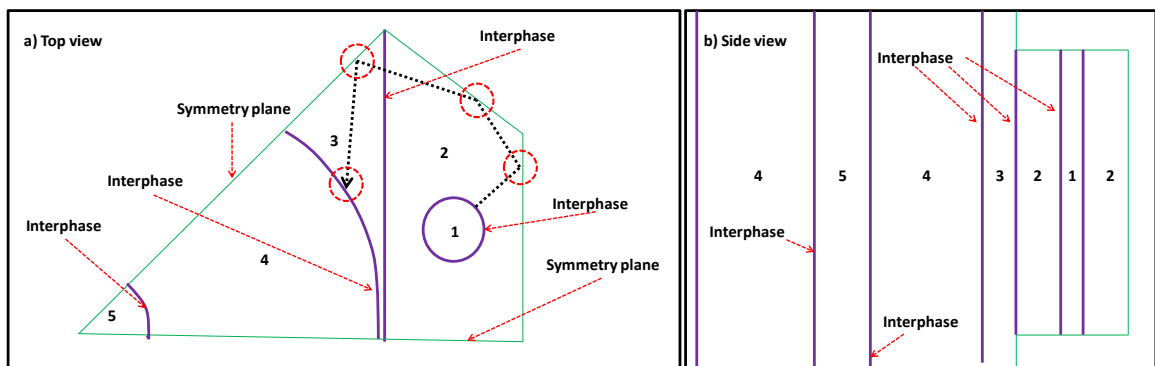


**Figure 5.10** Areas within the Solar Simulator Photo-CREC Water geometry, split to avoid convex geometries from presenting themselves. Areas split into: 1) Lamp space, 2) Reflector space, 3) Gap between reflector and reactor, 4) Annular section and 5) Inner cylinder.



As a result, once relevant subspace information regarding photon interaction is established, the outcome of this interaction has to be determined. This is done stochastically by considering the following factors: i) location of the interaction, ii) photon direction/incidence angle and iii) properties of both the reactor wall and photon wavelength. For instance, the probability of absorption at interfaces with zero transmittance is chosen according to the material absorbance properties within the lamp emission range (e.g. ~7% of absorption for polished aluminum reflectors within the 320 to 388 nm). Furthermore, the reflection angle, as reported in Figure 5.11, is based on the photon incidence angle and on a reflection mechanism at every reactor surface (i.e. diffuse or specular). On the other hand, for semi-transparent surfaces (i.e. quartz-air and quartz-water interfaces), the angle of refraction and the probability of absorption are calculated based on the incidence angle and the refraction index as determined by Snell's law.

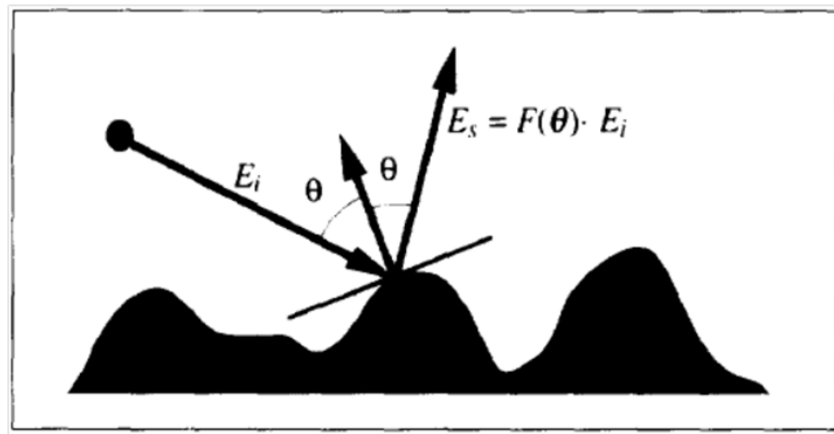


**Figure 5.11** A rough surface can be modeled by the tangent plane approximation, taken from He et al., 1991.

Additionally, in the regions where scattering takes place (refer to Figure 5.6b), a random photon flight-length is calculated based on Beer's Law, as shown in the following equation:

$$l_{cat} = -\frac{1}{(\sigma_{\lambda} + \kappa_{\lambda})} * \ln(R_n) \quad \text{Eq. 5-1}$$

where  $l_{cat}$  represents the photon flight length before a photon-photocatalyst particle interaction takes place,  $\sigma_\lambda$  and  $\kappa_\lambda$  are the wavelength specific scattering and absorption coefficients respectively, and  $R_n$  is a uniformly distributed random number between zero and one. The scattering and absorption coefficients were considered to depend on both photon wavelength and photocatalyst concentration, as proposed by [Cabrera et al. \(1996\)](#).

Based on the “smallest, positive, non-zero parametric distance” criteria depicted in Figure 7, one can determine whether or not a collision between a photocatalyst particle and a photon takes place. If the  $l_{cat}$  is larger than any other calculated parametric distance, then the photon-photocatalyst particle interaction does not occur. On the other hand, if the  $l_{cat}$  is smaller than any other calculated parametric distance, then photon-photocatalyst particle interaction takes place.

Furthermore, once the photon collides with the photocatalyst particle, it can be either absorbed or scattered. The absorption criterion (absorption probability) is proportional to the photocatalyst albedo (Puma et al. 2007), i.e. the ratio between the absorption and extinction coefficients, as described with:

$$P(a) = \frac{\kappa_\lambda}{\beta_\lambda} = \frac{\kappa_\lambda}{\sigma_\lambda + \kappa_\lambda} \quad \text{Eq. 5-2}$$

On the other hand, when a photon is scattered, the photon direction is recalculated, according to two random numbers. Each random number represents, scattering and azimuth angles, as shown in Figure 5.12. The scattering angle " $\varphi$ " is chosen from a probability density function (PDF) represented by the phase function and the azimuth angle " $\theta$ " is selected from an uniform distribution.

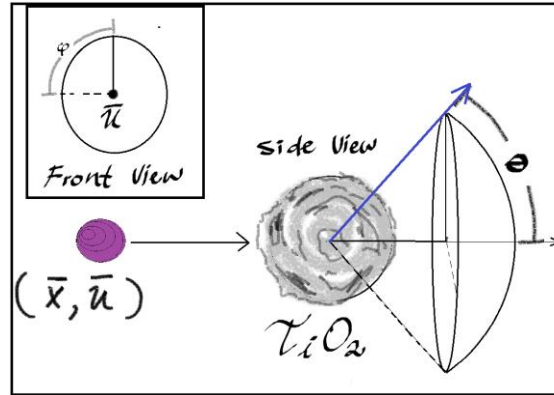


**Figure 5.12** Photon-particle interaction where direction is modified due to scattering. The scattering angle " $\theta$ " is chosen, according to the phase function and an azimuth angle " $\varphi$ " from an uniform distribution.

Finally and in the calculations of the present study, the Henyey-Greenstein (H-G) was adopted as a PDF to determine the scattering angle. The H-G phase function equation is:

$$P(\theta) = \frac{1}{2} \frac{(1 - g^2)}{(1 + g^2 - 2 \cdot g \cdot \cos \theta)^{\frac{3}{2}}} \quad \text{Eq. 5-3}$$

where  $p(\cos \varphi)$  is the probability of a photon being scattered with a given scattering angle " $\theta$ " and " $g$ " is the asymmetric parameter. The H-G phase function with a  $g$  value of 0.68 was established as being adequate for Degussa P25, as determined in section 4.5 (Valades-Pelayo et al., 2014).

#### 5.4.2 MC method subroutines

To implement the various calculations described in the previous sections, a Monte Carlo Method was considered including seven subroutines, namely: a) The photon emission calculation, b) The photon tracking in the reflector, c) The photon fate in the reflector gap, d) The photon evolution in the reactor annular section, e) The photon-sensor interaction in the inner cylindrical section subroutine, f) The absorption field generation and g) Irradiance profile calculations. Figure 5.13 describes the interconnection between subroutines and possible photon trajectory-termination outcomes. Regarding these various subroutines, their functionality and rationale will be described and detailed in the upcoming subsections.

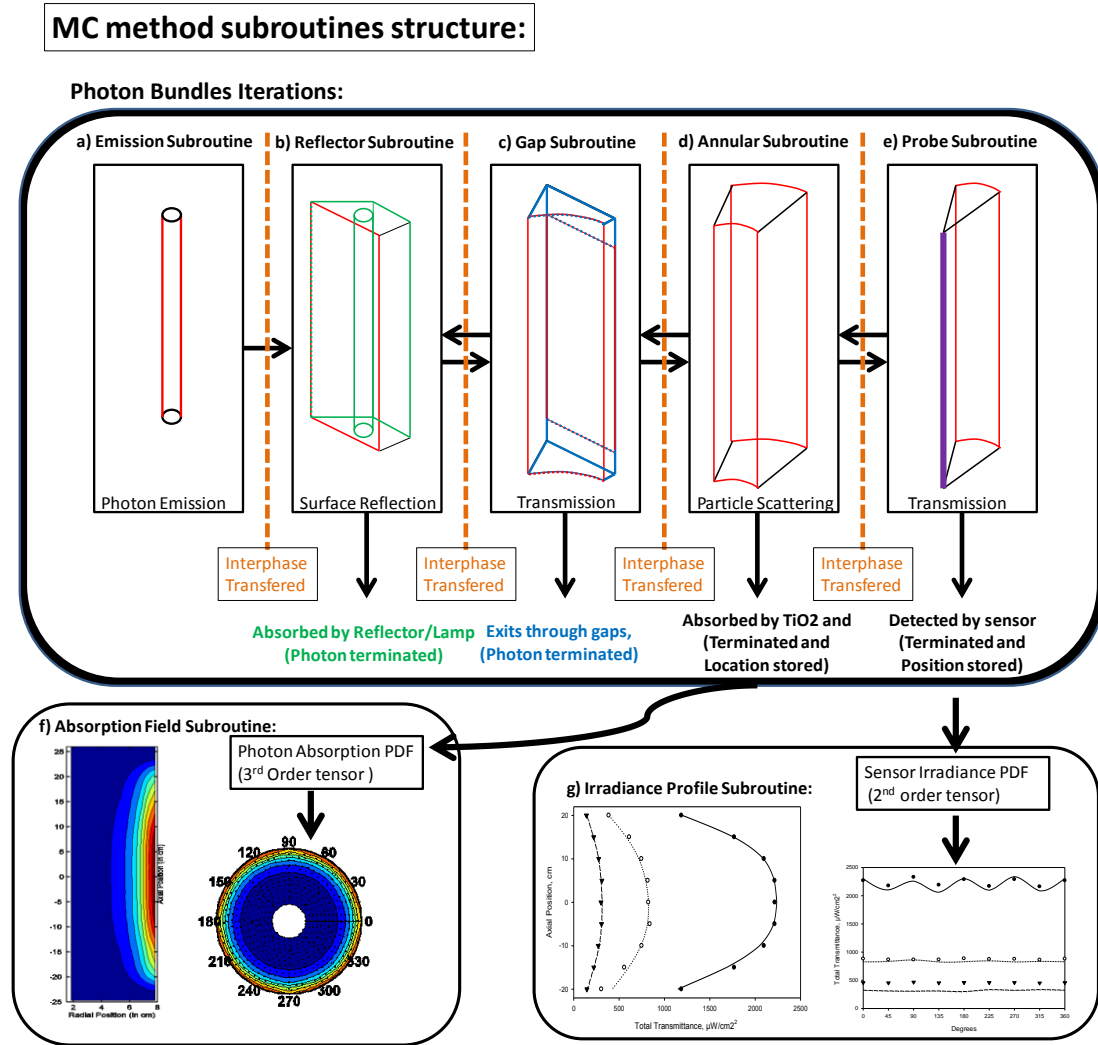


**Figure 5.13** Schematic Description of the Subroutine Structure within the MC method for the RTE in the "Solar Simulator Photo-CREC Water" photo reactor. Interphases are reported in red , planes in blue and green, symmetry planes in black and sensing surfaces in purple.

#### 5.4.2.1 Emission Subroutine

The emission calculation subroutine includes the lamp as a photon source. Within the MC method, a subroutine assigns an initial position and direction as well as a specific wavelength to every photon. With this end, a surface emission model was selected with photon emissions at the lamp surface (i.e. surface emission model). Furthermore, the following is considered: a) The axial photon emission position on the lamp surface was

chosen according to a probability density function (PDF) as in Chapter 3 (Valades-Pelayo et al., 2014a ; Tsekov et al., 1997)), b) The azimuthal position was selected according to an uniform PDF distribution, c) The photon direction of emission was considered to be Lambertian (i.e. ideally diffused with respect to the surface normal at the point of emission).

The wavelength of the emitted photon, is determined based on a random number. The outcome of this stochastic process is determined according to a PDF proportional to the lamps' emission spectra, as described in Figure 3.3 and as reported in Chapter 3 and Chapter 4 (Valades-Pelayo et al, 2014a ; Valades-Pelayo et al, 2014b).

It is worth mentioning that a variable named "octant" is created to keep track of the octant (or lamp section, as described in Figure 5.6a) in which a photon is located. This is needed in cases where there are no symmetric irradiance conditions, i.e. when certain lamps are "turned off" or alternatively when there is no symmetric irradiance in the photoreactor. This "octant" variable is stochastically chosen, with an evenly distributed probability of emission among all the lamps that are turned "on" and zero for any lamp that is "turned off".

#### 5.4.2.2 Reflector and Gap Subroutine

Following photon emission, and before the photon enters the reactor annular section, the photon crosses the reflector-gap section. To properly implement these calculations, two subroutines were developed: a) one that accounts for the surfaces within the reflector which is designated as "reflector subroutine" and b) one that accounts for the surfaces found in the gap between the reflector and the slurry annular section which is called the "gap subroutine".

A separation into two different subroutines is needed to account for a non-concave geometry, as explained in section 5.4.1 and presented in Figure 5.8. Both subroutines consider the interaction of photons and reactor surfaces, i.e. refraction, reflection and absorption. Reflection on non-transparent surfaces is assumed to be diffuse. This is due to both the nature of the reactor walls and the emitted radiation wavelengths. One should

note that in these subroutines, no particle scattering effects are included given that the media is free from  $\text{TiO}_2$  particles.

Figure 5.14 describes the reflector subroutine. This subroutine model includes irradiance-reflection phenomena on seven surfaces: (1) One totally specularly reflective virtual plane (symmetry plane), (2) Two partially reflective polished aluminum surfaces, (3) Two non-reflective planes placed at the top and bottom of the reflector, (4) One cylindrical surface (lamp) and (5) One totally transparent virtual surface delimiting the interface between the gap region and the reflector (also shown in Figure 5.15).

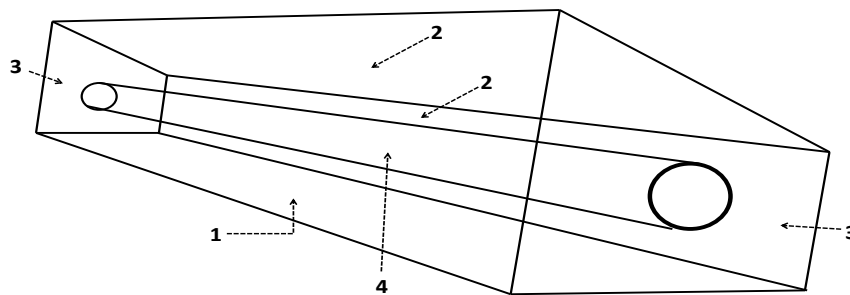


**Figure 5.14** Surfaces considered for the reflector subroutine: 1) One totally specular virtual plane (symmetry plane), 2) Two partially reflective planes, 3) Two non-reflective planes and 4) One lamp surface.

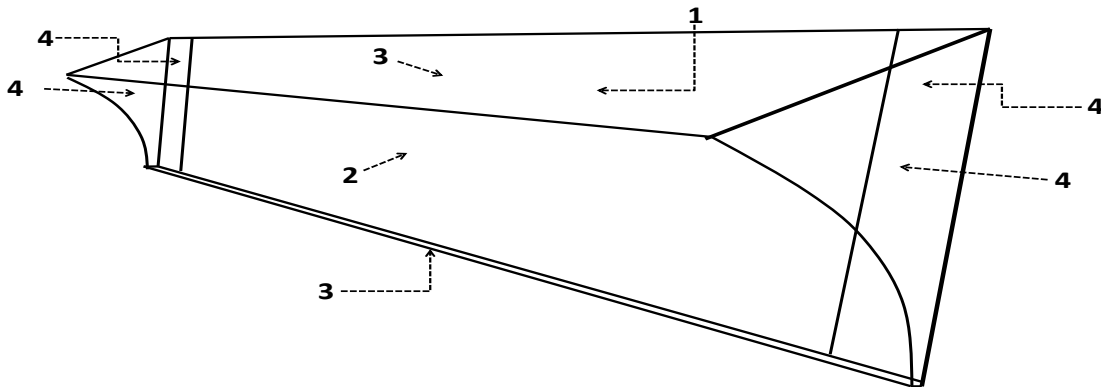


**Figure 5.15** Surfaces considered for the gap subroutine: 1) A totally transparent virtual surface delimiting the interface between the gap region and the reflector, 2) A totally transparent virtual surface delimiting the reactor gap boundary with the annular reactor section, 3) Two virtual transparent symmetry planes and 4) Four non-reflective planes.

Figure 5.15 shows the "gap subroutine" (surfaces) which also includes seven surfaces: (1) The plane surface connecting the gap region with the reflector subroutine, (2) A cylinder representing the quartz glass, limiting the annular section and accounting for absorption, reflection and refraction, (3) Two totally reflective virtual planes encompassing two symmetry planes and (4) Four non-transparent surfaces displaying total absorption of radiation, representing the gaps through which radiation can escape.

### 5.4.2.3 Annular Photoreactor Section Subroutine

Once the appropriate series of events direct the photons into the annular photo reactor section, the annular section subroutine keeps track of the photon trajectory. As presented in Figure 5.16, this subroutine, considers the relevant physical phenomena taking place inside the annular section involving photons and photocatalysts:

1. Forward scattering taking place in the annular photo reactor section,
2. Absorption by the photocatalyst particles,
3. Backscattering out of the annular region
4. Transmission through the annular section.

A variable named "Cond1" determines the "state" of the photons at the end of each iteration, whether they are terminated (Cond1=0), transmitted to a different subroutine (Cond1=3 and Cond1=1) or keep being scattered within the annular section (Cond1=2).

For a more detailed description regarding the scattering/absorption phenomena, one must refer to Chapter 3 (Valades-Pelayo et al, 2014a). Additionally, an in depth explanation of the Henyey-Greenstein phase function can be found in Moreira et al 2011. Further details, regarding RTE numerical solution using Monte Carlo for slurry photoreactors, are found in Pasqualli et al. 1996.

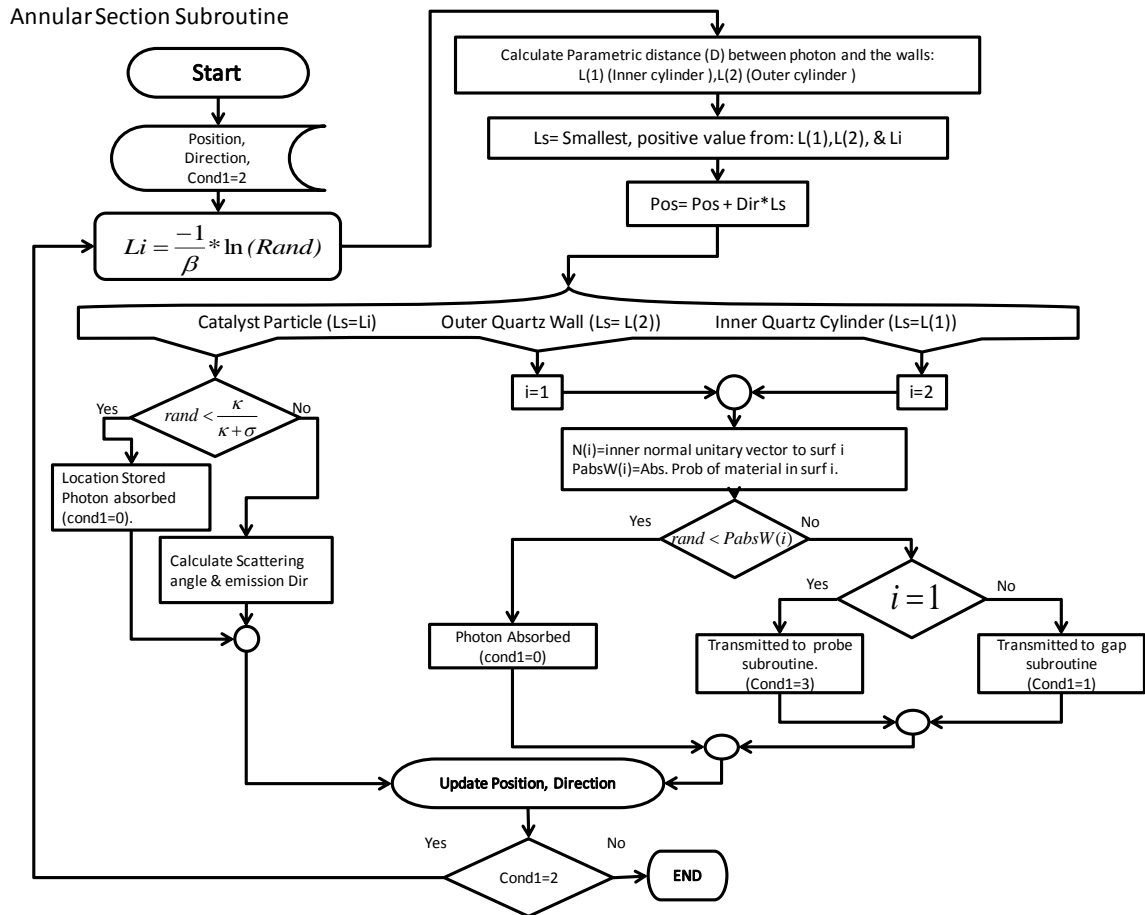


**Figure 5.16** Algorithm of the Annular Photo Reactor Section Subroutine, within the MC Simulation, Used to Model the Reaction Media. The schematic algorithm was adapted from Chapter 3 (Valades-Pelayo et al. 2014a). Note: "Cond1" establishes photon state after iteration. Cond1=0, means that photon trajectory is terminated by  $\text{TiO}_2$  absorption.

#### 5.4.2.4 Sensor Irradiance Subroutine

Once the photons are transmitted/forward-scattered through the slurry annular section, the MC method keeps track of the photons, determining whether the photons' "flight" ends at the reactor inner annulus, is back-scattered or transmitted to the slurry or if they interact with the Solar Simulator Photo-CREC Water sensor-probe. Refraction, absorption or reflection are also considered for all photons reaching the inner annulus. Once a photon interacts with the probe-sensor, its position (axial location and probe angle) is stored.



### 5.4.2.5 Absorption field and Irradiance Profiles Subroutine

Once all the photon bundles are followed and their fates determined, the location and wavelength of every photon is stored. On this basis, the Absorption Field Subroutine and the Irradiance Profile Subroutine are algorithms employed to "group" photons by location and add up their respective energies. This is done to determine the probability of energy absorption at every location. In this manner, PDFs for i) photon absorption within the annular section and ii) sensor irradiance profiles, are calculated.

As PDFs are available for photon absorption within the annular section, the absorbed energy per unit volume per unit time or LVREA is approximated by using the following:

$$LVREA = \lim_{\Delta Z \rightarrow 0, \Delta \theta \rightarrow 0, \Delta r \rightarrow 0} \frac{\dot{N}_{t e} * \int_{\theta}^{\theta+\Delta\theta} \int_r^{r+\Delta r} \int_z^{z+\Delta z} P_a(\rho, \theta, z) \rho dz d\rho d\theta}{\Delta Z * ((r + \Delta r)^2 - r^2) * (\Delta \theta / 2)} \quad \text{Eq. 5-4}$$

where  $\rho$ ,  $\theta$  and  $z$  are the radial, azimuthal and axial coordinates respectively;  $\dot{N}_{t e}$  are the total emitted photons per second (from all lamps);  $P_a$ , is the photon absorption PDF obtained by the MC method; and  $\Delta r$ ,  $\Delta \theta$  and  $\Delta Z$  delimit the volume delta where the LVREA is to be approximated by a locally averaged value.

In the present study, the reaction annular section was split into 27, 52 and 80 subsections for the radial, axial and azimuthal directions, respectively. In a similar way, the photon irradiance along the reactor central axis, can be calculated by using the sensor area. This procedure is further explained in chapter 4 ([Valades-Pelayo et al., 2014b](#)). For a rigorous definition of LVREA and its role regarding photocatalytic reaction engineering, refer to [Cassano and Alfano, 2000](#).

## 5.5 Results and Discussion

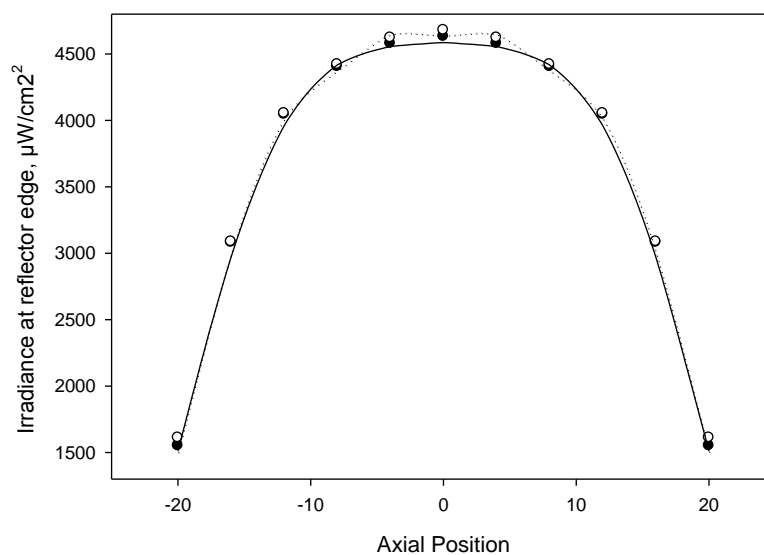
The present study imparts a predictive MC RTE model in a Photo-CREC Reactor, as a potential scale-up tool, relevant in the context of solar slurry photocatalytic reactor modeling. In order to show its applicability, special consideration is given to the irradiance field for LVREA prediction. This is done by calculating irradiance profiles at

different properly considered photo reactor locations, photocatalyst concentrations and irradiance conditions.

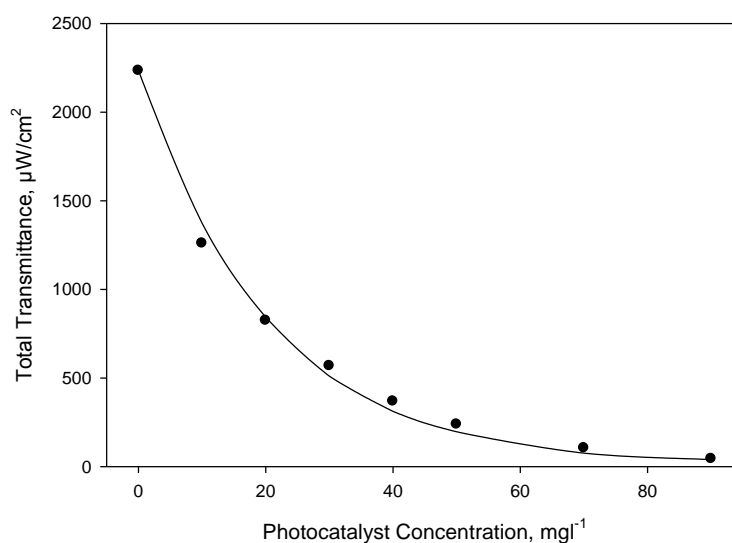
In addition, the irradiance-based model validation is accomplished by using the following strategies: i) A determination of the irradiance profiles at the reflector edges, to ensure an accurate estimation of the radiation entering the photo reactor annular section, ii) A prediction of the axial, azimuthal and photocatalyst dependence on the experimental sensor irradiance within the inner annulus (refer to Figure 5.5). This is done with all four pairs of lamps turned “on”. Furthermore and to complement this validation analysis, calculations of the azimuthal irradiance profiles of the transmitted radiation are developed for four additional lamp configurations, where the following lamps within each reflector were turned on: a) three, b) two opposite, c) two adjacent and d) one.

Figure 5.17 reports a comparison of experimental and simulated irradiance profiles at the reflector/lamp system edges (singular or plural). The sensor head detecting the surface is set facing the reflectors in all cases. Profiles shown describe measurements at 11 axial positions and four different azimuthal positions: -4, -2, 2 and 4 cm away from the reflector center plane and located half-way between adjacent lamps. Figure 5.17 reports very good agreement between experimental and simulation results at all the measured axial and azimuthal positions.

Figure 5.18 describes the Total Transmittance dependence with photocatalyst concentration when having the four reflectors “on”. The reported irradiances are the values measured by the sensor facing the reflectors (space between lamps), at the central axial position ( $z=0$ , as shown in Figure 5.19). Four measurements were taken (one facing each reflector) and then averaged. This process was repeated for various photocatalyst concentrations of 0, 10, 20, 30, 40, 50, 70 and 90  $\text{mg l}^{-1}$ . It can be observed in Figure 5.18 that the 2,200  $\mu\text{W/cm}^2$  irradiance for water (free of  $\text{TiO}_2$ ), drops to about one half at  $\sim 15 \text{ mg l}^{-1}$ , to reach almost zero at 90  $\text{mg l}^{-1}$ . Simulation results, represented by the solid line, are found to predict reasonably well the experimental data, within a 10% error band.



**Figure 5.17** Axial irradiance profiles in  $\mu\text{W}/\text{cm}^2$  at the reflector edges, ( $\bullet$ ) -2/2 cm and ( $\circ$ ) -4/4 cm away from the reflector center plane (located between the two lamps) and simulation results for (—) -2 ,2 cm and ( $\bullet\bullet\bullet$ ) -4, 4 cm.



**Figure 5.18** Changes of Total Transmittance in  $\mu\text{W}/\text{cm}^2$  with the photocatalyst concentration as measured within the central annulus, at the central axial position, from zero to 90  $\text{mg}/\text{l}^{-1}$  photocatalyst concentration. Codes: ( $\bullet$ ) Experimental Data and (—) Simulated Results.

Furthermore, Figure 5.19 describes the axial irradiance profiles for photocatalyst concentrations of zero, 20 and 40 mg $l^{-1}$ , when the four reflectors are “on”. Experimental irradiance profiles tend to be close to flat for axial positions in the  $\pm 10$  cm range, dropping to about one half when they are 20 cm away from the central axial position ( $z=0$ ). Magnitude changes for different photocatalyst concentrations are observed to be proportional to the values reported in Figure 5.18. Moreover, in Figure 5.18, simulation results are seen to again exhibit tendencies close to the ones observed in the experimental data.

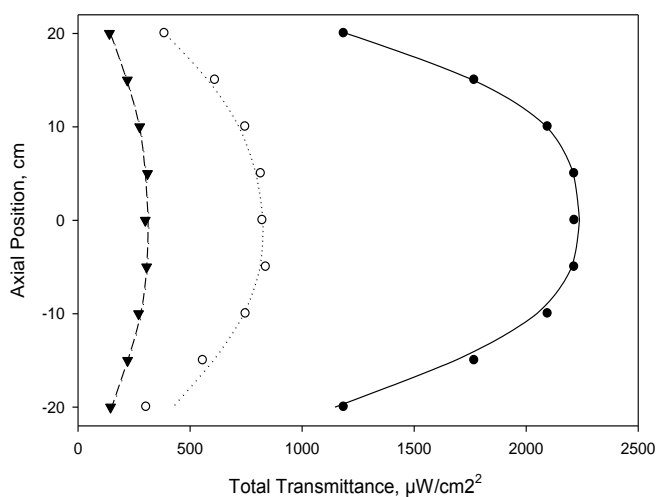


**Figure 5.19** Changes in Total Transmittance in  $\mu W/cm^2$  as measured within the central annulus, at different axial positions, in cm. Experimental data for (•) zero, (o) 20 and (▲) 40 mg $l^{-1}$ , as well as simulations for (—) zero, (•••) 20 and (---) 40 mg $l^{-1}$  are presented.

Figure 5.20 describes the irradiance azimuthal profiles within the inner annulus of the Solar Simulator Photo-CREC Water reactor, for photocatalyst concentrations of zero, 20 and 40 mg $l^{-1}$  with all four reflectors kept “on” (8 lamps turned on). One can notice that experimental irradiance profiles are seen to display an oscillatory behavior with a periodicity of 90 degrees. This oscillatory behavior tends to be dampened as photocatalyst concentration increases.

One can also notice that this reduction in Total Transmittance decreases proportionally to the photocatalyst concentration and up to a one order of magnitude (also reported in Figure 5.18). Model predictions are found to represent experimental values reasonably well. For instance, in Figure 5.20, the deviations in Total Transmittance between experimental and simulated profiles at  $40 \text{ mg l}^{-1}$ , are a maximum of 20%. As far as we are aware of, oscillatory irradiance predictions and measurements with these features have not been reported in the literature for this kind of photo reactor and scale.

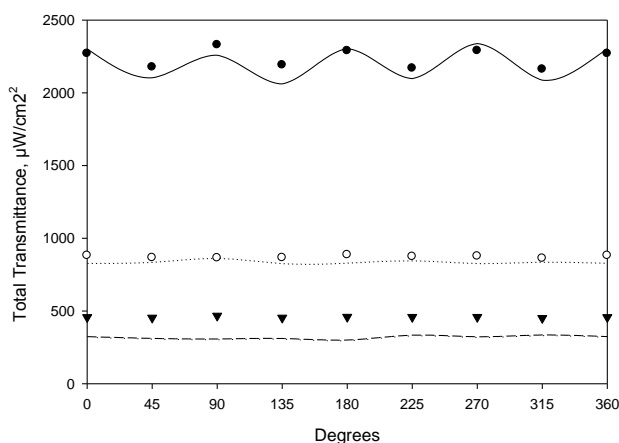


**Figure 5.20** Total transmittance ( $\mu\text{W}/\text{cm}^2$ ), as measured within the central annulus, at different azimuthal values (degrees), with all four reflectors on. Experimental data for (●) zero, (○) 20 and (▲)  $40 \text{ mg l}^{-1}$ , as well as simulations for (—) zero, (••) 20 and (---)  $40 \text{ mg l}^{-1}$  are presented.

In spite of this thorough analysis of the MC method having four reflectors (8 lamps) “on”, it was one of the goals of the present study to extend the MC model validation to other highly relevant cases, such as solar energy irradiance in photo reactors. One should expect, in these situations, non-homogenous and non-symmetric irradiation of the photocatalytic reactor system. To address these issues, irradiation conditions were changed in the Solar Simulator Photo-CREC Water Reactor. This was accomplished by turning “off” some of the reflectors and keeping others “on”, in order to create different irradiance patterns.

Figure 5.21 reports the irradiance angular profiles, for photocatalyst concentrations of zero, 20 and 40  $\text{mg l}^{-1}$ , under different irradiance conditions, in namely: i) Figure 5.21a which has three reflectors “on”, ii) Figure 5.21b which has two opposite reflectors “on”, iii) Figure 5.21c which has two adjacent reflectors and iv) Figure 5.21d which has one reflector “on”.

As in the case of four reflectors “on”, dampening effects in the oscillations were observed as photocatalyst concentration increased, namely for (•••) 20 and (---) 40  $\text{mg l}^{-1}$ . This scattering effect observed is mainly due to the high albedo of Degussa P25 (Li Puma,2005). As reported in Figure 5.21a-d, the sensor irradiance (transmittance) displayed a consistent change in periodicity with respect to the angular coordinates.

One can also observe in Figure 5.21a-d that experimental and simulated irradiance profiles both in terms of irradiance oscillatory behavior and magnitude were found to agree in all cases when the photocatalyst was loaded in the unit. The only exception is the case of the photocatalyst free of water, shown with solid lines (—) in Figure 5.21.

It is worth noting that in some regions of these profiles, the calculated irradiance tends to underpredict the experimental data. Model underprediction is noticeable for angular positions where the detector is facing a reflector whose lamps are “off”. One can notice, however, that when small amounts of photocatalyst are added ( $\sim 20 \text{ mg l}^{-1}$ ), simulated and experimental irradiance distributions agree well in all cases and for the entire range of angular positions.

On the basis of the information provided in Figure 5.21a-d, one can see that the RTE MC method provides a good representation of all conditions when the Solar Simulator Photo-CREC Water unit is loaded with a photocatalyst. As stated above, one should notice that for cases when the sensor is facing reflectors turned "off", model deviations increase as photocatalyst loading tends to decrease to zero. Main reasons for these findings are related to the reflector surface reflection model, specifically that: i) the average reflector-photon interactions per photon increase exponentially as photocatalyst concentration decreases, ii) the reflectance model used by MC present accuracy issues for large numbers of reflector-photon interactions per photon.

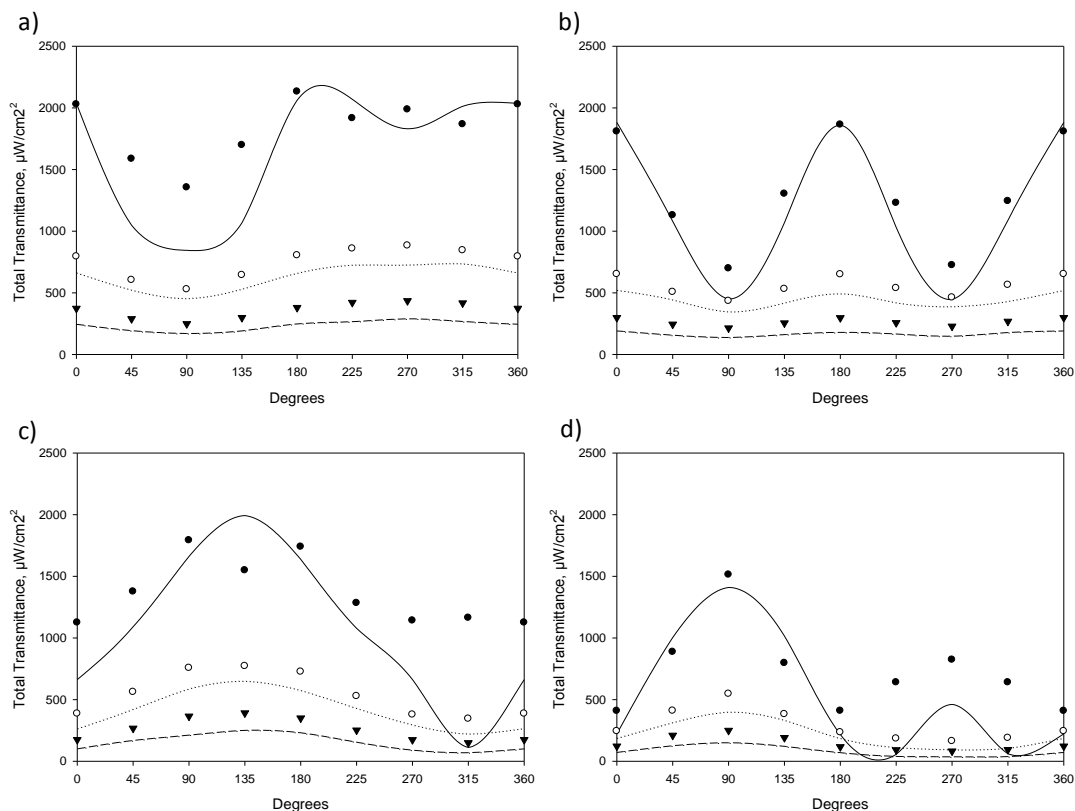


**Figure 5.21** TT ( $\mu\text{W}/\text{cm}^2$ ), as measured within the central annulus, at different azimuthal values (degrees), for the following reflectors on: a) three, b) two opposite, c) two adjacent, and d) one. Experimental: ( $\bullet$ ) zero, ( $\circ$ ) 20 and ( $\blacktriangle$ ) 40  $\text{mg}/\text{l}^{-1}$ . Simulations: (—) zero, ( $\bullet\bullet$ ) 20 and (---) 40  $\text{mg}/\text{l}^{-1}$ .

Based on the above information, the accurate determination of the irradiance field, at low photocatalyst concentrations ( $< 20 \text{ mg}/\text{l}^{-1}$ ), for all lamp set-ups, requires the independent experimental validation of a physically based BDRF (Bidirectional Reflectance Distribution Function) specifically for the UVA range. This, however, is an active field of research (Berger et al., 2012; Hyde et al., 2009; Colbert et al., 2006) and completely out of the scope of the present manuscript.

Furthermore and focusing on the use of irradiance profiles, as a mean for LVREA determination, it is important to point out that LVREA errors are expected to be proportional to the difference between the entering and transmitted radiation (Valades-Pelayo et al., 2014b). Thus, given the magnitude of the irradiance entering the annular

section ( $\sim 4,500 \mu\text{W}/\text{cm}^2$ ), the accurate determination of the radiation entering the reactor (refer to Figure 5.17) and the magnitude and deviations of the transmitted irradiance, the LVREA percentual errors are expected to be, on average, smaller than 5%, as reported in Table 5.1.

**Table 5.1.** Calculated average and maximum percentual errors for LVREA (%), for the reported lamp configurations and photocatalyst concentrations ( $\text{mg}/\text{l}^{-1}$ ), at the reactor midsection ( $z=0$ ).

Lamp Config.:	Four "On"		Three "On"		Two opposite "On"		Two adjacent "On"		One "On"		
	$C_{\text{cat}}$	average	max	average	max	average	max	average	max	average	max
0.0		2.7	5.6	7.9	20.2	4.3	7.3	12.5	31.5	7.4	15.1
20.0		0.9	1.5	2.5	3.3	2.8	4.0	3.1	4.4	1.8	3.7
40.0		3.4	4.0	2.8	4.1	2.2	2.8	2.4	3.7	1.4	2.4
<b>Average</b>		2.4		4.4		3.1		6		3.5	

In the worst-case scenario, shown in Figure 5.21c and , at an angular position of 315 degrees and a central axial position ( $z=0$ ), when photocatalyst concentration tends to decrease to zero (—), the expected LVREA error is 31.5%.

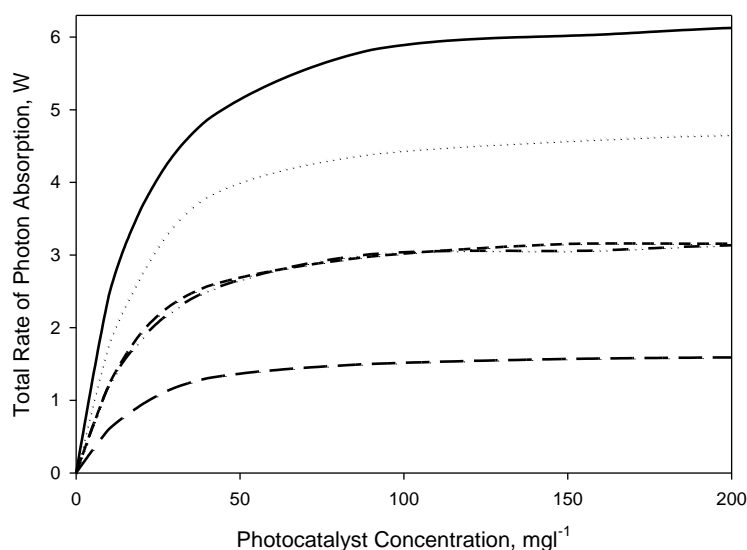


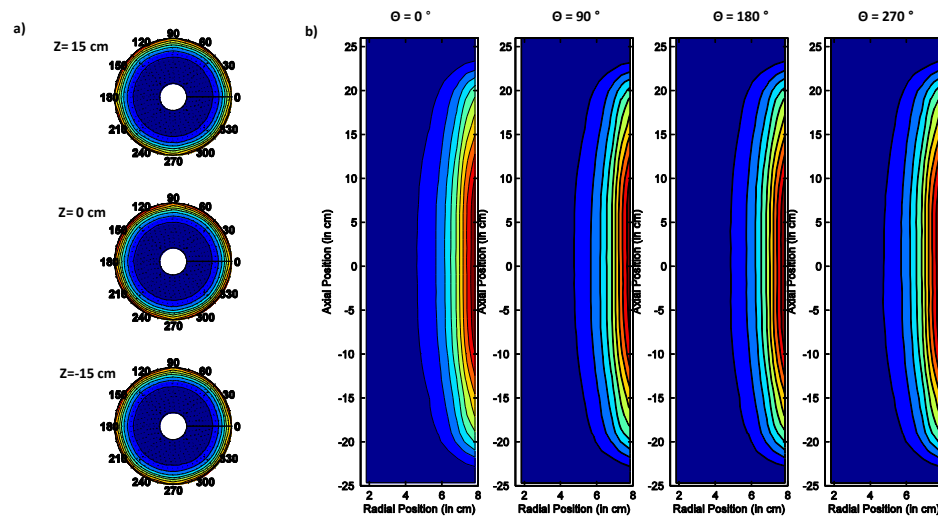
**Figure 5.22.** The Total Rate of Photon Absorption (TRPA) is calculated for photocatalyst concentrations ranging from zero to  $200 \text{ mg}/\text{l}^{-1}$ , for (—) four, (•••) three, (- -) two



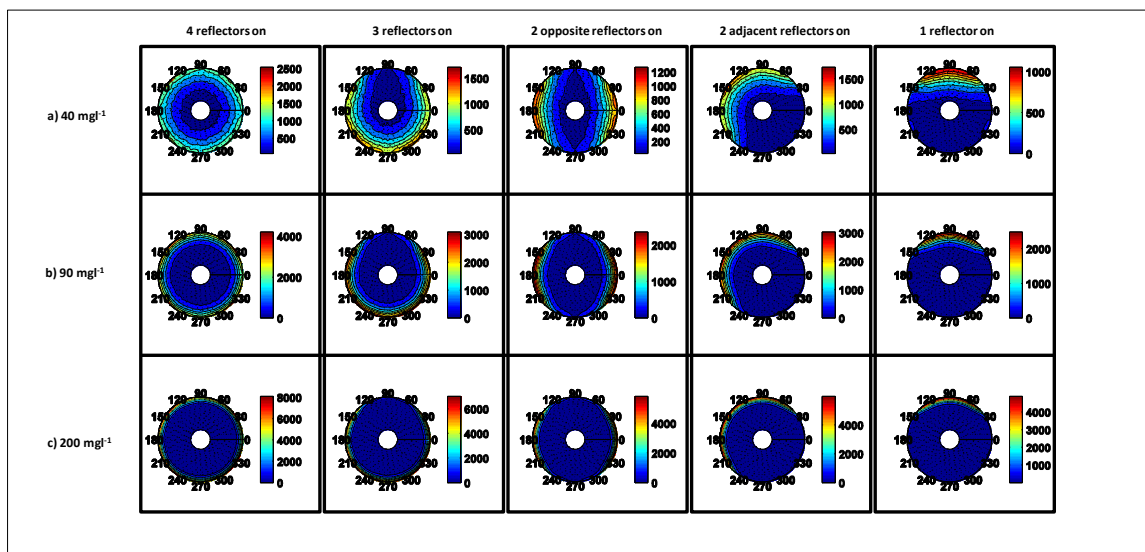
adjacent, (-.-) two opposite and (— —) one reflector "on". The optimum photocatalyst concentration is found, for all cases, to be close to  $91 \text{ mg l}^{-1}$ .

Figure 5.22 describes the TRPA (Total Rate of Photon Absorption) from zero to  $200 \text{ mg l}^{-1}$ , for all 5 different lamp set-ups. One can see, on this basis, that there is an optimum TRPA, in all cases, for a  $91 \text{ mg l}^{-1}$  photocatalyst loading (95% of the maximum TRPA).

Figure 5.23 shows the LVREA, in  $\mu\text{W}/\text{cm}^3$ , for all four lamps, having the optimum  $91 \text{ mg l}^{-1}$  photocatalyst loading. Figure 5.23a, reports LVREA for three sections at a constant axial position and Figure 5.23b, describes LVREA at four constant angular sections. Specifically, sections are located at  $Z=0 \text{ cm}$  (mid height),  $Z=15 \text{ cm}$  above the midsection level and  $Z=-15 \text{ cm}$  below the midsection level. Angular positions reported are  $\theta = 0, 90, 180,$  and  $270$  degrees.



**Figure 5.23.** LVREA profiles, for a  $91 \text{ mg l}^{-1}$  photocatalyst concentration and 4 reflectors "on", in  $\mu\text{W}/\text{cm}^3$ , at a) constant axial positions for  $Z = 15, 0$  and  $-15 \text{ cm}$ , and at b) constant azimuth for zero,  $90, 180$  and  $270$  degrees. Energy absorption ranges from  $4000 \mu\text{W}/\text{cm}^3$  to zero. Each contour represents a 10% drop.



**Figure 5.24.** LVREA profiles at constant axial position, for a) 40, b) 90 and c) 200  $\text{mg l}^{-1}$  photocatalyst concentrations and all reflector combinations, in  $\mu\text{W/cm}^3$ . Each contour represents a 10% drop with respect to the scale presented to the right of each contour plot.

As a result of the described analysis, the present chapter validates the optical parameters obtained by [Cabrera et al., 1994](#) and in section 4.5 ([Valades-Pelayo 2014b](#)), for scaling-up slurry photo reactors using Degussa P25 with both symmetric and asymmetric irradiation. On the other hand, validation of a predictive MC model, for a wide range of photocatalysts and irradiance configurations of interest is also demonstrated. As a result, the approach reported in the present paper, provides significant confidence on the ability of extending the MC method of this study, to the scale-up of Photo-CREC configurations under solar irradiation, where non-symmetric angular distribution of irradiance is expected.

On this basis, the use of the MC method can be considered of prime importance for the future of photocatalytic reaction engineering and for the development of scale-up procedures for slurry photocatalytic reactors irradiated with solar energy.

## 5.6 Conclusions

- The radiation and absorption field of a 24 L scale externally irradiated Solar Simulator Photo-CREC Water Photo Reactor is successfully modeled for different asymmetric irradiance conditions by using a RTE MC method adapted from Valades-Pelayo et al. 2014a.
- The RTE MC method is optimized by i) taking advantage of angular periodicity, ii) splitting the reactor geometry into “concave” subsets and iii) employing a "shortest-positive distance" criteria.
- The established predictive MC method includes an "a priori" approach for various photon-surface and photon-photocatalyst interactions with optical parameters previously determined by Valades-Pelayo et al. 2014b and Cabrera et al. 1995, for smaller scale photo reactor units.
- The reported irradiance predictive approach for the Solar Simulator Photo-CREC Water is proven to be adequate for different lamp configurations with various lamps being turned "on" and various photocatalyst concentrations.
- The reported MC model allows predicting the Total Rate of Photon Absorption and LVREA in all studied cases; including five different irradiance configurations and photocatalyst loadings ranging from 20 to 200 mgL<sup>-1</sup>.

## 5.7 References

Ahmed, S., Rasul, M., Martens, W., Brown, R., & Hashib, M. (2011). Advances in Heterogeneous Photocatalytic Degradation of Phenols and Dyes in Wastewaters: A Review. *Water Air and Soil Pollution* , 215, 3-29.

Ahmed, S., Rasul, M., Martens, W., Brown, R., & Hashib, M. (2010). Heterogeneous photocatalytic degradation of phenols in wastewater: A review on current status and developments. *Desalination* , 261, 3-18.

Alfano, O. M., Bahnemann, D., Cassano, A. E., Dilliert, R., & Goslich, R. (2000). Photocatalysis in Water Environments Using Artificial and Solar Light. *Catalysis Today* , 58, 199-230.

Alfano, O. M., Cabrera, M. I., & Cassano, A. E. (1997). Photocatalytic Reactions Involving Hydroxyl Radical Attack. *Journal of Catalysis* , 172, 370–379.

Bahnemann, D. (2004). Photocatalytic Water Treatment: Solar Energy Applications. *Solar Energy* , 77, 445-459.

Ballari, M. d., Alfano, O. M., & Cassano, A. E. (2010). Mass transfer limitations in slurry photocatalytic reactors: Experimental Validation. *Chemical Engineering Science* , 65, 4931-4942.

Baniasadi, E., Dincer, I., & Naterer, G. F. (2012). Radiative heat transfer and catalyst performance in a large-scale continuous flow photoreactor for hydrogen production. *Chemical Engineering Science* , 84, 638-645.

Berger, K., Weidlich, A., Wilkie, A., & Magnor, M. (2012). Modeling and Verifying the Polarizing Reflectance of Real-World Metallic Surfaces. *IEEE Computer Graphics and Applications* , 32(2).

Bhatkhande, D., Pangarkar, V., & A.A., B. (2001). Photocatalytic degradation for environmental applications: a review. *Journal of Chemical Technology and Biotechnology* , 77, 102-116.

Black, R. (2009, february 2nd). Water-another global 'crisis'? Retrieved from BBC News Science and Environment: <http://news.bbc.co.uk/2/hi/science/nature/7865603.stm>

Braham, R. J., & Harris, A. T. (2009). Review of major design and scale-up considerations for solar photocatalytic reactors. *Industrial and Engineering Chemistry Research* , 48, 8890-8905.

Braun, M., Maurete, M., & Oliveros, E. (1991). *Photochemical Technology* (Eds. D.F. Ollis, N. Serpone). Chichester: Wiley.

Camera-Roda, G., Santarelli, F., & Martin, C. A. (2005). Design of photocatalytic reactors made easy by considering the photons as immaterial reactants. *Solar Energy* , 79, 343-352.

Cassano, A., & Alfano, O. (2008). Photoreactor Modelling: Applications to advanced Oxidation Processes. *International Journal of Chemical Reactor Engineering* , Vol. 6.

Cassano, A., & Alfano, O. (2000). Reaction engineering of suspended solid heterogeneous photocatalytic reactors. *Catalysis Today* , 58, 167-197.

Cassano, A., Martin, C., Brandi, R., & Alfano, O. (1995). Photoreactor Analysis and Design: Fundamentals and Applications. *Industrial Engineering Chemistry Research* , 34, 2155-2201.

Changrani, R., & Raupp, G. (1999). Monte Carlo Simulation of the Radiation Field in a Reticulated Foam Photocatalytic Reactor. . *AIChE* , 45(5), 1085.

Colbert, M., Patanaik, S., & Krivanek, J. (2006). BRDF-Shop: creating physically correct bidirectional reflectance distribution functions. *IEEE Computer Graphics and Applications* , 26(1) , p. 30-36.

Curcó, D., Giménez, J., Addardak, A., Cervera-March, S., & Esplugas, S. (2002). Effects of radiation absorption and catalyst concentration on the photocatalytic degradation of pollutants. *Catalysis Today* , 76, 177-188.

Davydov, L., Tsekov, R., & Smirniotis, P. G. (2001). Optimal radiation field in one-dimensional continuous flow heterogeneous photocatalytic reactors. *Chemical Engineering Science* , 56, 4837-4847.

de Lasa, H., Serrano, B., & Salaices, M. (2005). *Photocatalytic Reaction Engineering*. New York: Springer.

Denny, F., Scott, J., Pareek, V., Peng, G., & Amal, R. (2010). Computational fluid dynamics modelling and optimal configuring of a channelled optical fibre photoreactor. *Chemical Engineering Science* , 65, 5029-5040.

Duran, A., Monteagudo, J. M., San Martin, I., & Aguirre, M. (2010). Decontamination of industrial cyanide-containing water in a solar CPC pilot plant. *Solar Energy* , 84 1193-1200.

Fujishima, A., Kohayakawa, K., & Honda, K. (1975). Hydrogen Production under Sunlight with an Electrochemical Photocell. *Journal of Electrochemical Society* , Vol. 22, Issue 11 , pag. 1487-1489.

Gaya, U. I., & Abdullah, A. H. (2008). Heterogeneous photocatalytic degradation of organic contaminants over titanium dioxide: A review of fundamentals, progress and problems. *Journal of Photochemistry and Photobiology C:Photochemistry Reviews* , 9, 1-12.

Gora, A., Toepfer, B., Puddu, V., & Li Puma, G. (2006). Photocatalytic oxidation of herbicides in single-component and multicomponent systems: Reaction kinetics analysis. *Applied Catalysis B: Environmental* , 65, 1-10.

He, X. D., Torrance, K. E., Sillion, F. X., & Greenberg, D. P. (1991). A Comprehensive Physical Model for Light Reflection. *Computer Graphics* , Vol. 25, Num4. Pag. 177-182.

Hoffmann, M., Scot, T., Wonyong, C., & Bahnemann, D. (1995). Environmental Applications of Semiconductor Photocatalysis. *Chemical Reviews* , 95, 69-96.

Hyde, M. W., Schmidt, J. D., & Havrilla, M. J. (2009). A geometrical optics polarimetric bidirectional reflectance distribution function for dielectric and metallic surfaces. *Optics Express* , Vol. 17 , Issue 24, pag. 22138-22153.

Imoberdorf, G. E., Irazoqui, H. A., Alfano, O. M., & Cassano, A. E. (2007). Scaling-Up from first principles of a photocatalytic reactor for air pollution remediation. *Chemical Engineering Science* , 62, 793-804.

Imoberdorf, G. E., Taghipour, F., Keshmiri, M., & Mohseni, M. (2008). Predictive radiation field modeling for fluidized bed photocatalytic reactors. *Chemical Engineering Science* , 63, 4228-4238.

Irazoqui, H. I., & A., C. (2000). Simplified Extense Source Model for Photoreactor Analysis and design. *Industrial and Engineering Chemistry Research* , 39, 4260-4271. .

Ismail, A. A., & Bahnemann, D. W. (2014). Photochemical splitting of water for hydrogen production by photocatalysis: A review. *Solar Energy Materials & Solar Cells* , 128, 85-101.

Kapinus, E., Viktorova, T., & Khalyavka, T. (2009). Dependence of the rate of photocatalytic decomposition of safranin on the catalyst concentration. *Theoretical and Experimental Chemistry* , Vol. 45, No.2 .

Kawaguchi, H. (1994). Dependence of Photocatalytic Reaction Rate On Titanium Dioxide Concentration In Aqueous Suspensions. *Environmental Technology* , 15:2, 183-188.

Koc'í, K., Reli, M., Kozák, O., Lacny', Z., Plachá, D., Praus, P., et al. (2011). Influence of reactor geometry on the yield of CO<sub>2</sub> photocatalytic reduction. *Catalysis Today* , 176, 212-214.

Lawless, D., Serpone, N., & Meisel, D. (1991). Role of the OH radicals and trapped Holes in Photocatalysis. A Pulse Radiolysis Study. *Journal of Physical Chemistry* , 95, 5166-5170.

Li Puma, G. (2005). Dimensionless Analysis of Photocatalytic Reactors Using suspended Solid Photocatalyst. *Chemical Engineering Research and Design* , 83(A7), 820-826.

Li Puma, G. (2003). Modelling of Thin-Film Slurry Photocatalytic Reactors Affected by Radiation Scattering. *Environmental Science & Technology* , 37, 5783-5791.

Li Puma, G., & Brucato, A. (2007). Dimensionless analysis of slurry photocatalytic reactors using two-flux and six-flux radiation absorption-scattering models. *Catalysis Today* , 122 78-90.

Li Puma, G., & Brucato, A. (2007). Dimensionless analysis of slurry photocatalytic reactors using two-flux and six-flux radiation absorption–scattering models. *Catalysis Today* , 122, 78-90.

Li Puma, G., Puddu, V., Tsang, H. K., Gora, A., & Toepfer, B. (2010). Photocatalytic oxidation of multicomponent mixtures of estrogens under UVA and UVC radiation: Photon absorption, quantum yields and rate constants independent of photon absorpt. *Applied Catalysis B: Environmental* , 99, Issue3-4, 388-397.

Li Puma, G., Toepfer, B., & Gora, A. (2007). Photocatalytic Oxidation of Multicomponent Systems of Herbicides: Scale-up of Laboratory Kinetics Rate Data to Plant Scale. *Catalysis Today* , 124, 124-132.

Liao, H., & Reitberger, T. (2013). Generation of Free OH Radicals by Black Light Illumination of Degussa (Evonik) P25 TiO<sub>2</sub> Aqueous Suspensions. *Catalysts* , 3, 418-443.

Malato, S., & Blanco, J. (2004). Engineering of Solar Photocatalytic Reactors. *Solar Energy* , Vol. 77, Pag. 513-524.

Malato, S., Blanco, J., Vidal, A., & Richter, C. (2002). Photocatalysis with solar energy at a pilot-plant scale: an overview. *Applied Catalysis B: Environmental* , 37, 1-15.

Marugan, J., Van Grieken, R., Alfano, O., & Cassano, A. (2006). Optical and Physicochemical Properties of Silica-Supported TiO<sub>2</sub> Photocatalysts. *AIChE* , 52(8), 832.

Marugan, J., van Grieken, R., Cassano, A. E., & Alfano, O. M. (2009). Scaling-up of slurry reactors for the photocatalytic oxidation of cyanide with Ti<sub>2</sub>O and silica-supported Ti<sub>2</sub>O suspensions. *Catalysis Today* , 144, 87-93.

Marugan, J., van Grieken, R., PAblos, C., & Sordo, C. (2010). Analogies and differences between photocatalytic oxidation of chemicals and photocatalytic inactivation of microorganisms. *Water Research* , vol.44 , 789-796.

Marugan, J., van Grieken, R., Pablos, C., Satuf, L. M., & Cassano, A. E. (2013). Modeling of a bench-scale photocatalytic reactor for water disinfection from laboratory-scale kinetic data. *Chemical Engineering Science* , 224, 39-45.

McCullaugh, C., Skillen, N., Adams, M., & Robertson, P. (2011). Photocatalytic reactors for environmental remediation: a review. *Journal of Chemical Technology and Biotechnology* , 86, 1002-1017.

Minero, C., & Davide, V. (2006). A quantitative evaluation of the photocatalytic performance of TiO<sub>2</sub> slurries. *Applied Catalysis B: Environmental* , 67, 257–269.

Mohamed, H. H., & Bahnemann, D. W. (2012). The role of electron transfer in photocatalysis: Fact and fictions. *Applied Catalysis B: Environmental* , 128, 91-104.

Moreira, J., Serrano, B., Ortiz, A., & de Lasa, H. (2011). TiO<sub>2</sub> absorption and scattering coefficients using Monte Carlo method and macroscopic balances in a photo-CREC unit. *Chemical Engineering Science* , 66, 5813-5821.

Motegh, M., Cen, J., Appel, P. W., van Ommen, R., & Kreutzer, M. T. (2012). Photocatalytic-reactor efficiencies and simplified expressions to assess their relevance in kinetic experiments. *Chemical Engineering Journal* , 207-208, 607-615.

Ortiz-Gomez, A., Serrano-Rosales, B., Salices, M., & De Lasa, H. (2007). Photocatalytic Oxidation of Phenol: Reaction Network, Kinetic Modeling, and Parameter Estimation . *Industrial & Engineering Chemistry Research* , 46(23), 7394-7409.

Oyama, T., Otsu, T., Hidano, Y., Takayoshi, K., Serpone, N., & Hidaka, H. (2011). Enhanced remediation of simulated wastewaters contaminated with 2-chlorophenol and other aquatic pollutants by TiO<sub>2</sub>-photoassisted ozonation in a sunlight-driven pilot-plant scale photoreactor. *Solar Energy* , 85, 938-944.

Pasquali, M., Santarelli, F., Porter, J., & Yue, P. (1996). Radiative Transfer in Photocatalytic Systems. *AIChE* , 42(2), 532.

Salices, M., Serrano, B., & de Lasa, H. (2002). Experimental Evaluation of photon absorption in an aqueous TiO<sub>2</sub> Slurry reactor. *Chem. Eng. J.* , 90, 219.

Takashi, A., & Takashi, S. (1972). Effect of Light-Source Characteristics On the Performance Of Circular Annular Photochemical Reactor. *Journal of Chemical Engineering of Japan* , 5, 385-391.

Turchi, C., & Ollis, D. (1989). Photocatalytic Degradation of Organic Water Contaminants: Mechanisms Involving Hydroxyl Radical Attack. *Journal of Catalysis* , 122, 178-192.



Valades-Pelayo, P. J., Moreira, J., Serrano, B., & de Lasa, H. I. (2014a). Boundary conditions and phase functions in a Photo-CREC Water-II Reactor Radiation Field. *Chemical Engineering Science* , 107, 123-136.

Valades-Pelayo, P. J., Moreira, J., Solano-Flores, P., Serrano, B., & De Lasa, H. (2014b). Establishing photon absorption fields in a Photo-CREC Water II Reactor using a CREC-spectroradiometric probe. *Chemical Engineering Science* , 116, 406-417.

Yokota, T., Cesur, S., Suzuki, H., Baba, H., & Takahata, Y. (1999). Anisotropic Scattering Model for the Estimation of Light Absorption Rates in Photoreactor with Heterogeneous Medium. *J. Chem. Eng. Jpn.* , 32, 314.

## Chapter 6

### 6 Eight-Lamp Externally Irradiated Bench-Scale Photocatalytic Reactor: Scale-up and Performance Prediction

The information presented in this chapter is based on the article entitled "Eight-Lamp Externally Irradiated Bench-Scale Photocatalytic Reactor: Scale-up and Performance Prediction.", submitted to *Journal of Chemical Engineering* on, November 16th, 2014. The sections presented in this chapter consist of stage iv) in section 1.1 and present results towards the completion of general objectives b) and c) in section 1.2.

#### 6.1 Abstract

The present study considers a scale-up methodology for photocatalytic slurry reactors. The Photo-CREC Water units used includes: a) a 2.65 L internally irradiated annular photoreactor, b) a 9.6 L externally irradiated scaled-up unit. The LVREA (Local Volumetric Rate of Energy Adsorption Field) calculation for the bench-scale and the scaled-up reactors at different operation conditions are determined by using approaches established by [Valades-Pelayo et al. \(2014b\)](#) and [Valades-Pelayo et al. \(2014c\)](#). In the bench-scale photoreactor, degradations of oxalic acid are carried out at different photocatalyst concentrations and lamp emissions. Residence time distributions are determined for both Photo-CREC Water II and Photo-CREC Solar Simulator (Photo-CREC water III) by using glucose as a tracer. An efficiency factor is calculated in both cases including mixing mechanisms and charge/recombination phenomena using a simplified kinetic model. To avoid cross-correlation issues, all relevant parameters are determined by independent experiments. Model validation is also accomplished by comparing model predictions to experimental degradation rates at different photocatalyst concentrations in the larger Photo-CREC Solar Simulator (Photo-CREC Water III). The proposed methodology confirms the applicability of reaction engineering principles for scale up while moving from bench to pilot plant photoreactors.

## 6.2 Introduction

Based on all of the above mentioned facts, presented in Chapter 2 and considering the insights provided in Chapter 3, Chapter 4 and Chapter 5, validation of physically-based scale-up models at larger scales and non-idealized operating conditions is needed. Furthermore, these models should not only predict concentration profiles during batch experiments at different scales, but also predict reaction rates at different photocatalyst concentrations and irradiance conditions and configurations. Lastly, to avoid over-parameterization while retaining model meaningfulness, these kinetic models, should also be based on independently-validated, physically-based radiation models that accurately represent radiation gradients at all scales.

Given the significance of research in this area, this chapter reports an original way to evaluate parameters at different lamp irradiances combined with the successful application of a physically-based kinetic model for photocatalytic degradation rate at different scales and geometric conditions. Moreover, we are not aware of a similar study considering the scale-up of two reactor designs, such that the methodology is relevant for its applicability in the scale-up from bench to pilot-plant solar photocatalytic reactors, such as: i) the Photo-CREC Water II Reactor, an internally irradiated bench-scale annular photoreactor with 2.65 L of irradiated volume and ii) the Photo-CREC Solar Simulator (Photo-CREC Water III), an externally-irradiated annular photoreactor with 9.6 L of irradiated volume. Parameter regression for this kinetic model has the additional advantage of being supported by previously and independently validated MC RTE methods, proposed in Chapter 4 ([Valades-Pelayo et al., 2014b](#)) and Chapter 5 ([Valades-Pelayo et al. 2014c](#)) in earlier studies.

## 6.3 Experimental

This manuscript reports a scale-up methodology for photocatalytic reactors. To accomplish this, relevant kinetic parameters for the proposed kinetic model are determined in a smaller bench-scale photoreactor (Photo-CREC Water II reactor) considering the photodegradation of oxalic acid. Oxalic acid was chosen as a model organic pollutant due to the absence of intermediates during its degradation mechanism.

Following this, photocatalytic oxalic acid degradation rates are predicted in the externally irradiated Photo-CREC Solar Simulator (Photo-CREC-Water III) which is about four times larger than Photo-CREC Water II .

### 6.3.1 Bench-Scale and Scaled-up System Description

The bench-scale reactor system used to determine relevant kinetic and radiative parameters consists of a 2.65 L annular Photo-CREC Water II Photoreactor, a pump and a tank with its respective sampling ports and air supply, as presented in sections 3.3.1 and 4.3.1. The photoreactor system has a total volume of 6 L, as presented in Figure 3.1. Figure 4.1 describes this annular reactor with one lamp positioned at the reactor central axis. More specifically (refer to Figure 4.1), the photoreactor unit is comprised of the following components: (a) a 15-W black light lamp, (b) a Pyrex glass inner tube, (c) silica windows (d) a black outer tube, (e) an outlet and (f) an inlet. The lamp used in the photoreactor is a 15-W 1.33-cm radius, 41.3-cm length, black-light UV lamp, covered with a high transmittance Pyrex reactor tube. The pump allows a recirculation of up to 16 L min<sup>-1</sup>.

The reactor used to validate the scale-up methodology is a Photo-CREC Solar Simulator (Photo-CREC-Water III), a 9.8 L, annular photoreactor operated in slurry mode. Just like in the bench-scale system, the photoreactor system has a pump and a tank with its respective sampling ports and air supply. As explained in section 5.3.1 and presented in Figure 5.1, this annular reactor is externally irradiated by eight UV Lamps, allocated around the annular section, in pairs inside four equally-spaced reflectors. The annular photoreactor unit is composed of: (1) eight 15-W black light lamps, (2) a Pyrex glass inner tube, (3) outer Pyrex glass tube, (4) an inlet and (5) an outlet. The lamps and the pump used for this system have the same specifications as the ones used for the bench-scale reactor unit.

### 6.3.2 Additional equipment for photocatalytic degradations and tracer experiments

Oxalic acid quantification for photodegradation was carried out by using the Total Organic Carbon (TOC) content analyser in the liquid aliquots, determined with a

Shimadzu TOC-V<sub>cph</sub> instrument. This instrument operates as follows: the sample is automatically and mechanically injected into a furnace, at 680°Celsius, that contains a Platinum-based catalyst, and uses hydrocarbon-free high-purity air as a carrier gas. At this temperature, the oxalic acid is broken down and completely oxidized, generating the final products H<sub>2</sub>O and CO<sub>2</sub>. Dried CO<sub>2</sub> is then flown through a Non-Dispersive Infrared Detector (NDIR) for quantification purposes. Before analysis, liquid samples are filtered using 0.2-micrometer paper to avoid introducing any bacteria/microorganisms or photocatalyst particles. The injected sample volume was 25 micro-liters. A broad-range calibration curve obtained from different concentrations of 99.5 % D-(+)-Glucose (Sigma G8270) solutions in de-ionized and distilled water was used to quantify the carbon content of the experimental samples. Standard deviations were 0.100 or less. The detection limit of the instrument is 4 micro-gram/Litre and the measuring range is 0-30000 milligram/Litre. The reproducibility ability of the instrument, is within 1.5%.

Moreover, acidity was monitored by an Orion 2-star pH Benchtop from Thermoscientific. This instrument allows pH measurements up to three decimal digits. Temperature was measured by an Omega digital thermometer whose probe was immersed in the TiO<sub>2</sub> slurry in both system mixing tanks. Oxygen supply was controlled by rotameters. Additionally, lamp emission intensity was regulated by using a POWERSTAT variable voltage autotransformer, able to vary voltage between zero and 140 V. Lamp emission was monitored by measuring the transmitted irradiance with a EPP 2000 Stellar Net Spectroradiometer connected to a quartz sensor through an optical fiber cable.

### 6.3.3 Determining RTD in both photoreactor systems

Tracer experiments were run in both the Photo-CREC Water II Photoreactor and the Photo-CREC Solar Simulator (Photo-CREC-Water III). The average residence times were independently determined by measuring for systems, reactor volume and volumetric flow. Volumetric flows were determined by the use of a container laid on top of a Sartorius weighing scale able to weight up to 60,000 grams and a VWR stopwatch. The system was turned on and the volumetric flow was obtained from the slope of the observed weight plotted against time. This procedure was repeated at least three times for each reactor configuration. The volumes were determined by filling each reactor unit

with water and weighting all the water contained. For all calculations, water density at STP was considered.

To obtain the RTDs-curves in both reactors, glucose was used as a tracer, mainly due to its safety and high solubility in water. Before the experiments were started, both systems were filled by turning the pumps on and allowing water to enter the reactor from the top. A valve located in both reactors bottom sections was closed, so that water could accumulate inside the reactor units. While the reactors were being filled, air was being pushed out through a top vent. Once all the air had been removed from the units, the vent was closed and hermetically sealed. This methodology ensured that no empty zones or air pockets remain during operation, within the annular reactor sections of both reaction systems.

The RTD experiments were then run, by injecting a highly concentrated glucose solution in a pulse, through injection ports located at the reactor top while taking timed samples at the reactor outlet every 3 to 5 seconds. These tracer experiments were repeated five times for each reaction system. For the Photo-CREC Water II, 250 mg of glucose were injected in 5 ml. On the other hand, for the Photo-CREC Solar Simulator, 2 g of glucose were injected in 10 ml.

#### 6.3.4 Degradations procedure in bench-scale system

In the Photo-CREC Water II Photoreactor, the degradation of oxalic acid was performed at different photocatalyst concentrations and lamp emission intensities. For all cases, pH was kept between 3.15 and 3.35 and temperature was set at  $23 \pm 2$  °C during all degradation experiments. A solution was prepared by adding  $600 \text{ mg l}^{-1}$  of oxalic acid in 250 ml of water. Additionally, different loadings of commercial  $\text{TiO}_2$  were added to 250 ml of water. Both solutions were sonicated for at least 10 minutes before being added to the reactor system.

First, the reactor (The Photo-CREC Water II Photoreactor) was filled with 6 L of water, as explained in subsection 2.4. Then, the oxalic acid solution was added and let to homogenize for at least 5 minutes, until the pH could stabilize at about 3.200.

Afterwards, the TiO<sub>2</sub> solution was added and let to homogenize again for 5 minutes, until the pH could be stable again. Lamps were then turned on and an initial sample was taken. From this point on, subsequent samples were taken every 10 to 20 minutes, depending on lamp emission intensity and photocatalyst concentration. Reactions were followed by TOC analysis for up to 3 hours, or until oxalic acid degraded, to a point where pH could increase to a value of 3.300.

Runs were carried out for photocatalyst concentrations of 25, 50, 75, 100 and 150 mg l<sup>-1</sup> with a nominal lamp emission. For this, at least five repeats were carried out. Additionally, for 25, 50, 75 and 100 mg l<sup>-1</sup> photocatalyst concentrations, degradations were also performed at different lamp emissions. Lamp emission power was inspected between 40% and 140% of the nominal lamp emission by varying the voltage with a POWERSTAT Variable Autotransformer. Approximately ten runs were developed for each photocatalyst concentration.

The percentual lamp emission during the degradation runs was determined using two different approaches. First, an empirical equation, reported in Figure 6.1, correlating Percentual Lamp Emission with voltage was established. This correlation was obtained by directly measuring the lamp axial emission profiles, using the reactor windows as shown in Figure 6.1. In this respect, axial emission profiles were measured at different voltages. The axial emission profiles were integrated and as a result the total lamp emission at set voltages were calculated. The total lamp emission were used to define the Percentual Total Lamp Emission Fraction by equating the Total Lamp Emission over the Total Lamp Emission at the 110V reference voltage. It is worth mentioning that changes in the shape of the lamp axial emission profiles were consistently below 10%. This ensured reproducibility of the Total Lamp Emission at various input voltages.

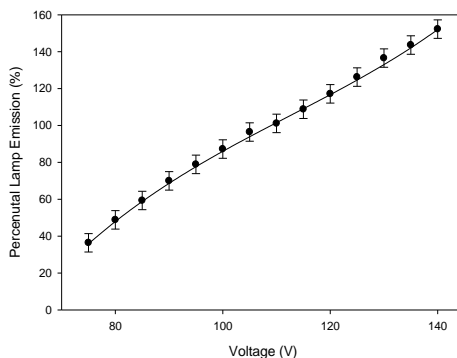


**Figure 6.1.** Empirical equation, correlating the input voltage for the UV-Lamp and the percentual emission, determined while the reactor was filled with water only.

As well, the radiation transmitted through the central quartz windows, reported in Figure 3.2, was continuously monitored during the degradation experiments. From these data, an average lamp emitted radiation was calculated from all the experiments. This average radiation was defined using a fitted linear regression function from the MC simulations proposed in section 4.4.1 (Valades-Pelayo et al 2014b) to the experimental transmittance profiles obtained.

### 6.3.5 Degradations procedure in scaled-up system

In the Photo-CREC Solar Simulator (Photo-CREC-Water III), degradations of oxalic acid were run at different photocatalyst concentrations. More specifically, photocatalyst concentrations of 30, 60, 90 and 120 mg l<sup>-1</sup> were used. As for the conditions under which the degradations in the bench-scale unit were performed: pH was kept between 3.20 and 3.30 for all cases, while temperature was set at 23±1° C during all degradation experiments. With this end, an oxalic acid water solution was prepared by adding 1800 mg of oxalic acid in 500 ml of water. Additionally, different loadings of commercial TiO<sub>2</sub> were added to 500 ml of water. All slurry suspensions were sonicated for at least 10 minutes before being added to the reactor system.

The reactor system was first filled with 18 L of water, as explained in subsection 2.4. Following this, the oxalic acid solution was added and let to homogenize for at least 5 minutes, until the pH stabilized at a value of 3.2. Afterwards, the TiO<sub>2</sub> solution was



added and let to homogenize again for 5 minutes until the pH was stable again. Lamps were then, turned on and an initial sample was taken. From this point on, subsequent samples were taken every 10 to 20 minutes, depending on the photocatalyst concentration. Reactions were followed until oxalic acid would degraded to a point where the pH increased to a value of 3.300. Each experiment was repeated 3 times.

## 6.4 Mathematical Models and Scale-Up Methodology

As mentioned in Chapter 1, when proposing a mathematical model for scale-up purposes, the following phenomena need to be properly accounted for: i) the LVREA distribution within the reaction system, ii) the charge separation/recombination mechanism as a function of the LVREA, iii) the free-radical generation/depletion mechanisms at the scale of the photocatalyst particle, and iv) the hydrodynamics affecting the free radical distribution.

### 6.4.1 Radiative models: pH Correction

In the present chapter, the irradiance and absorption fields for both reactors were obtained from radiative models reported in Chapter 4 (Valades-Pelayo et al. 2014 b) and Chapter 5 (Valades-Pelayo et al. 2014 c) where the simulations and phase function determination were determined at  $\text{pH} = 7$ . Given that the present degradations are to be carried out at a  $\text{pH}$  of  $3.25 \pm 0.05$ , this same methodology was used to determine a corrected scattering parameter that accounts for the  $\text{pH}$  change.

With this end in mind, radial irradiance profiles were determined for  $\text{pH}=3.25$ , and below  $150 \text{ mg l}^{-1}$ , by measuring the radial irradiance profiles at five different radial positions in the Photo-CREC Water II at three photocatalyst loadings: i) water only, ii)  $50 \text{ mg l}^{-1}$  and iii)  $100 \text{ mg l}^{-1}$ . Measurements were repeated five times. Figure 6.2 presents the experimental measurements. Furthermore, in this figure, the simulations for the optimized  $g = 0.41$  are presented. Additionally, for comparison purposes, experimental data with a  $\text{pH}=7$ , and simulations with the  $g$  determined by Valades-Pelayo et al., (2014)b are reported.

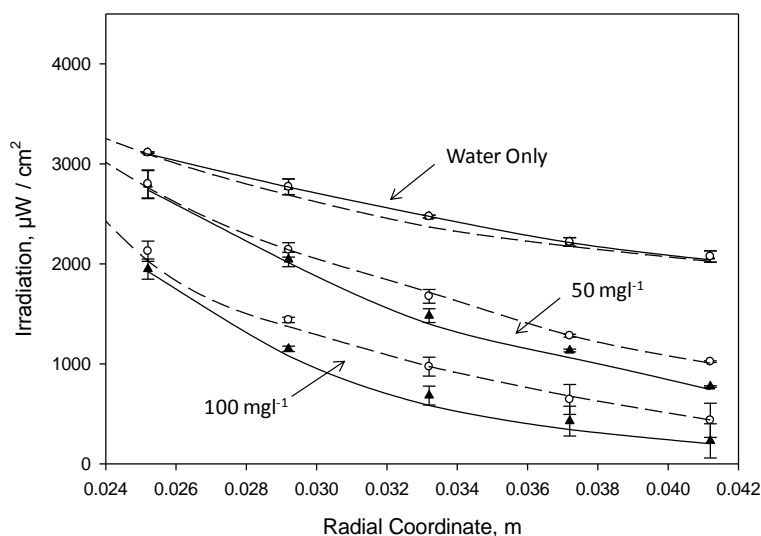


**Figure 6.2** Radial Irradiance Profiles ( $\mu\text{W}/\text{cm}^2$ ) obtained as proposed by Valades-Pelayo et al. 2014b at five different radial positions for three photocatalyst loadings: a) water only, b)  $50 \text{ mg l}^{-1}$  and c)  $100 \text{ mg l}^{-1}$ . At a  $\text{pH}=7$  ( $\circ$ ) and a  $\text{pH}=3.25$  ( $\blacktriangle$ ), MC simulations with  $g=0.41$  (—) and  $g=0.68$  (---) are shown.

Since both reactors (the Photo-CREC Water II and the Photo-CREC Solar Simulator) use lamps with the same specifications, the same considerations for lamp emissions apply for both RTE MC methods. Lamp emissions for both simulations were determined to be at around 13-17% for the range below 388nm (given the band gap for  $\text{TiO}_2$ ), with respect to the nominal 15W input power for the UVA range. The lamp spectra were considered for both reactors, as presented in Figure 3.3.

#### 6.4.2 Kinetic models: Charge separation and rate equation

As mentioned in section 1 of this manuscript, the charge separation/recombination mechanism is key towards proposing a physically sound equation that is able to predict photocatalyst behaviour with respect to both photocatalyst loading and lamp emission intensity. This was proposed by a number of researchers such as Motengh et al. (2012), Camera-Roda et al. (2005), Kawaguchi (1994), Kapinus et al. (2009), Curco et al. (2002), among others.

Regarding photoconversion kinetics, several models have been proposed. Some of them assume a behaviour similar to a Langmuir or Michaelis-Menten type of kinetic equation (Marugan et al. 2013). These models however, are not set to predict the change in the reaction rate with different photocatalyst concentrations and therefore do not allow estimating an optimum photocatalyst concentration (Minero and Vione, 2006). On the other hand, a model that accounts for back reactions and charge separation/recombination effects (Alfano et al. 1997) has proven to be more adequate for predicting the photocatalytic behaviour in laboratory scale photoreactors (Marugan et al 2009 ; Marugan et al , 2013).

In this respect, the photocatalytic kinetics considered in this manuscript are described by proposing a reaction scheme that considers: i) electron and electron-hole generation by photo-absorption on the photocatalyst particle, ii) charge recombination producing heat via the re-combination step and iii) electron and electron-holes leading to the production free radicals.

Following this approach, a balance for electrons and electron holes can be obtained, as presented in Eq. 6-1 and Eq. 6-2:

$$\frac{d[h^+]}{dt} = k_\lambda \frac{LVREA}{Sp C_{cat}} - k_r[h^+][e^-] - k_1[h^+][H_2O_{ads}] - k_2[h^+][OH_{ads}] \quad \text{Eq. 6-1}$$

$$\frac{d[e^-]}{dt} = k_\lambda \frac{LVREA}{Sp C_{cat}} - k_r[h^+][e^-] - k_3[O_{2ads}][e^-] \quad \text{Eq. 6-2}$$

where  $[e^-]$  and  $[h^+]$  are the electron and electron-hole concentrations on the surface of the photocatalyst particle, respectively.  $k$  with different sub-indexes represent the proportionality constants.

The first term of the RHS of equations Eq. 6-1 and Eq. 6-2, describes the rate of charge separation and recombination of electron and electron-hole pair. This rate is based on the unit area of photocatalyst surface and is the result of photons being absorbed with a quantum energy superseding the band gap. This rate involves the LVREA standing for

the Local Volumetric Rate of Energy Absorption,  $S_p$  denotes the photocatalyst external specific surface and  $C_{cat}$  represents the photocatalyst concentration. Additionally, it should be noted that the second RHS term in Eq. 6-1 and Eq. 6-2 accounts for charge recombination, while the third RHS term, in both equations, accounts for the reaction path leading to the formation of adsorbed free radicals. In this regard, it is assumed that the surface concentrations of all other intermediate species before the formation of free radicals are in pseudo-steady state.

Moreover, based on the time scale in which these charge separation/recombination processes take place (Hanan and Bahnemann, 2012), it is possible to assume pseudo-steady states and to obtain an expression for the rate of adsorbed free-radicals formed (Alfano et al, 1997; Minero et al. 1999), as reported in Eq. 6-3:

$$r_{free\ rad} = \alpha \left( \sqrt{\gamma \frac{LVREA(\rho, \theta, z)}{C_{cat} S_p} + 1} - 1 \right) \quad \text{Eq. 6-3}$$

Where  $\rho, \theta, z$  are the radial, azimuth and axial position respectively and  $\alpha$  and  $\beta$  as can be defined as:

$$\alpha = \frac{(k_1[H_2O_{ads}] + k_2[OH^-_{ads}] + k_3[O_{2ads}])}{k_r} \quad \text{Eq. 6-4}$$

$$\gamma = \frac{4k_\lambda k_r}{k_3[O_{2ads}][k_1[H_2O_{ads}] + k_2[OH_{ads}]]} \quad \text{Eq. 6-5}$$

For a more detailed explanation regarding the derivation of Eq. 6-3, Eq. 6-4 and Eq. 6-5, readers are referred to the work of Minero and Vione (2006), Minero (1999) and Alfano et al. (1997). For the purpose of the present study,  $\alpha$  and  $\beta$  will be regarded as constants, with units of  $m^2W^{-1}$  and  $OH\ mol\ s^{-1}m^{-2}$  respectively. One should note that the LVREAs, for both reactors, presented in sections 4.5 and 5.5, are a function of the position within both annular sections.

Furthermore and considering that the volumetric degradation rate of oxalic acid can be described using a Langmuir-Hinshelwood kinetic equation, as reported in Eq. 6-6. As well as on the basis of the adsorbed free radicals concentration, it results:

$$r_{ox} = k_{ox}\theta_f \theta_{ox} = k_{ox}\theta_f \frac{K_A C_{ox}}{1 + K_A C_{ox}} \quad \text{Eq. 6-6}$$

where  $\theta_f$  represents the concentration of adsorbed free radicals per activated unit surface area and  $\theta_{ox}$  considers the fraction of  $\text{TiO}_2$  sites occupied by oxalic acid.  $K_A$  stands for the adsorption constant and  $C_{ox}$  is the concentration of oxalic acid in the slurry, where non-competitive adsorption between free radicals and organic pollutants is assumed. It is worth mentioning that,  $K_A$  does not depend on irradiance conditions (Kawaguchi, 1993). To avoid needless complications with the cross-correlation between parameters, the kinetic study of the present manuscript was developed within the linear region of Eq. 6-6 or at conditions where  $K_A C_{ox} \gg 1$ .

Regarding the mathematical and kinetic scheme under consideration, adsorbed free radicals are assumed to be the ones mainly responsible for photocatalytic activity (Liao and Reitberger, 2013; Hanan and Bahnemann, 2012). This is the case given that the probability of having a free radical adsorbed on the photocatalyst surface determine, among other factors, the rate at which adsorbed chemical species can be photo-degraded. Thus, a proper accounting of the distribution of adsorbed free radicals in a photocatalytic reaction system, is critical to determine the relative performance between the two reactors differing in scale and/or geometry only (the Photo-CREC Water II and the Photo-CREC Solar Simulator).

### 6.4.3 Transport Models: Free radical distribution and photocatalyst activity

Among the main phenomena affecting the concentration of adsorbed free radicals on the photocatalyst particle surface, the following can be cited: i) free radical generation by charge-separation, ii) free radical consumption during degradation reactions, iii) free radical depletion due to side-reactions. Additionally, different mixing patterns affect the

photocatalyst particles residence times, inside different sections of each photoreactor system. This leads to different distributions of irradiated and non-irradiated slurry volume fractions. Not accounting for these factors, can increase errors when determining relevant kinetic parameters, undermining the accuracy of the predictions of the scale-up methodology.

Specifically for the two reaction systems considered in the present study, the Photo-CREC Water II and the Photo-CREC Solar Simulator (Photo-CREC-III), two main components or sections can be considered in each system: a) an evenly or unevenly irradiated annular plug-flow reactor with axial dispersion and b) a non-irradiated and perfectly mixed tank (CSTR).

On this basis, a balance equation describing the change of adsorbed free radicals (Eq. 6-7) valid for both photoreactor systems, is proposed. This equation includes: i) generation of free radicals, ii) depletion of free radicals as a proportional function of the adsorbed free radicals concentration, iii) free radical axial dispersion and iv) free radical convection. While phenomena i) and ii) occur on the photocatalyst particle and as such are surface phenomena, the last two effects, iii) and iv), are considered to arise due to mixing or hydrodynamic effects experimented by the photocatalyst particles. Due to this, the balance equation has to be defined in terms of  $C_f$ , the concentration of adsorbed free radicals per unit volume of the slurry, as follows:

$$\frac{\partial C_f}{\partial t} = C_{cat} S_p r_{free\ rad} - k_{all} C_f - D_z \frac{\partial^2 C_f}{\partial z^2} + v_z \frac{\partial C_f}{\partial z} \quad \text{Eq. 6-7}$$

where  $t$ , stands for the irradiation time; and  $z$  represents the length along the photoreactor axial coordinate, being zero at the reactor inlet and increasing downwards, in the flow direction.  $D_z$  represents the axial dispersion coefficient and  $v_z$  denotes the average flow velocity in the axial direction. One should note that the concentration of free radicals per unit volume ( $C_f$ ) and per unit surface area ( $\theta_f$ ) are related as:

$$C_f = C_{cat} S_p \theta_f \quad \text{Eq. 6-8}$$

One should also note that the  $r_{free\ rad}$  is defined using Eq. 6-3. As well that Eq. 6-9 considers  $k_{all}$  which represents a lumped kinetic parameter, accounting for all the reactions and side reactions, consuming free radicals on the photocatalyst surface, as follows:

$$k_{all} = k_{rec} + \sum_{i=1}^n \beta_i r_i \quad \text{Eq. 6-9}$$

where  $k_{rec}$ , is the constant for the rate of free radical disappearance due to side reactions. On the other hand, the second RHS term accounts for free radical depletion due to various photocatalytic reactions where  $\beta_i$  represents the stoichiometric coefficients for free radicals in the pollutant photodegradation reactions, as proposed by [Serrano et al. 2009](#).

In particular, when considering oxalic acid under the conditions mentioned in sections 6.3.4 and 6.3.5, Eq. 6-9 can be further simplified for to yield Eq. 6-10. This is the case given that there is only one reaction consuming oxalic acid with a stoichiometry of 2 moles of OH consumed per mole of oxalic acid degraded:

$$k_{all} = k_{rec} + 2k_{ox} \quad \text{Eq. 6-10}$$

On the other hand, since the irradiated section (annular sections of the Photo-CREC Water II unit and the Photo-CREC Water Solar Simulator) and the non-irradiated well mixed tank section are configured in a closed loop, the boundary conditions for Eq. 6-7 are determined by the non-irradiated well mixed tank section. This unit can be described by a CSTR. As a result, the following physically sound assumptions can be adopted: i) the inlet stream is the one exiting the reactor unit, ii) there is a uniform depletion of free radicals throughout the non-irradiated tank and iii) the outlet stream is the one fed to the photoreactor unit inlet. Thus, the following Eq. 6-11 stands as adequate:

$$V \frac{dC_f^{tank}}{dt} = \dot{v} C_{f\ in} - \dot{v} C_f^{tank} + V(-r_{all}) \quad \text{Eq. 6-11}$$

where the LHS accounts for accumulation in the mixing tank, the 1st and 2nd RHS terms account for the free radicals going in and out, respectively, and the 3rd RHS term

considers depletion of free radicals due to all the reactions. Additionally, by substituting Eq. 6-10 into equation Eq. 6-11, the following Eq. 6-12, can be obtained:

$$\tau_{tank} \frac{dC_f^{tank}}{dt} = C_{f,z=L}^{\downarrow} - (\tau_{tank} k_{all} + 1) C_f^{tank} \quad \text{Eq. 6-12}$$

Where  $C_f^{tank}$  represents the surface concentration of adsorbed free radicals on the photocatalyst particles evolving in the non-irradiated mixing tank;  $C_{f,z=L}^{\downarrow}$  denotes the free radical concentration at the photoreactor unit outlet and  $\tau_{tank}$  stands for the mixing tank average residence time.

#### 6.4.4 Efficiency factor

The above described sets of equations, considers radiation models, kinetic models and mixing models. They can be combined to establish an expression for the overall reactor performance. This equation allows one to define an efficiency factor to compare the performance of slurry photocatalytic reactors of different geometries and scales in a practical yet comprehensive manner.

With this end, Eq. 6-3 is substituted within Eq. 6-7 and integrated within the internal radius ( $r_{int}$ ) and the external radius ( $r_{ext}$ ) for all azimuth positions yielding Eq. 6-13:

$$\frac{\partial C_f}{\partial t} = A C_{cat} \int_0^{2\pi} \int_{r_{int}}^{r_{ext}} \left( \sqrt{B \frac{LVREA(\rho, \theta', z)}{C_{cat}} + 1} - 1 \right) r dr d\theta' - k_{all} C_f - D_z \frac{\partial^2 C_f}{\partial z^2} + v_z \frac{\partial C_f}{\partial z} \quad \text{Eq. 6-13}$$

Additionally, under the experiments conducted for the present study, steady state can be assumed for the absorbed free radical balance. It is important to mention that, even when the reactor is considered to be operated in batch mode the  $C_f$  concentration under constant irradiance, becomes a function of spatial coordinates only. Thus, Eq. 6-14 and Eq. 6-15, simplifies as follows:

$$D_z \frac{\partial^2 C_f}{\partial z^2} - v_z \frac{\partial C_f}{\partial z} + k_{all} C_f = A C_{cat} \int_0^{2\pi} \int_{r_{int}}^{r_{ext}} \left( \sqrt{B \frac{LVREA(\rho, \theta', z)}{C_{cat}} + 1} - 1 \right) r dr d\theta' \quad \text{Eq. 6-14}$$



$$f_{tank} = \frac{1}{(\tau_{tank}k_{all} + 1)} C_{f_{z=L}}^{\downarrow} \quad \text{Eq. 6-15}$$

Eq. 6-14 and Eq. 6-15 can be expressed in dimensionless form, by assuming  $z^* = \frac{z}{L}$ ,  $\vartheta = \frac{C_f}{C_{f_0}}$  and  $\varphi^*(\rho, \theta', z^*) = B \frac{LVREA(\rho, \theta', z)}{C_{cat}}$ , to obtain Eq. 6-16 and Eq. 6-17:

$$\left(\frac{D_z}{CL^2}\right) \frac{\partial^2 \varepsilon}{\partial z^{*2}} - \left(\frac{v_z}{CL}\right) \frac{\partial \varepsilon}{\partial z^*} + \varepsilon = \left(\frac{A C_{cat}}{k_{all}}\right) \int_0^{2\pi} \int_{r_{int}}^{r_{ext}} \left(\sqrt{\varphi^*(\rho, \theta', z^*) + 1} - 1\right) r dr d\theta' \quad \text{Eq. 6-16}$$

$$\varepsilon_{z^*=0}^{\downarrow} = \frac{1}{(\tau_{tank}k_{all} + 1)} \varepsilon_{z^*=1}^{\downarrow} \quad \text{Eq. 6-17}$$

Furthermore and considering a volume averaged dimensionless variable " $\vartheta$ ", a dimensionless factor can be obtained, as presented in equation Eq. 6-18:

$$\eta = \left( \phi_{reactor} \left( \int_0^1 \vartheta dz^* \right) + (1 - \phi_{reactor}) (\vartheta_{z^*=0}^{\downarrow}) \right) \quad \text{Eq. 6-18}$$

where  $\phi_{reactor}$  represents the ratio between the volume of the annular photoreactor unit, divided by the total volume of the reaction system.

Finally  $\eta$ , being a dimensionless volume-averaged value of  $C_f$ , can be substituted into Eq. 6-6, when  $K_A C_{Ox} \gg 1$  to obtain Eq. 6-19:

$$r = \eta k^* \quad \text{Eq. 6-19}$$

where  $k^*$  is a zero-th order kinetic constant, and  $r$  is the oxalic acid degradation rate.

One should notice that Eq. 6-19 is able to account for changes on the most relevant scale-up variables in annular photoreactors such as i) size, ii) geometry, iii) mixing, iv) irradiance conditions and v) photocatalyst concentration.

Additionally, if the rate of free radical generation/depletion on the photocatalyst particle is much faster than potential concentration changes resulting from hydrodynamic effects,

the latter does not affect the photocatalytic reactor performance, i.e.  $\left(\frac{D_z}{CL^2}\right)\frac{\partial^2\vartheta}{\partial z^{*2}} - \left(\frac{v_z}{CL}\right)\frac{\partial\vartheta}{\partial z^*} \approx 0$  and  $\tau_{tank}k_{all} \gg 1$ .

By taking advantage of this condition Eq. 6-16, Eq. 6-17, Eq. 6-18 and Eq. 6-19 can be simplified to yield:

$$r_{ox} = \phi_{reactor}(k^{**} C_{cat}) \int_0^{2\pi} \int_{r_{int}}^{r_{ext}} \int_0^L \left( \sqrt{B \frac{LVREA(\rho, \theta', z^*)}{C_{cat}} + 1} - 1 \right) r \, dz dr d\theta \quad \text{Eq. 6-20}$$

where,  $k^{**} = \left(k^* \frac{A}{k_{all}}\right)$ , is a lumped zero-th order kinetic parameter. One should note that all the other symbols retain their respective meanings and notations.

It is interesting to point out that for most cases considered in the present study Eq. 6-20 is expected to hold true. This equations have never been proven to hold for reactors above the laboratory scale (i.e. above 1-2 L of irradiated volume). One should always have however as a reference the most general radiation-kinetic model as reported in Eq. 6-16, Eq. 6-17, Eq. 6-18 and Eq. 6-19, particularly useful when unsteady or periodic irradiation is applied or for cases where a high efficiency photocatalyst is considered.

## 6.5 Results and Discussion

The methods proposed by [Valades-Pelayo et al., 2014b](#) and [Valades-Pelayo et al. 2014c](#) for solving RTE using MC in the Photo-CREC Water II and Photo-CREC Solar Simulator, required the combined solution of Eq. 6-16 to Eq. 6-19.

To be able to apply these equations seven parameters have to be determined: i) axial dispersion coefficients ( $D_z$ ) and average axial velocities ( $v_z$ ) for both reactors, ii) charge recombination parameters for  $\text{TiO}_2$  ( $B$ ), iii) free radical source ( $A$ ) and sink term ( $k_{all}$ ) coefficients and iii) the oxalic acid kinetic constant ( $k^*$ ). To minimize cross correlation issues, these seven parameters were obtained by via non-linear regression with independent data sets.

First, the  $v_z$  and  $D_z$  for both photoreactors were determined using non-reactive tracer experiments. Second,  $A$ ,  $B$  and  $k_{all}$  were established by degradation experiments at different photocatalyst concentrations and lamp emissions in the bench-scale Photo-CREC Water II photoreactor. Finally, degradations in the Photo-CREC Solar Simulator (Photo CREC Water III) were performed at different photocatalyst concentrations, to assess the suitability of the proposed scale-up approach.

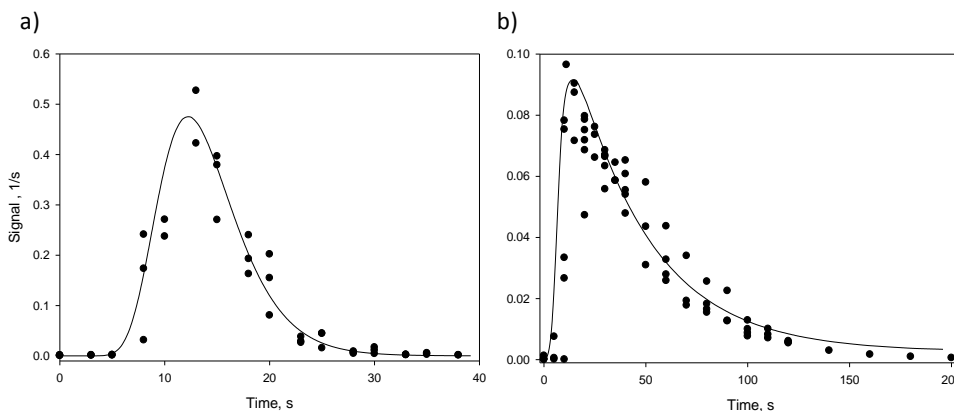


**Figure 6.3** Figure 8 RTD tracer experiments (•) and simulations (–) for (a) the Photo-CREC Water II and (b) the scaled-up Photo-CREC Solar Simulator. Simulations used axial dispersion coefficients ( $D_z$ ) of (a)  $12.0 \text{ cm}^2\text{s}^{-1}$  and (b)  $65.0 \text{ cm}^2\text{s}^{-1}$ . Both systems had a volumetric flow of  $13.5 \text{ cm}^3\text{s}^{-1}$ .

Figure 6.3 reports the RTD fitting using a plug flow reactor, with axial dispersion. The axial dispersion model fits the experimental data well for; a) Photo-CREC Water II reactor with a  $v_z$  of  $1.22 \text{ m/s}$  and an  $D_z$  of  $12 \text{ cm}^2/\text{s}$ , b) the scaled-up Photo-CREC Solar Simulator (Photo-CREC Water III) with a  $v_z$  of  $1.00 \text{ m/s}$  and an  $D_z$  of  $65 \text{ cm}^2/\text{s}$ .

Kinetic parameters were determined in the bench scale Photo-CREC Water II using least square fitting as shown in Figure 6.4. Figure 6.4a) reports the reaction rate dependence with respect to lamp emission, at four different photocatalyst loadings. Both model reaction rates (–) and experiments are reported in this figure. Furthermore Figure 6.4b) shows the simulated (–) and experimental (○) reaction rate dependence with respect to photocatalyst loading, for a 100% nominal lamp emission.

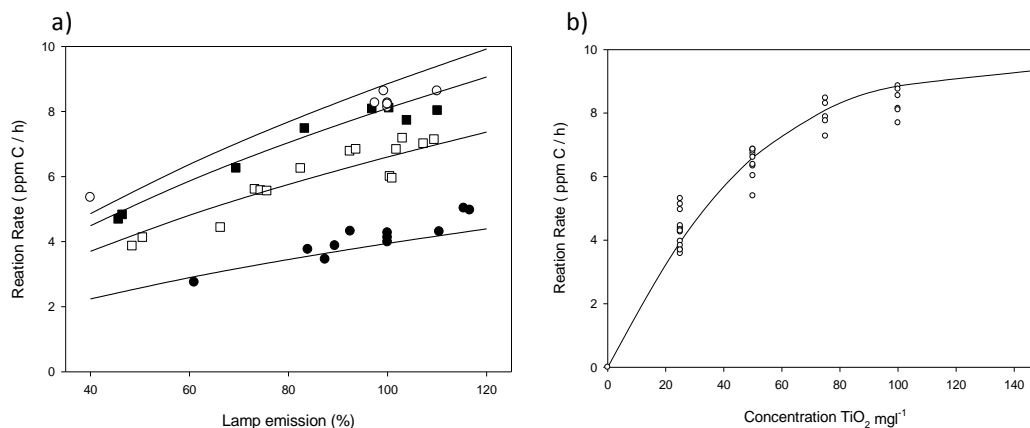


**Figure 6.4** Experimental degradation rates for oxalic acid in the Photo-CREC Water II Photoreactor, under a) different lamp irradiances at (●) 25 mg<sup>l</sup><sup>-1</sup>, (□) 50, (■) 75 and (○) 100 mg<sup>l</sup><sup>-1</sup> photocatalyst loadings. (b) Degradation rates at (○) different photocatalyst loadings (100% lamp emission) in the Photo-CREC Water II photoreactor. Simulations (—) presented for both cases.

Table 6.1 reports the optimized parameters with their respective 95% C.I. One can notice that the proposed methodology yields satisfactory results with the photocatalytic reactor performance successfully modelled at different catalyst loadings and lamp irradiances. Furthermore Table 6.1 also shows large 95% C.I. for parameters A and C. The 95% C.I. are even larger than the parameter values themselves. Thus, it is on this statistically sound basis, that the model can be safely simplified as reported in Eq. 6-20 eliminating A,  $k_{all}$  and  $k^*$  from the analysis, by considering a single lumped parameter,  $k^{**}$ , as presented in section 6.4.4.

**Table 6.1.** Optimized parameters for the model considering Eq. 6-16 to Eq. 6-19.

Parameter	Value	Units	95% C.I. span
A	$3.03 \times 10^{-4}$	$l \text{ g}^{-1} \text{ h}^{-1}$	$\pm 1940\%$
B	$2.51 \times 10^{-6}$	$\text{g W}^{-1}$	$\pm 5.95\%$
$k_{all}$	$6.70 \times 10^{-2}$	$\text{h}^{-1}$	$\pm 1740\%$
$k^*$	$1.05 \times 10^6$	$\text{ppm C h}^{-1}$	$\pm 1651\%$

Table 6.2 shows the B and k\*\* regressed parameters of the simplified model, displaying in this case with limited 95% C.I. and suggesting as a result a satisfactory kinetic model.

**Table 6.2.** Optimized parameters for the model considering Eq. 6-20.

Parameter	Value	Units	95% C.I. span
B	$2.56 \times 10^{-6}$	$\text{g W}^{-1}$	$\pm 4.72\%$
k**	$4.75 \times 10^5$	$\text{ppm C h}^{-1}$	$\pm 5.61\%$

As a result, it can be observed that scale up model needs to account for the quick photocatalyst deactivation, with essentially no additional reaction taking place in the mixing tank. This is true for both Photo-CREC-Water II and Photo-CREC Solar Simulator (Photo-CREC Water III).

Furthermore, by using the model of Eq. 6-20 and previously determined parameters reported in Table 6.2 for the scaled-up annular photoreactor, the photocatalytic performance in the Photo-CREC Solar Simulator (Photo-CREC Water III) is calculated. Figure 6.5 shows model predictions (–) and experimental results (○) for the degradation rate of oxalic acid. One can notice that the model capture the rapid increase of photoreaction rate before  $30 \text{ mg l}^{-1}$ , and the fact that once the photocatalyst concentration reaches  $30 \text{ mg l}^{-1}$ , the photoreaction rate augments at a slower pace.

As it can also be noticed from Figure 6.5, that the proposed model display a slight overestimation with respect to the experimentally determined reaction rates in the Photo-CREC Water Solar Simulator (Photo-CREC Water III). This is most likely a consequence of the overprediction of the LVREA calculated by the RTE Monte Carlo method proposed, as mentioned in section 5.5 and 5.6 (Valades-Pelayo et al., 2014c).

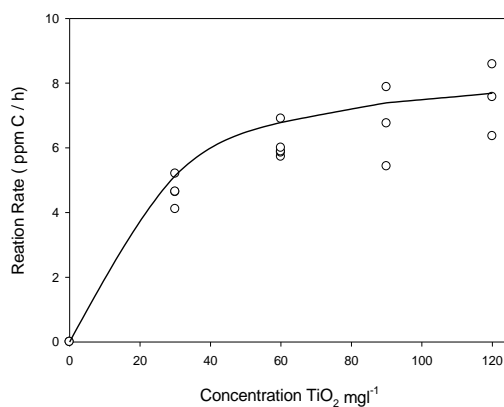


**Figure 6.5** (o) Experimental and (—) simulated degradation rates for oxalic acid in the Photo-CREC Water Solar Simulator (Photo-CREC-Water II) under different photocatalyst loadings at nominal lamp emission (100% lamp emission), with all 8 lamps turned on.

On this basis, a physically sound model, using 2 kinetic parameters, was successfully employed to model the oxalic acid photodegradation in two slurry bench-scale photocatalytic reactors at different irradiance conditions and photocatalyst concentrations. More importantly, this model can be used to calculate energy efficiency factors such as the Photocatalytic Thermodynamic Efficiency Factor (PTEF) and the Quantum Yields (QY) to compare on a quantitative basis, the relative reactor efficiencies.

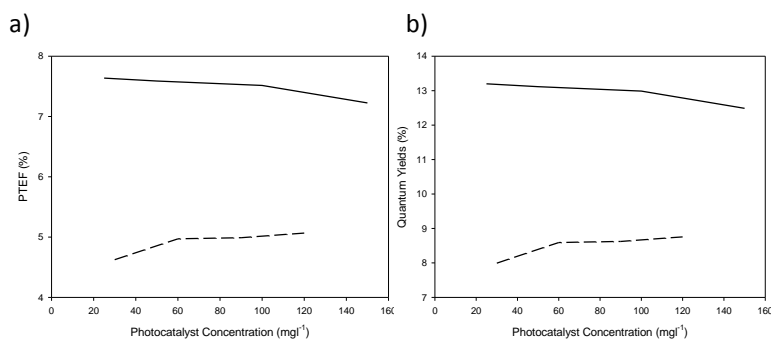


**Figure 6.6** a) Photocatalytic Thermodynamic Efficiency Factors (PTEF) and b) Quantum Yields (QY) are presented for (—) the photo-CREC Water II and (---) the Photo-CREC Solar Simulator, for photocatalyst concentrations of  $25 \text{ mg l}^{-1}$  to  $150 \text{ mg l}^{-1}$ .

In Figure 6.6 the PTEF and b) the QY are shown for different reactors and photocatalyst concentrations, ranging from 20 to 150 mg $l^{-1}$ . Figure 6.6a presents the PTEF. For the Photo-CREC Water II reactor, is seen to lay between 7.5-8.0%, while for the Photo-CREC Water Solar Simulator, PTEF drops between 4.5-5.0%. Additionally, Figure 6.6b presents QY. For the Photo-CREC Water II reactor, QY lays between 12.5-13.0%, while for the Photo-CREC Water Solar Simulator, drops to values of 8.0-8.5%.

On this basis, with the aid of the proposed model, one can conclude that during the scale-up process, going from the Photo-CREC Water II to the Photo-CREC Water Solar Simulator, a photocatalytic efficiency loss of 44% is expected when both reactors are operated at 40 mg $l^{-1}$ . More importantly, this efficiency loss decreases as concentration is increased, dropping to 30%, at about 120 mg $l^{-1}$ .

## 6.6 Conclusions

- a) A physically based, simplified, predictive approach for bench to pilot plant scale reactors is proposed.
- b) The proposed model considers irradiance boundary conditions, photocatalyst concentration as well as optical properties, reactor hydrodynamics and physically based degradation rates account for charge separation/recombination along with pollutants adsorption on the photocatalyst surface.
- c) The proposed model of the present study is able to predict important parameters for photocatalytic reaction engineering, with this model being suitable at two photocatalytic reactor scales: 2.6 liters and 9.6 liters.
- d) The proposed model provides adequate prediction of changes of oxalic acid concentrations by accounting for a distribution of adsorbed free radicals on the photocatalyst particle.
- e) The proposed model, applied under the conditions of the photocatalytic reactors considered in this study (Photo-CREC water II and Photo-CREC Water Solar Simulator),

allows one establishing the changes of quantum yields and PTEF as a result, important parameters for the scale up of photocatalytic reactors.

## 6.7 References

Ahmed, S., Rasul, M., Martens, W., Brown, R., & Hashib, M. (2010). Heterogeneous photocatalytic degradation of phenols in wastewater: A review on current status and developments. *Desalination* , 261, 3-18.

Alfano, O. M., Bahnemann, D., Cassano, A. E., Dilliert, R., & Goslich, R. (2000). Photocatalysis in Water Environments Using Artificial and Solar Light. *Catalysis Today* , 58, 199-230.

Alfano, O. M., Cabrera, M. I., & Cassano, A. E. (1997). Photocatalytic Reactions Involving Hydroxyl Radical Attack. *Journal of Catalysis* , 172, 370–379.

Bahnemann, D. (2004). Photocatalytic Water Treatment: Solar Energy Applications. *Solar Energy* , 77, 445-459.

Baniasadi, E., Dincer, I., & Naterer, G. F. (2012). Radiative heat transfer and catalyst performance in a large-scale continuous flow photoreactor for hydrogen production. *Chemical Engineering Science* , 84, 638-645.

Berger, K., Weidlich, A., Wilkie, A., & Magnor, M. (2012). Modeling and Verifying the Polarizing Reflectance of Real-World Metallic Surfaces. *IEEE Computer Graphics and Applications* , 32(2).

Camera-Roda, G., Santarelli, F., & Martn, C. A. (2005). Design of photocatalytic reactors made easy by considering the photons as immaterial reactants. *Solar Energy* , 79, 343-352.

Cassano, A., & Alfano, O. (2000). Reaction engineering of suspended solid heterogeneous photocatalytic reactors. *Catalysis Today* , 58, 167-197.

Colbert, M., Patanaik, S., & Krivanek, J. (2006). BRDF-Shop: creating physically correct bidirectional reflectance distribution functions. *IEEE Computer Graphics and Applications* , 26(1) , p. 30-36.

Curcó, D., Giménez, J., Addardak, A., Cervera-March, S., & Esplugas, S. (2002). Effects of radiation absorption and catalyst concentration on the photocatalytic degradation of pollutants. *Catalysis Today* , 76, 177-188.



Davydov, L., Tsekoy, R., & Smirniotis, P. G. (2001). Optimal radiation field in one-dimensional continuous flow heterogeneous photocatalytic reactors. *Chemical Engineering Science* , 56, 4837-4847.

de Lasa, H., Serrano, B., & Salaices, M. (2005). *Photocatalytic Reaction Engineering*. New York: Springer.

Duran, A., Monteagudo, J. M., San Martin, I., & Aguirre, M. (2010). Decontamination of industrial cyanide-containing water in a solar CPC pilot plant. *Solar Energy* , 84 1193-1200.

Fujishima, A., Kohayakawa, K., & Honda, K. (1975). Hydrogen Production under Sunlight with an Electrochemical Photocell. *Journal of Electrochemical Society* , Vol. 22, Issue 11 , pag. 1487-1489.

Gaya, U. I., & Abdullah, A. H. (2008). Heterogeneous photocatalytic degradation of organic contaminants over titanium dioxide: A review of fundamentals, progress and problems. *Journal of Photochemistry and Photobiology C:Photochemistry Reviews* , 9, 1-12.

Hyde, M. W., Schmidt, J. D., & Havrilla, M. J. (2009). A geometrical optics polarimetric bidirectional reflectance distribution function for dielectric and metallic surfaces. *Optics Express* , Vol. 17 , Issue 24, pag. 22138-22153.

Imoberdorf, G. E., Irazoqui, H. A., Alfano, O. M., & Cassano, A. E. (2007). Scaling-Up from first principles of a photocatalytic reactor for air pollution remediation. *Chemical Engineering Science* , 62, 793-804.

Imoberdorf, G. E., Taghipour, F., Keshmiri, M., & Mohseni, M. (2008). Predictive radiation field modeling for fluidized bed photocatalytic reactors. *Chemical Engineering Science* , 63, 4228-4238.

Ismail, A. A., & Bahnemann, D. W. (2014). Photochemical splitting of water for hydrogen production by photocatalysis: A review. *Solar Energy Materials & Solar Cells* , 128, 85-101.

Kapinus, E., Viktorova, T., & Khalyavka, T. (2009). Dependence of the rate of photocatalytic decomposition of safranin on the catalyst concentration. *Theoretical and Experimental Chemistry* , Vol. 45, No.2 .

Kawaguchi, H. (1994). Dependence of Photocatalytic Reaction Rate On Titanium Dioxide Concentration In Aqueous Suspensions. *Environmental Technology* , 15:2, 183-188.

Koc̃í, K., Reli, M., Kozák, O., Lacny', Z., Plachá, D., Praus, P., et al. (2011). Influence of reactor geometry on the yield of CO<sub>2</sub> photocatalytic reduction. *Catalysis Today*, 176, 212-214.

Lawless, D., Serpone, N., & Meisel, D. (1991). Role of the OH radicals and trapped Holes in Photocatalysis. A Pulse Radiolysis Study. *Journal of Physical Chemistry*, 95, 5166-5170.

Li Puma, G., & Brucato, A. (2007). Dimensionless analysis of slurry photocatalytic reactors using two-flux and six-flux radiation absorption-scattering models. *Catalysis Today*, 122 78-90.

Liao, H., & Reitberger, T. (2013). Generation of Free OH Radicals by Black Light Illumination of Degussa (Evonik) P25 TiO<sub>2</sub> Aqueous Suspensions. *Catalysts*, 3, 418-443.

Malato, S., Blanco, J., Vidal, A., & Richter, C. (2002). Photocatalysis with solar energy at a pilot-plant scale: an overview. *Applied Catalysis B: Environmental*, 37, 1-15.

Marugan, J., van Grieken, R., Cassano, A. E., & Alfano, O. M. (2009). Scaling-up of slurry reactors for the photocatalytic oxidation of cyanide with Ti<sub>2</sub>O and silica-supported Ti<sub>2</sub>O suspensions. *Catalysis Today*, 144, 87-93.

Marugan, J., van Grieken, R., Pablos, C., Satuf, L. M., & Cassano, A. E. (2013). Modeling of a bench-scale photocatalytic reactor for water disinfection from laboratory-scale kinetic data. *Chemical Engineering Science*, 224, 39-45.

Minero, C., & Davide, V. (2006). A quantitative evaluation of the photocatalytic performance of Ti<sub>2</sub>O slurries. *Applied Catalysis B: Environmental*, 67, 257-269.

Mohamed, H. H., & Bahnemann, D. W. (2012). The role of electron transfer in photocatalysis: Fact and fictions. *Applied Catalysis B: Environmental*, 128, 91-104.

Moreira, J., Serrano, B., Ortiz, A., & de Lasa, H. (2011). TiO<sub>2</sub> absorption and scattering coefficients using Monte Carlo method and macroscopic balances in a photo-CREC unit. *Chemical Engineering Science*, 66, 5813-5821.

Motegh, M., Cen, J., Appel, P. W., van Ommen, R., & Kreutzer, M. T. (2012). Photocatalytic-reactor efficiencies and simplified expressions to assess their relevance in kinetic experiments. *Chemical Engineering Journal*, 207-208, 607-615.

Ortiz-Gomez, A., Serrano-Rosales, B., Salaices, M., & De Lasa, H. (2007). Photocatalytic Oxidation of Phenol: Reaction Network, Kinetic Modeling, and Parameter Estimation. *Industrial & Engineering Chemistry Research*, 46(23), 7394-7409.

Oyama, T., Otsu, T., Hidano, Y., Takayoshi, K., Serpone, N., & Hidaka, H. (2011). Enhanced remediation of simulated wastewaters contaminated with 2-chlorophenol and other aquatic pollutants by TiO<sub>2</sub>-photoassisted ozonation in a sunligh-driven pilot-plant scale photoreactor. *Solar Energy*, 85, 938-944.

Salaices, M., Serrano, B., & de Lasa, H. (2002). Experimental Evaluation of photon absorption in an aqueous TiO<sub>2</sub> Slurry reactor. *Chem. Eng. J.*, 90, 219.

Serrano, B., Ortiz, A., Moreira, J., & de Lasa, H. (2009). Energy Efficiency in Photocatalytic Reactors for the Full Span of Reaction Times. *Industrial and Engineering Chemistry Research*, 48, 9864-9876.

Turchi, C., & Ollis, D. (1989). Photocatalytic Degradation of Organic Water Contaminants: Mechanisms Involving Hydroxyl Radical Attack. *Journal of Catalysis*, 122, 178-192.

Valades-Pelayo, P. J., Moreira, J., Serrano, B., & de Lasa, H. I. (2014a). Boundary conditions and phase functions in a Photo-CREC Water-II Reactor Radiation Field. *Chemical Engineering Science*, 107, 123-136.

Valades-Pelayo, P. J., Moreira, J., Solano-Flores, P., Serrano, B., & De Lasa, H. (2014b). Establishing photon absorption fields in a Photo-CREC Water II Reactor using a CREC-spectroradiometric probe. *Chemical Engineering Science*, 116, 406-417.

Valades-Pelayo, P.J., Guayaquil-Sosa, F., Serrano, B., de Lasa, H. (2014c). Scaled-up Photocatalytic Reactor Under Different Irradiance Conditions: Validation of a Fully Predictive Radiation Absorption Model. *Chemical Engineering Science*. Accepted in November 2014.

## Chapter 7

### 7 Conclusions and Recommendations

As described in the literature section of this PhD thesis, there is a lack of scale-up methodologies for designing photocatalytic reactors. There is in fact, a pressing need to evolve from bench-scale units to the pilot plant designs. In this respect, one can envision larger externally irradiated pilot plant reactors. To successfully accomplish this, radiation absorption fields and related parameters such as LVRPA have to be established. As reported in Section 2.4 of this PhD Dissertation, in order to calculate the LVRPA, one has to be able to determine suitable phase functions. Furthermore, one can also notice the need for better methods to assess photocatalyst performance, together with improved radiation modelling. Thus, there are significant gaps in current photocatalytic reaction engineering design, with these issues being thoroughly addressed in the present PhD research.

#### 7.1 Conclusions

The following can be considered as the most significant contributions of this PhD research:

- a) A Monte Carlo (MC) probabilistic based method was developed. This probabilistic approach was established in a 3D framework, allowing slurry photocatalytic reactor modelling and LVRPA calculations. This comprehensive method also considered detailed boundary conditions. By using this approach, it was proven that photon scattering plays a significant role in identifying critical simulation factors such as BCs (boundary conditions) and scattering parameters.
- b) MC simulations of this PhD dissertation allowed one to show that the Total Rate of Photon Absorption (TRPA) provides limited discrimination between scattering models and boundary conditions (BCs) when using the Total Transmittance measurements (TT) as a basis for comparison.
- c) The MC simulations of this study, demonstrated as described in Chapter 3, that the MC yields adequate predictions of the experimental TT of Degussa P25 in the

Photo-CREC Water II Reactor. These valuable findings were obtained when considering a forward scattering mode phase function (H-G phase function with “ $g$ ” in the 0.6-0.8 range) and a highly absorptive outer BC ( $P_{\text{absWall}}$  close to 1).

- d) A novel radiometric probe (CREC-PS) was designed and developed in the context of the present PhD research. This radiometric probe allows one to reduce the uncertainty of the radiation radial profiles as described in Chapter 4. This probe was designed to obtain radial irradiance distributions in the annular channel of a Photo-CREC Water II Reactor. One should also note that the MC method reported in Chapter 3, was modified later in Chapter 4 to account for probe intrusion in the slurry.
- e) Regarding the determination of the radiation absorption fields, the coupling of radial measurements, with a modified MC method, yielded a significantly increased accuracy. This gave LVRPA with reduced spans (as defined in section 4.4.2) of  $\pm 6\%$  and “ $g$ ” H-G phase function values of  $0.68 \pm 0.03$ . On this basis, the combined data from the MC model and the experimental radial irradiance profiles, as reported in Chapter 4, allowed one to clarify both boundary conditions for the Radiative Transfer Equation (RTE) and radiation gradients within the annular section.
- f) The radiation and absorption fields of an externally irradiated Solar Simulator Photo-CREC Water Photo Reactor with 10 L of irradiated volume were successfully modelled as shown in Chapter 5. This "a priori" MC method considers: i) all photon-surface interactions being either ideally diffuse or specular, depending on the material optical properties and ii) all photon-photocatalyst interactions being defined by optical parameters previously determined in Chapter 4 and by Cabrera et al. 1995. This "a priori" MC method, with no adjustable parameters was validated by solving the RTE (Radiative Transfer Equation) for different asymmetric irradiance conditions. Additionally, this MC method was optimized by considering the following: i) the radiation

angular periodicity, ii) the value of splitting the reactor geometry into “concave” subsets and iii) the importance of employing a “shortest-positive distance” criteria. This original approach allowed predicting the TRPA and LVREA for five different irradiance configurations and photocatalyst loadings, in the 20 to 400  $\text{mg l}^{-1}$  range.

- g) A comprehensive kinetic model accounting for radiation field computations as reported in Chapter 3, Chapter 4 and Chapter 5, is established in Chapter 6. This kinetic model is proposed as a scale-up tool for bench to pilot plant scale reactors. Additionally, Chapter 6 reports the experimental validation of the proposed kinetic model by considering the photodegradation of oxalic acid at a pH of 3.25, using Degussa P25. This was accomplished in both the Photo-CREC Water II Reactor and the Photo-CREC Solar Simulator Reactor at various photocatalyst concentrations and different irradiance conditions.
- h) The significance of the pH in the slurry optical properties, affecting particle agglomeration was considered in Chapter 6. To accomplish this, the optical slurry parameters as well as the radiation absorption fields were recalculated by applying the methodology of Chapter 4 at a pH of 3.25. From this analysis, a “ $g$ ” = 0.41 for the H-G phase function was found to predict the radial irradiance profiles. Therefore, it is determined that for Degussa P25, the phase function, needs to consider reduced forward scattering as pH decreases.
- i) The validation of the comprehensive photocatalytic reactor radiation-kinetic model of Chapter 6 was achieved by calculating the concentration of adsorbed free radicals on the photocatalyst particle surfaces. This involved establishing the following: i) detailed irradiance boundary conditions, ii) agglomerate optical properties, iii) photocatalyst charges recombination and surface properties, iv) RTD in the annular photoreactor and mixing tanks at both scales and v) Langmuir-Hinshelwood kinetics for pollutant absorption on the photocatalyst particles. To our knowledge, this is the first physically based radiation-kinetic

model reported in the literature, able to predict radiation as well as degradation rates at reactor scales larger than the laboratory scale.

## 7.2 Future Work

There are several important issues that have arisen, based on the models examined and the observations made during this PhD thesis dissertation. In addition, there are areas of opportunity and possible approaches for future work. On this basis, a number of recommendations are provided in this section, regarding how the reported models could be improved and the experimental methodologies could be refined. Such improvements are necessary if aiming to extensively apply the scale-up and optimization methodologies to commercial scale photocatalytic reactors.

A first area of opportunity consists in improving the proposed model by accounting for the pH and agglomeration effects at a radiative, as well as at a chemical kinetic level. This, of course, would require the following:

- i) Determining the optical properties at different pHs, under different mixing patterns and intensities for a wide range of photocatalyst concentrations. This would provide insights into the dependency of the radiation absorption fields when changing the pH, the mixing and the radiation conditions. This could be accomplished by using the reported MC method of Chapter 4.
- ii) Characterizing the agglomerate size distribution when changing agitation, pH and photocatalyst concentration. From this information, the PSD (Particle Size Distribution) analysis could be employed, to establish the “correct” photocatalyst external specific surface area, " $S_p$ ", currently used to represent the actual irradiated surface area. By considering this important parameter, a physically based model could be proposed to account for agglomeration as well.
- iii) Validating kinetic models that account for agglomeration. This should be done using a wide range of photocatalyst concentrations and pHs. Targeted conditions will be the ones where agglomeration and other particle properties are suspected to influence photocatalytic activity. The value of these model improvements could

influence reaction rates and radiation fields improvements of photocatalytic reactors of different scale.

A second area of opportunity for future work would be the extension of these methodologies for cases where the chemical paths differ from the single step oxidation scheme (oxalic acid) considered in Chapter 6. This could encompass:

- i) The study of photodegradation reactions involving several reaction steps and intermediates.
- ii) The determination of whether all the chemical species involved in the photodegradation scheme, present the same dependence with respect to the radiation absorption fields and charge separation-recombination mechanisms.

Finally, a third area of opportunity could be the study of the direct application of the methodologies presented in this PhD dissertation at the commercial scale (e.g. 2000 liters/day of drinking water for a population of 1000 inhabitants). This would be done for the purpose of promoting photocatalysis to become more standardized and/or competitive at an industrial scale. This could involve the following:

- i) The application of the scale-up methodologies for photocatalysts suitable for solar irradiation (lower band gaps) or with minimum charge recombination.
- ii) The study of methodologies to determine key scale-up parameters of important reactions such as phenol photodegradation, water-splitting or even for real-life scenarios where several types of photocatalytic processes may take place (e.g. pollutants converted via photo-oxidation and photo-reduction).
- iii) The standardization of a methodology for complete chemical and optical photocatalyst characterization. The aim would be to establish a benchmark that would facilitate quantification of the overall photocatalytic activity under different conditions and designs. This would allow an objective comparison between novel and existing photocatalysts for their applicability to specific photocatalytic reactor designs.



## Curriculum Vitae

**Name:** Patricio Javier Valades Pelayo

**Post-secondary Education and Degrees:** Doctor of Philosophy in Chemical Engineering  
The University of Western Ontario  
London, Ontario, Canada  
2010–2014

Bachelor of Chemical Engineering  
Universidad Autonoma de Nuevo Leon  
Monterrey, Nuevo Leon, Mexico  
2004–2009

**Honours and Awards:** PhD Scholarship  
Consejo Nacional de Ciencia y Tecnologia  
Mexico D.F., Mexico  
2010–2014

Honorary Bachelor's Degree  
Universidad Autonoma de Nuevo Leon  
Monterrey, Nuevo Leon, Mexico  
2004–2009

Exchange Student Scholarship (Technische Universitat Munchen)  
Deutscher Akademischer Austausch Dienst  
Munchen, Bayern, Deutschland  
2006–2007

**Related Work Experience** Teaching Assistant  
The University of Western Ontario  
London, Ontario, Canada  
2011–2014

Jr. R&D Process Engineer  
Grupo TEVA, SICOR de Mexico  
Toluca, Estado de Mexico, Mexico  
2010

**Publications:**

Moreira, J., Serrano-Rosales B., Valades-Pelayo, P.J., de Lasa, H. (2013). Determination of Kinetic Parameter in a Unified Kinetic Model for the Photodegradation of Phenol by Using Nonlinear Regression and the Genetic Algorithm. *International Journal of Chemical Reaction Engineering*, Vol. 11, Issue 2, p. 641-656.

Valades-Pelayo, P. J., Moreira, J., Serrano, B., & de Lasa, H. I. (2014). Boundary conditions and phase functions in a Photo-CREC Water-II Reactor Radiation Field. *Chemical Engineering Science*, Vol. 107, p. 123-136.

Valades-Pelayo, P. J., Moreira, J., Solano-Flores, P., Serrano, B., & De Lasa, H. (2014). Establishing photon absorption fields in a Photo-CREC Water II Reactor using a CREC-spectroradiometric probe. *Chemical Engineering Science*, Vol. 116, p. 406-417.

Navarro-Tovar, G., Moreira, J., Valades-Pelayo, P.J., de Lasa, H. (2014). Diffusion and Equilibrium Adsorption Coefficients of Aromatic Hydrocarbon Species in Capillary Columns. *International Journal of Chemical Reaction Engineering*. Accepted.

Valades-Pelayo, P.J., Guayaquil-Sosa, F., Serrano, B., de Lasa, H. (2014). Scaled-up Photocatalytic Reactor Under Different Irradiance Conditions: Validation of a Fully Predictive Radiation Absorption Model. *Chemical Engineering Science*. Accepted in November 2014.

Valades-Pelayo, P.J., Guayaquil-Sosa, F., Serrano, B., de Lasa, H. (2015). Eight-Lamp Externally Irradiated Bench-Scale Photocatalytic Reactor: Scale-up and Performance Prediction. *Chemical Engineering Journal*. Submitted in November 2014.